Understanding and Minimising Water Vapour Co-Adsorption for Activated Carbons in Post-Combustion CO_2 Capture

A Thesis Submitted to
The Univesity of Nottingham

By

Shaima Albazzaz
BSc, MSc Chemical Engineering

For the degree of

Doctor of Philosophy

Project Supervisors

Professor Colin Snape, Professor Hao Liu, Dr. Chenggong Sun, Dr. Lee Stevens

School of Chemical and Environmental Engineering
The University of Nottingham
United Kingdom

January 2020

Abstract

The adsorption properties of activated carbons for post-combustion CO_2 capture are affected by water vapour, where co-adsorption can significantly increase the regeneration energy for desorbing CO_2. This research aims to understand and minimise water vapour co-adsorption on activated carbons while maintaining a high capacity for CO_2, and determining the role of organosiloxane compounds as a coating agent to increase the hydrophobic nature of activated carbons.

The activated carbons CS and PR that used in this work were derived separately from coconut shell and phenolic resin. Intercalation of potassium into the carbons was investigated since it is established that this increases CO_2 adsorption capacities significantly. The KOH-activated carbons (CSK and PRK) were coated using a range of organosiloxane compounds and heat treatment of coated activated carbon at different temperatures was investigated to try to maximise CO_2/H_2O selectivity. Heat treatment was used to achieve an acceptable balance between the amount of CO_2 adsorbed and the effect of the coating film. At equilibrium, the coated samples gave much lower CO_2 adsorption capacities and H_2O uptakes compared to the initial KOH-activated carbons due to pore blockage. The two samples, CSKV450 and PRK450, which coated by vinyltrimethoxysilane (VTMOS) and heated to 450 ^oC exhibited the best results compared to other heat-treated samples, a significant reduction in H_2O uptake was observed but the reductions in CO_2 adsorption were still evident.

A detailed assessment of H_2O uptake was performed on the CSKV450 sample using dynamic vapour sorption at 25 ^oC with different relative humidities (10 %, 50 % and 95 %RH). The results were compared with those obtained from non-calcined samples (CS, CSK, and CSKV). At low RH (10 %) and a short contact time (10 minutes), the CO_2/H_2O selectivity for CSK was 2.37 compared to only 0.77 for CS. This provides evidence that intercalation of potassium ions increase CO_2 adsorption at the expense of H_2O. Additionally, the selectivity for CSKV450 (2.12) was close to the selectivity of CSK due to removing most of coating layers after heat treatment. Although the same trend was observed at 50 % and 95 %RH, no significant differences were observed between the samples, and the CO_2/H_2O selectivity remained low, not exceeding 0.6.

At working capacity (75% of the equilibrium capacity of CO_2), the H_2O uptake of CSKV450 is 4.2 wt%, the regeneration heat (Q_{reg}) is 2.26 GJ/tonne CO_2, which is nearly double the regeneration heat in dry conditions, which means, each 1% of moisture led to increase about 0.25 GJ/tonne CO_2 of the regeneration heat. Q_{reg} in wet condition is lower than that in different types of aqueous amine solutions (about 3 GJ/tonne CO_2) and PEI/silica (2.46 GJ/tonne CO_2 in wet condition 2 wt%).

Acknowledgements

I am thankful to Allah for his mercy and bless for doing this work. I would like to express my great appreciation to the Iraqi Ministry of Higher Education and Scientific Research, and the Iraqi Cultural Attaché for the financial support during my study.

I would like to express my sincere gratitude and thanks to my supervisors; Professor Colin E. Snape, Dr. Lee Stevens, Professor Hao Liu, and Dr. Chenggong Sun for their guidance, help, encouragement and advice during the course of this research. A special thanks to, Dr. Lee Stevens and Dr. Xin Liu I have learnt how to do experiments with a strict and careful science attitude and for their help with BET testes. In addition, Professor Colin Snape has been very helpful in understanding the fundamentals and scientific problems. Also I would like to thank Nottingham Transportation Engineering Centre research group, Professor. Gordon Airey, Jonathan Watson and Martyn Barrett for their help with DVS testes.

I would also like to acknowledge the support of my friends, students and staff at the University of Nottingham, particularly, Dr. Shalini Graham, Dr. Wenbin Zhang, Dr. Farooq Sher, Fatih Güleç, Dianne Vincent, Adrian Quinn and Special thanks to Dr. Emily Smith and their colleagues for their help with SEM, XPS and XRF who have all provided me with their time, support, and advice towards the successful completion of this research work. Finally, I would like to express my utmost appreciation to my beloved family; Special thanks to my husband, my children, my

parents, and my lovely sisters for their infinite prayer, support, love and great words of encouragement during the completion this research work all through the years

Table of Contents

Abstract ..... **iii**

Acknowledgements ..... **iii**

Table of Contents ..... **v**

Table of Figures ..... **xi**

List of Tables ..... **xviii**

List of Abbreviations ..... **xx**

Chapter 1: Introduction **1**

1.1 Background 1

1.2 The Greenhouse Gas Effect 1

1.3 Political Response to Reduce Greenhouse Gas Emissions 5

1.4 Energy Supply and Consumption 6

1.5 Reducing CO_2 Emissions 8

1.5.1 Employment of Energy Efficiency and Conservation Practices 8

1.5.2 Switching to Carbon-Free or Reduced-Carbon Sources of Energy 8

1.5.3 Development of CCS Technologies 10

1.6 Aim and Objectives 11

1.7 Organisation of the Thesis 13

Chapter 2: Literature Review **15**

2.1 Introduction 15

2.2 Carbon Dioxide Capture Technologies 15

2.2.1 Pre-Combustion 16

2.2.2 Oxy-Fuel Combustion 17

2.2.3 Post-Combustion 18

2.3 Capture & Separation Processes 19

2.3.1 Chemical Absorption for CO_2 Partial Pressures 19

2.3.2 Physical Absorption for High CO_2 Partial Pressures 20

2.3.3 Membrane Separation....21
2.3.4 Adsorption....22
2.4 Solids Adsorbents for Post Combustion CO_2 Capture....23
2.4.1 Zeolites/Silicas & Adsorbed Bases....23
2.4.2 Metal-Organic Frameworks....26
2.4.3 Activated Carbons....28
2.4.3.1 Textural Characteristics....29
2.5 Activation Methods....31
2.5.1 Physical Activation....31
2.5.2 Chemical Activation....32
2.5.2.1 KOH Activation....32
2.6 Criteria for the Efficiency of Adsorbent Materials....35
2.7 Regeneration Energy for Post Combustion CO_2 Capture....37
2.8 CO_2 Cycle Processes....38
2.9 Cost of CO_2 Capture & Storage....41
2.10 Modification of Activated Carbon for CO_2 Adsorption....42
2.11 Organosiloxane Compounds....46
2.11.1 Introduction....46
2.11.2 Chemical Reactions of Organosiloxane Compounds with Activated Carbon Surfaces....47
2.12 Effect of H_2O on CO_2 Adsorption with Activated Carbon....51
2.13 Conclusions....57
Chapter 3: Experimental and Relevant Theory for the Techniques Used....58
3.1 Materials....58
3.2 Methods....60
3.2.1 Activation & Reactivation of Materials....60
3.2.1.1 Physical Treatment....61
3.2.1.2 Organosiloxane Compound Treatment....61
3.3 Characterisation Techniques....64
3.3.1 Thermogravimetric Analyser (TGA)....64
3.3.1.1 TGA Experimental Procedures....65

3.3.2 N_2 Sorption 66
3.3.2.1 Experimental Procedure 66
3.3.2.2 Theory for Calculations 67
3.3.3 H_2O Sorption Isotherm 71
3.3.4 Heat of Adsorption and Desorption Measurements 72
3.3.5 Calculation Heat of Adsorption 72
3.3.6 Fourier Transform Infrared (FTIR) Spectroscopy 73
3.3.7 Elemental Analysis (EA) 74
3.3.8 Proximate Analysis by TGA 74
3.3.9 SEM-EDX Analysis 75
3.3.10 X-ray Photoelectron Spectroscopy 76
3.3.11 Control of Humidity by Saturated Salt Solutions 77
3.3.12 X-Ray Fluorescence Spectrometry (XRF Analysis) 79
3.3.13 Mechanical Strength Testing 79
3.3.14 Bulk Density 80
3.4 Fundamentals of Adsorption 80
3.4.1 Introduction 80
3.4.2 Theory of Adsorption 82
3.4.3 Types of Isotherms 84
3.4.4 CO_2 Isotherm Models 86
3.4.4.1 Langmuir Model 86
3.4.4.2 Dual-site Langmuir (DSL) Equation 88
3.5 Adsorption Isotherms of Water Vapour on Activated Carbon 90
Chapter 4: Characterisation of the Activated Carbons Investigated 92
4.1 Introduction 92
4.2 Effect of KOH Treatment on Characterisation of Activated Carbons 92
4.3 Effect of Physical and Organosiloxane Compound Treatment on the Characteristics of Activated Carbon 96
4.3.1 Physical Treatment 96
4.3.2 Organosiloxane Compound Treatment 100

4.3.2.1 The Influence of Heat Treatment on the Characteristics of the Coated Activated Carbon 103
4.4 CO_2 Adsorption Measurement (Volumetric) 108
4.5 Micropore Size Distributions of Coconut Shell Activated Carbons 110
4.6 Fourier Transform Infrared Spectroscopy (FTIR) 111
4.7 Elemental Analysis 114
4.8 Proximate Analysis 115
4.9 SEM-EDX Analysis 116
4.10 XPS 119
4.11 Effect of Humidity on Physical Characterisations of Activated Carbon 121
4.12 Conclusions 130
CHAPTER 5: Impact of KOH Treatment on Water Vapour Co-Adsorption for CO_2 Capture of Activated Carbons 131
5.1 Introduction 131
5.2 Effect of Activation Temperature on CO_2 Adsorption 131
5.3 Measurement of the Kinetic Adsorption of CO_2 133
5.4 Measurement of the Static & Dynamic Adsorption of H_2O 135
5.5 Selectivity for CO_2 139
5.6 Conclusions 141
Chapter 6: CO_2 & H_2O Adsorption Capacities of Physically and Organosiloxane Compounds-treated KOH-Activated Carbons 142
6.1 Introduction 142
6.2 Effect of Physical and Organosiloxane Compounds Treatment on CO_2 Adsorption Capacity of KOH-Activated Carbons 143
6.2.1 Coconut Shell-Activated Carbon 143
6.2.1.1 Physical Treatment 143
6.2.1.2 Organosiloxane Compound Treatment 144
6.2.1.3 The Influence of Heat Treatment on the CO_2 Adsorption Capacities of the Organsiloxane-Coated Samples 148
6.2.2 Phenolic Resin-Activated Carbon 151
6.2.2.1 Physical Treatment 151

6.2.2.2 Organosiloxane Compounds Treatment 152
6.2.2.3 The Influence of Heat Treatment on CO_2 Adsorption Capacity.... 153
6.3 Effect of Physical and Organosiloxane Compounds Treatments on H_2O Equilibrium Capacities..... 156
6.3.1 Coconut Shell-Activated Carbon..... 156
6.3.1.1 Physical Treatment 156
6.3.1.2 Organosiloxane Compound Treatment..... 157
6.3.1.3 The Influence of Heat Treatment on H_2O Uptakes 158
6.3.2 Phenolic Resin-Activated Carbon 159
6.3.2.1 Physical Treatment 159
6.3.2.2 Organosiloxane Compounds Treatment 160
6.3.2.3 The Influence of Heat Treatment on H_2O Equilibrium Capacities 161
6.4 Conclusions..... 162
CHAPTER 7: Impact of Organosiloxane Coatings on Water Vapour Co-Adsorption for CO_2 Capture on the KOH-Activated Carbons 163
7.1 Introduction..... 163
7.2 Measurement of the Dynamic Adsorption of CO_2..... 163
7.3 Measurement of the Static Adsorption of H_2O 166
7.4 Measurement of the Dynamic Adsorption of H_2O 168
7.5 Selectivity for CO_2 171
7.6 Humidity Control 173
7.6.1 Comparative Study between TGA and DVS on CS Sample..... 173
7.6.2 CO_2 Adsorption Capacities on Water Vapour Equilibrated Samples .. 174
7.7 Conclusions..... 178
CHAPTER 8: Investigation of Factors Affecting CO_2 Adsorption in Post Combustion Capture 179
8.1 Introduction..... 179
8.2 Volumetric Capacities of Selected Activated Carbons 180
8.3 Heat of Adsorption and Specific Heat of CSs Series..... 182
8.4 Calculation of Regeneration Heat..... 185
8.4.1 Effect of Water Vapour on the Regeneration Heat 187

8.5 Conclusions 189
Chapter 9: Conclusions and Future Work 190
9.1 Conclusions 190
9.2 Recommendations for Further Research 191
References 193
Appendix A 218
BET Isotherm Analysis 218
Appendix B 220
Appendix C 221
Appendix D 224
Appendix E 225

Table of Figures

Figure 1. 1: Sea level rising since 1993 (Cazenave et al., 2018). 2
Figure 1. 2: Increasing CO_2 concentration in the atmosphere (Mauna Loa Observatory). 3
Figure 1. 3: Observed Global Mean Surface Temperature anomalies and record-breaking events (Yin et al., 2018). 3
Figure 1. 4: Average monthly Arctic sea ice extent each September since 1980, derived from satellite observations (Xu, 2018). 4
Figure 1. 5: Global Primary Energy Consumption (BP, 2018). 7
Figure 1. 6: World Gross Domestic Product (GDP) and energy consumption growth (UN, 2019). 7
Figure 1. 7: Global Renewable Power Capacity 2007-2017 (WHO, 2018). 9

Figure 2. 1: Pre-combustion CO_2 capture (Gharaie, 2013). 16
Figure 2. 2: Oxy-Fuel-Combustion CO_2 Capture system (Gharaie, 2013). 18
Figure 2. 3: Simplified flow sheet of the CO_2 absorption process (Gharaie, 2013). 20
Figure 2. 4: Membrane Separation Technology in Carbon Capture (Ji and Zhao, 2017). 22
Figure 2. 5: Schematic representation (a) three-dimensional and (b) two dimensional (Rodriguez-Reinoso, 1998). 29
Figure 2. 6: N_2 and O_2 surface groups on carbon (Figueiredo, 2013). 30
Figure 2. 7: CO_2 adsorption isotherms at 0 ^oC (O), 25 ^oC (□) and 50 ^oC (Δ) for the porous carbons obtained when KOH/AC = 2 at the following activation temperatures: (a) 600 ^oC (AC-2-600), (b) 650 ^oC (AC-2-650), (c) 700 ^oC (AC-2-700) and (d) 800 ^oC (AC-2-800) (Sevilla et al., 2011) 45
Figure 2. 8: Possible products of the reaction of alkytrialkoxysilanes in the 48
Figure 2. 9: The effect of heat treatment temperature on the concentration of total carboxylic surface groups (Tazibet, Boucheffa et al. 2013). 52
Figure 2. 10: The H_2O uptake of AC and AC 500 at 20 ^oC and 70 %RH (Tazibet, Boucheffa et al., 2013). 52
Figure 2. 11: Water adsorption isotherm on activated carbons and its derivatives (Cosnier, et al. 2005). 55
Figure 2. 12: Breakthrough curves of ACF, ACF-R and ACF-H (Xie, Wang et al., 2011). 56

Figure 3. 1: Horizontal Tube Furnace. 61
Figure 3. 2: Experimental Procedure Flowchart.....62
Figure 3. 3: Hydrophobisation System. 63
Figure 3. 4: TGA Q-500 from TA Instruments. 66
Figure 3. 5: Desiccator System. 78
Figure 3. 6: Plot of 10 %, 50 % and 95 %RH against time measured inside the desiccator using data logger during experiment form humidity sensor at 20 ºC. 79
Figure 3. 7: Lennard-Jones Potential Φ as a function of the distance of the molecule r to the solid surface as both graphical and mathematical description. A and B are constants (Schwarz and Contescu, 1999). 81
Figure 3. 8: Isotherm shapes classification (Thommes et al., 2015). 84

Figure 4. 1: N_2 sorption isotherms at -196 °C of the samples prepared at different temperatures (650, 700, and 750 °C). 94
Figure 4. 2: Logarithmic N_2 sorption isotherms at -196 °C of the samples prepared at different temperatures (650, 700, and 750 °C). 94
Figure 4. 3: N_2 isotherms at -196 °C of CSK, CSKN700 and CSKN900. 97
Figure 4. 4: N_2 isotherms at -196 °C of PRK, PRKN700 and PRKN900. 98
Figure 4. 5: Logarithmic N_2 isotherms at -196 °C of CSK, CSKN700 and CSKN900.....99
Figure 4. 6: Logarithmic N_2 isotherms at -196 °C of PRK, PRKN700 and PRKN900.....99
Figure 4. 7: N_2 isotherms at -196 °C of CSK and coated CSKs series.....101
Figure 4. 8: N_2 isotherms at -196 °C of the coated PRKs series. 102
Figure 4. 9: Logarithmic N_2 isotherms at -196 °C of CSK and coated CSKs series. 103
Figure 4. 10: N_2 adsorption isotherm at -196 °C of samples CSKVs series. 105
Figure 4. 11: Logarithmic N_2 adsorption isotherm at -196 °C of samples CSKVs series. 106
Figure 4. 12: CO_2 adsorption isotherms of the CSs at 25 ºC (symbols represent the measured values and lines are the fitted values with DSL). 109
Figure 4. 13: CO_2 adsorption isotherms of the CSs at 0 ºC (symbols represent the measured values and lines are the fitted values with DSL). 109
Figure 4. 14: The micropore size distribution of the coconut shell CS, CSK, CSKV and CSKV450 using NLDFT on carbon slit pore model. 111
Figure 4. 15: FTIR spectra of CSK, CSKV and CSKV450. 114

Figure 4. 16 : SEM images of carbon (a,) CSK, (b) CSKV (c) CSKV450. 117
Figure 4. 17: SEM-EDX analysis of carbon (a,) CSK, (b) CSKV (c) CSKV450. 118
Figure 4. 18: XPS analysis of CSKV450 showing the high-resolution O, C and Si peaks. 119
Figure 4. 19: N_2 isotherms of CS at the vacuum dried and 10 %, 50 %, 95 %RH. 122
Figure 4. 20: N_2 isotherms of CSK at the vacuum dried and 10 %, 50 %, 95 %RH. 125
Figure 4. 21: Logarithmic N_2 isotherms of CSK at the vacuum dried and 10 %, 50 %, 95 %RH. 125
Figure 4. 22: N_2 isotherms of CSKV at the vacuum dried and 10 %, 50 %, 95 %RH. 127
Figure 4. 23: N_2 isotherms of CSKV450 at the vacuum dried and 10 %, 50 %, 95 %RH. 128
Figure 4. 24: Logarithmic N_2 isotherms of CSKV450 at the vacuum dried and 10 %, 50 %, 95 %RH. 129

Figure 5. 1: CO_2 adsorption of CS, CSK650, CSK700, and CSK750 at 25 ^oC using TGA in 15 % CO_2 and 85 % N_2 at 25 ^oC. The mean of triplicate measurements are plotted and the error bars are the difference between the maximum and minimum values. 132
Figure 5. 2: CO_2 adsorption for the ACs using TGA in 15 % CO_2 and 85 % N_2 at 25 ^oC. 134
Figure 5. 3: H_2O adsorption isotherms of the ACs using DVS in 100 % N_2 at 25 ^oC. 135
Figure 5. 4: H_2O uptake of the CS, CSK, PR, and PRK 10 %RH using a DVS in 100 % N_2 at 25 ^oC. 137
Figure 5. 5: H_2O uptake of the CS, CSK, PR, and PRK 50 %RH using a DVS in 100 % N_2 at 25 ^oC. 137
Figure 5. 6: H_2O uptake of the CS, CSK, PR, and PRK 95 %RH using a DVS in 100 % N_2 at 25 ^oC. 138

Figure 6. 1: CO_2 adsorption of CSK, CSKN700 and CSKN900 with error bars using TGA in 15 % CO_2 and 85 % N_2 at 25 ^oC. The mean of triplicate measurements are plotted and the error bars are the difference between the maximum and minimum values. 144

Figure 6. 2: CO_2 adsorption capacities of the CSK sample after coating with different concentration of VTMOS and PTES using TGA in 15 % CO_2 and 85 % N_2 at 25 ^oC. 145

Figure 6. 3: H_2O uptake capacities of the CSK sample after coating with different concentration of VTMOS and PTES using TGA in 100 % N_2 at 25 ^oC and close to 100 %RH. 146

Figure 6. 4: CO_2 adsorption capacities of CSK and coated CSK samples using TGA in 15 % CO_2 and 85 % N_2 at 25 ^oC. The mean of triplicate measurements are plotted and the error bars are the difference between the maximum and minimum values. 147

Figure 6. 5: CO_2 adsorption capacities of CSK before and after modification with VTMOS and different temperatures with error bars using TGA in 15 % CO_2 and 85 % N_2 at 25 ^oC. The mean of triplicate measurements are plotted and the error bars are the difference between the maximum and minimum values. 148

Figure 6. 6: CO_2 adsorption capacities of CSK before and after modification with OTES and different temperatures using TGA in 15 % CO_2 and 85 % N_2 at 25 ^oC. 149

Figure 6. 7: CO_2 adsorption capacities of CSK before and after modification with POTS temperatures using TGA in 15 % CO_2 and 85 % N_2 at 25 ^oC. 150

Figure 6. 8: CO_2 adsorption capacities of CSK before and after modification with HDTMS and different temperatures using TGA in 15 % CO_2 and 85 % N_2 at 25 ^oC. 150

Figure 6. 9: CO_2 adsorption capacities of CSK before and after modification with PTES and different temperatures using TGA in 15 % CO_2 and 85 % N_2 at 25 ^oC. 150

Figure 6. 10: CO_2 adsorption of the best performing coated-heated CSK samples using TGA in 15 % CO_2 and 85 % N_2 at 25 ^oC. 151

Figure 6. 11: CO_2 adsorption capacities of PRK, PRKN700 and PRKN900 using TGA in 15 % CO_2 and 85 % N_2 at 25 ^oC.....152
Figure 6. 12: CO_2 adsorption capacity of PRKs series using TGA in 15 % CO_2 and 85 % N_2 at 25 ^oC.....153
Figure 6. 13: CO_2 adsorption amounts of PRK before and after modification with VTMOS and different temperatures using TGA in 15 % CO_2 and 85 % N_2 at 25 ^oC. 154
Figure 6. 14: CO_2 adsorption amounts of PRK before and after modification with OTES and different temperatures using TGA in 15 % CO_2 and 85 % N_2 at 25 ^oC. 154
Figure 6. 15: CO_2 adsorption amounts of PRK before and after modification with POTS and different temperatures using TGA in 15 % CO_2 and 85 % N_2 at 25 ^oC. 154
Figure 6. 16: CO_2 adsorption amounts of PRK before and after modification with HDTMS and different temperatures using TGA in 15 % CO_2 and 85 % N_2 at 25 ^oC. 155
Figure 6. 17: CO_2 adsorption amounts of PRK before and after modification with PTES and different temperatures using TGA in 15 % CO_2 and 85 % N_2 at 25 ^oC. 155
Figure 6. 18: CO_2 adsorption of the best performing coated-heated PRK samples using TGA in 15 % CO_2 and 85 % N_2 at 25 ^oC.....156
Figure 6. 19: H_2O adsorption capacities and equilibrium CO_2/H_2O selectivities of CSK, CSKN700 and CSKN900 using TGA in 100 % N_2 at 25 ^oC close to100 %RH. 157
Figure 6. 20: H_2O uptakes and equilibrium CO_2/H_2O selectivities of coated CSKs using TGA in 100 % N_2 at 25 ^oC close to 100 %RH.....158
Figure 6. 21: H_2O uptakes and equilibrium CO_2/H_2O selectivities of the best performing coated–heated CSK samples at a different temperature using TGA in 100 % N_2 at 25 ^oC close to100 %RH.....159
Figure 6. 22: H_2O uptake and equilibrium CO_2/H_2O selectivities of PRK, PRKN700 and PRKN900 using TGA in 100 % N_2 at 25 ^oC close to100 %RH. 160

Figure 6. 23: H_2O uptake and equilibrium CO_2/H_2O selectivities of coated PRKs using TGA in 100 % N_2 at 25 ^oC close to100 %RH.....161
Figure 6. 24: H_2O uptake and equilibrium CO_2/H_2O selectivities of coated-heated PRK samples at a different temperature using TGA in 100 % N_2 at 25 ^oC close to 100 %RH. 162

Figure 7. 1: CO_2 adsorption for the CSKV and CSKV450 using TGA in 15% CO_2 and 85 % N_2 at 25 ^oC. 164
Figure 7. 2: Adsorption isotherms of H_2O for samples CSKV and CSKV450 using DVS in 100 % N_2 at 25 ^oC.....167
Figure 7. 3: H_2O uptake (close to 100 %RH) for samples CSKV, and CSKV450 at 25 ^oC using TGA in 100 % N_2.....168
Figure 7. 4: H_2O uptake (10 %RH) for samples CSKV and CSKV450 using DVS in 100 % N_2 at 25 ^oC.....169
Figure 7. 5: H_2O uptake (50 %RH) for samples CSKV and CSKV450 using DVS in 100 % N_2 at 25 ^oC.....170
Figure 7. 6: H_2O uptake (95 %RH) for samples CSKV and CSKV450 using DVS in 100 % N_2 at 25 ^oC.....170
Figure 7. 7: H_2O uptake isotherms of the CS using DVS and TGA in 100 % N_2 at 25 ^oC. 173
Figure 7. 8: CO_2 adsorption for sample CS at the dry conditions and 10 %, 50 %, 95 %RH using TGA in 15% CO_2 and 85% N_2 at 25 ^oC. 176
Figure 7. 9: CO_2 adsorption for sample CSK dry and at 10, 50, 95 %RH using TGA in 15 % CO_2 and 85 % N_2 at 25 ^oC.....176
Figure 7. 10: CO_2 adsorption for sample CSKV dry and at 10 %, 50 %, 95 %RH using TGA in 15 % CO_2 and 85 % N_2 at 25 ^oC. 177
Figure 7. 11: CO_2 adsorption of CSKV450 dry and at 10 %, 50 %, 95 %RH using TGA in 15 % CO_2 and 85 % N_2 at 25 ^oC.....177

Figure 8. 1: Fitted isosteric adsorption heat of CSs series as a function of absolute CO_2 loading using MicroActive software.....182
Figure 8. 2: Average heat capacities of CS samples over temperature range 25–150 ^oC. 184
Figure 8. 3:H_2O adsorption of the CSKV450 using TGA in 100 % N_2 at 25 ^oC and 95 %RH. 188

List of Tables

Table 2. 1: Typical flue gas compositions of coal and natural gas-fired power plants (Drage et al., 2012).....19

Table 3. 1: The organosiloxane compounds used in the synthesis of coated adsorbents. 64

Table 3. 2: Equilibrium RH of Selected Sutured Salt Solation at 20 ^{o}C.....78

Table 4. 1: Physical properties of the activated carbon samples. 95
Table 4. 2: SEM-EDX analysis of the CSK650, CSK700 and CSK750. 96
Table 4. 3: Physical properties of CSK, CSKN700, CSKN900, PRK, PRKN700 and PRKN900. 97
Table 4. 4: Pore texture parameters for CSKs series. 101
Table 4. 5: Pore texture parameters of the coated PRKs series. 102
Table 4. 6: Pore texture parameters for the CSKVs series. 104
Table 4. 7: Pore texture parameters of the best performing coated CSK calcined samples. 107
Table 4. 8: Pore texture parameters of the best performing coated PRK calcined samples. 107
Table 4. 9: Elemental compositions of CSKV and CSKV450. 115
Table 4. 10: Proximate analysis of CSK and CSKV. 116
Table 4. 11: EDX results of K and Si concentrations for CSKs. 118
Table 4. 12: Chemical composition of VTMOS coating film obtained by XPS measurement. 120
Table 4. 13: Pore texture parameters for CS sample at the vacuum dried and 10 %, 50 %, 95 %RH. 123
Table 4. 14: Pore texture parameters for coated CSK samples at the vacuum dried and 10 %, 50 %, 95 %RH. 126
Table 4. 15: Pore texture parameters for CSKV samples at the vacuum dried and 10 %, 50 %, 95 %RH. 127
Table 4. 16: Pore texture parameters for CSKV450 samples at the vacuum dried and 10 %, 50 %, 95 %RH. 129

Table 5. 1: Comparison of adsorption time of CO_2 for ACs using TGA in 15 % CO_2 and 85 % N_2 at 25 ^{o}C. 134

Table 5. 2: H_2O adsorption of the samples at different RH (10 %, 50 % and 95 %) after 10 minutes using DVS in 100 % N_2 at 25 ^oC. 139
Table 5. 3 :CO_2 and H_2O adsorption (10 %RH) capacities and the selectivity ratio of the CS, CSK, PR and PRK after 10 minutes. 140
Table 5. 4: CO_2 and H_2O adsorption (50 %RH) capacities and the selectivity ratio of the CS, CSK, PR and PRK after 10 minutes. 140
Table 5. 5: CO_2 and H_2O adsorption (95 %RH) capacities and the selectivity ratio of the CS, CSK, PR and PRK after 10 minutes. 140

Table 7. 1: Comparison of adsorption times of CO_2 under dry conditions for CSKV and CSKV450 using TGA in 15 % CO_2 and 85 % N_2 at 25 ^oC. 164
Table 7. 2: CO_2 adsorption of the activated carbon samples, static vs Dynamic at 0 and 25 ^oC in 0.15 and 1.0 bar of CO_2 partial pressures using ASAP 2420 and TGA. 165
Table 7. 3: H_2O adsorption on samples CSKV and CSKV450 at different RH (10, 50 and 95 %) after 10 minutes using a DVS in 100 % N_2 at 25 ^oC. 171
Table 7. 4: CO_2 and H_2O (10 %RH) adsorption capacities and the selectivity ratios for samples CSKV and CSKV450 after10 minutes. 172
Table 7. 5: CO_2 and H_2O (50 %RH) adsorption capacities and the selectivity ratios for samples CSKV and CSKV450 after 10 minutes. 172
Table 7. 6: CO_2 and H_2O (95 %RH) adsorption capacities and the selectivity ratios of the CSKV and CSKV450 after 10 minutes. 172
Table 7. 7: H_2O equilibrium capacities of samples CS, CSK, CSKV and CSKV450 at 20 ^oC. 174

List of Abbreviations

Carbon Dioxide	CO_2
Potassium Hydroxide	KOH
Methane	CH_4
Sulphur Oxides	SO_x
Nitrogen Oxides	NO_x
Monethanolamine	MEA
Sodium Hydroxide	NaOH
Zinc Chloride	$ZnCl_2$
Thermogravimetric analysis	TGA
Pulverized Coal Combustion	PC
Natural Gas Combined Cycle	NGCC
Integrated Coal Gasification Combined Cycle	IGCC
International Energy Agency	IEA
United Nations Framework Convention on Climate Change	UNFCCC
Metal organic frameworks	MOF
Granulated activated carbons	GAC
fibrous activated carbons	FAC
scanning electron microscope	SEM
Brunauer-Emmett-Teller	BET
Volatile Organic Compounds	VOCs
Relative Humidity	RH
Carbon Capture and Storage	CCS
Water-Gas Shift	WGS
Air Separation Unit	ASU

Powder Activated Carbon	PAC
Granulated Activated Carbon	GAC
Temperature Swing Adsorption	TSA
Pressure Swing Adsorption	PSA
Vacuum Swing Adsorption	VSA
Accelerated Surface Area and Porosimetry System	ASAP
Activated carbon	AC
Coconut Shell	CS
Phenolic Resin	PR
Coconut Shell modified by KOH	CSK
Phenolic Resin modified by KOH	PRK
Vinyltrimethoxysilane)	VTMOS
Trimethoxy(octyl)silane	OTES
Perfluorodecyltriethoxysilane	POTS
Hexadecyltrimethoxysilane	HDTMS
Triethoxyphenylsilane	PTES
Non-Local Density Functional Theory	NLDFT
Dynamic Vapour Sorption	DVS
Fourier Transform Infrared	FTIR
Electron Microscope	SEM

Chapter 1: Introduction

1.1 Background

While recognising the industrial revolution began the transformation of humanity to a very advanced stage based on increasing fossil energy consumption, the negative consequences, in particular global warming cannot be ignored. A large body of evidence has led to the belief that global surface temperatures have increased due to anthropogenic greenhouse gas emissions. In fact, carbon dioxide (CO_2) represents about three-quarters of total global greenhouse gases (GHG) emissions (Khoshandam et al., 2010). Although the atmospheric concentration of CO_2 has remained relatively steady for thousands of years, where the land and oceans have absorbed most of the emissions from natural sources, such as decomposition, oceans release and respiration. However, the situation has changed over the past two centuries, requiring effective technologies capable of reducing CO_2 emissions from human sources to the atmosphere.

1.2 The Greenhouse Gas Effect

The majority of climate scientists agree that GHG such as CO_2, methane (CH_4), water vapour (H_2O), sulphur oxides (SO_x) and nitrogen oxides (NO_x) can absorb heat in the lower part of the atmosphere, raising the temperatures of the air close to the Earth's surface (Travis, 2015). This phenomenon has resulted in many changes with great impact that have been occurring around the world , such as sea levels rising (Figure 1.1), an increase in the numbers of ocean storms, higher levels of

ocean acidity, floods and a high decrease of the land ice level (IPCC, 2001, Wang et al., 2014).

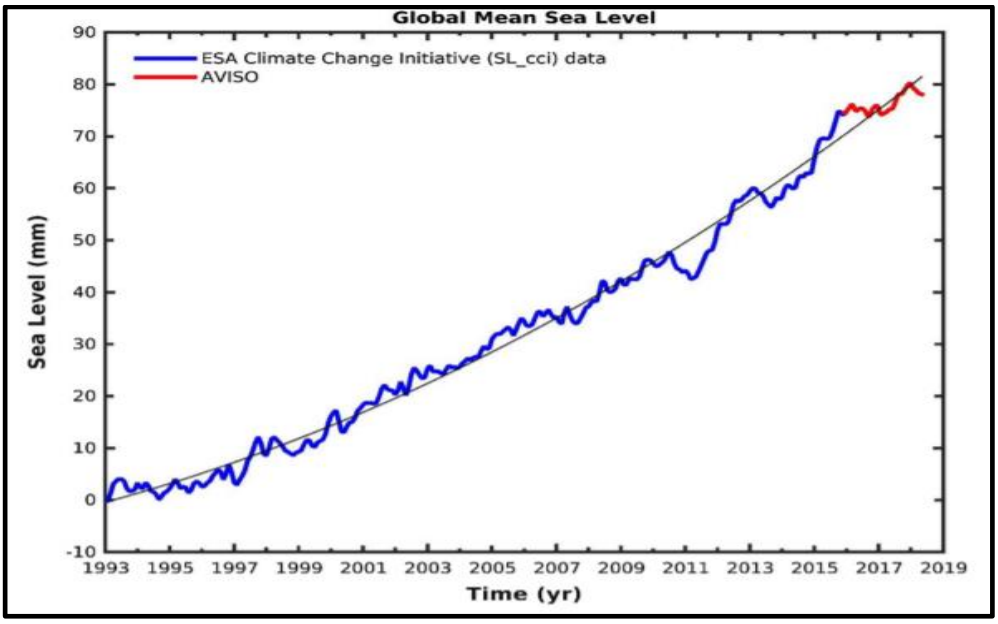


Figure 1. 1: Sea level rising since 1993 (Cazenave et al., 2018).

Figure 1.2 shows the gradual CO_2 increase over the last 60 years from 320 to exceed 415 ppm in 2019 as observed by the Mauna Loa Observatory. Furthermore, Figure 1.3 shows the mean surface temperature of the Earth increased by about 0.8 ^{o}C since 1890. And as a result, September Arctic sea ice is now declining at a rate of 12.8 percent per decade, relative to the 1980 to 2010 average (Xu, 2018). As shown in Figure 1.4, the Arctic sea ice extent for September 2019 averaged 4.7 million square kilometres. This was 8 million square kilometres in 1980. Although it is difficult to accurately predict the size of GHG emissions in the coming decades, the projected emissions depend primarily on the population size, economic activity, lifestyle, energy use, land use patterns, technology and climate policy (Pachauri and Meyer, 2014).

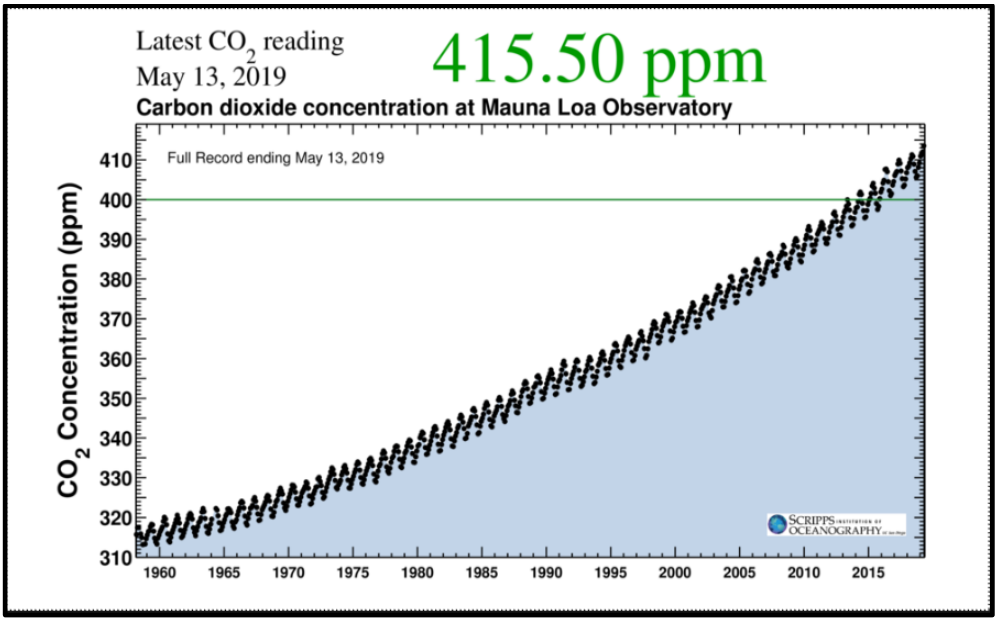


Figure 1. 2: Increasing CO_2 concentration in the atmosphere (Mauna Loa Observatory).

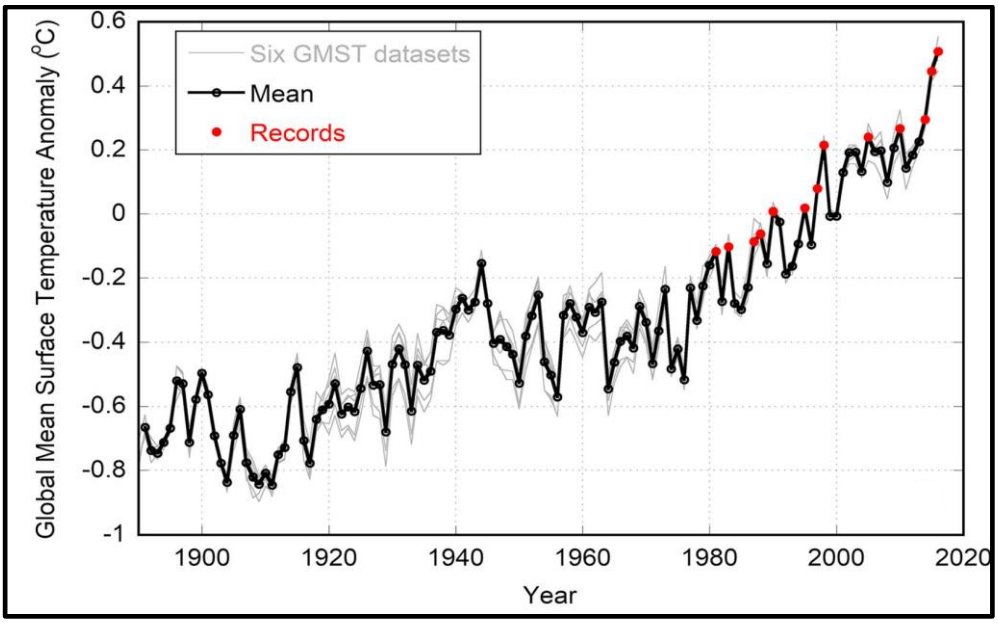


Figure 1. 3: Observed Global Mean Surface Temperature anomalies and record-breaking events (Yin et al., 2018).

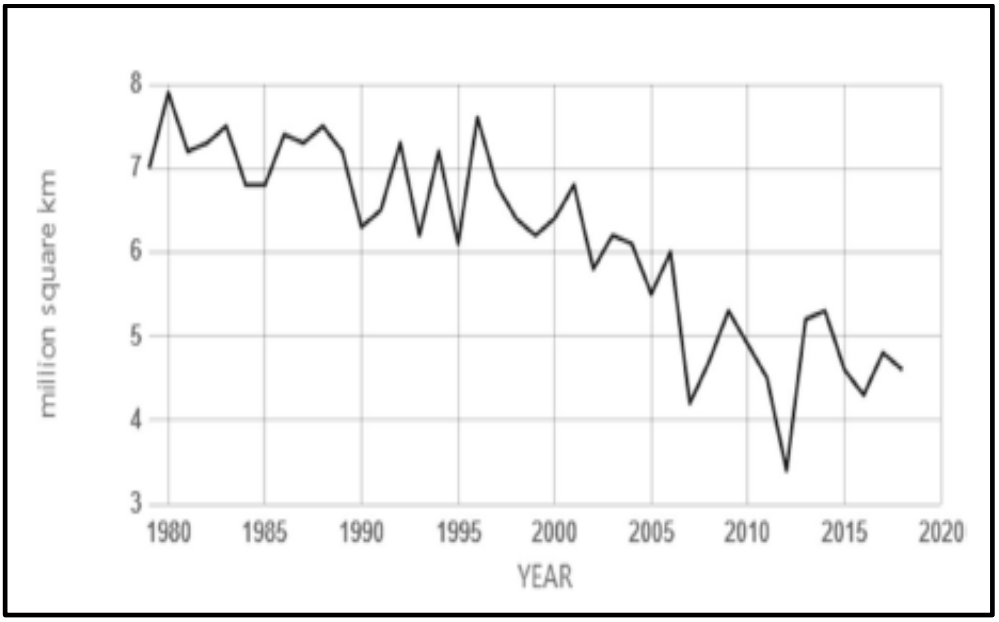


Figure 1. 4: Average monthly Arctic sea ice extent each September since 1980, derived from satellite observations (Xu, 2018).

In fact, CO_2 emissions arise mainly from the combustion of fossil fuels (coal, natural gas, and oil) for energy production, transportation and other applications. The remainder results from the clearing of forests and other land use changes, as well as some industrial processes such as cement manufacturing (Le Quéré et al., 2012). In 2017, 34.7 % of the CO_2 emitted from global fossil fuel combustion came from electricity generation (BP, 2018).

For most fuels, such as diesel oil, coal or wood, pyrolysis occurs before combustion. Under conditions of insufficient oxygen (O_2) supply, incomplete combustion processes can emit organic pollutants, metals, and particulate matter, as well as CO. According to International Energy Agency (IEA) (OECD, 2016), air pollution is one of the biggest health crises today with about 6.5 million deaths per year caused by cancer or by other health problems, making it the fourth largest threat to human health in the world.

1.3 Political Response to Reduce Greenhouse Gas Emissions

In the face of global warming, some governments and global organisations have acted in response. The Kyoto Protocol (1997) tried to establish a kind of mechanism to control the emissions between the industrialised countries. This in order to reduce global greenhouse gas emissions by 5 % in the period 2007-2012 compared with the 1990 levels. The major polluting countries have ratified the obligations contained in this protocol with one notable exception, the second greatest emitter in the world, the United States. Unfortunately, at the end of the targeted period, the rate of emissions increased by up to one fourth revealing that the ratifying countries have violated their commitments (Diringer, 2011).

Regarding the fact that climate change is a growing threat to this planet, it requires strong political attention to tackle its reasons. Recently, more than 200 countries have ratified the Paris Climate Agreement, adopted under the United Nations Framework Convention on Climate Change (UNFCCC) in 2015, to develop effective solutions to this issue for the post-2020 period. The main goal of the international treaty is to keep global temperatures well below 2.0 ^{o}C above pre-industrial times and endeavour to limit them even more to 1.5 ^{o}C (Rogelj et al., 2016). In order to achieve this goal, Australia has a target to reduce its emissions of GHGs by 25 %, EU 20 %, Canada 17 %, Ukraine and Russia Federation 20 %, relative to 2005 levels (UN, 2018).

According to the UK, the energy policy clearly focuses on reducing CO_2 emissions by the development of alternative energy sources and Carbon Capture and Storage (CCS) technologies. In 2017, 10.2 % of final energy consumption was from

renewable sources (NS, 2018), and the target is to deliver 15 % of its total energy consumption from renewable sources by 2020 (Sher, 2017). The last report of the Committee on Climate Change's (CCC) referred that deploying CCS at scale in the 2030s will require deployment of CO_2 infrastructure and initial capture projects at a level of around 10 $MtCO_2$ per annum being captured and stored by 2030, on the path to at least 20 $MtCO_2$ per annum in 2035 (CCC, 2018). The UK CO_2 Capture and Research Centre (UKCCSRC) members expect that the availability of CCS will help the UK halve the costs of meeting its 80 % emission reduction targets for 2050, and will be even more valuable if it moves to net zero emissions. Depending on that, the UK can lead the global effort to further limit the rise to 1.5 °C.

1.4 Energy Supply and Consumption

Fossil fuel is the main source of energy today. Since 1965, global energy consumption more than tripled to 13.3 billion tons of oil equivalent, according to the Global (2017). As shown in Figure 1.5, the ratio of oil in that was 33 % in 2017, coal 28 %, natural gas 24 %, 6.9 % came from hydroelectricity, with 4.5 % coming from nuclear and 3.8 % from other renewable sources (BP, 2018).

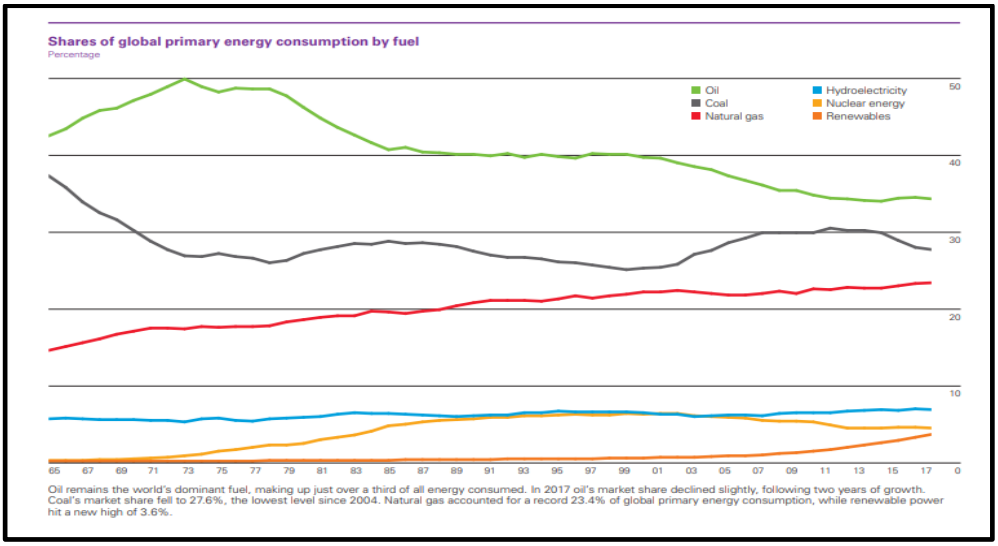


Figure 1. 5: Global Primary Energy Consumption (BP, 2018).

Global energy production tends to rise slightly each year and is expected to rise by more than 40 % by 2035 to meet increasing demand and consumption (Global and Worldwide, 2011). Figure 1.6 shows the relationship between the World Gross Domestic Product (GDP) and energy consumption growth. We see a close correlation, with energy consumption increases and decreases often preceding GDP growth changes, meaning there is a causal relationship between them (UN, 2019).

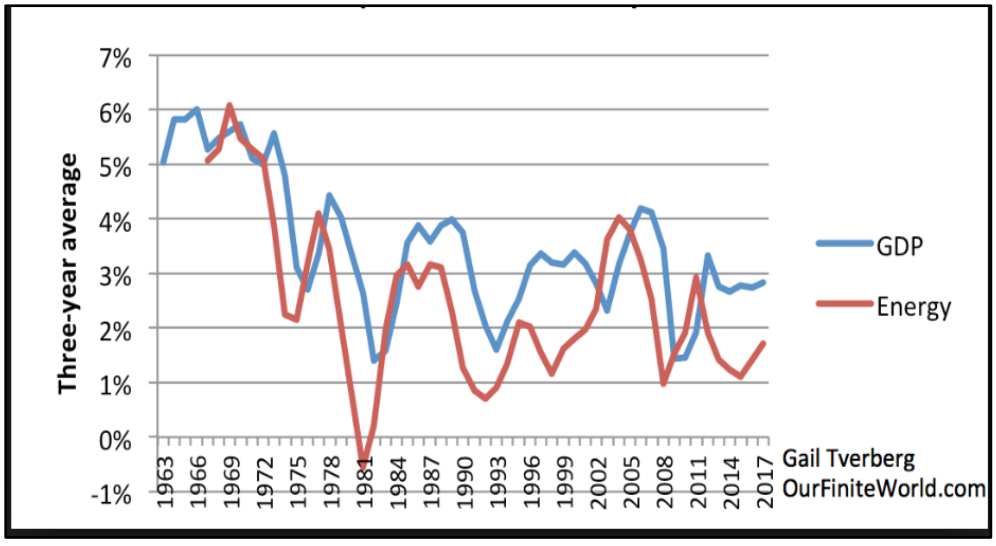


Figure 1. 6: World Gross Domestic Product (GDP) and energy consumption growth (UN, 2019).

1.5 Reducing CO_2 Emissions

Generally, there are three ways to reduce the CO_2 emissions (Yang et al., 2008): 1) Employment of energy efficiency and conservation practices, 2) Switching to carbon-free or reduced-carbon sources of energy, and 3) Development of CCS technology. These approaches are illustrated and now discussed.

1.5.1 Employment of Energy Efficiency and Conservation Practices

Two separate effects can be identified in this aspect: structural changes and behavioural factors. Higher levels of energy efficiency can be achieved in the foreseeable future through a concerted effort and a behavioural change strategy to increase awareness of individuals and organisations about the amount of energy we misuse. Many approaches can be used to achieve this goal such as training, education, policy, planning and communication (Barbu et al., 2013).

1.5.2 Switching to Carbon-Free or Reduced-Carbon Sources of Energy

Renewable energy is seen as being environmentally friendly and suitable clean alternative to all fossil fuels. A structural shift from an energy system based on fossil fuels to one based on renewable sources is required within several decades (Davis et al., 2010). The renewable energy sources such as hydroelectricity, solar energy, wind energy, and bioenergy are available on site or produced locally. Local control increases supply security and provides long-term stability in energy prices, making it easy to predict future energy costs. Over the last few decades, many projects have been established to produce large amounts of energy from renewable sources. The majority of renewable energy comes from hydropower, the amount of energy produced by solar and wind are growing rapidly (Figure 1.7) (WHO, 2018).

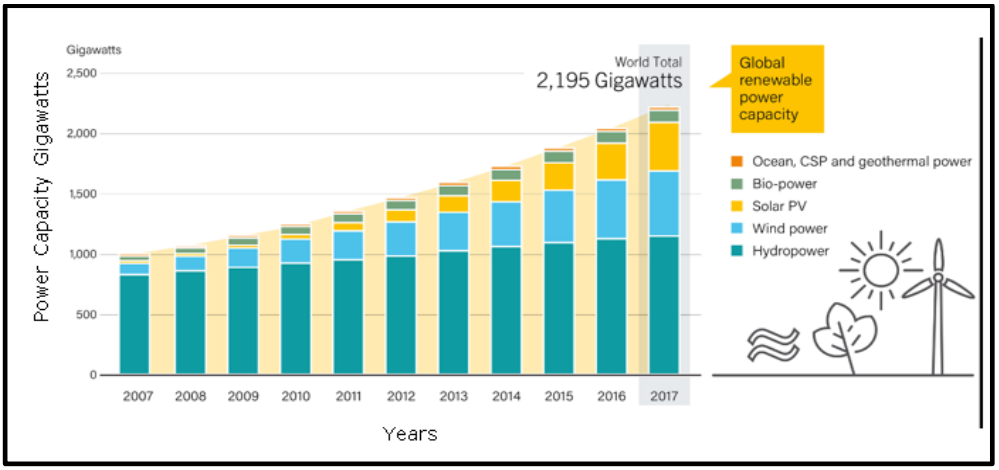


Figure 1. 7: Global Renewable Power Capacity 2007-2017 (WHO, 2018).

Additionally, for more than 40 years, the nuclear power industry (as a key source of zero-emissions generation) is making significant technological progress in terms of electricity security. According to the International Energy Agency (IAE) (Marcus, 2019), there are currently 452 civil nuclear power reactors around the world, with a further 54 under construction. In 2017, global nuclear electricity output was 2506 TWh, an increase of 29 TWh compared to 2016 (Rising, 2018). In fact, nuclear stations were originally designed for a life of about 30 years (Davis et al., 2010). Newer stations are designed for a 40 to 60-year operating life where extending the lifetime of nuclear power plants is becoming common practice on Organisation for Economic Co-operation and Development (OECD) member countries (Demirbas, 2007).

On the other hand, the negative impacts of wind and solar projects on the surrounding environment, as well as the enormous technical challenges facing nuclear waste disposal, are real barriers to replacing fossil fuels with large-scale renewable energy. For example, the wind energy facilities for the projects that produce >20 MW require about 85 acres per megawatt of power output capacity in

the USA (Vision, 2015). In densely populated countries such as the UK, despite offshore wind development is more costly (about 92 $/MWh compared to 29-56 $/MWh for onshore) the drive to develop this type of energy has increased steadily (Klinge Jacobsen et al., 2019). The UK will be deploying 9-10 GW of offshore wind power in 2020. In addition to the 3.7 GW of existing generation capacity, a further 1.4 GW is under construction. (Matthew Spencer and Coats, 2014). Additionally, for nuclear waste disposal, despite the billions of dollars spent to ensure that no harmful quantities of radioactivity ever reach the surface environment by isolating nuclear waste deep inside a suitable rock formation (at depths of 500–800 m), the difficulty of finding suitable places and develop a strong safety case capable of satisfying the public as well as some organisations has discouraged attempts to implement waste disposal programs in many countries (Beswick et al., 2014)

1.5.3 Development of CCS Technologies

Carbon emissions in 2018 were 33.1 Gt and grew by 1.7 % compared with the previous year (IAE) (Marcus, 2019), in addition the emissions are expected to start to decline by the mid-2020 s as a result of the drop in global coal demand and flatting oil demand (Global-Energy-Perspective, 2019), many studies refer to fossil fuels will be an essential source of energy in the next half century (IPCC.2014).

In fact, this technology is a promising option to deliver significant emission reductions to meet with the climate targets set by the Intergovernmental Panel on Climate Change (IPCC). The amount of CO_2 emissions could be reduced by approximately 80-90 % by equipping modern conventional power plants or

industrial plants with CO_2 capture technologies, i.e. post-combustion, pre-combustion and oxy-fuel combustion (IPCC 2005).

Seventeen large-scale projects are ongoing around the world and four due to become operational by the end of 2018. There are further 33 projects at various stages in the planning process. Sask Power Boundary Dam Power Station is an 824 MW coal-fired plant located in Estevan, Canada. The plant has been operational since 2015 and is the world's first large-scale CCS project in the power sector. The world's first steel plant with large-scale CCS was launched in Abu Dhabi in 2016 (Economics, 2018). Thus, CCS will be capable of reducing approximately 38 Mt of CO_2 emissions per annum in 2030 (DECC, 2012).

The number of CCS projects around the world are very few compared to the volume of emissions. Therefore, developing new methods to reduce CO_2 emissions still acquire intensive investigations. By devising a realistic and urgent strategy for CCS development and with contributing to other methods, emissions may be controlled in the future.

1.6 Aim and Objectives

In order to overcome the current shortcomings of water vapour co-adsorption on activated carbons and the relatively high regeneration energy required for post combustion CO_2 capture (that will be discussed in the next chapter), this research aims focus on understanding and minimising water vapour co-adsorption on activated carbons while maintaining a high capacity for CO_2, specifically determining the role of organosiloxane compounds as a coating agent to increase the hydrophobic nature of activated carbons. Two different precursors for activated

carbons, coconut shell, and phenolic resin have been investigated. Selected as the parent materials to produce activated carbons.

To achieve this overall aim, the following objectives were identified.

1. To compare the CO_2/H_2O selectivity of activated carbons before and after the KOH treatment that is essential to maximise CO_2 adsorption and minimise regeneration energy.

2. To modify KOH- activated carbons with organosiloxane and heat treatment to investigate the extent to which water vapour co-adsorption is reduced and how this affects CO_2/H_2O selectivity, both at equilibrium and kinetically over short periods of time relevant to plant operation (10 minutes).

3. To determine the characteristics of the activated carbons using Fourier transform infrared spectroscopy, X-ray photoelectron spectroscopy, transmission electron microscopy X-ray diffraction, thermogravimetric analysis and nitrogen (N_2) isotherms at -196 ^oC.

4. To understand the kinetics of CO_2 and H_2O adsorption onto modified activated carbons

5. To estimate the heat of adsorption of CO_2 and specific heat capacity of the modified activated carbons to ascertain the impact of water vapour co-adsorption on the regeneration energies.

1.7 Organisation of the Thesis

This thesis organised as follows:

Chapter Two: The literature review covers CO_2 capture technologies, capture and separation processes, costs of CCS, physical and chemical activation methods for activated carbons and organosiloxane compounds. Gaps in the literature with respect to water vapour co-adsorption for activated carbons are highlighting that have defined the scope of this study.

Chapter Three: This provides a detailed description of the modification methods used for activation and coating the activated carbons, and the experimental procedures used to investigate the characteristics and performance of the samples in Chapter 4, 5, 6 and 8.

Chapter Four: The basic characterisation of the activated carbons before and after any step of modification; intercalation of K ions, physical treatment by raising the temperature up to 900 ^{o}C and treatment via coating organosiloxane compounds and heating the coated samples.

Chapter Five: The impact of KOH treatment on CO_2/H_2O selectivity is evaluated for coconut shell and phenolic resin carbons after 10 minutes.

Chapter Six: The influence of organosiloxane treatments on CO_2 and H_2O adsorption behaviour has been evaluated at equilibrium for the two types of activated carbons.

Chapter Seven: The impact of organosiloxane compounds on CO_2/H_2O selectivity is evaluated for coated samples after the relatively short period 10 minutes to present a time typical of a CO_2 capture plant using adsorbents.

Chapter Eight: The potential application for KOH-activated carbon derived from coconut shell for CO_2 post combustion capture is evaluated with calculations of regeneration energy.

Chapter Nine: This lists the conclusions and provides recommendations for what further knowledge is required to acquire a deeper understanding of the impact of water vapour co-adsorption CO_2 capture performance under real processing conditions

Chapter 2: Literature Review

2.1 Introduction

This chapter presents an overview of the three leading CO_2 capture technologies; oxy-fuel combustion, pre-combustion and post-combustion capture. The following review of adsorbents for post-combustion capture aims to provide a comprehensive overview of activated carbons derived from different precursors, including material characteristics synthesis, structural features, CO_2 adsorption capacity and the effect of water vapour co-adsorption on CO_2 capture. This is followed by an explanation of how activated carbons can be modified by KOH to increase CO_2 adsorption capacities, and a discussion of the potential of organosiloxane compounds to reduce H_2O uptake.

2.2 Carbon Dioxide Capture Technologies

Carbon Capture and Storage (CCS) technology is a broad term referring to three essential stages: (1) capturing waste CO_2 from large point emission sources, such as fossil fuel power stations, refineries and iron and steel plants; (2) transporting it through pipelines to deep geological formations; (3) depositing it at these sites to prevent its accumulation in the atmosphere (sequestration sites). There are three main CO_2 capture technologies that can help reduce emissions from the power plants and industrial processes, namely pre-combustion capture, post-combustion capture and oxy-fuel combustion. Additionally, with the successful completion of pilot plant trials in the USA, chemical looping combustion is increasingly being viewed as a competitive technology.

2.2.1 Pre-Combustion

Pre-combustion capture is the removal of CO_2 from fossil fuel prior to combustion. This technology is particularly suitable for integrated coal gasification combined cycle (IGCC) power plants, which along with CO_2 capture, involves three steps: gasification, the water-gas shift reaction (WGS) and CO_2 separation (Figure 2.1) (Gharaie, 2013). In the first step, the synthesis gas (syngas), mainly consisting of CO and H_2, is produced by gasification of solid fuel (i.e., coal) by applying heat under pressure in the presence of oxygen. Then, WGS reaction is conducted by passing syngas through the shift converter (catalytic reactor) to produce CO_2 and more H_2 with added steam, as shown in Equation 2.1.

$$CO + H_2O \Longleftrightarrow CO_2 + H_2 \quad \Delta H \quad -41\ kJ\ /mol \qquad (WGS\ reaction) \qquad (2.1)$$

It is useful to separate and capture CO_2 because of the high pressure of the syngas (2–7 MPa) and the high concentration of CO_2 (Metz et al., 2005). The remaining H_2 can be combusted cleanly in a gas turbine to produce electricity (Kanniche et al., 2010).

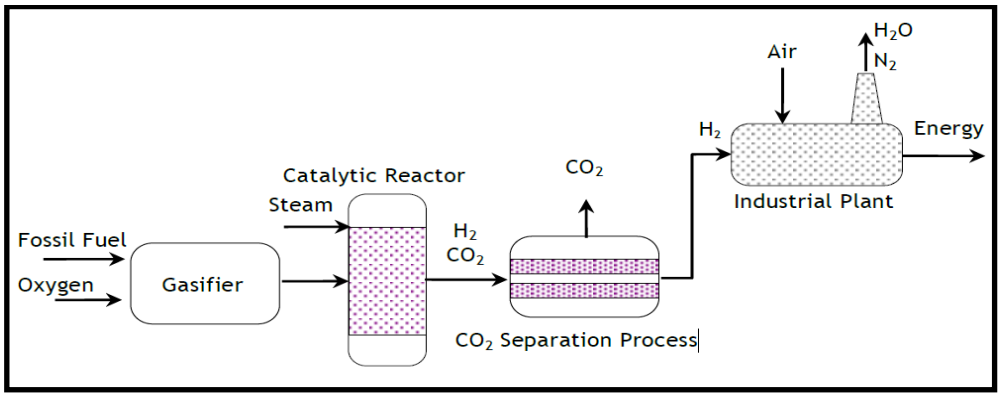


Figure 2. 1: Pre-combustion CO_2 capture (Gharaie, 2013).

2.2.2 Oxy-Fuel Combustion

Oxy-fuel combustion involves three main components: a cryogenic air separation unit (ASU), a fuel combustion unit, and CO_2 purification and compression (Figure. 2.2) (Gharaie, 2013). The process involves the combustion of pulverized coal in an atmosphere of nearly pure O_2 (greater than 95 % and up to 99 %). An ASU is used to provide the necessary O_2 to create a reaction after removing N_2 from liquid air [IPCC (2005) pp 126]. The exothermic combustion reaction occurs at atmospheric pressure of 1500 °C, and produces a high concentration of CO_2, H_2O and acid gases (SO_x and NO_x) (Yin and Yan, 2016). The flame temperature can exceed the bearing capacity of the combustion chamber. Therefore, two thirds of the exit flue gas are recycled back to the combustion chamber to keep the temperature within the desired limits and to increase the CO_2 concentration in the exhaust stream. The remainder is used as a suction stream for CO_2 compressors (Gharaie, 2013, Ogbuka, 2013). Cooling the exhaust flue gas below the water dew point can remove most of the water vapour. Thus, a CO_2-rich product stream leaves the system containing more than 80 % v/v of CO_2 [IPCC (2005) pp 122]. The existing research has focused on meeting key challenges that limit the uptake of this technology in industrial or commercial applications, such as the very high energy requirements for producing high purity O_2 (Huang et al., 2018).

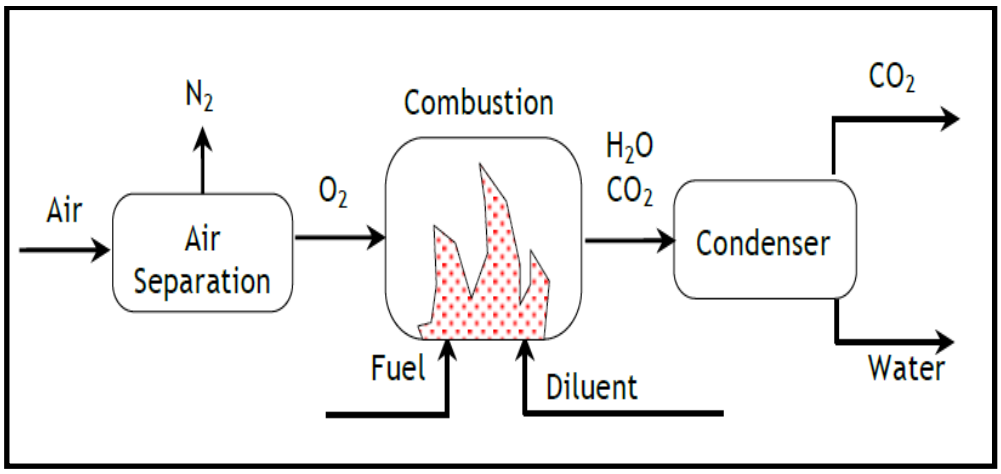


Figure 2. 2: Oxy-Fuel-Combustion CO_2 Capture system (Gharaie, 2013).

2.2.3 Post-Combustion

The separation of CO_2 occurs after the combustion of the fuel gas (e.g. coal, and biomass). As shown in Table 2.1, in addition to CO_2 (typically 12-15 v/v), the flue gas stream from coal combustion also contains N_2 (75-80 % v/v), H_2O (5–7 % v/v) and O_2 (3-4 % v/v). Some pollutants can also appear depending on the type of fossil fuel used, such as fly ash, SO_x and NO_x (Drage et al., 2012). Various established emission control technologies are available to address the most common targeted pollutants. Flue-gas desulfurisation (FGD) and selective catalytic reduction (SCR) systems are usually used to remove most of SO_x and NO_x (up to 98–99 %) from the flue gas produced by coal-fired power plants (Adams, 2010, AIRUSE, 2016). Drage et al. (2012) reported that the percentage of H_2O in the flue gas stream from coal combustion increases to 12-15% after FGD and SCR systems.

Table 2. 1: Typical flue gas compositions of coal and natural gas-fired power plants (Drage et al., 2012).

Component	Coal	Natural Gas
N_2	75-80 %	74-80 %
CO_2	12-15 %	3-5 %
SO_2	1800 ppm	<10 ppm
H_2O	5-7 %	7-10 %
NO_x	500 ppm	50 ppm
O_2	3-4 %	12-15 %
CO	<100 ppm-occasionally	<5 ppm

2.3 Capture & Separation Processes

Chemical and physical absorption, membrane separation and solid adsorption have all received major attention and are described in detail in this section.

2.3.1 Chemical Absorption for CO_2 Partial Pressures

Figure. 2.3 shows a schematic diagram of a CO_2 absorption process using an aqueous monoethanolamine (MEA) solution (Gharaie, 2013). The flue gas is passed through the packed bed absorption column (absorber) and makes contact with a CO_2 absorbing solvent. To date, most commercial post-combustion CO_2 capture plants utilise the reversible chemical reaction of CO_2 with an aqueous amine solution (Olajire, 2010). Although conventional amine solvents include primary, secondary and tertiary amines that can be used in the absorption processes, the MEA solution is still one of the most widely used solvents and is often considered a reference case for the development of new solvents (Putta et al., 2017). MEA has a high reaction

rate, it is quick to regenerate and does not appear to degrade easily when it reacts with CO_2 (Gharaie, 2013). The CO_2-rich solvents are passed to a stripper for the regeneration process, where CO_2 is stripped from the solution and removed from the upper part of the stripper (purity over 99 %), while the regenerated solvent is sent back to the absorber. Heat is required in the reboiler to heat the solvent and provide the energy requirements for the removal of CO_2 (Supekar and Skerlos, 2015).

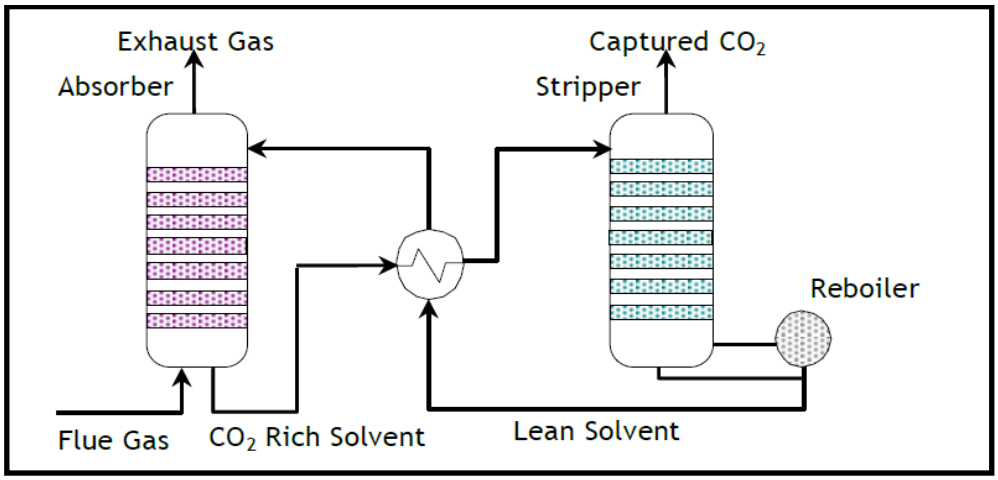


Figure 2. 3: Simplified flow sheet of the CO_2 absorption process (Gharaie, 2013).

2.3.2 Physical Absorption for High CO_2 Partial Pressures

Physical absorption depends on the ability of solvents to absorb CO_2 without chemical reactions. Henry's Law is used to determine the mass of dissolved CO_2. Absorption occurs under a high partial pressure of CO_2 and low temperature. The absorptive capacity of physical solvents is directly related to external gas pressure and inversely related to temperature (Kothandaraman, 2010, Zhai and Rubin, 2018). During pre-combustion in IGCC, the partial pressure of CO_2 is about 10-12 bar (Bogle and Fairweather, 2012). Depending on these characteristics, physical solvents such as cold methanol (Rectisol process), dimethylether of polyethylene

glycol (Selexol process) and propylene carbonate (Fluor process) are more suitable for the removal of CO_2 than chemical solvents. It is noteworthy that weak bonds (Van der Waals forces) between CO_2 and physical solvents can be easily broken without heat, by means of pressure swing processes (Keskes et al., 2006, Tande et al., 2013). This process has been widely used in various industrial applications, including natural gas, synthesis gas and hydrogen production with high CO_2 contents (Olajire, 2010).

2.3.3 Membrane Separation

Permeability and selectivity are the two main characteristics of materials used in the production of membranes such as polymers, cellulose acetate and ceramics (Gough et al., 2006). Generally, membrane separation is subjected to one of the following concepts: (1) the partial pressure of gas across the membrane and (2) reversible chemical reaction with carriers such as carbonate, amines molten salt hydrates dissolved in membrane liquid, or porous inorganic materials such as zeolites, palladium alloy tubes and ceramics (Gough et al., 2006, Olajire, 2010, Travis, 2015). Usually, membranes separation processes are more suitable for oxy-fuel combustion and pre-combustion, especially IGCC, as shown in Figure 2.4. Although membranes require less operational energy than other capture systems, they still need further development due to drawbacks such as high membrane cost, low chemical and temperature resistance and the need for multi-stages to increase separation efficiency in some industrial processes.

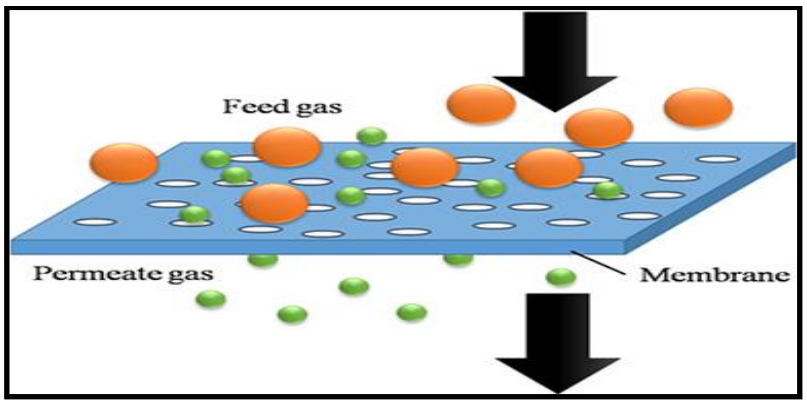


Figure 2. 4: Membrane Separation Technology in Carbon Capture (Ji and Zhao, 2017).

2.3.4 Adsorption

Adsorption is a surface-based separation process involving the formation of a film around the surface of the solid material (adsorbent) as a result of the adhesion of separated chemical species of a gas or liquid (known as adsorbate). To reduce the cost and energy penalty for conventional post combustion CO_2 capture technologies (using amine solvents), many studies have been focused on improving the performance of adsorbents (Yang, 2013). Adsorption involves either Van der Waals forces between the adsorbate molecules and the adsorbent surface (physisorption), or chemical interactions with covalent ionic and hydrogen bonds with the adsorbent surface (chemisorption).

Adsorption units typically consist of vessels (adsorbent beds) filled with porous materials. These materials have a good ability to selectively remove a certain gas from gas mixtures due to the molecular sieving properties of adsorbents. For the recovery of the heavy component from ambient pressure streams (e.g., CO_2 removal from flue gas), circulating fluidized beds or moving beds are applied with temperature swing adsorption (TSA) processes for post-combustion CO_2 capture,

while the fixed beds are applied to pressure swing adsorption (PSA) processes to recover CO_2 from a high pressure stream (Wu et al., 2018).

2.4 Solids Adsorbents for Post Combustion CO_2 Capture

Adsorbents are proposed as suitable candidates for CO_2 capture due to their many advantages, such as highly hydrophobic surface (repellent of water vapour), resistance to degradation under high temperatures, resistance to alkaline and acidic media, tunable surface chemistry and low energy consumption in desorption (Wickramaratne and Jaroniec, 2013). Some of the most suitable adsorbents for CO_2 capture will be described next.

2.4.1 Zeolites/Silicas & Adsorbed Bases

Zeolites are a varied group of natural and synthetic crystalline structures made of SiO_4 and AlO_4 tetrahedron units linked to each other through O_2 atoms to form regular cavities and channels containing cations and H_2O. The general chemical composition of a zeolite is:

$$\mathbf{wNa_2O.\ xAl_2O_3.\ ySiO_2.\ zH_2O}$$

Where, w is the cation type, such as Ca^{+2}, Mg^{+2}, Li^{+1}, x is a number of aluminium tetrahedral in moles, y is a number of silicon tetrahedral in moles and z is the amount of H_2O of crystallisation in moles (Ogbuka, 2013). Mechanistically, the interaction between CO_2 molecules and zeolite particles occurs primarily via physisorption, with a small quantity of CO_2 being chemisorbed on the surface, leading to the formation of various carbonate species (Travis, 2015). Zeolites under PSA were successfully used to separate CO_2 from the gas mixture, offering better CO_2

selectivity than activated carbon, (Meghani, 2015). To enhance the efficiency of CO_2 separation and to control the CO_2 adsorptive properties, three methods are used: (1) structural adjustments of the framework; (2) exchanging cations within the pore structure; and (3) using high purity zeolite (Wang et al., 2014). Among the various types of adsorbents, Zeolite 13X is one of the most common commercial types for CO_2 adsorption (Pour et al., 2015). The critical and supercritical operating conditions for CO_2 removal studies had been inspected by Kareem et al. (2018) on 13X and 5A Zeolites in terms of CO_2 adsorption, at 150 bars and two different operating temperatures, 50 and 70 °C. 13X zeolite showed higher adsorption which was 330 mg/g at 50 °C and 300 mg/g at 70 °C for CO_2 at supercritical conditions, compared to 5A zeolite 280 mg/g, 230 mg/g, respectively.

However, the efficiency of CO_2 adsorption reduces in the presence of H_2O. For instance, the CO_2 loading is reduced from 2.3 mmol/g under dry conditions to 0.33 mmol/g in the presence of 2.79 % Relative Humidity (RH) (Li et al., 2009).

In addition to zeolites, silica can also be used to support the CO_2 reactive amine polymers. Different types of silanol groups with different acidity are linked to the silica surface through its synthesis or when treated with H_2O or an aqueous solution, thus allowing it to interact with basic amine groups (Zhuravlev and Potapov, 2006). The relatively low cost of different types of silica, such as nano-particles, hollow spheres, nanotubes and fumed silica, is an important factor for using these materials as adsorbents for CO_2 capture (Wang et al., 2014).

The performance of absorbents can be influenced by the structural characteristics of the support. Due to the high porosity of silica, it is used as a support for polyethleneimine (PEI) (Fryxell and Cao, 2012). The pioneering work of Leal et al. (1995) opened the door to study CO_2 adsorption in amine loaded silica. Xu et al. (2005) developed a "molecular basket" system as a promising candidate for capturing CO_2 using a branched mesoporous silica MCM-41 support that served as a basket to retain large amounts of polyethyleneimine (PEI, MW600). They investigated the efficiency of MCM-41 with/without different loading of PEl (prepared by a wet impregnation method) for capturing CO_2. They found that the amount of CO_2 adsorption mainly depends on the levels of accessible amine components inside the supported amine polymers.

The importance of the impregnated polyamines method has been confirmed by Pirngruber et al. (2009). Using a commercial mesoporous silica gel, the experimental adsorption isotherms and kinetic data in the VSA/PSA process showed that PEI–silica adsorbents prepared from impregnation adsorb more CO_2 than that those prepared by grafting of aminosilanes. On the other hand, Huang et al. (2003) showed that the amount of CO_2 adsorbed on an amine-grafted MCM-48 adsorbent can be doubled in the presence of water vapour. These findings are promoted by similar results from other studies. For example, Xu et al. (2005) and Miller et al. (2005) confirmed that MCM-41-PEI adsorbent displayed higher CO_2 capacity in the presence of water vapour.

The most significant drawbacks of silica are the deactivation of the adsorbent (usually low molecular weight amines (such as MEA) and the drop in CO_2

adsorption capacity, which occurs with thermo-oxidative aging. This phenomenon leads to amine leaching from the largest pores of the support and reduced amine accessibilities at the small pores. Moreover, some amounts of amine may also be easily vaporised during this operation (Quang et al., 2016). Organosiloxane-functionalised amine impregnated silica was used to overcome the steam aging problem, as reported by (Starkie, 2016). These findings demonstrate that the presence of hydrophobic organosiloxane coatings act to reduce the H_2O uptake and diminish the rate of solubilisation of the amine polymer, thus preventing leaching. However, it also reduces the CO_2 adsorption capacities of the adsorbents after ageing. The best results can be obtained by striking a balance between adsorbent stability and CO_2 adsorption (Belmabkhout et al., 2016).

2.4.2 Metal-Organic Frameworks

Metal Organic Frameworks (MOFs) are microporous materials consisting of one-, two-, or three-dimensional hybrid structures containing metal-based nodes (e.g. Al^{+3}, Cr^{+3}, Cu^{+2}, Fe^{+2} or Zn^{+2}) linked by organic linkers (e.g. nitrile, carboxylate and pyridine) through coordination bonds (Zhou, 2015). In recent years, much attention has been paid to this new family of porous materials because of their unique characteristics. As a result of extensive research, approximately 10,000 new MOFs, with a wide array of compositional and structural variations, have emerged. Some samples offered exceptionally Brunauer-Emmett-Teller (BET) surface areas close to 7000 m^2/g, which equals more than twice the surface area of zeolites or activated carbon (Farha et al., 2010). Generally, the adsorption behaviour of most metal ions onto MOF-based materials follows the pseudo-first-order model, suggesting that

chemical adsorption is dominant over physical adsorption (Li et al., 2018). In fact, the unique structural properties of MOFs such as robustness, high thermal and chemical stabilities, high void volume, low densities, in addition to their chemical tunable structures and the possibility of tailoring their functionalities, have enabled MOFs to find a number of applications. For example, a variety of organic mineral frameworks have been successfully used in gas storage and separations, enantioselective separations, heterogeneous catalysis, chemical sensing and drug delivery (Smit et al., 2014, Sun and Zhou, 2015). Nonetheless, the powder form and the need to determine the thermal stability of MOFs over a huge number of cycles are still the main drawbacks in realistic conditions (Chen et al., 2014).

Many approaches have been used to enhance CO_2 capture capacity on MOFs, such as modification with an amine or some other polar groups, and creating active sites on the adsorbent surface by removing terminal bound solvent molecules (Wang et al., 2014). To study the effect of H_2O on MOF-based CO_2 adsorbents at low pressure, Liu et al. (2012) investigated the effects of trace amounts of H_2O on CO_2 adsorption capacity and CO_2/N_2 selectivity for the Ni-MOF-74. The experiments were conducted using a fixed-bed breakthrough method under dry and 3 %RH at 25 °C and 0.15 bar. The findings revealed a decline in both CO_2 capacities from 3.74 mmol/g to 2.2 mmol/g and CO_2/N_2 selectivity from 38 to 22. As a result, MOFs cannot be considered a good promising candidate for CO_2 adsorption in the presence of H_2O. On the other hand, Khan et al. (2019) used amine functionalized metal organic framework materials as dry adsorbents for post-combustion CO_2 capture. This research work focused on the synthesis of a new amino functionalized Cu based

MOF using 2-aminoterephthalic as a linker. The structure was confirmed by Single Crystal XRD studies that revealed free $–NH_2$ group in the amine functionalized MOF led to increase the CO_2 adsorption. The results exhibited that the MOF is a better CO_2 capture tendency of 5.85 mmol/g at 25 °C as compare to Cu-BDC MOF.

2.4.3 Activated Carbons

Activated carbons are a unique adsorbent derived from carbonaceous feedstocks activated by physical and/or chemical treatments for use in different applications, such as purification, hydrogenation, agriculture, pharmaceutical, and analytical chemistry applications (Ogbuka, 2013). Three main groups of carbonaceous materials can be identified for the manufacture of activated carbons: coals (bituminous coals, lignite, pit moss), industrial by-products (scraps of polymeric materials, petroleum, coke pitch), and wood or other biomass materials (coconut and peanut shells, olive stones, etc.). Activated carbon is mainly available in three forms or shapes: powder, granular and fibrous. While powder activated carbon (PAC) is widely used in the water treatment industry for the removal of a variety of organic contaminants (Freese et al., 2000), granulated activated carbons (GAC) have been successfully used for gas purification, solvent recovery, gas separation by PSA and as catalysts (Menéndez Díaz and Martín-Gullón, 2006). The last shape, fibrous activated carbons (FAC), is commonly used in the desulfurisation process, and also to prepare woven clothes and non-woven mats (Inagaki, 2000).

2.4.3.1 Textural Characteristics

Regarding the most important factors in determining the performance of activated carbon in particular applications, surface area, pore volume, pore size distribution and the chemical surface of activated carbon all play a significant role (Shafeeyan et al., 2010, Allwar, 2012). The total porous structure of activated carbon comprises a wide range of pore sizes that usually have different shapes (the pore size distribution). Depending on the interlayer spacing, the International Union of Pure and Applied Chemistry (IUPAC) classified the pore sizes by N_2 sorption isotherms into three main groups: (1) Micropores (width less than 2 nm); (2) Mesopores (width between 2 and 50 nm), and (3) Macropores (width larger than 50 nm) - see Figure 2.5. Although activated carbons with different pore structures can be produced from the same precursor by varying the operating variables and activation agents (Şentorun-Shalaby et al., 2006), the structure of pores largely depends on the nature of the raw material and activation process route (Gottipati, 2012). For example, agricultural biomass waste materials, such as coconut shells, can be used to produce micropores (Sun et al., 2017), while micro-mesopores structures can be produced from rice husk shell (Vu et al., 2017).

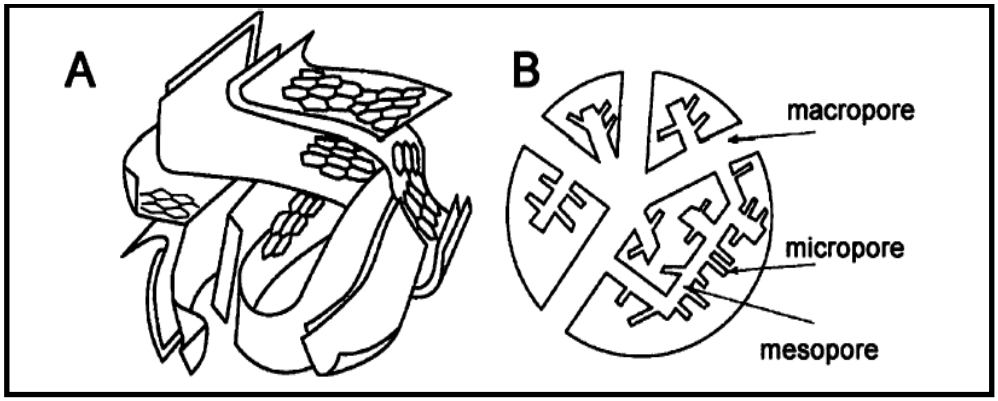


Figure 2. 5: Schematic representation (a) three-dimensional and (b) two dimensional (Rodriguez-Reinoso, 1998).

Although it is difficult to obtain accurate information about the design of porous solid carbon, micropores usually appear in three main shapes: cylindrical, ink-bottle and slit-shaped pores, while the other porous carbon acts as transport channels (Alaya et al., 2000, Wei et al., 2013). During the activation process, a high level of structural imperfections and defects can occur on the layers. Therefore, two types of active sites can be distinguished on the carbon surface: basal planes and edges of the planes. As shown in Figure 2.6, a variety of O_2 functionalities arise during oxidation, including lactone, phenolic hydroxyl, carboxyli and carbonyl, as well as pyridinic and pyrrolic N_2 functionalities (Bansal and Goyal, 2005, Figueiredo, 2013). This highlights the fact that the adsorption capacity of activated carbon is not defined only by its physical or porous structure, but it is strongly influenced by the chemical nature of its surface.

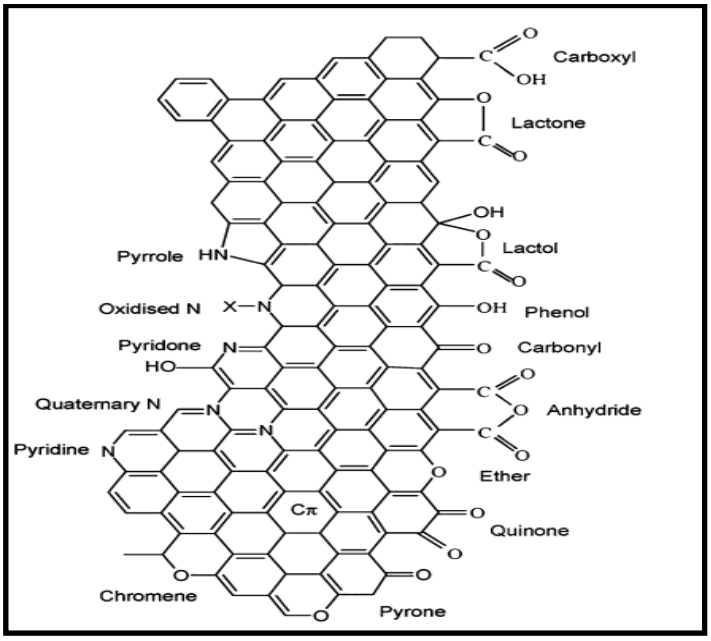


Figure 2. 6: N_2 and O_2 surface groups on carbon (Figueiredo, 2013).

2.5 Activation Methods

2.5.1 Physical Activation

Physical activation mainly consists of two steps: carbonisation and oxidation. Carbonisation is a pyrolytic reaction in the presence of the inert gas, which converts raw materials into solid carbon (char). This process involves the heat treatment of raw materials, mostly up to 800 ^{o}C in an inert atmosphere, in order to eliminate the volatile matter and water vapour, and increase the porosity and fixed carbon content to 70-85% in char (McDougall, 1991, Bansal and Goyal, 2005). Most characteristics of activated carbon, such as its porous texture, hardness, and density appear during this step (Menéndez Díaz and Martín-Gullón, 2006). The second step is the physical activation (oxidation) process, which is carried out by treating chars with one or more oxidizing agents, such as steam, air, or CO_2. The purpose of this process is to develop the incipient microporosity, promote the number of active sites on the surfaces and connect the micropores with the external surface of channels of meso and macropores. The reactions that can occur during the oxidation process are shown below (equations 2.1-2.5):

$$C + H_2O \Longleftrightarrow CO + H_2 \qquad \Delta H\ 132\ KJ/mol \qquad (2.2)$$

$$C + CO_2 \Longleftrightarrow 2CO \qquad \Delta H\ 159\ KJ/mol \qquad (2.3)$$

$$C + O_2 \Longrightarrow CO_2 \qquad \Delta H\ -387\ KJ/mol \qquad (2.4)$$

$$2C + O_2 \Longrightarrow 2CO \qquad \Delta H\ -226\ KJ/mol \qquad (2.5)$$

The endothermic reactions between carbon and steam or CO_2 can occur at temperatures of up to 1000 ^oC. The possibility of controlling the endothermic reaction conditions inside the kiln leads to generally the higher yields of activated carbon with higher surface areas than those produced by exothermic reactions with O_2 (Bandosz, 2006).

2.5.2 Chemical Activation

Chemical activation is a carbonisation process with added reagents in an inert atmosphere. It is preferred over physical activation in industrial applications, because of its ability to inhibit the formation of tar (aromatic hydrocarbons) and increase the yield of activated carbon at low temperatures and short times (Ahmadpour and Do, 1996, Lee and Pyun, 2007). Several studies have thoroughly investigated the impact of dehydration agents in developing the porosity of carbonaceous materials. A variety of acids, strong bases and salts, such as phosphoric acid (H_3PO_4), sodium hydroxide (NaOH) potassium hydroxide (KOH), and zinc chloride ($ZnCl_2$), can be mixed separately as dehydrating agents with raw materials to form a paste. In a range of 200 to 650 ^oC, the paste is carbonised in an inert gas to open up micropores (McDougall, 1991, Ahmadpour and Do, 1996). The impregnation ratio and soaking time have a significant effect on the quantity and the properties of the activated carbon that is produced.

2.5.2.1 KOH Activation

KOH is a chemical agent that has shown promising findings in terms of increasing the efficiency of activated carbon. Compared to other agents, widening micropores with negligible amounts of mesopores can be better obtained using KOH (Marsh

and Reinoso, 2006). After intercalation of KOH, the weak bonds between the layers of carbon atoms break easily as the activation temperature increases. Based on that, the layers lose their flat shapes and turn slightly into wrinkled or folded shapes, creating interlayer voids. Potassium salts or residual potassium species are removed mostly by being washed with water, leaving the intercalated potassium metal inside the layers of crystallites. The –OK groups are transformed into polar functional groups like –OH by ion exchange during the washing process, making the carbon surface hydrophilic (Viswanathan et al., 2009). In addition, more pores arise by removing K^+ (Madhu et al., 2014).

Many researchers have proposed various mechanisms for activating carbon materials by KOH. For example, Otowa et al. (1993) suggested that several reactions can occur during the activation process, some of which are shown in equations (2.6) - (2.9). The pores are formed at approximately 400 ^oC by removing the amorphous carbon as CO_2 after reacting with steam, as described in equation (2.7) and (2.8), while the carbonate (K_2CO_3) is formed when the temperature exceeds 600 ^oC.

$$2KOH \longrightarrow K_2O + H_2O \quad (2.6)$$

$$C + H_2O \longrightarrow CO + H_2 \quad (2.7)$$

$$CO + H_2 \longrightarrow CO_2 + H_2 \quad (2.8)$$

$$CO_2 + K_2O \longrightarrow K_2CO_3 \quad (2.9)$$

At about 700 ºC, metallic K^+ is produced after the reduction of K_2O by carbon or hydrogen, as shown in equations (2.10) and (2.11). These reactions give a positive indication of the successful intercalation of K^+ into a carbon matrix. Moreover, several atomic layers of carbon are fused, and the surface area increases with an increasing activation temperature to reach a maximum above 600 °C.

$$K_2O + H_2 \Longrightarrow 2K + H_2O \quad (2.10)$$

$$K_2O + C \Longrightarrow 2K + CO \quad (2.11)$$

However, as shown in equation (2.12), Lozano-Castello et al. (2007) explained that the dominant overall reaction stoichiometry between KOH and carbon leads to form an intermediate carbamate K_2CO_3 and H_2 at approximately 400 to 600 ºC. At temperatures above 700 ºC, K_2CO_3 decomposes slowly, releasing CO_2. Carbamate disappears completely at approximately 800 ºC. This process occurs in conjunction with the consumption of carbon at the same degree to reduce K_2O to K^+, as shown in equations (2.16).

$$6KOH + 2C \Longrightarrow 2K + 3H_2 + 2K_2CO_3 \quad (2.12)$$

$$K_2CO_3 \Longrightarrow K_2O + CO_2 \quad (2.13)$$

$$CO_2 + C \Longrightarrow 2CO \quad (2.14)$$

$$K_2CO_3 + 2C \Longrightarrow 2K + 3CO \quad (2.15)$$

$$C + K_2O \Longrightarrow 2K + CO \quad (2.16)$$

Three types of mechanisms are generally accepted to explain the increase in carbon porosity after the intercalation of metallic K^+:

1) The structural etching of carbon, which develops the pore network as a result of the reaction between the carbon surface and various potassium compounds, as shown in equations (2.12), (2.15), and (2.16).

2) The formation of some H_2O and CO_2 as described in equations (2.6), (2.8) and (2.10). These then react with carbon, as shown in equations (2.7) and (2.14).

3) The expansion of the carbon lattice (carbon framework after the carbonisation process) as a result of a number of Metallic K -producing reactions (equations 2.12, 2.15, and 2.16). This process causes an increase in porosity (Wang and Kaskel, 2012).

2.6 Criteria for the Efficiency of Adsorbent Materials

Flue gas components and operating conditions are important factors to determine the suitable adsorbents for CO_2 capture. The most desirable properties for an adsorbent are summarised below:

1. High CO_2 Adsorption Capacity: The adsorption capacity may be determined by equilibrium adsorption isotherm, which can take several forms. The appropriate material should exhibit "high-affinity" isotherm for CO_2. CO_2 adsorption capacity increases in the initial part of the isotherm curve (at low partial pressure) up to the plateau where the function has a constant value. Working capacity (the difference between the amount adsorbed and the amount left after desorption), rather than equilibrium capacity (the maximum amount of gas (CO_2) that can be adsorbed per unit mass of carbon) is more important for practical application due to limited gas-solid contact time (Zhang et al., 2014).

2. Fast Adsorption Kinetics: Adsorption/desorption kinetics primarily affect the working adsorption capacity and the cycle time in dynamic processes. The kinetics of adsorption describe the mechanism of physical and chemical processes on the adsorbent surface with respect to time. In many cases, adsorption is a physical phenomenon with relatively fast kinetics, involving binding the gas molecules (adsorbates) with the adsorbent surface by the Van der Waals forces and diffusing them through the pores (Samanta et al., 2011).

3. High CO_2 Selectivity: Adsorbents that exhibit high CO_2 selectivity over other bulk gas components (e.g., N_2, O_2 and H_2O) are desirable for an economical CO_2 capture system, which includes the following stages (CO_2 transfer and sequestration) (Liu, 2017).

4. Heat of Adsorption: In industrial applications, the economic feasibility of adsorption depends on the ability of the system to regenerate the adsorbent materials. In this regard, the heat of adsorption gives an indication of the energy required for regeneration. For typical physisorption, weak interaction induces low CO_2 adsorption capacity at low pressures. The heat of physisorption usually ranges from -25 to -50 kJ/mol, whereas the heat of chemisorption is usually between -60 to -90 kJ/mol (Samanta et al., 2011). However, the stability of adsorbents during adsorption/desorption cycles is one of the most important factors which determines their performance in practical applications.

5. Tolerance to Impurities and Water Vapour: Typically, flue gas from fossil fuel combustion contains small amounts of impurities, such as SO_x, NO_x, H_2O

and O_2. Some factors, such as the concentration of contaminants in the flue gas, the degree of tolerance and the affinity of adsorbent to such impurities, play an important role in reducing CO_2 adsorption. For example, some adsorbents have a high affinity for H_2O, which have an adverse effect on CO_2 adsorption capacity and also increases the energy required for the regeneration step. Therefore, removing contaminants may require additional units, which means increasing the cost.

6. The Cost: The low cost of adsorbents minimises the total capital cost of the solid-adsorption system compared with liquid adsorption. In general, if the adsorbents cost no more than 15 $/kg, the adsorbent materials will continue to be economically viable (Samanta et al., 2011). As a matter of fact, the prices of activated carbons at present are far below this value (Sorrels et al., 2018).

7. High Stability: The stability of the adsorbent during extensive adsorption–desorption cycling is the key parameter for determining the lifetime of any adsorbent and thus the frequency of its replacement in the CO_2 capture system. Moreover, operating conditions such as high flowrates, high temperatures, H_2O or vibration may cause mechanical degradation after adsorption/desorption cycles. Therefore, the durability and stability of the materials have attracted considerable academic attention.

2.7 Regeneration Energy for Post Combustion CO_2 Capture

Two factors can play an important role in estimating the energy requirements for CO_2 adsorption: (1) the concentration of CO_2 in the flue gas, and (2) the type of material used to separate CO_2.

For existing power plants, and because of the low CO_2 content in flue gas (approximately 3 %), the highest energy penalty of CO_2 capture is for Natural Gas Combined Cycle (NGCC) post-combustion plants (about 3.6 GJ /tonne CO_2) that use MEA scrubbing (Karimi et al., 2012). On the other hand, some studies have shown that the thermal energy required for the sorbent regeneration is less than 2.3 GJ / tonne CO_2, making the adsorption process more economical than conventional methods (Zhang et al., 2016, Liu, 2017).

2.8 CO_2 Cycle Processes

Generally, to investigate the stability of solid adsorbents for long periods of time, multicycle adsorption/desorption processes are required.

1) **Temperature Swing Adsorption (TSA):** this technique is based on a spontaneous phenomenon of attraction between the molecules of gases and the surface of nearby solids at low temperatures, and is also based on releasing the molecules with increasing temperature. Over multiple regeneration cycles, the periodically changing temperature should not drastically affect the structure of adsorbents (Liu, 2017). Maintaining superior thermal stability during the regeneration process is one of the most important characteristics of good adsorbents. In TSA technology, the adsorber temperature can be raised by direct or indirect heating. The indirect heating process relies on heating jackets, electric heating tapes, coils wrapped around the adsorber, and hot/cold fluid carrying tubes to raise the temperature. During direct heating, the heat can be significantly increased by using hot non adsorbing gas (hot air or N_2) or steam. TSA is not particularly favourable due to the high vapour consumption required for heating the column (Ntiamoah et

al., 2016). For post combustion capture applications, quantities of low-grade waste heat can be exploited to reduce the cost of the energy requirements of CO_2 capture systems (Ling et al., 2014). Pirngruber et al. (2009) attributed the long period required for heating/cooling to lower thermal inertia of the adsorbents. In fact, TSA still faces many challenges that limit its use in different industrial applications, especially those containing a large number of adsorption columns with different types of adsorbents.

To study the effect of regeneration temperature on CO_2 recovery and purity, Ntiamoah et al. (2016) designed three fixed beds filled with NaUSY zeolite. The TSA process (adsorption and desorption steps) used to capture CO_2 from feed gas consists of 15 % CO_2 and 85 % N_2. The results showed that the purity of CO_2 was more than 91 % with 55 %, 76 % and 84 % CO_2 recoveries for regeneration temperatures of 150, 200 and 250 °C, respectively. This study indicated that regeneration temperatures of over 150 °C are necessary to enhance desorption capacity for commercial physisorbed. Additionally, Liu (2017) determined the peak desorption temperature of activated carbon to be around 150 ^{o}C. In fact, TSA is only favourable when the adsorption column maintains a good balance between adsorption and desorption time, which can be done if the feed stream contains a low concentration of adsorbates.

2) Pressure Swing Adsorption (**PSA**): This technique is based on the fact that gases are attracted to the adsorbent surface more easily at high pressure and released with decreasing pressure. It is highly useful for pre-combustion capture within an IGCC power plant due to the high purity of H_2 and CO_2 that is produced.

Ogbuka (2013) explained that there are three main steps to achieve PSA. First, adsorption occurs when particular gas species are separated from the gas mixture stream with increasing pressure and by condensing the adsorbents. This step is conducted when the fixed bed is under specific operating conditions (composition, T and P). When the bed reaches full capacity, the next step will begin. Feeding should be stopped and the overall pressure of the system should be reduced dramatically to release the adsorbed gases. Finally, the gas mixture stream acts to increase the bed pressure to repeat the adsorption-desorption cycle capture. In addition to the cost, the concentration of the component that needs to be separated from the gas mixture stream should be taken into account when selecting the appropriate adsorption technique for an industrial application. PSA is preferred for the processes that need to remove a large proportion of the components from the gas stream and create a balance between loading and unloading. This is because the loading of the bed may be completed within a short time and the adsorption-desorption process can rapidly change the overall system pressure (Grande, 2012).

3) Vacuum Swing Adsorption (VSA): The swing from ambient-pressure to low-pressure is performed using a vacuum pump to increase the desorption capacity of the adsorbent materials. This technique is a modification of the PSA process, except it is done without the pressurisation step. As a simple and low-cost technique, VSA has gained increasing importance in the gas processing industry, especially for post-combustion CO_2 capture where the flue gases are usually at atmospheric pressure and the CO_2 is an essential component. For economic reasons, it is very important

to find a balance between adsorption pressure and power consumption at the blower or vacuum pump.

In general, adding more beds can optimise the process to increase the recovery and purity of adsorbates (Xiao et al., 2009). When comparing the performance of cyclic adsorption processes of PSA, VSA, and TSA reveals that PSA efficiency is proportional to the density of adsorbed gases, where light gases play an important role in maximising productivity. Songolzadeh et al. (2014) advise that the cyclic duration of the PSA usually ranges from several seconds to several minutes, while classic TSA processes take longer because of the limited steps of the relatively slow heating and cooling process. Although recovery and purity are high for VSA, Pirngruber et al. (2014) stated, "but the very low pressure that required for regeneration of the adsorbents will be a serious handicap for the deployment of this technology on a large scale".

2.9 Cost of CO_2 Capture & Storage

Typically, the total cost of the CCS system covers the cost of three essential stages; capturing and separating CO_2, pipeline systems for the transportation of CO_2, and storage in geological sites such as gas reservoirs or deep oceanic sequestration. For the capture stage, an economic comparison of three gas separation technologies (chemical absorption, membrane separation and adsorption) reveals that the larger differences are usually confined to the cost of capital expenses and the cost of energy required for regeneration. Hongjun et al. (2011) analysed and compared the costs required for the three CO_2 separation technologies to capture the same quantity of CO_2 created in coal-fired power plants and compress captured CO_2 via pipeline to

about 10 MPa. No significant cost differences were detected between chemical absorption and adsorption; the costs ranged from $ 30 to $ 60 and $ 40 to $ 63 per tonne CO_2, respectively. The cost of CO_2 capture with membrane separation was around $ 50 to $ 78 per ton CO_2. In actuality, Hongjun's research group had ignored the additional cost of the high degradation rate of MEA and the cost of the process equipment corrosion that takes place usually after using the chemical solvents over a long period of time. The cost of transportation is directly proportional to the size of the power plant, and inversely with increases in the distance to storage places. Using a pipeline system, Grant et al. (2018) estimated the total cost of transporting one ton of CO_2 produced from 500 MMscf/d natural gas processing plant for 2186 km to the storage site about $ 155 per tonne. The literature agrees that the cost of CCS can be reduced with evolving technologies, gaining more practical experience, and increasing the economic benefits of using CO_2 in different sectors (Metz et al., 2005, Rubin and De Coninck, 2005, McFarland and Herzog, 2006).

2.10 Modification of Activated Carbon for CO_2 Adsorption

Many authors now agree that the unique adsorption properties of activated carbon are strongly influenced by surface groups (Yehaskel, 1978, Marsh and Reinoso, 2006, Menendez-Diaz and Martin-Gullon, 2006, Wickramaratne and Jaroniec, 2013, Lee et al., 2014). Therefore, the bulk of the existing research focuses on improving CO_2 adsorption capacity by modifying the surface chemistry of carbon using physical and chemical methods.

On the grounds of the acidic nature of CO_2 (a weak Lewis acid), a variety of physical methods have been highlighted recently to enhance the CO_2 adsorption capacity of

adsorbents in post-combustion capture, such as removing acidic groups by heat treatment and/or replacing them by basic functional groups (Khan, 2003, Okieimen and Ogbeide, 2009, Plaza et al., 2010). Figueiredo (2013) demonstrated that most surface O_2 groups can be released as CO and/or CO_2 during decomposition between 100 – 950 ^oC. A variety of nitrogen-enriched precursors, such as carbazole, melamine, and acridine are used in the preparation of activated carbon. However, there is no evidence that these precursors have an beneficial effect on the basicity of the carbon surface (Chen et al., 2014). According to various researchers (Plaza et al., 2007, Tazibet et al., 2013, Chen et al., 2014), for many nitrogen-containing reagents (i.e., ammonia, urea, amine), extended heat treatment with gaseous ammonia is an effective technique for microporous carbons due to its high efficiency in adsorbing CO_2 when compared with urea. In addition to the changes in the pore size distribution, introducing the N containing groups makes activated carbon surface more alkaline. The absorbability of acid agents such as CO_2 is expected to increase as a result. Przepiórski et al. (2004) indicated that the increase in CO_2 adsorption capacity of the ammonia-treated activated carbon depends on the treatment temperature. For instance, the sample treated at 400 °C showed the highest adsorption capacity of CO_2 (1.73 mmol/g) while a slight decrease in adsorption was observed with increasing temperatures above 400 °C. Chen et al. (2014) pointed out that the numbers, distribution, and types of N_2 species on activated carbon play an essential role in attracting the molecules of adsorbates such as CO_2.

Figueiredo et al. (1999) investigated the texture and surface properties of NORIT activated carbon, which was oxidised separately using two modification techniques:

oxidation in the gas phase and oxidation in the liquid phase. Using O_2 and N_2O gas at high temperatures 425 – 1100 ^oC, weak acid groups such as carboxyl and carbonyl increased on the surface of activated carbons. The best results were obtained from samples that underwent a long period of heating and showed a high burn off percentage. On the other hand, carboxylic acid groups increased after oxidation by liquids (nitric acid, and H_2O_2). In fact, in addition to the previous factors, the concentration of liquids plays a significant role in increasing strong acid groups. It is noteworthy that under gas treatment, the micropore volume increased when raising the carbon burn off percentage, while no important change in texture was noticed during the liquid phase oxidation. It has only recently been reported that the O_2 functional groups (in conjunction with N_2 groups) can enhance CO_2 adsorption. Using a quantum chemical calculation, Xing et al. (2014) provided a detailed understanding for the adsorption mechanism of carbon-based materials. They explained that the presence of O_2 atoms on the external surface can promote hydrogen bonding with CO_2. Additionally, the reactivated carbon with nitric acid exhibits CO_2 adsorption more than those without nitric acid, or they are modified by heat treatment.

Among the variety of activating agents used in chemical methods, reactions between KOH and carbon materials lead to a significant increase in CO_2 adsorption. Two main factors can affect CO_2 adsorption on chemically activated carbon with KOH: KOH/carbon ratio and activation temperature (Viswanathan et al., 2009). Sevilla et al. (2011) investigated the effect of K^+ intercalation via a KOH on the effectiveness of CO_2 adsorption on the activated carbon. Several types of biomass-based activated

carbon were intercalated via KOH with a mass: KOH/AC ratio of = 2/4 at different temperatures 600, 650, 700, 800 ^{o}C. As shown in Figure 2.7, the highest CO_2 adsorption was obtained by the modified sample with KOH/AC = 2 under 700 ^{o}C (6.6 mmol/g CO_2 adsorption at 0 ^{o}C and 1 atm), while the carbon material that was treated with the same KOH ratio under 600 ^{o}C has exhibited 4.8 mmol/g of CO_2 adsorption at room temperature. Different types of raw materials have had a slight effect on the CO_2 adsorption.

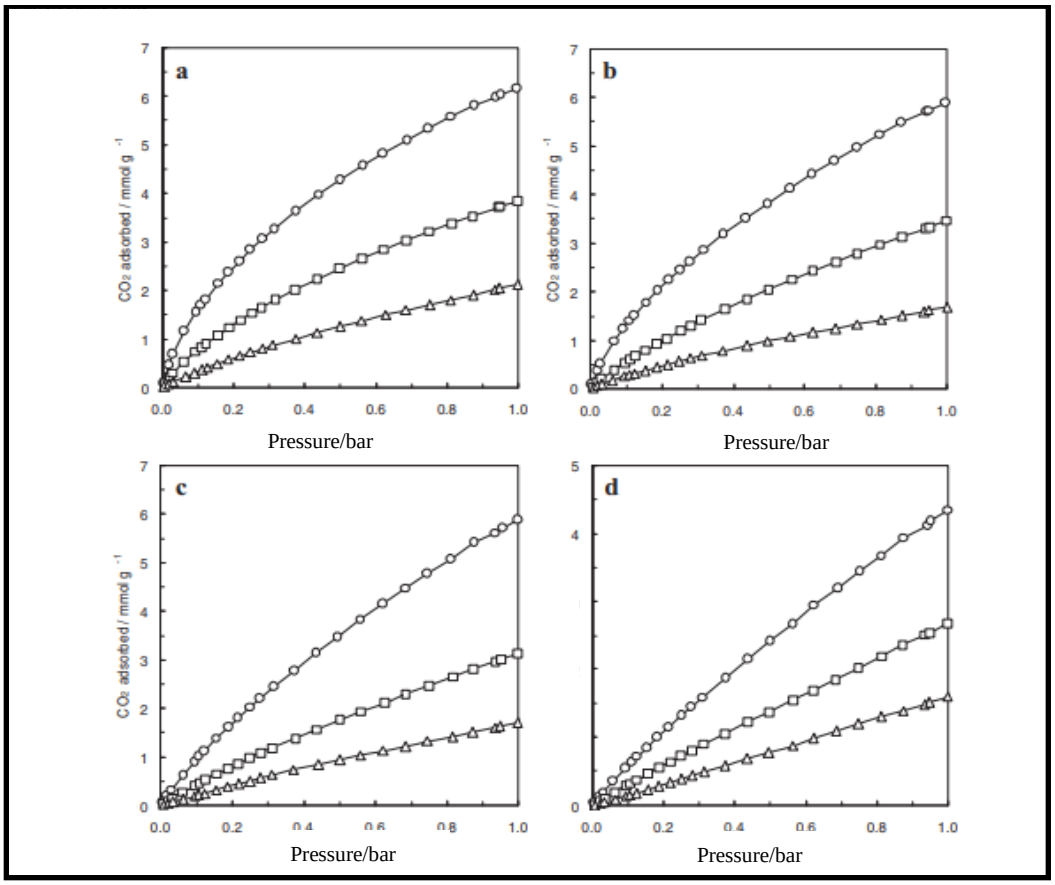


Figure 2. 7: CO_2 adsorption isotherms at 0 ^{o}C (O), 25 ^{o}C (□) and 50 ^{o}C (Δ) for the porous carbons obtained when KOH/AC = 2 at the following activation temperatures: (a) 600 ^{o}C (AC-2-600), (b) 650 ^{o}C (AC-2-650), (c) 700 ^{o}C (AC-2-700) and (d) 800 ^{o}C (AC-2-800) (Sevilla et al., 2011) .

Liu et al. (2015a) revealed that the adsorption capacity of activated carbon obtained from a nitrogen-free phenolic resin has doubled to 1.52 mmol/g (at 0.15 atm and 25 ^{o}C) with increasing KOH/AC mass ratios used in the chemical activation to 1:1. However, at 1 atm and using the same ratio of KOH/AC (1:1), the adsorption capacity of activated carbon increased only 25 %. All activation treatments were carried out at 700 ^{o}C.

Buczek (2016) found that reactivated carbon at 700 ^{o}C with 1 KOH: 3 AC (m/m) exhibited nearly double CO_2 adsorption of pure AC, as calculated from 3.0 MPa isotherms. The effect of KOH on activated carbon has been continuously proven in the recent years by many researchers (Chomiak et al., 2017, Singh et al., 2017, Liu et al., 2018a, Liu et al., 2018b, Kutorglo et al., 2019).

2.11 Organosiloxane Compounds

2.11.1 Introduction

Most organosiloxane compounds share a number of characteristics - they are colourless, have a high solubility in many organic solvents, are highly flammable and stable in the air, and have a hydrophobic surface due to their non-polarity organic (alkyl) groups. The procedure developed by Müller and Rochow in 1940 is widely used in industry today to produce various organosiloxane components. For example, alkyl or aryl halides react directly with organosiloxane compounds in a fluidized bed reactor in the presence of copper, which acts as a catalyst to form organohalosilanes (Kalchauer and Pachaly, 2009). Depending on the nature of the hydrolysable groups attached to silicon, four categories of silanes were

distinguished: chlorosilanes, silazanes, alkoxysilanes and acyloxysilanes. Organosiloxane compounds can be used in different fields (Materne et al., 2012):

1- Monomer can be used in the manufacturing of silicone polymers through hydrolysis and polymerisation.

2- They can be useful in the development of the properties of plastics, rubber, and paints.

3- They can be used in the synthesis of organic compounds in the pharmaceutical and cosmetic industries.

2.11.2 Chemical Reactions of Organosiloxane Compounds with Activated Carbon Surfaces

The formation and distribution of polysiloxanes on surfaces depend upon several factors, such as the number of organic functional group-containing alkoxysilane, the length of the alkyl chain, the efficiency of the silanisation reaction and the type of aqueous solvent used in the liquid phase (Hetem, 1990).

In general, the reaction of organosiloxane with solid surfaces can be broken down into two steps: hydrolysis and condensation. In the first step, one or more of the alkoxy (-OR) groups are replaced by (-OH) to form Si-OH groups (silanols). An alcohol (methanol, ethanol and propanol) or acid (acetic acid) is released depending on the type of silicon alkoxide used. Silanol groups have a high dipole moment. During the condensation step, the organosiloxane groups join with (1) adjacent organosiloxane groups to form a stable and flexible siloxane chain (-Si-O-Si-), and join with (2) surface hydroxyl groups by covalent bonding where the water plays a

catalytic role in the silation reaction, as shown in Figure 2.8 (Almanza-Workman et al., 2004).

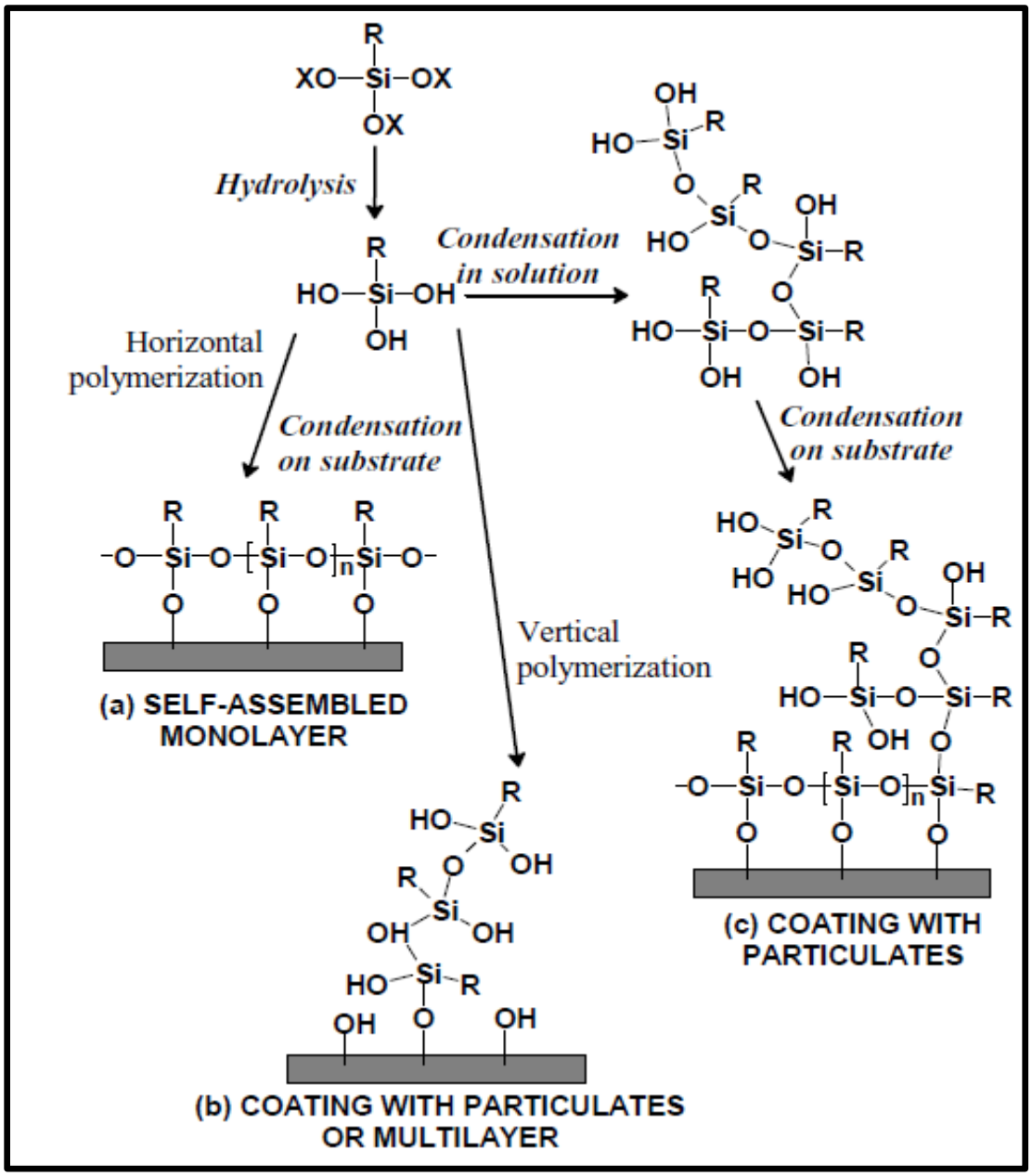


Figure 2. 8: Possible products of the reaction of alkytrialkoxysilanes in the aqueous phase and at the solution/substrate interface (Almanza-Workman et al., 2004).

The silylation reaction can occur either in the liquid or gas phase. While only monolayer or near-monolayer silylation coverage occurs in the gas phase, the multilayer structures can form on the surface using di- or trifunctional organosiloxane s in the liquid phase (Yoshida et al., 2001). Asenath Smith and Chen (2008) showed that hydrolysis and condensation of monofunctional alkoxysilanes can occur at the same time to form siloxanes in the presence of non-polar solvents, followed by the polymerisation step. Silane layers prepared in dry toluene at 70 ^{o}C are higher in packing density and exhibit greater hydrolytic stability than those prepared in the vapour phase at room temperature. However, the control of the silylation process is greatly affected by depositing a polymer film on the accessible surface areas, which creates the possibility of incomplete and non-uniform silylation coverage arising on the carbon surface. Generally, the hydrolysis of one or more of multifunctional silanes (di- or tri-functional alkoxysilane) can make hydrolyzed silane molecules more reactive with the surface hydroxyl groups (Yoshida et al., 2001).

The findings obtained by Gilles (2007) showed that the second method is more effective for controlling the silylation reaction and obtaining uniformly distributed polysiloxane structures on the silicon surfaces. For all methods, in addition to the accessibility of surface silanols, the number and distribution of silanols play an important role in achieving high deposition of silanols on the surface. Various types of solvents, such as toluene, cyclohexane and acetone have been used in liquid silylation reactions, and have different effects on the area of a surface covered and the number of layers that can be formed above the surface.

Several studies have reported that a trace amount of water in toluene is sufficient to regulate the degree of polymerisation (Chang et al., 2000, Sánchez-Soto et al., 2001). For the solution deposition of the silane, the limited increase in the amounts of water usually leads to homocondensation of silanes in the horizontal and vertical directions on the adsorbent surface and increases multilayer condensation. For example, Harlick and Sayari (2007) proved that some drops of water can add 30 % of silane loading, and therefore subsequently improve the CO_2 adsorption.

Alkyl chains can be twisted, extended and connected with adjacent alkyl chains by Van der Waals forces. The long alkyl thiols [number of carbon (n) ≥ 18] can form a high packing density and can provide complete coverage on the surface. Meanwhile, disordered and incomplete coverage can arise on the surface with short alkyl chains. Long alkyl chain thiols are commonly used to modify material surfaces toward lowering the surface energy without altering the surface chemistry (Schwarz and Contescu, 1999). In the same vein, classes of materials such as alkyl or fluorinated organic silanes, perfluorinated alkyl agents, long alkyl chain fatty acids, and polydimethylsiloxane-based polymers exhibited promising results (Jafari and Farzaneh, 2012).

In this work, five long-chain organosiloxane compounds were grafted onto activated carbons. The sterically demanding silanes were selected to provide a range of solid–vapour surface energies and condensation rates. Sterically demanding silanes were chosen to inhibit the deposition of the silanes within the pores of activated carbon. This strategy was applied before by Brühwiler, Calzaferri et al. (2009) to adjust the host–guest interactions on the mesoporous silica and to select the functionalisation

of the channel entrances of zeolite. Moreover, Starkie (2016) also used it to prevent leaching of the impregnated amine component from the large pores of support and also used it to increase the hydrothermal stability and hydrophobicity of silica. Given the small pore size diameters of the activated carbons, the diffusion rate of silanes to the pores is expected to be limited.

2.12 Effect of H_2O on CO_2 Adsorption with Activated Carbon

There are relatively few studies that characterise H_2O uptake on activated carbons. The following studies are focused on using physical and organosiloxane compounds treatments to modify activated carbon surfaces towards increasing hydrophobicity whilst maintaining high adsorption capacities for gases under humid conditions.

A series of experiments was conducted by Tazibet et al. (2013) to study the effects of thermal treatment at different temperatures (300, 400, 500, 600, 700 ^{o}C) on the texture properties and H_2O uptake of activated carbon prepared from an olive waste precursor. The work focused on the selective elimination of carboxylic acid functions from the activated carbon surface without altering its textural properties. The results showed that the optimum temperature of heat treatment, which provides the best hydrophobic properties of the activated carbon, is 500 ^{o}C, as shown in Figure 2.9 and 2.10. Additionally, a decrease in micropores was observed, which may be attributed to the intensive decomposition of acid surface groups that accompanies the collapse of some pore walls.

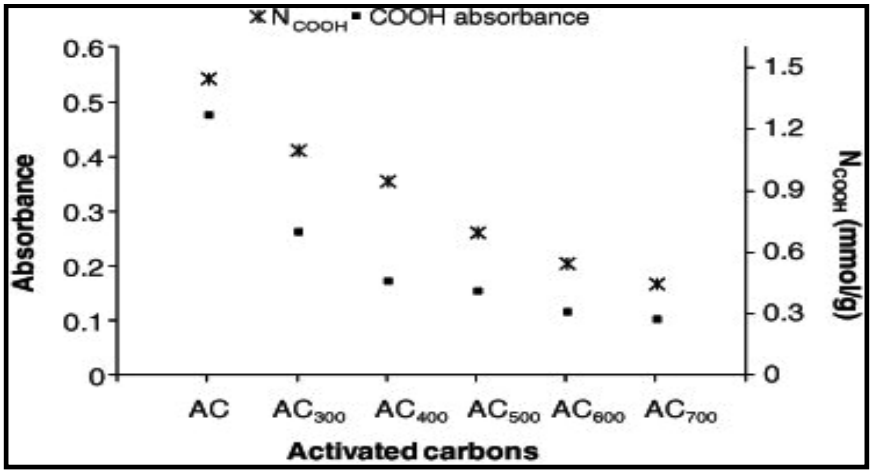


Figure 2. 9: The effect of heat treatment temperature on the concentration of total carboxylic surface groups (Tazibet, Boucheffa et al. 2013).

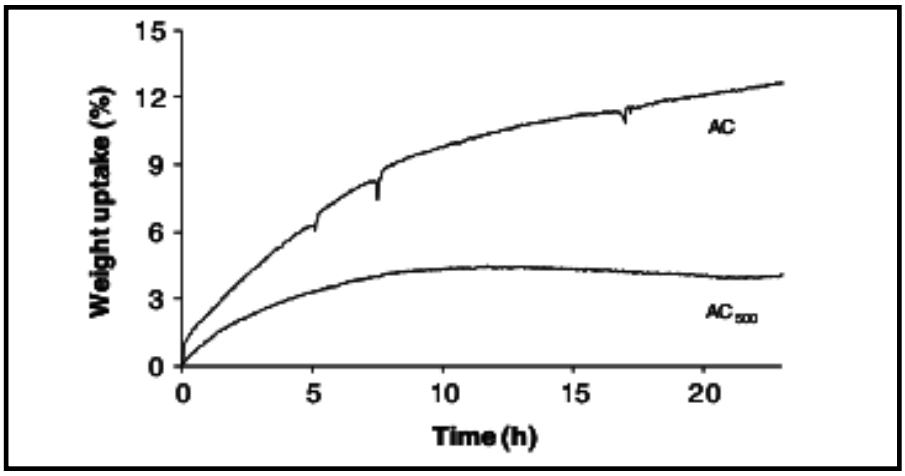


Figure 2. 10: The H_2O uptake of AC and AC 500 at 20 °C and 70 %RH (Tazibet, Boucheffa et al., 2013).

The pyrolysis of propene at a temperature between 300 and 600 °C was used to modify granular activated carbon towards increasing the hydrophobicity by depositing carbon on the surface active sites. The experiments performed by Gonçalves et al. (2010) demonstrated that the best result was at 300 °C, where only 1 % of carbon deposit on activated carbon was sufficient to reduce 35 % of the

adsorption active sites without an appreciable decrease in the volume of micropores, thus reducing the number of O_2 surface groups on the activated carbon.

Organosiloxane compounds methods have been used to improve the hydrophobicity of activated carbon, which mainly involves coating and impregnation. Two types of plasmas, tetrafluoroethylene (TFE; C_2F_4 or C_2F_6-H_2) and hexamethyldisiloxane (HMDSO) $C_6H_{18}Si_2O$ vapor were used for coating activated carbon in the gas phase. To compare the efficiency of these types of gas, Wertheimer et al. (1998) investigated the effect of the two types of plasmas on the hydrophobicity of activated carbon and the adsorption rate of CCl_4 vapor. The main variable was residence time in the plasma. Nominal residence times ranged from 3 to 40 seconds for HMDSO and from 30 to 120 s for TFE, resulting in a corresponding deposit thicknesses between 12.6 and 168 nm, and 36 and 144 nm, respectively. The best result was introduced by the HMDSO where the H_2O uptakes were much lower than those of the CCl_4, (H_2O reduction ~85 CCl_4 reduction < 20 %). C_2F_4 and C_2F_6-H_2 plasma proved to be much less effective than organosiloxane.

The pioneering work by Nakanishi et al. (1998) determined the efficiency of trimethyl chlorosilane as a coating for activated carbons to be used in the purification of the groundwater from organochlorine compounds. The coating process was conducted both in the gas phase and the liquid phase. The treatment with a solution of trimethyl chlorosilane increased the adsorption constant in Freandrich adsorption equation (k) from 93 to 217 (the adsorption capacity of organochlorine compounds is directly proportional to the k value). On the other hand, using trimethyl chlorosilane vapor raised k from 50 to 218. In both coating

cases, the adsorption ability of the surface hydrophobic active carbon improved markedly toward organochlorine compounds.

Budarin et al. (2000) revealed that the hydrophobisation of the activated carbon surface takes place by grafting non-polar functional groups on its surface. They reported that surface treatment of carbon with vinyltrimethoxysilane (VTMOS) can improve the selectivity of non-polar species and decreases their affinity toward polar material such as H_2O. This method was proven to be effective, and the only observed disadvantage was a slight reduction in the BET specific surface areas and total pore volumes. Based on this work, the organosiloxane coating method was used by Cosnier et al. (2005) to reduce the affinity of activated carbon (commercial granular and fibres derived from biomass) for water vapour and also to increase its selectivity toward the vapours of chlorinated volatile organic compounds (VOCs). Moreover, they explained that VTMOS causes many pores to block. Thermal treatment was performed under different temperatures (200, 300, 400, 600 ^{o}C) to restore initial porosity as far as possible and to investigate the stability of hydrophobised activated carbon. Figure 2.11 shows that the optimum temperature to achieve a balance between high pore volume and high hydrophobicity is 400 ^{o}C, where minimal H_2O uptake was achieved, which can enhance the selectivity for VOCs at 50 %RH.

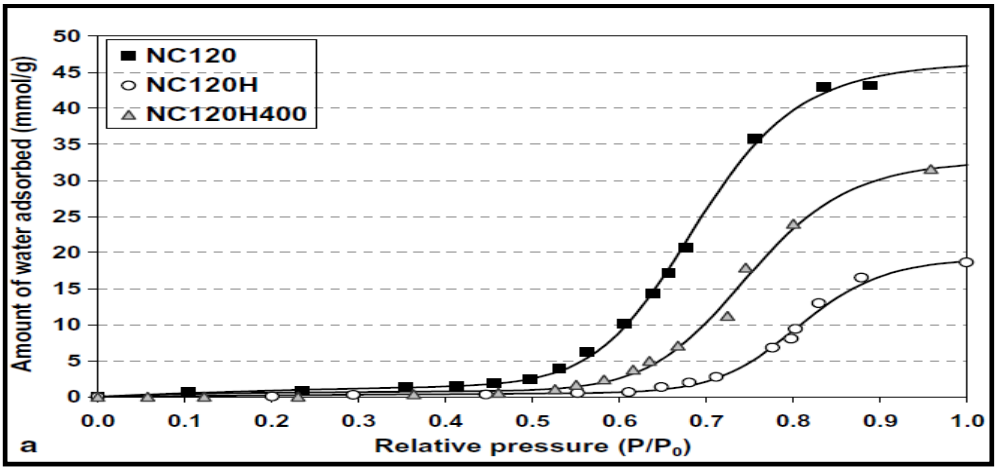


Figure 2. 11: Water adsorption isotherm on activated carbons and its derivatives (Cosnier, et al. 2005).

Xie et al. (2011) studied the difference between the static and dynamic adsorption of carbon disulfide (CS_2) over activated carbon fibre (ACF), activated carbon fibre after reduction treatment (ACF-R) and hydrophobised activated carbon (ACF-H) under humid conditions (70 %RH). They explained that VTMOS can be grafted on two sites: the edges of the carbon layers and the pore mouth. Depending on the alterations in pore texture after hydrophobisation, they assumed that most VTMOS were grafted on the active sites on the edges of carbon layers. Their findings showed that ACF displays the best performance for the CS_2 adsorption process. For dynamic adsorption, there was a significant decrease in H_2O uptake at high humidity, as shown in Figure 2.12, offering an increase in selectivity for CS_2 over the hydrophobised ACF. They attributed this to a number of factors: increasing the breakthrough time, a slight alteration in pore volume with increases in hydrophobicity, the differences in adsorption isotherm types and adsorption mechanisms between CS_2 and H_2O, along with the differences between the polarity of VTMOS and H_2O.

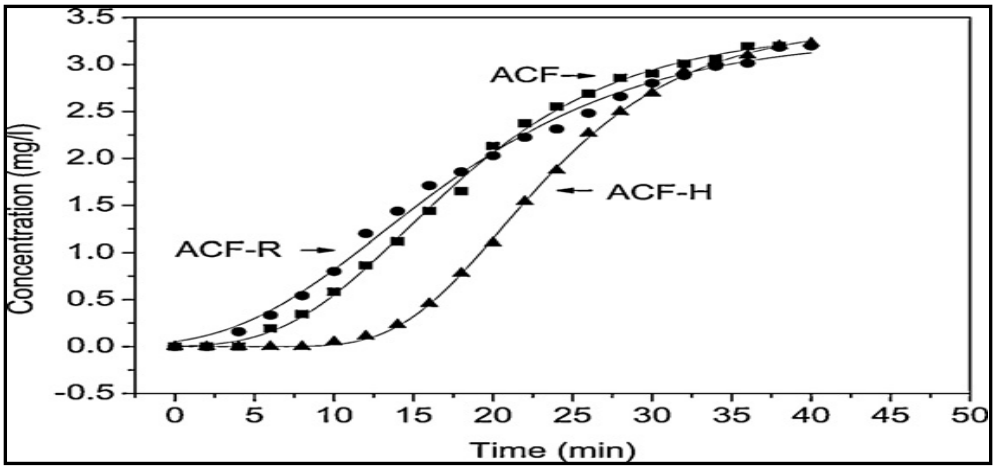


Figure 2. 12: Breakthrough curves of ACF, ACF-R and ACF-H (Xie, Wang et al., 2011).

There is still some controversy regarding the effect of H_2O on CO_2 capture performance. Shen et al. (2012), Chen et al. (2013) and Cen et al. (2014) have shown that H_2O has a considerable negative effect on the adsorption of CO_2 on the activated carbon. On the other hand, Dong et al. (2011) reported that the presence of H_2O may not cause significant changes in CO_2 adsorption rates, and the low H_2O sensitivity of activated carbon has made it a very promising candidate to separate CO_2 in specific conditions. They attribute this to differences in adsorption mechanisms between CO_2 and H_2O on activated carbon. Cen et al. (2014) explained that consecutive adsorption cycles with wet CO_2 lead to a slight decrease in breakthrough and saturation time due to the gradual accumulation of H_2O on the surface of activated carbon, which may cause the partial pore mouth closure of the active sites and minimise CO_2 adsorption capacity. Moreover, they proved that increasing the H_2O content of flue gas leads to a reduction in breakthrough CO_2 time, while Chen et al. (2014) indicated that the time of wet CO_2 breakthrough

decreased in some types of activated carbon, which contains many mesopores owing to the lower diffusion resistance through the pores.

In fact, the approximate diameter of a CO_2 molecule is 0.209 nm (Martín et al., 2011), and for an H_2O molecule, it is 0.275 nm (Haubrich et al., 2011). Therefore, these are incredibly small compared to other gases' molecules. According to the literature (Martín et al., 2010), the best adsorption capacity can be obtained at ambient pressure with micropore sizes between 1.5 to 2 nm.

2.13 Conclusions

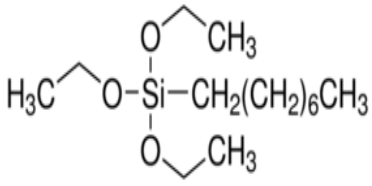
Regarding the use of activated carbons for the post-combustion capture of CO_2, this review has highlighted the beneficial effect of KOH treatment to maximise CO_2 adsorption capacity. However, there is a lack of knowledge on the impact of KOH treatment on the water vapour co-adsorption of CO_2 capture for activated carbons, given that H_2O significantly increases the regeneration energy. Therefore, further research is needed to better understand CO_2/H_2O selectivity for activated carbons. Furthermore, discovering whether the modification of activated carbons using organosiloxane compounds can potentially reduce the adsorption of H_2O and increase CO_2/H_2O selectivity.

Chapter 3: Experimental and Relevant Theory for the Techniques Used

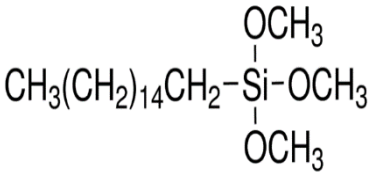
3.1 Materials

The granular activated carbon derived from coconut shell (CS) with particles size 1-1.4 mm (the particle sizes of the samples were measured by molecular sieve) was obtained from CPL Industries Group Limited, it was prepared via the carbonisation of coconut shell at 700 ^{o}C under N_2 for 30 minutes and steam activation at 850 ^{o}C. The carbonised phenolic resins (PR) with particles size 1.2-1.4 mm was supplied by the University of Nottingham (Details of the preparation steps for PR are presented in a previous Study (Liu et al., 2015b)). Sodium borohydride ($NaBH_4$), Potassium hydroxide (KOH), vinyltrimethoxysilane (VTMOS), trimethoxy(octyl)silane (OTES), perfluorodecyltriethoxysilane (POTS), hexadecyltrimethoxysilane (HDTMS), triethoxyphenylsilane (PTES) (98 % purity for all organosiloxane compounds), methanol (99.8 % purity), toluene (99.8 % purity) and hydrogen peroxide solution (H_2O_2) (30 % in H_2O) were obtained from Sigma-Aldrich. The following paragraphs give more details about the structure of organosiloxane compounds.

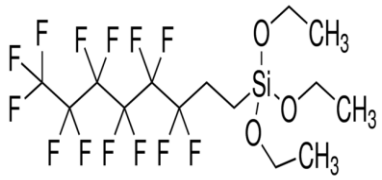
Trimethoxy(octyl)silane (OTES): This silane exhibits low steric hindrance and fast hydrolysis and condensation reactions rates due to containing short linear alkyl groups (C=8).



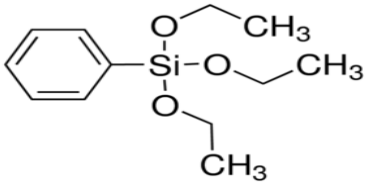
Hexadecyltrimethoxysilane (HDTMS): This silane exhibits high steric hindrance and low hydrolysis and condensation reactions rates due to containing long linear alkyl groups (C=16). Therefore, not all hydroxyl groups on the particle surface can react with it. The length of the alkyl group plays a significant role in determining the properties of silanes.



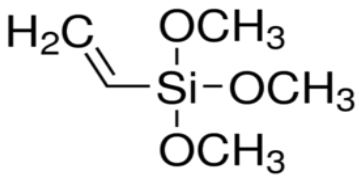
***1H,1H,2H,2H-Perfluorodecyltriethoxysilane (POTS)*:** This silane has a long perfluoro chain. Based on the fact that C-F bond length in fluorine (typically about 1.38 Å) is longer than C-H bond length (approximately 1.09 Å) (Ceretta, 2013), fluorine group is a much more sterically demanding compared with the methyl group and is expected to have a high contact angle with high hydrophobicity.



Triethoxyphenylsilane (PTES): The large size of the phenyl group increases the steric effect and reduces surface coverage leaving a great number of exposed silanol sites on the surface. Therefore, this type of silane exhibits low hydrophobicity. Otherwise, the phenyl group offers a promising result in providing additional sites for CO_2 adsorption (Starkie, 2016).



Vinyltrimethoxysilane (VTMOS): This type of silane is expected to yield high hydrophobicity on activated carbon due to the presence of a methylene (=CH_2) group.



3.2 Methods

3.2.1 Activation & Reactivation of Materials

The chemical treatment was carried out by the following steps:

1- The carbonised phenolic resin carbon was mixed with ground KOH in the ratio 1:2 (m/m).

2- Measured amount of mixture (usually less than 5 g) was put into the pot, which was placed inside a quartz tube, N_2 gas (1 bar, 1 L/min) was passed for approximately 15 minutes to remove any residual air. After this, the mixture was heated separately to 650, 700 and 750 ^oC in a horizontal tube furnace (Elite Thermal Systems Ltd., UK) at a rate of 3 ^oC/min in the presence of N_2 (Figure 3.1). After reaching the desired temperature, the temperature was held for 60 minutes and then cooled to ambient temperature.

3- The obtained activated carbon was washed several times with distilled water to remove residual KOH and obtain a neutral pH, the wet sample was dried in an oven under 100 ^oC for 24 hours. The activated carbons obtained were called PRK.

The same procedure was implemented to reactivate coconut shell activated carbon. The activated carbons obtained was labelled with acronyms CSK.

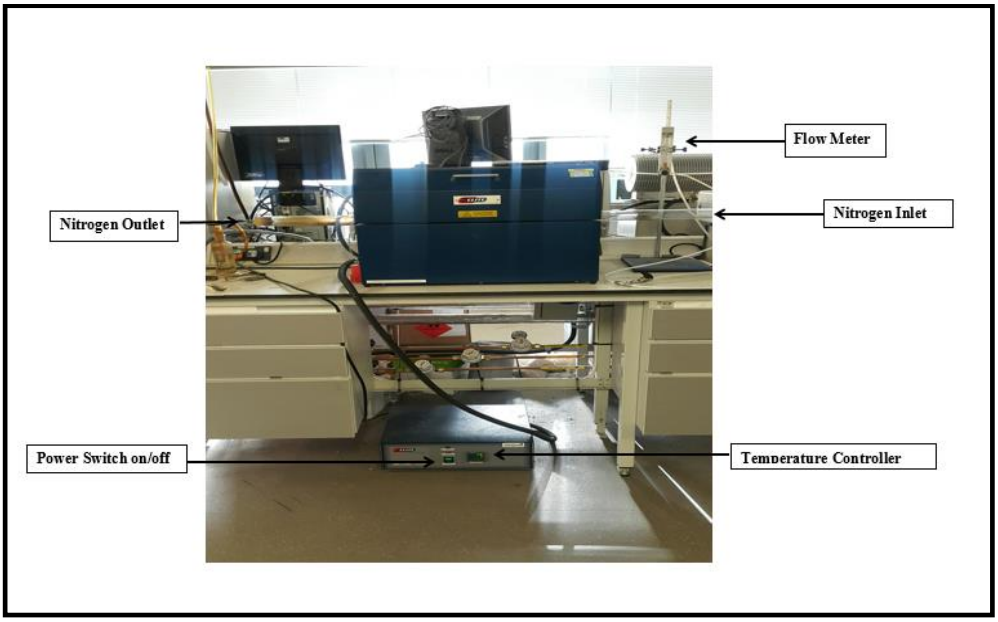


Figure 3. 1: Horizontal Tube Furnace.

3.2.1.1 Physical Treatment

A measured amount of activated carbon was submitted to physical treatment using the same horizontal tube furnace. The preparation of the furnace consisted of setting a ramp rate of 3 ^{o}C/min up to the desired temperatures, 700 and 900 ^{o}C, for 3 hours.

3.2.1.2 Organosiloxane Compound Treatment

Following the experimental protocol described by (Budarin et al., 2000), the hydrophobisation modification in this work was conducted in the following steps, as shown in Figure 3.2:

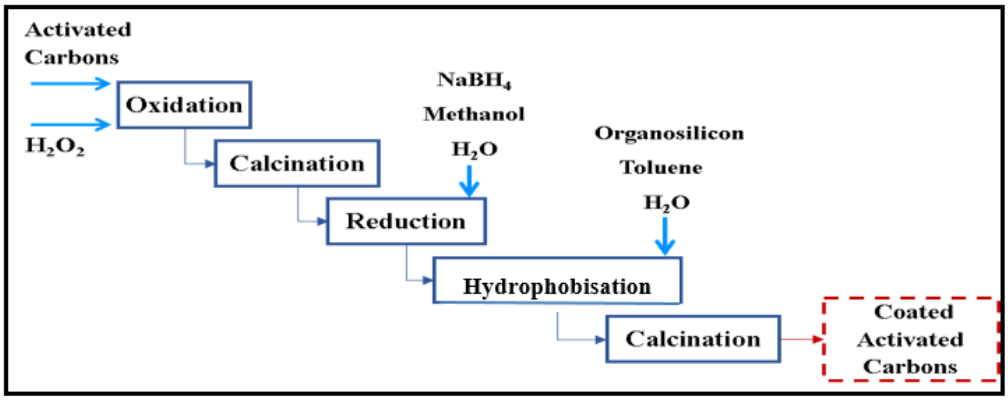


Figure 3. 2: Experimental Procedure Flowchart.

1- Oxidation: 2.5 g of activated carbon was added to 250 ml of 15 % H_2O_2 (w/w). The mixture was washed with distilled water and dried at 100 ^oC for 24 hours. The dried mixture was then heated at 450 ^oC for 3 hours under an N_2 atmosphere.

2- Reduction: 2.5 g of the $NaBH_4$ solution was mixed with 250 ml of anhydrous methanol. The sample was submerged in the mixture for 12 hours, the solution was then diluted by 250 ml of water and boiled for 3 hours. After that, the sample was taken out of the mixture, washed with water and dried in a vacuum oven for 24 hours at 100 ^oC.

3- Hydrophobisation: The hydrophobisation modification was carried out in the following steps: Firstly, at the distillation flask, the organosiloxane was dissolved partially by toluene at the ratio (1:10) v/v with some drops of water to induce the hydrolysis of the alkoxysilane molecules. Secondly, the sample was placed inside an extraction thimble and loaded into the main chamber of Soxhlet extractor. The soxhlet exactor was connected with distillation flask and reflux condenser. Finally, the distillation flask was heated, as shown in Figure 3.3, to the boiling point of

toluene (110.6 ^{o}C). The condensation reaction was operated by soxhlet extraction with toluene for 3 hours to obtain the hydrophobisation. Different kinds of terminal functional groups of the silane (methyl, linear alkyl, branched alkyl, fluorinated alkyl, and aryl) were employed in this work to modify the boundary layers of solids toward reacting with water under different levels of hydrophobicity. The experiments were repeated using PR activated carbon. The organosiloxane compounds used in the preparation processes and the names of the obtained samples are summarised in Table 3.1.

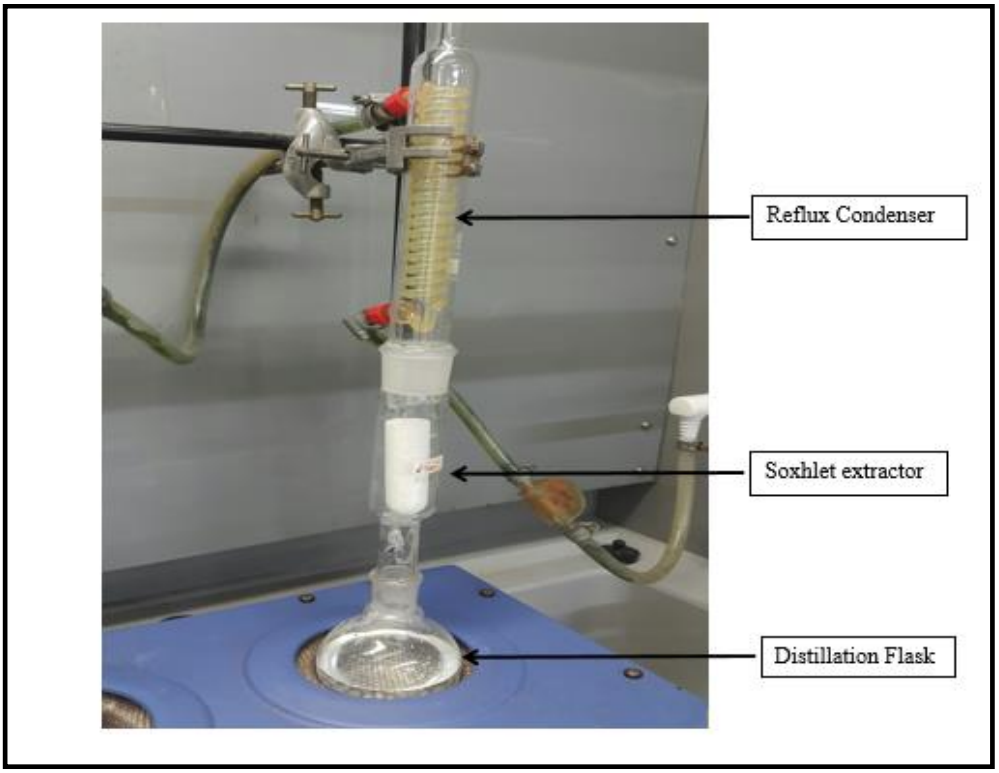


Figure 3. 3: Hydrophobisation System.

Table 3. 1: The organosiloxane compounds used in the synthesis of coated adsorbents.

Starting material	Organosiloxane	Abbreviation
CSK	VTMOS	CSKV
CSK	OTES	CSKO
CSK	POTS	CSKF
CSK	HDTMS	CSKH
CSK	PTES	CSKP
PRK	VTMOS	PRKV
PRK	OTES	PRKO
PRK	POTS	PRKF
PRK	HDTMS	PRKH
PRK	PTES	PRKP

4- Calcination: The coated activated carbons were submitted to further modification by thermal treatment under N_2 (1 bar, 100 mL/min) in the following procedure. Heat treatment was conducted by TGA at different temperatures (300, 350, 400, 450, 500, 550 and 600 ^oC) for 1 hour.

3.3 Characterisation Techniques

3.3.1 Thermogravimetric Analyser (TGA)

Thermogravimetric Analysis (TGA) Q-500 is an integrated thermal weight-change analyser instrument. It is equipped with standard mass flow controllers to measure the amount and rate of change in the weight of a material as a function of temperature or time. TGA Q-500 operates in the temperature range from ambient to

1000 ^{o}C and has an isothermal temperature accuracy of ±1 ^{o}C, isothermal temperature precision of ±0.1 ^{o}C, weighing capacity of 100 mg, a sensitivity of 0.1 μg and a precision of ± 0.01 %.

3.3.1.1 TGA Experimental Procedures

The analysis was conducted on the ACs to determine the amount of CO_2 adsorption by using a thermogravimetric analyser (TGA, Q-500, TA Instruments). As shown in Figure 3.4, the sample was placed in a platinum pan and heated to 150 ^{o}C for 30 min at a rate of 20 ^{o}C/min under the flow of (1 bar, 100 mL/min) N_2 atmosphere to remove any H_2O and/or pre-adsorbed CO_2. After drying, the sample was cooled down to 25 ^{o}C at a rate of 30 ^{o}C/min under the same flow of N_2. A flow of 100 ml/min of simulated flue gas (15:85 v/v of CO_2:N_2) was passed into the sample chamber at the adsorption temperature for 1 hour. The weight change of the sample was recorded to calculate the CO_2 uptake. Under the same temperature and pressure, N_2 was passed through the gas washer at different times to introduce a certain amount of H_2O into the TGA at an identical flow rate.

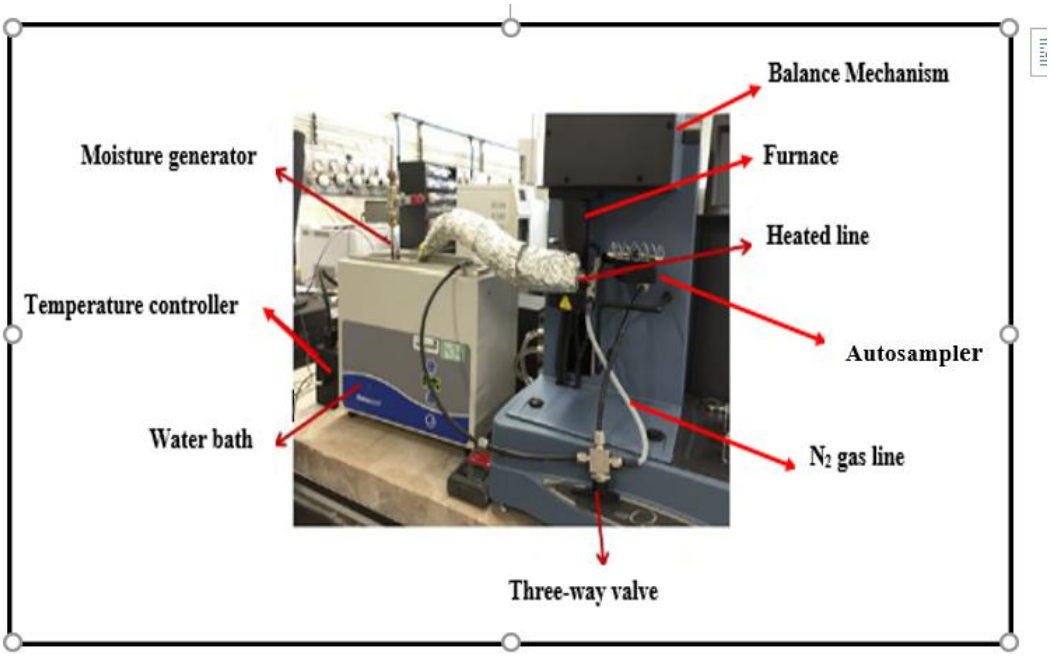


Figure 3. 4: TGA Q-500 from TA Instruments.

3.3.2 N_2 Sorption

The textural properties of the ACs such as specific surface area, pore volume and pore size distribution were characterised by N_2 sorption isotherms. In this section, porosity data was obtained by both the experimental technique and models such as BET and Non-Local Density Functional Theory (NLDFT) employed for data analysis.

3.3.2.1 Experimental Procedure

The textural properties of the unmodified and modified activated carbons were characterised with a Micromeritics Accelerated Surface Area and Porosimetry (ASAP) system 2420 instrument. The basics of the analytical technique are simple; the sample is first degassed to remove surface contamination and adsorbed species using vacuum, heat, and/or nitrogen.

In this work, and prior to the measurements, approximately 0.2 g was weighed into a sample tube and the degassing process was carried out under vacuum (less than 0.013 bar) at 120 °C for 15 hours to remove adsorbed H_2O and gases. The number of gas molecules adsorbed on the surface increases with each incremental increase in pressure. The pressure at which adsorption equilibrium occurs is measured and the universal gas law is applied to determine the quantity of gas (cm^3/g) adsorbed. In the low-pressure region ($P/P^o < 0.1$), the micropores in the surface are quickly filled, then, after multilayer adsorption, the free surface becomes completely covered, and finally larger pores (meso and macropores) are filled. The process may continue to the point of bulk condensation of the analysis gas ($P/P^o > 0.9$). The desorption process may begin in which pressure is systematically reduced, resulting in the liberation of the adsorbed molecules. As with the adsorption process, the changing quantity of gas on the solid surface is quantified. These two sets of data describe the adsorption and desorption isotherms. Analysis of the isotherms yields information about the surface characteristics of the material.

3.3.2.2 Theory for Calculations

The physical properties of activated carbons can be obtained using different models developed by a number of researchers. In instance, the surface area was calculated by the BET method using the N_2 adsorption isotherm data within the relative pressure ranging from 0.01 to 0.10 giving positive BET 'C' parameters. The cumulative pore volumes (V_{Total}), micro pore volume (V_{Micro}) and the pore size distribution (PSD) were obtained using a NLDFT carbon slit pore model. This was applied to the N_2 adsorption isotherms at -196 °C joined to a CO_2 isotherm at 0 °C.

A more detailed description of this method can be found in the (Thommes et al., 2015).

1. BET theory

It is very difficult to use mathematical methods which are based on the practical size information to calculate the true surface area of adsorbents, including surface irregularities and pore interiors. Therefore, Brunauer–Emmett–Teller (BET) used non-reactive gases such as N_2, (argon) Ar, and CO_2 to determine the surface area of adsorbents. According to Langmuir theory, which assumes the molecules of gas can form a monolayer on the surface of the solid material (Langmuir, 1918), BET's theory broadened this concept to include multilayers. The basic assumption for applying this theory is the adsorption begins on the strong surface energy sites, and then, with increased pressure, develops on the following energy level sites even if it is not completed on the first layer. The assumptions can be summarised as:

1- The surface is homogeneous.
2- There are no lateral interactions between neighbouring molecules but one-to-one adsorbate-adsorbent interaction.
3- The rate of adsorption onto an already adsorbed layer equals the rate of desorption.
4- The forces of physical adsorption are much higher for the first layer and constant for the subsequent layers, and the energies of adsorption of all molecules in the first layer are identical.

The resulting BET equation is expressed by (1):

$$\frac{P}{V_a(P-p^o)} = \frac{1}{V_m C} + \frac{C-1}{V_m C}\left(\frac{P}{p^o}\right) \quad (3.1)$$

P and P^0 are the equilibrium and the saturation pressure of the gas, Vα is the adsorbed gas quantity at a relative pressure of P/P^0. V_m is the quantity of the adsorbate constituting a monolayer of surface coverage. C is the BET constant, which is expressed by equation (3.2):

$$C = \exp\left(\frac{E_1 - E_L}{RT}\right) \quad (3.2)$$

E1 is the heat of adsorption for the first layer, and E_L is that for the second and higher layers and is equal to the heat of liquefaction, *R* is the ideal gas constant, and *T* is the absolute temperature. A plot of $[P/ Va (P^0-P)]$ versus P/P^0 should give a straight line with intercept **i** (1/ (*VmC*) and slope **s** $(C-1)/ (V_mC)$.

The software of MicroActive Version 5.0 by Micromeritics Instrument Corporation, USA was used to interactively evaluate isotherm data and reduces the time required to obtain surface area and porosity results, details of which can be found in the literature (Webb and Orr, 1997).

The surface area is given by:

$$S = \frac{V_m N A_{CS}}{Mw} \quad (3.3)$$

Where V_m is in units of volume which are also the units of the monolayer volume of the adsorbate gas, N is Avogadro's number which is 6.02×10^{23} molecules/mole, A_{CS} is the adsorption cross section of the adsorbing species (N_2, Ar or CO_2), M_w is the molecular weight of the adsorbate molecule, and w is the sample weight. *Vm* can be obtained from the inverse of the sum of intercept and slope.

2. Total Pore Volume Theory

The general concept of the total volume includes all cracks, fissures, holes, and channels within the body of particles or of larger objects (Webb and Orr, 2008). For meso or micropores, the total pore volume can be determined from N_2 adsorption measurements by assuming that, in the range $0.95 < p/p_0 < 1$, all pores in the adsorbent are filled with condensed gas. By converting the amount adsorbed to a volume of liquid adsorbate at Standard Temperature and Pressure (STP), the total pore volume is then simply calculated as:

$$V_{Liq} = \frac{P_a V_{ads} V_m}{RT} \quad (3.4)$$

V_{Liq}, which stands for the volume of liquid N_2, is the targeting total pore volume. P_α is the ambient pressure, V_{ads} is the volume of adsorbed N_2 gas, V_m is the molar volume of the liquid N_2 (34.7 cm^3/mol), R is the ideal gas constant and T is the ambient temperature.

3. Non-Local-Density Functional Theory (NLDFT)

In general, the adsorption isotherms in model pores are determined by the intermolecular potentials of the fluid-fluid and solid-fluid interactions. Non-local-density functional theory (NLDFT) based methods for pore size/volume analysis of nanoporous materials is usually used to interpret the data for the adsorption of N_2 on the adsorbents at -196 ^oC. They are included in commercial software and are also featured in international standards (such as ISO 15901-3). The relation between isotherms determined by these microscopic approaches and the experimental

isotherm on a porous solid can be interpreted in terms of a Generalized Adsorption Isotherm (GAI) equation:

$$N\left(\frac{P}{p^o}\right) = \int_{W_{MIN}}^{W_{MAX}} N\left(\frac{P}{p^o}, W\right) f(W) dW \quad (3.5)$$

$N\left(\frac{P}{p^o}\right)$: $expermental\ adsorption\ isotherm\ data$

W: $microspore\ volume$

$N\left(\frac{P}{p^o}, W\right)$: $isotherm\ on\ a\ single\ pore\ of\ width\ W$

$f(W)$: pore size distribution function

3.3.3 H_2O Sorption Isotherm

Dynamic Vapour Sorption (DVS) was used to acquire H_2O adsorption isotherms for the samples. About 0.2 g of sample was placed in the sample pan, while the reference pan was left empty. In order to remove H_2O and other adsorbed gases, the sample and empty reference pans were heated to 150 °C at a 10 °C/min heating rate and held isothermally for 30 minutes in in pure N_2 gas (1 bar, 100 ml/min). Next, the temperature was lowered to 25 °C and held for 10 minutes. Finally, the H_2O was dosed in the N_2 carrier gas to reach 10 %, 50 % or 95 %RH. The time taken to reach equilibrium was about 220 minutes. To obtain the adsorption isotherms, the H_2O content of the sample was measured at equilibrium over a RH range from 0 to 95 %RH.

3.3.4 Heat of Adsorption and Desorption Measurements

The heat of adsorption and desorption of the CSs were determined using TGA-DSC instrument (Setaram Instrumentation) under a N_2 flow rate of 60 ml/min at 1 bar. This instrument can simultaneously provide mass changes and heat flows. Only 16 mg of the samples were used to measure the heat of adsorption and desorption in TGA-DSC. The flow rate of N_2 in DSC was 60 ml/ min at a heating rate of 1 ^{o}C/min from 20 to 150 ^{o}C.

3.3.5 Calculation Heat of Adsorption

The isosteric heat of adsorption (Q_{st}) refers to the energy difference between the state of the system before and after the adsorption process, and represents "the average of all adsorption sites that can be potentially occupied at a certain coverage level" (McDonald et al., 2011, Mathias et al., 1996). For a gas-phase adsorption process, Q_{st} can be estimated through two steps:

(1) Fit the experimentally obtained isotherms taken at different temperatures to isotherm equations in order to obtain the pressure value (P) required to reach the same adsorption capacity (q) at different temperatures.

(2) Calculate Q_{st} using the pressure values determined in step (1) along with adsorption capacities in the Clausius-Clapeyron equation (3.6)

$$Q_{st} = -RT \left[\frac{\partial \ln p}{\partial T}\right]_q \qquad (3.6)$$

Where R represents specific gas constant, q stands for the adsorption capacity and T and P are the temperature and pressure, respectively.

Firstly, in order to calculate the isosteric heats of adsorption for parent AC's as a function of adsorbed CO_2, the isotherm data at two temperatures were fitted using a dual-site Langmuir (DSL) equation to obtain the pressure (P) (Mason et al., 2011, Herm et al., 2012). The DSL equation is more applicable than the one-site Langmuir equation due to the surface heterogeneity of the carbon surface.

A TGA-DSC was used to study the thermodynamics of adsorption of gases onto adsorbents, and to confirm the Q_{st} values obtained using the dual-site Langmuir model. Using equation 3.7 and the experimental values of Q_{st}, the integral quantities were calculated over defined ranges of sorption-phase concentration from 0 to *n*, where *n* is equal to the equilibrium CO_2 adsorption capacity obtained by TGA-DSC in a calorimetric analysis (Bülow et al., 2002) :

$$Q_{int} = \int_0^n Q_{st} dn \qquad (3.7)$$

3.3.6 Fourier Transform Infrared (FTIR) Spectroscopy

Fourier transforms infrared spectroscopy (FTIR) was conducted using a Perkin Elmer Spectrum 100 and collecting eight scans from 380 – 4000 cm^{-1} with a resolution of 2 cm^{-1} (Swann and Patwardhan, 2011). A sample of 0.0015 g was ground with 0.25 g of KBr using a mortar. The very fine powder was placed in a circular die under a mechanical pressure of 10 kPa/mm^2. The pressure was maintained for up to 10 seconds. The sample was then placed in a drying oven at

100 ^{o}C for 48 hours under vacuum to prevent any interface between the mix and any existing H_2O vapour or CO_2 molecules. The oven was cooled down to room temperature under vacuum overnight. Finally, the sample was transferred to the FTIR analyser to detect the functional groups present in the sample.

3.3.7 Elemental Analysis (EA)

The chemical contents of samples were obtained by using Elemental Analysis (EA) through a LECO CHN 628 Series to detect elements N, C and H and S. 100mg of each sample were put in the alumina crucible for elemental analysis. Three tests for each sample were conducted and the reported results were the average value of the three tests.

3.3.8 Proximate Analysis by TGA

The prepared samples were subjected to proximate analyses to determine the chemical composition of carbon. Proximate analysis was also performed in the thermogravimetric analyser (TGA, Q-500, TA Instruments). The analysis consists of the following steps:

1- At ambient temperature and air flow (100 ml/min), approximately 30 mg of the sample was weighed directly into platinum.

2- The sample was heated from ambient temperature up to 110 ^{o}C at a rate of 5 ^{o}C/min and maintained at this temperature for 60 minutes. The weight loss at this stage is mainly due to H_2O.

3- The sample was further heated up to 815 ^{o}C at 15 ^{o}C/min and maintained at this temperature for a further 30 minutes. Weight loss is equal to carbon content. The residual weight may correspond to the ash content of the sample.

3.3.9 SEM-EDX Analysis

The morphology of the materials was investigated by FEI Quanta 600 Scanning Electron Microscope (SEM) while the composition of the materials was determined by Energy Dispersive X-ray spectroscopy (EDX) that is installed on the SEM. SEM/EDX analysis is the best known and most widely-used of the surface analytical techniques because it is rapid, inexpensive, and basically non-destructive approach to surface analysis. Techniques to be implemented can vary depending on how the specimen is exposed to a fine beam of electrons in synchronism with the spot of a cathode ray tube. Depending on the electrons energy and the nature of the material, the elastic and inelastic scattering of electrons occurs, as well as variations in electromagnetic radiation. Although many signals can be recognised by SEM, two of them are commonly used for imaging samples: Back-scattered electrons and secondary electron signal**,** while X-ray can be identified by EDX to detect elemental analysis for the specimen (Kutchko and Kim, 2006). In fact, the interaction between the electron beam with atoms at various depths leads to the production of a secondary electron signal while the back-scattered electrons represent the number of electrons passing out of the specimen (Goldstein et al., 2017). The characteristic X-ray and continuum X-rays signals are emitted when higher energy electrons fill the electron hole in the specimen. The electron hole creates normally after removing an electron from the inner shell as a result of hitting it with a primary electron beam.

Generally, X-ray energies are characteristic of the atomic structure of the elements (Reed, 2005).

The specimens were first mounted on the SEM sample holder. The SEM analysis was done under vacuum to remove the air from the inside of the microscope. A small amount of sample (20 mg) was bound on carbon sticky tabs. Secondly, a fine beam of electrons was focused on a selected area of the sample by the electron gun and two lens sets: the condenser lens and the objective lens. The working distance (WD = distance between the bottom of the objective lens and the specimen) was 10 mm and the microscope images were captured at one magnification of 50x. Finally, the image on the SEM viewing screen was formed by the objective lens while the data was generated by an EDX analysis showing multiple peaks. In fact, each element in the specimen has characteristic peak positions corresponding to the possible transitions in its electron shell.

3.3.10 X-ray Photoelectron Spectroscopy

Surface chemistry analysis of activated carbon was conducted on a Kratos AXIS ULTRA DLD X-ray Photoelectron Spectroscopy instrument (XPS). XPS is a quantitative spectroscopic technique that can be used to understand the surface chemistry of solid materials within the first 10 nm (Van der Heide, 2014). Typically, under an ultrahigh vacuum conditions, the sample is exposed to a low energy X-ray beam (approximately 1keV), the resultant photoelectrons are analysed with high precision of kinetic energy, then the results are displayed as a spectrum (Fadley and Shirley, 1970). The binding energy of an electron can be calculated by Hollander and Jolly (1970) (equation 3.9):

$$Ehv = Ek + E\phi + EB(i) \quad (3.9)$$

Where Ehv is the X-ray energy, *Ek* represents the photoelectron kinetic energy, $E\phi$ is the small correction for solid effects (work function, etc.), and *EB(i)* is the electron binding energy of the (i) level. Each element has a characteristic binding energy and is represented as a set of peaks which relate directly with a core atomic orbital. An atomic orbital is a mathematical function that describes the wave-like behaviour of either one electron or a pair of electrons in an atom which is a wave function for an electron in an atomic orbital (Fadley and Shirley, 1970) which allows the identification of the specific elements in any sample. The shift in the binding energies of core electrons between the neighbouring atoms, which can be detected by XPS, is used to determine the chemical state of elements.

3.3.11 Control of Humidity by Saturated Salt Solutions

Because it is important to investigate the CO_2 adsorption at different levels of relative humidity, and it is very difficult to control the humid environment in TGA, a vacuum desiccator containing a saturated salt solution and humidity sensor was used at a controlled temperature of 20 ^{o}C to get an accurate control of humidity in the laboratory, by following these steps (Greenspan, 1977):

1-Washing the desiccator and greasing the ground-glass rim of the desiccator lid with a thin layer of vacuum grease before each run.

2-The salt solution was prepared by dissolving the amount of salt with 10 ml of deionized water and stirring the mixture until precipitation occurs. The mixture was poured on the base of the desiccator, the sample and humidity sensor (use to measure

the relative humidity in percent) was placed on the aluminium plate above the mixture.

3-The sleeve valve was closed and the vacuum pump was operated for 3 hours to discharge air from desiccator and then sealed by closing the outlet valve. Samples were allowed to equilibrate for 48 hours Figure (3.5).

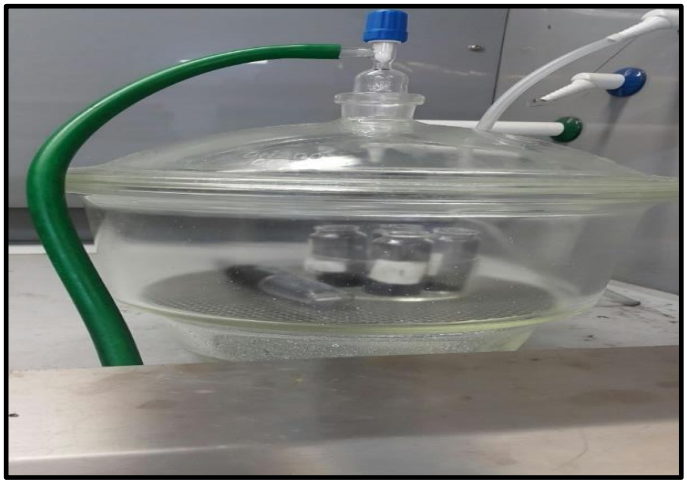


Figure 3. 5: Desiccator System.

In the desiccator, three different types of salts were used separately to obtain required %RH (Table 3.2), measured by humidity sensor (Figure 3.6). Salt concentrations were between 16 % and 50 % higher than the degree of saturation to achieve precipitation.

Table 3. 2: Equilibrium RH of Selected Sutured Salt Solation at 20 ^{o}C.

Salt	%RH	Salt concentration
Potassium hydroxide	10	14.1 g/10 H_2Oml
Magnesium nitrate hexahydrate	50	18.7 g/10 H_2Oml
Potassium nitrate	95	8.2 g/10 H_2Oml

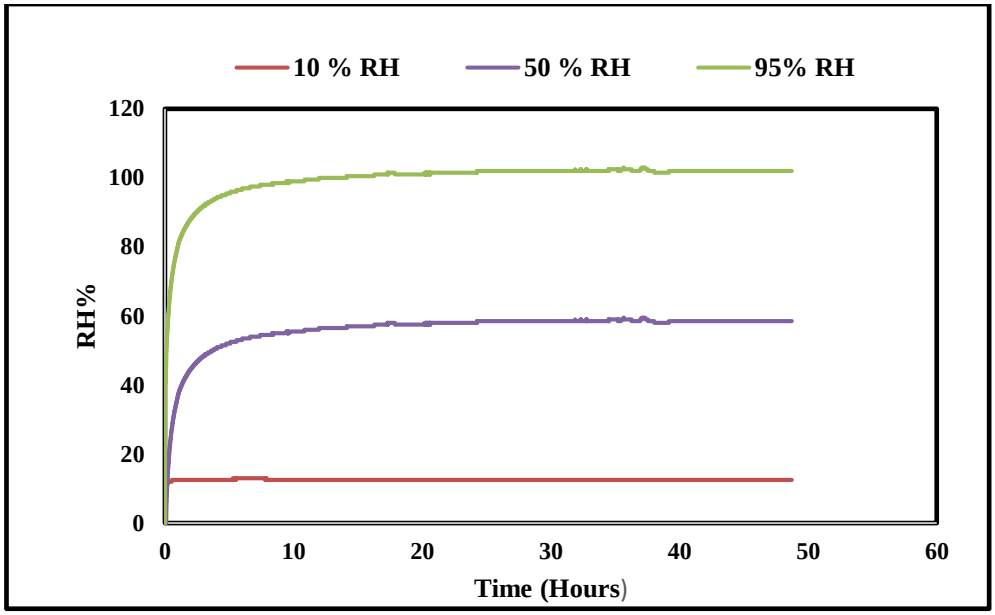


Figure 3. 6: Plot of 10 %, 50 % and 95 %RH against time measured inside the desiccator using data logger during experiment form humidity sensor at 20 ^{o}C.

3.3.12 X-Ray Fluorescence Spectrometry (XRF Analysis)

XRF is an analytical technique used to obtain elemental and chemical information of the material. The penetrating of the material with X-Rays or gamma rays results in the release of characteristic "secondary" (or fluorescent) X-rays that can provide good information about the composition of the material. In this work, the XRF test was conducted on a Bruker S8 Tiger Spectrometer using 200 mg of each sample to measure K^{+} and Si. The test was repeated in duplicate for each sample to make sure the results are reproducible.

3.3.13 Mechanical Strength Testing

The dynamic mechanical analyser (Model 5966, Instron) is used to accurately measure the mechanical strengths of solid materials. The change in the shape due to the application of force with temperature can be observed. In this work, each sample

was tested ten times to ensure the accuracy of the results and the results are reproducible.

3.3.14 Bulk Density

In this study, 0.5 g of the activated carbon was dried in a vacuum oven at 120 °C for 48 h to remove the H_2O. The sample was placed in a 0.67 cm^3 plastic sample cup (V_c) and weighted (W_d). Bulk density of activated carbon was calculated by dividing the dry weight of the sample (W_d) on the volume of a plastic cup (V_c) as shown in equation (3.10).

$$Bulk\ Density = \frac{W_d}{V_c} \tag{3.10}$$

3.4 Fundamentals of Adsorption

3.4.1 Introduction

Adsorption is the interaction between the gas or liquid particles (atoms, ions, molecules) with the solid surface molecules. John Lennard-Jones suggested that the potential energy of interaction between two non-bonding atoms or molecules is based on the distance between them. The minimum potential energy can be determined when the distance between them does not exceed one molecular radius of a gas molecule (Lim, 2009). Figure 3.7 shows the potential energy curve for the gas as a function of the position of solid surface which is known as Lennard-Jones potential.

Basically, the potential energy between the gas molecule and the adsorbent is composed of two types of forces: the repelling electrostatic forces ($-B/r^6$) and the attracting forces (A/r^{12}). When the potential energy is in an equilibrium state

(r_g) under these forces, a minimum value is displayed. Adsorption energy depends on the nature of the adsorbate (gas) and adsorbent (solid). If one or both has a polar nature, the polarisation and electrostatic forces between permanent electric dipole moment (EDM) and the electric field of the solid may contribute to calculating the total adsorption energy.

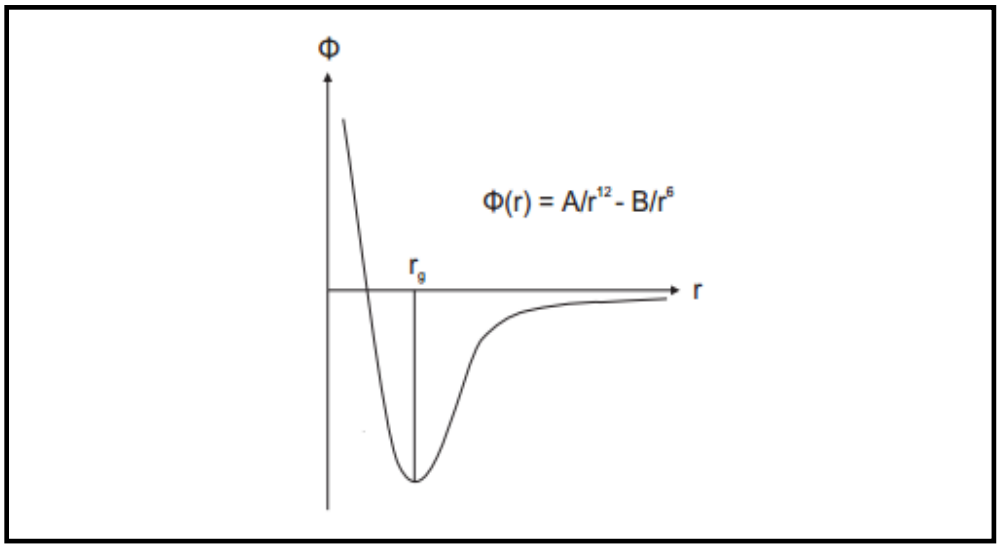


Figure 3. 7: Lennard-Jones Potential Φ as a function of the distance of the molecule r to the solid surface as both graphical and mathematical description. A and B are constants (Schwarz and Contescu, 1999).

The overall interaction potential energy (Φ_T) for a polar adsorbate molecule on a the heteropolar surface can be divided into five types of electrostatic interactions (Chapman, 1995) as shown in equation (3.11):

$$\Phi_T = \Phi_D + \Phi_P + \Phi_F + \Phi_{FQ} + \Phi_R \qquad (3.11)$$

Where Φ_D = the energy due to dispersion forces; Φ_P = the energy due to polar nature of adsorbent and/or adsorptive; Φ_F and Φ_{FQ} = the energy due to the permanent dipole and quadrupole moments of the adsorptive molecules respectively; and Φ_R = the energy due to repulsion forces. The terms Φ_D and Φ_R are the non-specific

contributions, which are always present in physisorption, whereas the other terms provide the specific contribution, which may be important to the overall adsorption energy according to the polar nature of the molecules and the adsorbents.

In the case of adsorption of H_2O on ACs, all terms must be considered. For narrow micropores (less than 0.7 nm), non-specific contributions are weak in the case of H_2O and the micropore wall, as a consequence of the low polarias ability of both H_2O and the adsorbent. Thus, the higher dispersion forces between the adsorbent micropore walls represent most of the adsorption potential forces. The effects of other terms are negligent.

For medium sized micropores (0.7-1.2 nm), the dispersion force term decreases strongly due to increasing micropores size, so the effect of $\Phi_P + \Phi_F + \Phi_{FQ}$ terms (a function of surface groups) is more appreciable. For micropores with a diameter larger than 1.2-2.0 nm, the influence of surface groups is scarce, even though their concentrations are high (Alcañiz-Monge et al., 2002). Therefore, changing the surface chemistry by increasing the -OH groups plays a significant role in increasing H_2O uptake on the carbon surface.

3.4.2 Theory of Adsorption

The description of this phenomenon poses great challenges for researchers, and the adsorption mechanisms of adsorbates on the adsorbent surfaces are still under discussion. There are two types of adsorption processes which can be recognized based on the type of forces that may arise between the adsorbate and the adsorbent; physical and chemical adsorption.

Physical adsorption (physisorption) occurs when the inter-molecular attractive forces between molecules of the solid (adsorbent) and the gas are greater than those between molecules of the gas itself (the adsorbate). Under high pressure and low temperature, two main types of intermolecular forces exist between molecules of the adsorbents surface and the gas: Van-der-Waals forces, which are always present due to the non-polar nature of physisorbents, and electrostatic interactions, comprising of pole-ion and pole-pole interactions between gases and the ionic or/and polar sites of the solid adsorbent surface (Samanta et al., 2011) .

Physical adsorption can form one or multimolecular layers of adsorbates by exothermic reactions that take place rapidly under high pressure and low temperatures, therefore less energy is required for the regeneration process. The main drawback of this type of adsorption is the low selectivity of physisorbents such as zeolites and activated carbons because their surfaces are not site-specific to any particular component in the fluid (Meghani, 2015).

Chemical adsorption, or chemisorption, involves reactions between the adsorbate and the chemical adsorbent (chemisorbent). In general, at high temperatures greater than 200 ^{o}C, the molecules of adsorbate create stronger chemical bonds with the surface of adsorbent by transferring electrons between atoms or by sharing of electrons pairs between atoms. Chemisorption systems have high selectivity and low capacity, as well as their adsorption energy, being greater than those for physical adsorption.

3.4.3 Types of Isotherms

The shape of an adsorption isotherm depends on the interplay between the strength of the fluid–fluid and fluid–wall interactions as well as confined geometry effects, coupled with the state of pore and bulk fluid. Six types of isotherm shapes are classified according to the IUPAC classification (Thommes et al., 2015) as shown schematically in Figure 3.8.

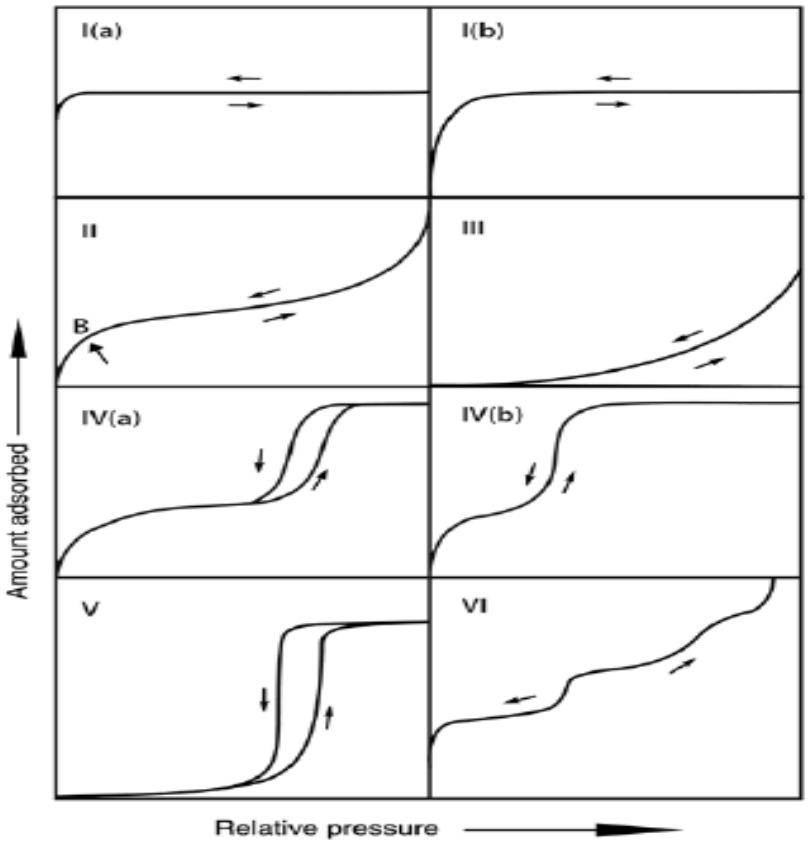


Figure 3. 8: Isotherm shapes classification (Thommes et al., 2015).

1) Type I: This kind of adsorption is typical of the microporous materials, most adsorption occurs at a relative pressure below 0.1 to fill monolayer pores only (Keller and Staudt, 2005). The adsorption of CO_2 on activated carbon is generally

of this type (Meghani, 2015). At -196 ^{o}C, N_2 is physically adsorbed on the surface of micropores having mainly narrow micropores (<~ 1 nm) showing Type I(a) isotherms; while Type I(b) isotherms are found with materials having wider micropores and possibly narrow mesopores (< ~ 2.5 nm).

2) Type II: This isotherm describes formed monolayer and multilayers of adsorbates over the mesoporous and macroporous solids. Water vapour and other polar components on silica gel give type II (Ogbuka, 2013).

3) Type III: This isotherm describes formed monolayer and multilayers of adsorbates over the non-porous and macroporous solids. No identifiable monolayer formation can be determined because of the relatively weak interactions between adsorbent-adsorbate molecules. Adsorption of water vapour on hydrophobic macroporous adsorbents exhibits this type of isotherm (Keller and Staudt, 2005).

4) Type IV: IV isotherms follow the same shape as the Type II isotherm on mesoporous materials, such as silica like MCM-41 and SBA-15 (Thommes et al., 2015). Adsorbent adsorbate interactions as well as interactions between the molecules in the condensed state determine the adsorption behaviour. Depending on the mesopores size, two types of isotherms IV(a) and IV(b) can be recognised. For IV(a) isotherm, when the pore width exceeds a certain critical width (wider than ~ 4 nm in cylindrical pores), capillary condensation of N_2 gas at – 196 ^{o}C is accompanied by hysteresis (Landers et al., 2013). For narrow mesopores (conical and cylindrical pores less than ~4 nm), the isotherm is completely reversible (i.e., Type IV(b)).

5) Type V: Describes the formation of multilayers on the micropous or mesoporous walls with increasing partial pressure. In the low P/P^o range, the type V isotherm shape is very similar to that of type III due to the nature of interactions between adsorbent–adsorbate molecules. At higher P/P^o, clustering of adsorbate molecules is followed by pore filling. Water vapour adsorption on these adsorbents may exhibit type V.

6) Type VI: Indicates adsorption on homogenous, non-porous surfaces such as adsorption of krypton on carbon black (graphitised at 2727 ^oC).

3.4.4 CO_2 Isotherm Models

The adsorption isotherm is a fundamental source of information on the adsorption process. The analytical forms of adsorption isotherm equations depend on the type of the surface phase that can be considered as a monolayer or multilayer. These models are complex due to structural and energetic heterogeneity of the adsorbent surfaces, which is characteristic of a great number of adsorbents used at industrial or experimental scale (Saadi et al., 2015).

3.4.4.1 Langmuir Model

The semi-empirical isotherm derived by Langmuir in 1918 still provides a useful insight into the relationship between the number of surface active sites and the adsorbate under isothermal conditions. Langmuir showed that the dynamic equilibrium occurs based on the following assumptions:

1- Adsorbent surface consists of a fixed number of similar active sites, each of them can react with one molecular of adsorbate through the same mechanism without any subsidiary interactions

2- Only a monolayer is formed (if the adsorption is at maximum).

3- The probability of a molecule is adsorbed is independent of neighbouring sites being occupied or otherwise.

4-The enthalpy of adsorption is constant.

As the adsorption process continues at a constant temperature, a dynamic equilibrium is established between the molecules in the gas phase (adsorbate) and the molecules (or atoms) in the solid surface (adsorbent). The Langmuir equation (3.12) that describes the single-component isotherm equilibrium is:

$$qi = \frac{q_{max,i} \times b_i \times P_i}{1 + b_i \times P_i} \qquad (3.12)$$

Depending on the Arrhenius equation (3.13), with decreasing temperature, T, the Langmuir equilibrium constant (bi) is increased and the adsorption capacity is increased accordingly.

$$b_i = b_{io} \exp\left(\frac{E}{RT}\right) \qquad (3.13)$$

Where:

q_i: equilibrium adsorption capacity of adsorbate i (mol/kg)

$q_{max,i}$: saturation loading of adsorbate i (mol/kg)

b_i: Langmuir equilibrium constant of i (Pa^{-1})

P_i: partial pressure of adsorbate i in fluid (Pa)

b_{io}: pre-exponential factor (Pa^{-1})

E_i: heat of adsorption of i (J/mol)

R: ideal gas constant (J/ mol. K)

T: temperature (K)

At very low partial pressures of adsorbate, the limit ($1+ b_i \times p_i$) can almost be ignored. So the Langmuir equation (3.14) reduces to :

$$q_i = q_{max,i} \times b_i \times p_i \qquad (3.14)$$

While at very high pressure, the factors ($b_i \times p_i$) ≈ ($1+ b_i \times p_i$), so the equilibrium capacity of the adsorbent reaches the maximum adsorption loading as sown in equation (3.15):

$$q_i = q_{max,i} \qquad (3.15)$$

3.4.4.2 Dual-site Langmuir (DSL) Equation

Many investigations have been carried out to derive mathematical equations that can give an accurate conception of the effect of surface chemical heterogeneity on adsorption capacity. In general, adsorption theories on heterogeneous surfaces are based on the concept of independent sites, therefore, the total adsorbed amount of any component is calculated by summing up the amount adsorbed of this component over all the different parts. For example, Halsey equation and Harkins-Jura isotherm equation are good representation of adsorption data regarding isotherms similar to type II which appear in heteroporous solids. In the Brunauer-Emmett-Teller (BET) model, the second, third, and higher layers have the same energy of adsorption, and

are not influenced directly by adsorbent- adsorbate interactions. However, the energy for the first layer is different from that for the second or other layers. Frenkel-Halsey-Hill (FHH) adsorption isotherm describes multilayer adsorption, assuming variation of adsorption potential based on distance from the adsorbed molecule layer from the surface of the adsorbent (Saadi et al., 2015). Recent studies have indicated that DSL equation is the best fit model for the adsorption isotherms of carbons with high surface heterogeneity (Ben et al., 2012, Lu et al., 2013, Li et al., 2010, Rudziński, 2013).

The DSL equation (3.16) can be expressed as follows (Rudziński, 2013) :

$$q = \frac{q_{s,A} \times b_A \times P}{1 + b_A \times P} + \frac{q_{s,B} \times b_A \times P}{1 + b_A \times P} \qquad (3.16)$$

q_i: equilibrium adsorption capacity of adsorbate i (mol/kg).

$q_{s,A}$ and $q_{s,B}$: the monolayer capacity of adsorbate i on site A and B (mol/kg).

$b_{i,A}$ and $b_{i,B}$: Langmuir equilibrium constant of i for site A and B (Pa^{-1}) which can be found by Equation (3.11).

Pi: partial pressure of adsorbate i in fluid (Pa).

From the equation of this model, it can be seen there are different saturation loadings for each site. The DSL equation is more applicable than the one-site Langmuir equation due to the surface heterogeneity of the carbon surface.

3.5 Adsorption Isotherms of Water Vapour on Activated Carbon

Although many researchers have extensively studied the behaviour of the H_2O interaction on carbon (Dubinin, 1980, Dubinin and Serpinsky, 1981, Barton et al., 1991, Lee and Reucroft, 1999, McCallum et al., 1999, Salame and Bandosz, 1999, Do and Do, 2000, Rodríguez-Mirasol et al., 2005), there is still no clear picture of the precise mechanism of water vapour.

AC surface contains a variety of atoms incorporated in the aromatic rings (functional groups) such as hydroxyl groups (Lizzio et al., 1990). The monolayer of water molecules (diameter ≈ 0.275 nm) is adsorbed first on the functional groups which represent the primary active sites. These groups that are located usually at the edges and corners of the basal planes can form hydrogen bonds with water vapour at low relative pressure, creating a film of water on the activated carbon surface (Mowla et al., 2003).

Secondary adsorptive sites consist of previously adsorbed water molecules. The bridging between the water molecules bonded by hydrogen bonds creates water clusters, followed by the growth of these clusters around the chemisorption sites with increasing water vapour relative pressure. The critical size of the clusters enables them to have sufficient dispersive energy to fill the carbon pores (Gregg and Sing, 1982,Budarin et al., 2000, Do and Do, 2000). At equilibrium, the isotherms of water on the pores surface usually show a type close to the V or IV topology. This is due to the hydrophobic nature of activated carbon that establishes a direct relationship with water vapour relative pressure, and the density of active sites (Plantier et al., 2015). The adsorption behaviour of water is determined by the ratio

of the water-wall attractive interaction to the water-water attractive interaction. This ratio is also very small if it is compared with the strong hydrogen bonds between water molecules, due to the weak interactions between water-carbon. Therefore there are three types of water interactions that can be recognised during the adsorption process on the surface of activated carbon : the strong water–water interactions, the weak water–carbon interactions, and the interchange of hydrogen atoms between the molecules of water and the hydroxyl groups (Brennan et al., 2001). Despite the research efforts in this area, little progress has been made to build a sufficient understanding of the behaviour of water in porous carbon. This may due to the presence of a wide range of precursors that can be used to produce activated carbons.

Chapter 4: Characterisation of the Activated Carbons Investigated

4.1 Introduction

The pore structure characteristics of activated carbons derived from coconut shell and phenolic resin were estimated by determining the micropore surface area, the micropore volume and both their respective contributions to total surface area and total pore volume before and after modification. To become more acquainted with other properties, various other characterisations such as pore size distribution (PSD), SEM analysis, EDX, FTIR spectroscopy and XRF were carried out on the CSK and CSKV450 samples that exhibited the best performance toward adsorption of CO_2 and H_2O (as will be discussed in the Chapter 6). This enabled a closer inspection of changes in surface structure of activated carbons resulting from coating. The effect of relative humidity on the porosity of parent activated carbons was studied also, and the results were compared with those obtained after modification. CO_2 and H_2O adsorption will be considered in the following two chapters.

4.2 Effect of KOH Treatment on Characterisation of Activated Carbons

Sorption isotherms of N_2, at low temperatures of about -196 ^oC, were used to estimate the textural properties of the activated carbon samples before and after modification. The isotherms are presented in Figure 4.1. The sharp N_2 uptake in the low pressure region and the relative stabilisation in the medium and high pressure indicate to type I(a) isotherm for all samples, suggesting that all samples are mainly

microporous materials according to the IUPAC classification for physical sorption (Thommes et al., 2015). Small hysteresis loops were observed for some samples (CS and CSK650) and these point to a relatively minor development of mesoporous structures during the modification as well as possibility of the presence of ink bottle type pores. For the better understanding of the structural characteristics of the coconut shell activated carbon, the adsorption isotherm was plotted on a semi-logarithmic scale and presented in in Figure 4.2. Adsorption processes can be divided into several distinct stages at relative pressures of 10^{-6}–10^{-4}, 10^{-4}–10^{-2}, 10^{-1}, and 0.9–1.0 which can be attributed to multiple stage pore filling processes (Ryu et al., 2000), such as: (i) filling of narrow micropores; (ii) monolayer formation on the surfaces of wider micropores such as supermicropores; (iii) filling of these wider micropores; (iv) monolayer formation and filling of mesopores by capillary condensation, and (v) filling of macropores by capillary condensation, which takes place at relative pressures close to unity. As seen from these semi-logarithmic plots, all samples show no uptake of nitrogen under a relative pressure of 10^{-5}, indicating the presence of a few ultra micropores. There is significant uptake of nitrogen of the CSK700 in the relative pressure range of 10^{-5} –10^{-4} indicating that this sample has great part of its pores as super micropores. For other samples, significant uptake of nitrogen was noticed in the relative pressure range of 10^{-3}–10^{-1} for CS and 10^{-2}–10^{-1} for CSK650 and CSK750, indicating that these samples have wider micropores.

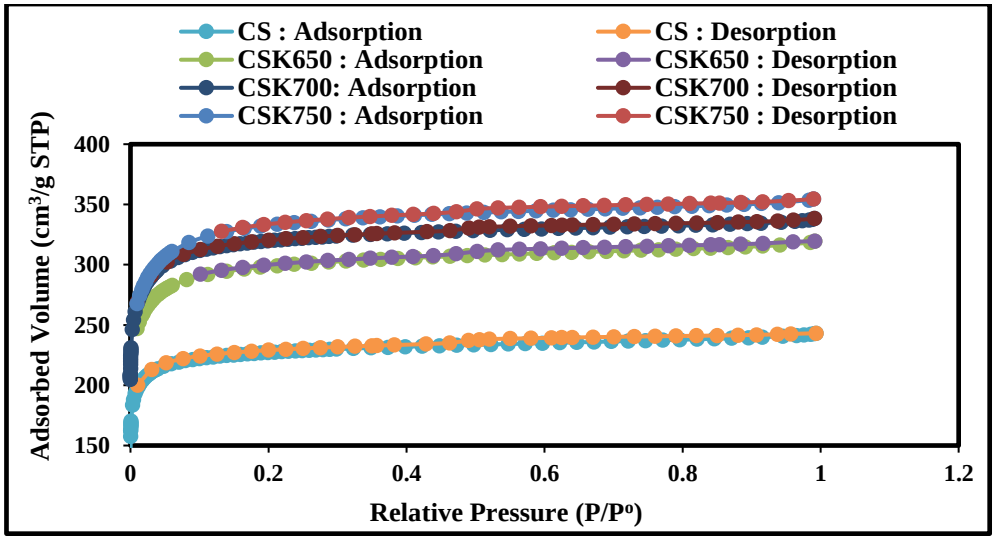


Figure 4. 1: N_2 sorption isotherms at -196 °C of the samples prepared at different temperatures (650, 700, and 750 °C).

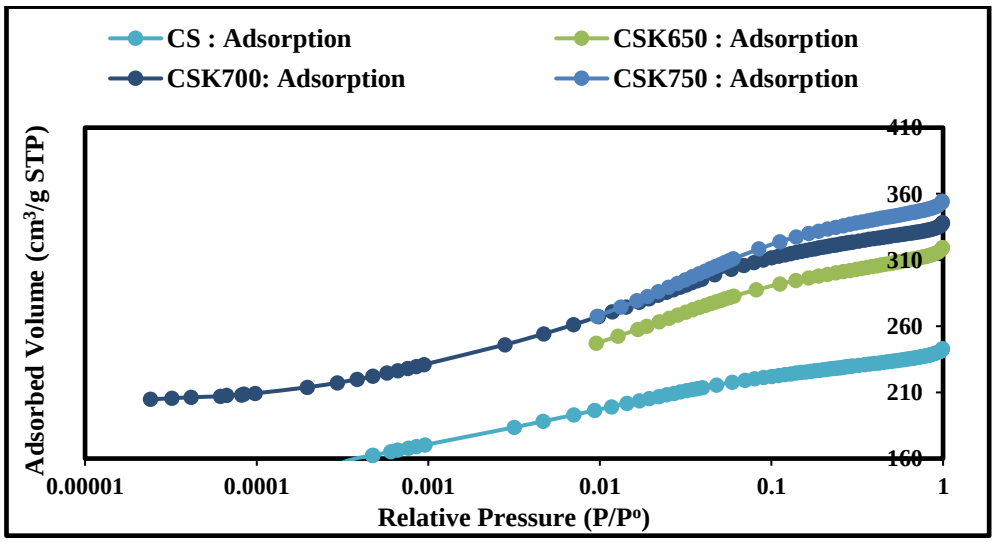


Figure 4. 2: Logarithmic N_2 sorption isotherms at -196 °C of the samples prepared at different temperatures (650, 700, and 750 °C).

The physical properties of all samples are summarised in Table 4.1 with analysis of the results reported in Appendix A. It can be seen that the parent activated carbon (CS) exhibited the lowest value of S_{BET}, of 912 m^2/g, which can be considered typical for natural CS activated carbons (Hung, 2012). The surface area and pore volume of the samples rose with increasing activation temperature. CSK750 showed a well-developed porous structure with a specific surface area of 1310 m^2/g, a total pore volume of 0.49 cm^3/g, and a micropore volume of 0.48 cm^3/g. These results agree with the findings obtained by Liu et al. (2017), who reported that the volume of ultra-micropores develops with increasing temperature up to 800 ^oC.

Table 4. 1: Physical properties of the activated carbon samples.

Samples	**S_{BET} (m^2/g)**	**V_{Micro} (cm^3/g)**	**V_{Meso} (cm^3/g)**	**V_{Total} (cm^3/g)**
CS	912	0.33	0.01	0.34
CSK650	1187	0.42	0.02	0.44
CSK700	1275	0.46	0.02	0.48
CSK750	1310	0.48	0.01	0.49

The concentrations of potassium ions on the surfaces were obtained from SEM-EDX analysis and are reported in Table 4.2. A drastic lowering of K^+ concentration was observed at CSK750 and was around 65 % of its value at CSK650. This indicates that most of the guest species (the potassium ions) had been successfully intercalated onto activated carbons at this range, causing the development of porosity (Liu et al., 2015a).

Table 4. 2: SEM-EDX analysis of the CSK650, CSK700 and CSK750.

Samples	Norm. (Wt. %)		
	C	**O**	**K**
CSK650	77.1	12.1	10.9
CSK700	85.5	10.3	4.3
CSK750	86.8	9.9	3.3

4.3 Effect of Physical and Organosiloxane Compound Treatment on the Characteristics of Activated Carbon

4.3.1 Physical Treatment

CSK and PRK samples were heated at 700 ^{o}C and 900 ^{o}C separately as explained in the Section 3.2.1.1. The samples were labelled as CSKN700, CSKN900, PRKN700 and PRKN900 respectively. The physical properties of unmodified and modified samples are shown in Table 4.3. The porosity of all samples decreased after increasing the temperature. Compared with other samples, the surface area and pore volume of the PRKN900 decreased to 37 % and 33 %, respectively. This can be attributed to the thermal shrinkage of structure and forming of closed cavities inside the carbon matrix which leads to the collapse of some pore walls at this temperature (Tazibet et al., 2013). From the N_2 sorption isotherms in Figure 4.3 and Figure 4.4, it can be seen that obtained carbons still have type I(a) isotherms, indicating that microporosity is still preserved.

Table 4. 3: Physical properties of CSK, CSKN700, CSKN900, PRK, PRKN700 and PRKN900.

Samples	S_{BET} (m^2/g)	V_{Micro} (cm^3/g)	V_{Meso} (cm^3/g)	V_{total} (cm^3/g)
CSK	1275	0.46	0.03	0.48
CSKN700	1189	0.42	0.01	0.43
CSKN900	1092	0.39	0.02	0.41
PRK	1336	0.48	0.03	0.51
PRKN700	1243	0.41	0.04	0.45
PRKN900	838	0.30	0.04	0.34

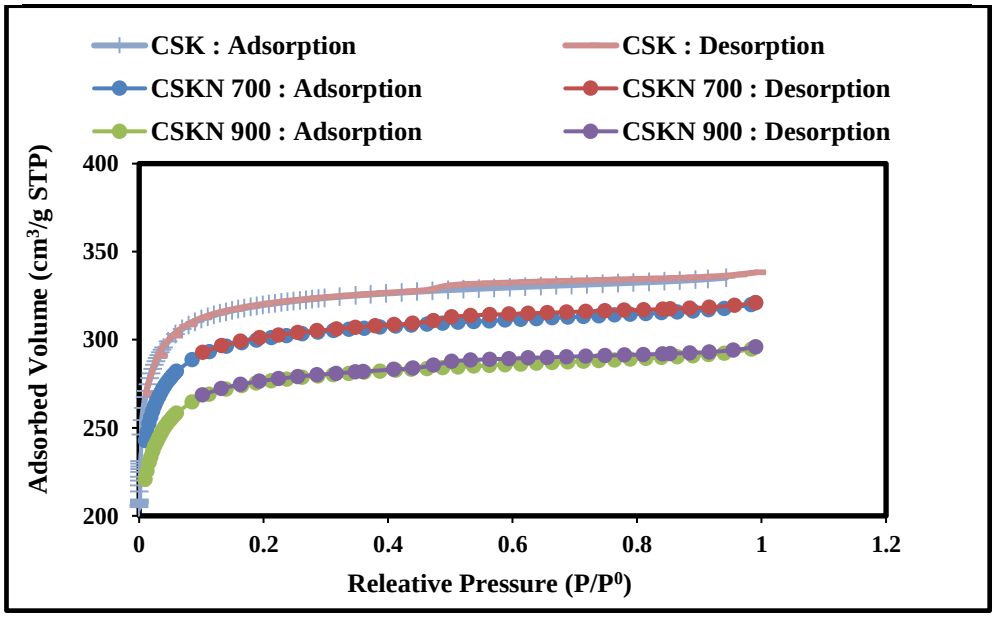


Figure 4. 3: N_2 isotherms at -196 °C of CSK, CSKN700 and CSKN900.

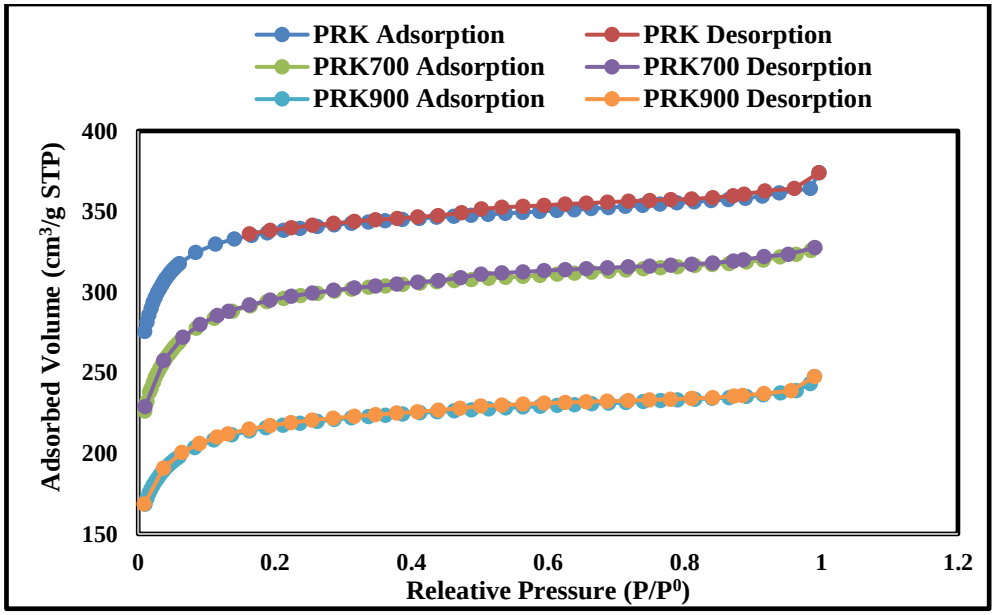


Figure 4. 4: N_2 isotherms at -196 °C of PRK, PRKN700 and PRKN900.

A much clear view of the microporosity can be obtained when these isotherms are replotted on a logarthem P/P^0 scale (Figure 4.5). CSKN700 and CSKN900 samples show no uptake of nitrogen under a relative pressure of 10^{-2} indicating the presence of ultra and super micropores. There is significant uptake of nitrogen of the two samples in the relative pressure range of 10^{-2} –10^{-1}, suggesting that these samples have wider micropores. The same trends was observed for PRKN700 and PRKN900 samples (Figure 4.6).

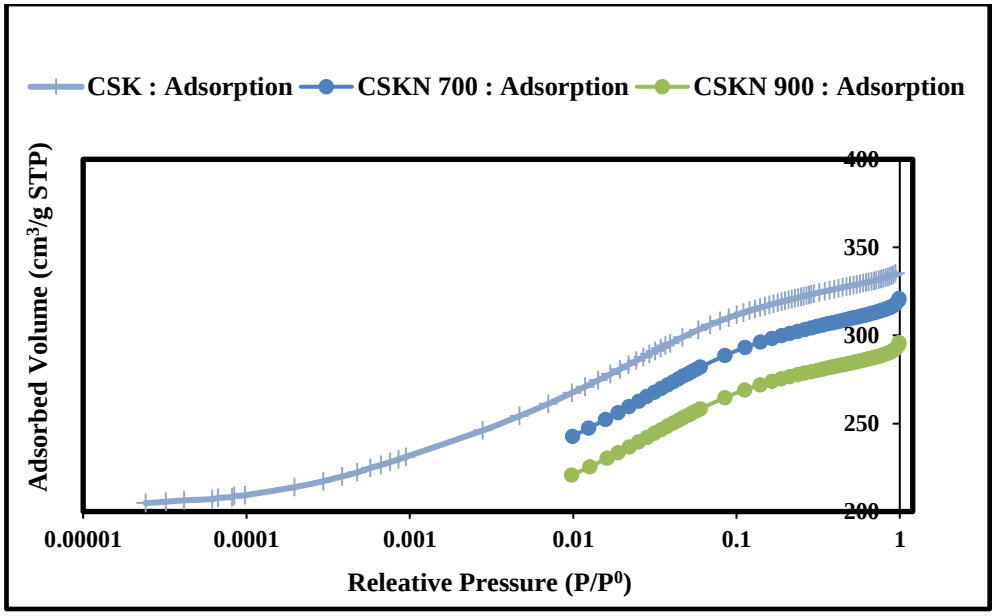


Figure 4. 5: Logarithmic N_2 isotherms at -196 °C of CSK, CSKN700 and CSKN900.

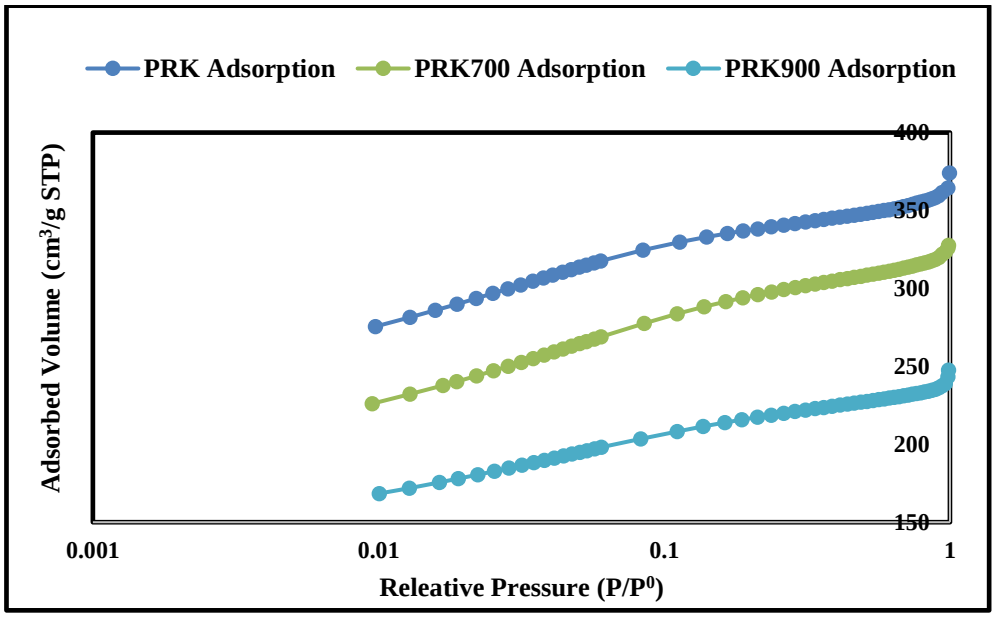


Figure 4. 6: Logarithmic N_2 isotherms at -196 °C of PRK, PRKN700 and PRKN900.

4.3.2 Organosiloxane Compound Treatment

The five organosiloxane compounds (VTMOS, OTES, POTS, HDTMS and PTES), dissolved in toluene (1 % v/v), and were coated separately onto CSK and PRK surfaces using the preparation method described in Section 3.2.1.2 (the next step of modification, heat treatment, will be demonstrated in the next section). The pore texture parameters for the CSK series are presented in Table 4.4 and Figure 4.7, and those for the PRK series are presented in Table 4.5 and Figure 4.8. With the exception of PRKV, the intercalation of organosiloxane molecules led to the decrease of BET surface area and micropore volume of the samples; CSK (about 11-21 %, and 10-21 % respectively) and PRK (about 6-7 % and 4-14 %). While related to the nature of the material, specifically its structure, this may also be due to the presence of organosiloxane compounds around the pore mouths restricting access of N_2 molecules to the micropores, so that just a small fraction of coating materials is residing within the pores (Cosnier et al., 2005). A wide reduction in surface area and pore volume for the PRKV sample (about 31 % and 29 %) could provide an indication of a large portion of VTMOS within the PRK pores.

Table 4. 4: Pore texture parameters for CSKs series.

Samples	S_{BET} (m^2/g)	V_{Micro} (m^3/g)	V_{Meso} (m^3/g)	V_{Total} (m^3/g)
CSK	1275	0.46	0.03	0.48
CSKV	1077	0.39	0.01	0.41
CSKO	1135	0.41	0.02	0.43
CSKF	1092	0.39	0.02	0.42
CSKH	1052	0.39	0.02	0.41
CSKP	1005	0.36	0.02	0.38

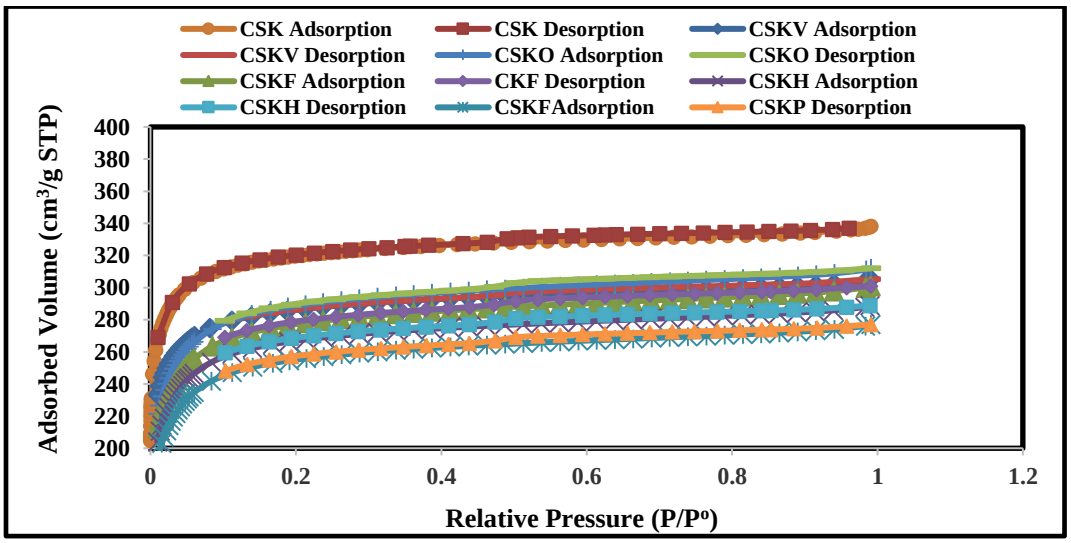


Figure 4. 7: N_2 isotherms at -196 °C of CSK and coated CSKs series.

Table 4. 5: Pore texture parameters of the coated PRKs series.

Samples	S_{BET} (m^2/g)	V_{Micro} (m^3/g)	V_{Meso} (m^3/g)	V_{total} (m^3/g)
PRK	1336	0.48	0.03	0.51
PRKV	925	0.33	0.03	0.36
PRKO	1245	0.46	0.03	0.49
PRKF	1224	0.47	0.03	0.44
PRKH	1262	0.46	0.03	0.49
PRKP	1225	0.44	0.04	0.48

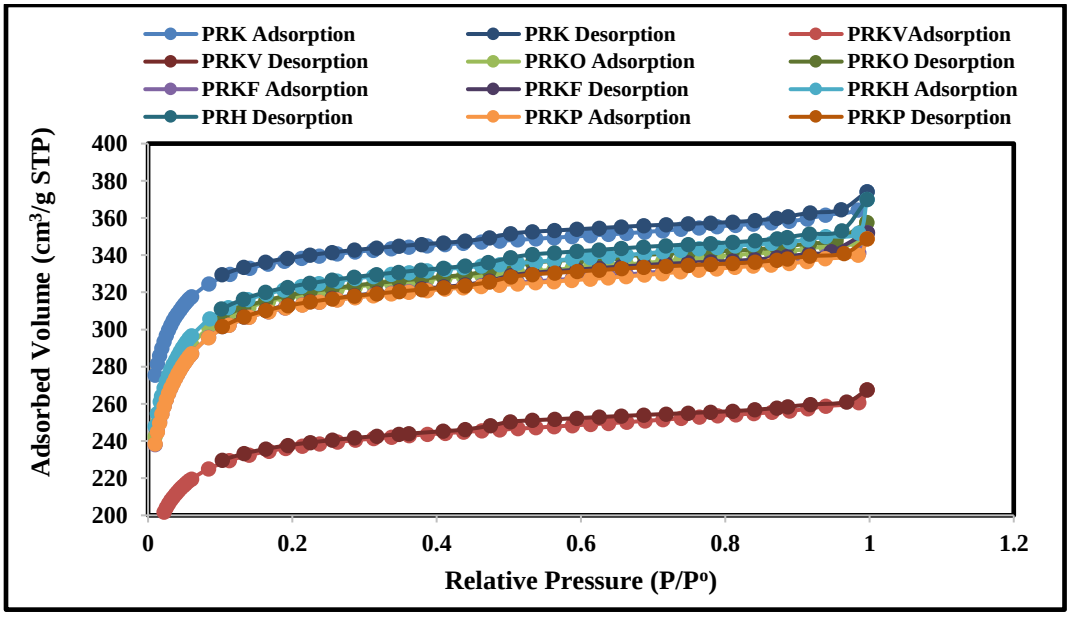


Figure 4. 8: N_2 isotherms at -196 °C of the coated PRKs series.

The adsorption isotherms for samples were plotted on a semi-logarithmic scale and presented in in Figure 4.9. Compared with CSK sample, all coated activated carbons derived from coconut shell showed significant uptakes of nitrogen in the relative pressure range of 10^{-2} –10^{-1} indicating blocking of the most super micropres, and the majority of adsorption occurred on the wide micropores.

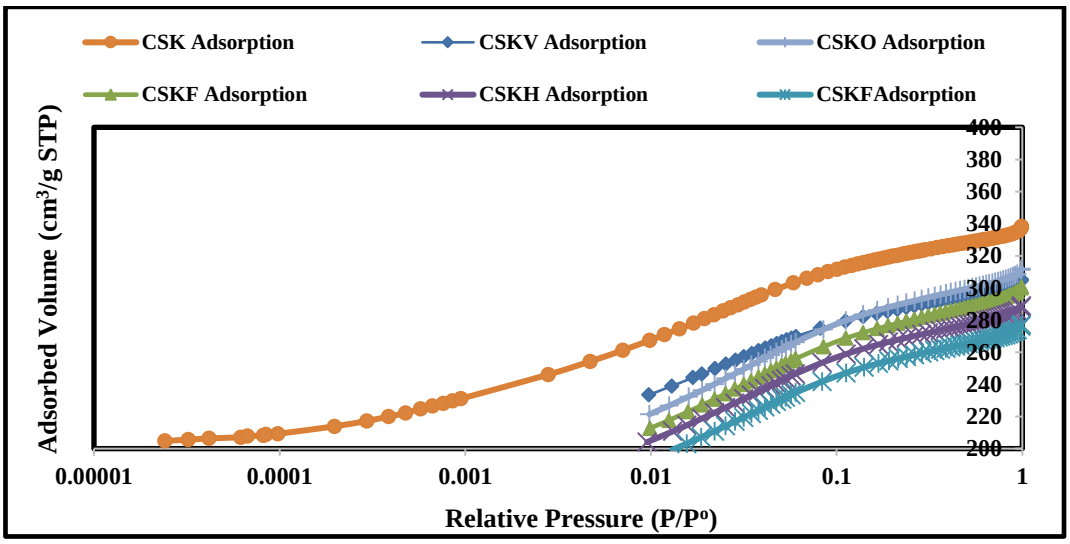


Figure 4. 9: Logarithmic N_2 isotherms at -196 °C of CSK and coated CSKs series.

4.3.2.1 The Influence of Heat Treatment on the Characteristics of the Coated Activated Carbon

By following the procedure described in Section 3.2.1.2, the calcination treatments were performed firstly for CSKV in the TGA at different temperatures. The corresponding samples were labelled CSKV300, CSKV350 and so on. It is noteworthy that the porosity of CSKV developed with increasing temperature up to 600 ^{o}C and approached the surface area and pore volume of CSK (Table 4.6). This suggests that a high fraction of polymerised silonal groups are splitting and decomposing from their locations in the pores and around the pore mouths (Poole,

2003). As shown in Figure 4.10, all N_2 adsorption isotherms maintained the type I(a) shape. These results reveal that the CSKV series samples are mainly microporous. In fact, the modification treatment did not alter the pore texture drastically, and the most remarkable uptake occurred at a low relative pressure ($P/P^o \leq 0.1$) due to the effect of micropore filling.

Table 4. 6: Pore texture parameters for the CSKVs series.

Samples	**S_{BET} (m^2/g)**	**V_{Micro} (cm^3/g)**	**V_{Merso} (cm^3 /g)**	**V_{total} (cm^3/g)**
CSKV	1077	0.39	0.01	0.41
CSKV300	1211	0.44	0.01	0.46
CSKV350	1229	0.44	0.02	0.46
CSKV400	1237	0.44	0.02	0.46
CSKV450	1249	0.44	0.03	0.47
CSKV500	1255	0.46	0.02	0.48
CSKV550	1258	0.47	0.02	0.50
CSKV600	1265	0.46	0.02	0.48

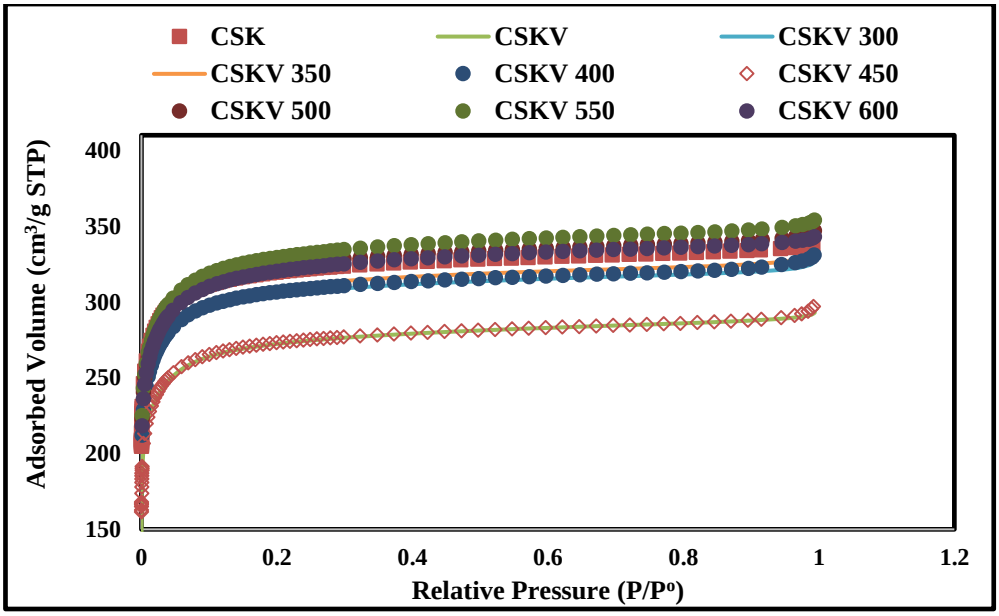


Figure 4. 10: N_2 adsorption isotherm at -196 °C of samples CSKVs series.

The N_2-adsorption isotherms that replotted on a logarithmic P/P^o scale showed the adsorption potential of the heat treated samples (Figure 11). Except CSKV450 that showed a significant uptake of nitrogen under a relative pressure of 10^{-5}, indicating the presence of ultra micropores that may reopened after heat treatment, the uptake of nitrogen for other heat treated samples were noticed under higher relative pressure (10^{-3}), which indicates that some larger pores may reopened after increasing the temperature.

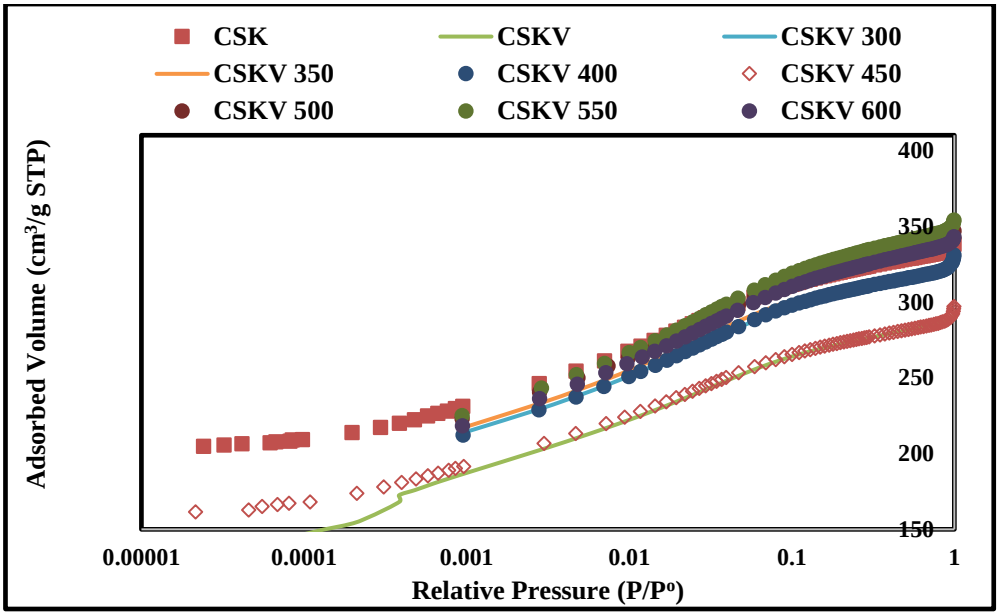


Figure 4. 11: Logarithmic N_2 adsorption isotherm at -196 °C of samples CSKVs series.

The experiments were repeated using the other organosiloxane compounds. For samples that were heated over the range 450 to 550 ^{o}C, showed a high CO_2 uptake and approached the adsorption capacity of KOH-activated carbon (which will be discussed in Chapter 6).

The highest surfaces area and porosities of the calcined CSK samples and calcined PRK samples were displayed in Table 4.7 and Table 4.8. Further investigations were therefore carried out using activated carbon derived from coconut shell for a closer inspection of the changes in surface structure of activated carbons by coating.

Table 4. 7: Pore texture parameters of the best performing coated CSK calcined samples.

Samples	**S_{BET} (m^2/g)**	**V_{Micro} (m^3/g)**	**V_{Meso} (m^3/g)**	**V_{total} (m^3/g)**
CSKV450	1249	0.44	0.03	0.47
CSKO500	1207	0.43	0.04	0.47
CSKF500	1106	0.34	0.05	0.39
CSKH550	1198	0.43	0.02	0.45
CSKP500	1127	0.41	0.03	0.44

Table 4. 8: Pore texture parameters of the best performing coated PRK calcined samples.

Samples	**S_{BET} (m^2/g)**	**V_{Micro} (cm^3/g)**	**V_{Meso} (cm^3/g)**	**V_{total} (cm^3/g)**
PRKV450	1028	0.35	0.04	0.39
PRKO500	1074	0.39	0.03	0.42
PRKF450	1122	0.41	0.05	0.46
PRKH500	1149	0.42	0.05	0.47
PRKP450	1107	0.41	0.06	0.46

4.4 CO_2 Adsorption Measurement (Volumetric)

Micromeritics ASAP 2420 was used to investigate the effect of calcination on the characteristics of CS, CSK, CSKV and CSKV450 samples (see Section 3.3.2.1). Figure 4.12 and Figure 4.13 show that the reduction of the kinetic energy of CO_2 molecules at 0 ^oC led to an enhanced CO_2 adsorption capacity compared to that achieved at 25 ^oC. These results are consistent with the findings obtained by Liu (2017) that refered to the enhancing of CO_2 adsorption capcity for the activated carbons at 0 ^oC. All samples show a Type I isotherm that is characteristic of a microporous structure. As expected, the CSK sample presented a substantially higher CO_2 adsorption capacity than other samples at both temperatures, especially at the relatively low-pressure region (less than 0.15 bar). This highlights the effectiveness of K^+ intercalation in developing extra microporosity and improving the surface affinity of the carbons for CO_2 adsorption particularly. The effects of both organosiloxane coating and heat treatment on the activated carbon surface can also be observed; at atmospheric pressure, the CSK sample adsorbed CO_2 3.69 mmol/g and 5.73 mmol/g at 25 and 0 ^oC, respectively, while the CSKV sample adsorbed only 2.37 mmol/g and 3.52 CO_2 mmol/g. The CSKV450 sample adsorbed 2.69 mmol/g and 4.26 mmol/g at the same conditions.

Furthermore, the isotherm data at two temperatures 0 and 25 ^oC were fitted using a dual-site Langmuir (DSL) equation to obtain the pressure (P) (Figure 4.12 and Figure 4.13). The equation was discussed in Section 3.4.4.2. The parameters, such as $q_{S,A}$, $q_{S,B}$, b_A and b_B, for each plot can be found in Appendix B. Q_{st} was calculated

using the pressure values determined above, along with adsorption capacities in the Clausius-Clapeyron equation which will discussed in Chapter 8.

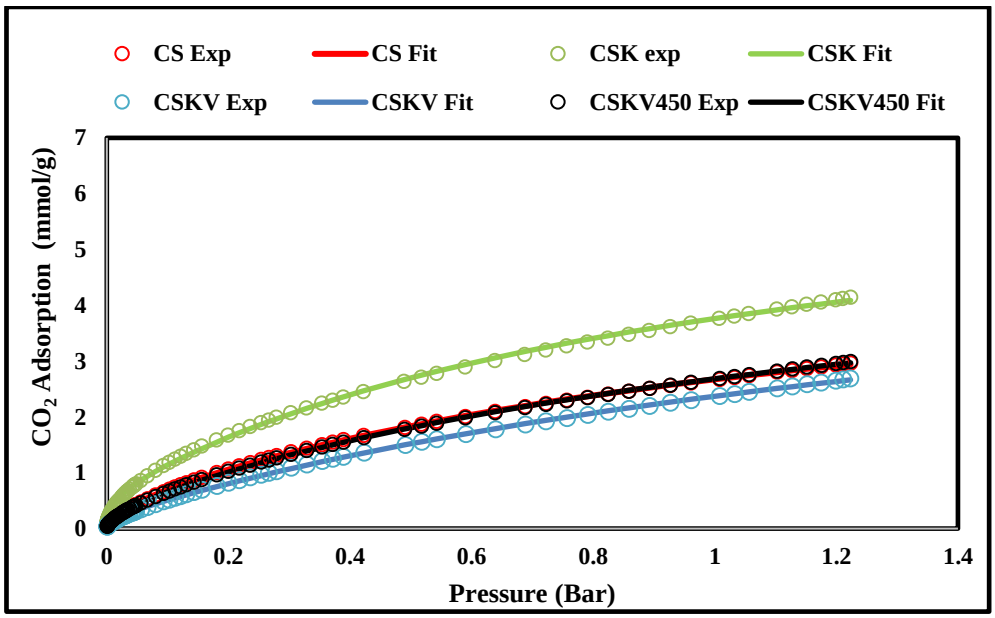


Figure 4. 12: CO_2 adsorption isotherms of the CSs at 25 ºC (symbols represent the measured values and lines are the fitted values with DSL).

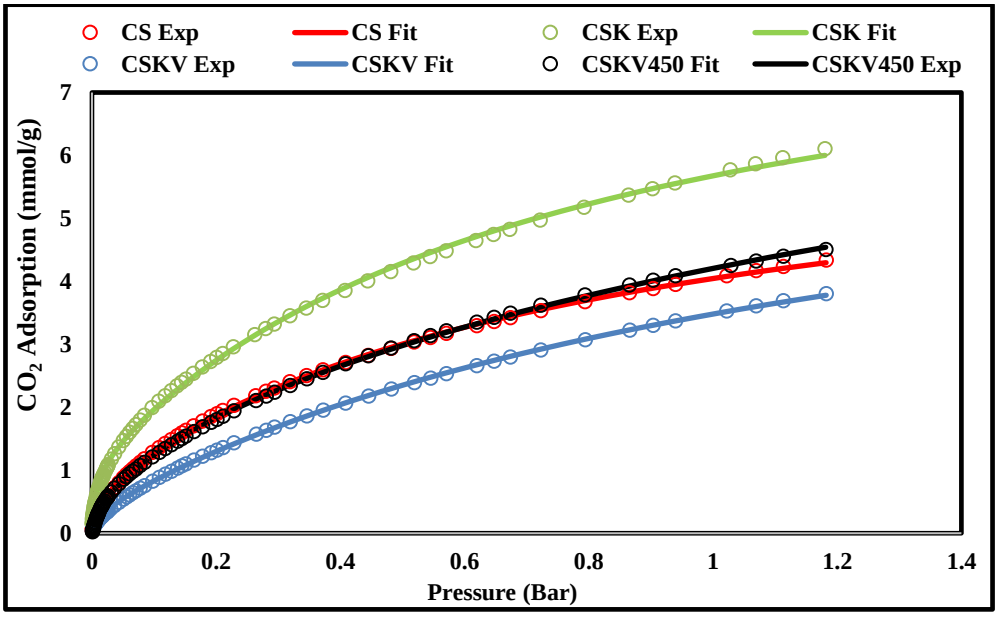


Figure 4. 13: CO_2 adsorption isotherms of the CSs at 0 ºC (symbols represent the measured values and lines are the fitted values with DSL).

4.5 Micropore Size Distributions of Coconut Shell Activated Carbons

N_2 adsorption isotherms at -196 ^oC and CO_2 adsorption isotherms at 0 ^oC were fitted using the NLDFT carbon slit pores model to obtain the micropore size distributions (MPSDs) for the CS, CSK, CSKV and CSKV450 samples from 0.3 to 100 nm. Figure 4.14 shows the relative proportion of micropores widths up to 3 nm for clarity. Much higher volumes of micropores were found at sizes between 0.8 and 2.0 nm and volumes with narrow micropores (<0.8 nm) centred at 2 points, 0.37 and 0.53 nm. As can be seen from this Figure, the slight difference between the pore texture of parent CS and CSK is found at the larger micropore sizes (> 0.9 nm). CSK tends to have a narrower distribution, and larger volumes of pores occur in the narrow micropore range, centred around 0.37 and 0.53 nm respectively. These results appear consistent with previous findings obtained by Wang and Kaskel (2012). Comparing the micropore size distribution (MPSDs) of CSK sample with CSKV reveals that the relative proportion of pores are larger with sizes of 0.8-2.1 nm for both samples, but there is a reduction in pore volume for CSKV at pore width around 0.37 nm, indicating pore blocking. Although the maximum molecular diameter of VTMOS is 0.73nm (Xie et al., 2011), this has only an effect on pore volumes less than this. Lower volumes for the pore width of less than 0.43 nm were noticed, indicating that some ultra micropores were blocked by VTMOS. Other than this, heat treatment of coated activated carbon at 450 ^oC led to an increase in pore volume similar to that of the CSK sample.

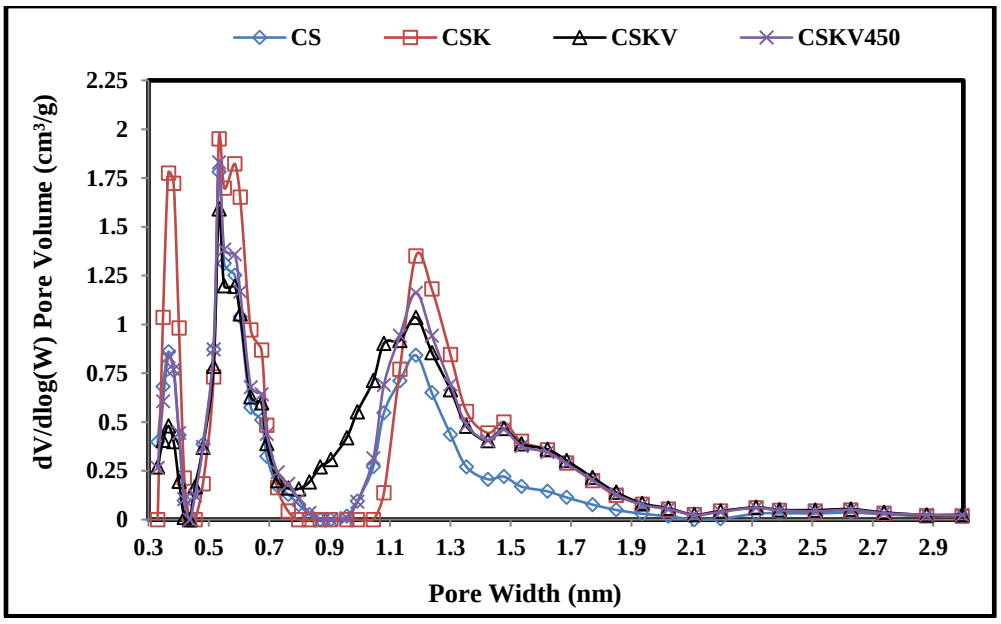


Figure 4. 14: The micropore size distribution of the coconut shell CS, CSK, CSKV and CSKV450 using NLDFT on carbon slit pore model.

4.6 Fourier Transform Infrared Spectroscopy (FTIR)

In this work, FTIR spectroscopy was performed for activated carbons derived from coconut shell according to the protocol described in Chapter 3. This was done in order to study the chemistry of CSKV, to ensure that VTMOS-grafting had occurred on the carbon surface during the processing, and to evaluate the effect of heat treatment on the chemical structure of VTMOS.

For the CSKV, and as shown in Figure 4.15, the plot of % transmittance versus wavenumber showed distinct adsorption bands at 2904, 1703, 1431, 1382, 1136 and 1062 cm^{-1}. The main intensity changes at 1062 cm^{-1}, the strongest in the spectrum, was completely governed by the stretching vibrations of Si–O in Si–O–CH_3. The intensity of this band decreased to a weak shoulder after heat treatment due to a decrease in the number of absorbing molecules in CSKV450, showing a new band

at 1031 cm^{-1}. Interestingly, in addition to the absorption bands at 1429 and 1136 cm^{1} that corresponded to asymmetric deformation and rocking vibrations of CH_3 in Si–O–CH_3, a large absorption band was observed in the CSKV spectrum at 2904 cm^{-1} and was assigned to another type of methyl group vibration: asymmetric stretching vibration. The last mode of vibration was also observed on CSKV450 at 2920 and 2851 cm^{-1}.

These findings indicated the existence of methoxysilyl structural units corresponding to VTMOS on CSKV, and in a smaller proportion, on CSKV450. In addition, further evidence for the existence of VTMOS on CSKV came from another absorption band at 1703 and 1382 cm^{-1}, which had not been observed on CSK and CSKV450. These were assigned to C=C stretching vibration in the H_2C=CH– group and CH deformation vibration in the H_2C=CH– group and gave further evidence of the existence of VTMOS (Semba and Morita, 2002) .

The absorption bands of CSKV found at 2904, 1703, 1431, 1382, 1136 and 1062 cm^{-1} were different from those at 2945, 1600, 1458, 1411, 1088 and 2843 cm^{-1} in the standard spectrum of VTMOS (Xie et al., 2011). Such a shift closely relates to a possible variation in the rigidity of the molecule grafted onto the CSKV surface. Furthermore, an absorption band at 2843 cm^{-1} in the standard spectrum of VTMOS, corresponding to asymmetric stretching vibrations of CH_3 in Si–O–CH_3 and also appearing as a very strong and broad absorption, was not found in the spectrum of CSKV. This gives further indication of the variation in molecule rigidity of VTMOS. The results demonstrate that the VTMOS is not simply adsorbed but is grafted onto the CSK surface (Xie et al., 2011). Simultaneously, the FTIR spectra of CSKV450 showed some interesting changes. Only four absorption bands were

observed, at 2920, 2851, 1448 and 1033 cm^{-1}, after elevated temperature and this indicates the removal of a number of absorbing VTMOS molecules.

The different vibration types of CH_3 groups mentioned above show that condensation of the CH_3 groups in Si–O–CH_3 with OH groups was taking place on the CSK surface. Thus, further condensation reactions of VTMOS on CSK surface can occur during the hydrophobisation process (Cosnier et al., 2005). This may explain why hydrophobisation does not penetrate deeply into the structure of activated carbon and does not close all pores (see Table 4.6). Moreover, the weak peak at 723 cm^{-1} that appeared only in CSKV could correspond to those, shifted, usually occurrs at 773 cm^{-1}, which is attributed to the stretching vibrations of Si-O bond within the group Si-O-CH_3 group.

Such a shift of the peak toward lower wavenumbers may account for a possible increase in the rigidity of the molecule, induced by the grafting (Fang and Binder, 2006). Meanwhile, the potential of VTMOS polymerisation was reduced by grafting of VTMOS onto the CSK surface. This explains the disappearance of the absorption band at 817 cm^{-1} which may occur due to a -C-C-C- in-plane bending ascribed to the polymer of VTMOS.

The O-H stretching vibration of surface hydroxyl groups does not usually appear as a sharp peak. A strong broad band CSKV was observed at 3125–3647 cm^{-1} with a maximum at about 3408 cm^{-1}, possibly due to the characteristics of the stretching vibration of hydrogen bonded hydroxyl groups (Zarubin, 1999). However, the broad band decreased drastically after heat treatment, possibly referring to the removal of some hydroxyl groups.

In conclusion, the results obtained from FTIR spectroscopy indicate that the VTMOS was not simply adsorbed on the surface of CSKV but reacted chemically with it, and that the heat treatment has drastically affected the chemistry of CSKV by removing some of hydroxyl groups.

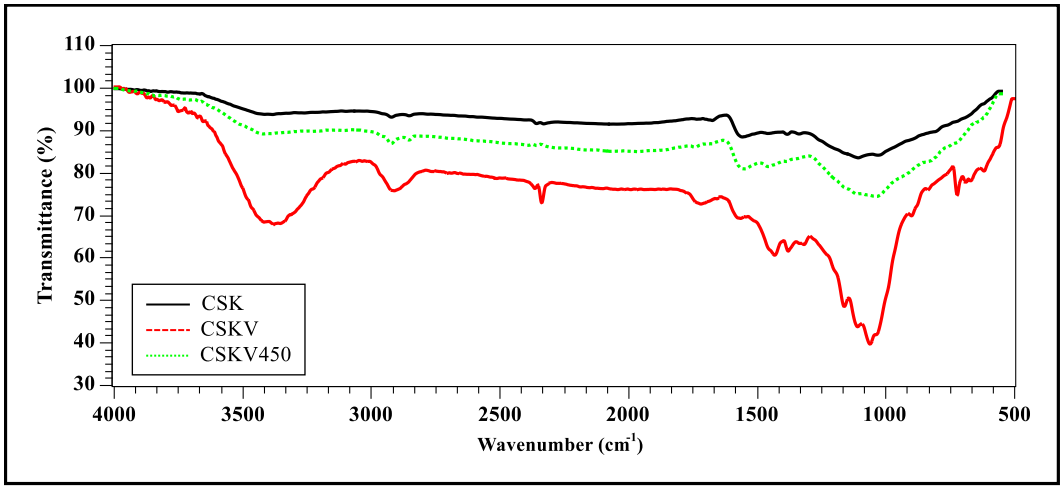


Figure 4. 15: FTIR spectra of CSK, CSKV and CSKV450.

4.7 Elemental Analysis

As shown in Table 4.9, the elemental composition of CSK sample consisted of 71 wt% of C, 0.4 wt% of N, 2.3 wt% of H, and 10.7 wt% of O. It is important to mention that water washing did not remove all potassium from the carbon and a certain amount of potassium (15.4 wt%) was left in it. According to Cosnier et al. (2005), the amount of VTMOS used to cover activated carbon surfaces depends on the O_2 content of the hydroxylated materials, where 1 mol of the O_2 atom is reacted with 1.3 mol of VTMOS. Based on that, 0.004 mol (0.66 g) of VTMOS was used in this work to cover the CSK surface. The content of potassium for CSKV was lowered significantly to 0.1 wt% and the content of silica increased drastically to 8.3 wt%,

which can be explained by the fact that most potassium sites on the carbon surface would have been covered by the coating layer.

Table 4. 9: Elemental compositions of CSKV and CSKV450.

Samples	Elemental Analysis (wt%)					
	C	**N**	**H**	**O***	**K^+**	**Si^+**
CSK	71.2	0.4	2.3	10.7	15.4	0.0
CSKV	76.7	0.6	1.3	12.9	0.1	8.3

$^+$The content of K^+ and Si^+ was determined by XRF.
* The content of O_2 was obtained by difference.

4.8 Proximate Analysis

For the proximate analysis, it can be seen that the H_2O content in the CSK sample was more than twice the amount in the CSKV (Table 4.10). This may be because the surface chemistry of CSK has become more hydrophilic due to the introductions of O_2 functional groups through K^+ intercalation, while the coating layers have increased the surface hydrophobicity of the CSKV and inhibited the passage of water molecules through it. Furthermore, the quantity of organic matter in the CSKV may be the reason why the amount of materials evaporating from the CSKV had increased compared to that from the CSK.

The particle residue that remains after burning carbon is called ash. The ash content in a natural activated carbon is usually less than 7 % (Jaguaribe et al., 2005). In the present study, although CSK contained some amount of potassium, its ash content did not exceed 6 %. This indicates only a very small amount of residual potassium

in CSK. However, the amount of ash content almost doubled for the CSKV due to the VTMOS-derived silica from the coating process.

Table 4. 10: Proximate analysis of CSK and CSKV.

Samples	Proximate analysis			
	M (%)	**VM (%)**	**FC (%)**	**Ash (%)**
CSK	12.7	14.4	66.2	5.7
CSKV	6.8	14.9	65.0	13.1

M: water vapour, VM: volatile matter, FC: fixed carbon.

4.9 SEM-EDX Analysis

For a closer examination of the changes in the surface structure of activated carbon after VTMOS-coating and heat treatment, the surface morphology of samples CSK, CSKV and CSKV450 was observed by SEM in μm scale. A 50x higher magnification used than that for the original image (1000x) as shown in Figure 4.16a, b and c. The images revealed changes in the CSK structure after VTMOS-coating. The large cavities of CSK sample has disappeared with forming low-level pore network. A few amount of organosiloxane may be deposited on the inner walls (the thickness of VTMOS deposited could be ulter-thin in the nanometer scale). It is interesting to note that the macropores of CSKV after treatment at 450 ^{o}C is reopened (where the SEM does not permit direct visualisation of scale of microporosity) suggesting the collapse of most VTMOS coating on the coated surface. The SEM characteristics of the three samples are consistent with the results

obtained from the N_2 adsorption isotherms of these samples, where a slight decrease in the pore diameter from 1.5nm to 1.4nm was observed after coating CSK, as well as the return of pore diameter to its initial value after heat treatment.

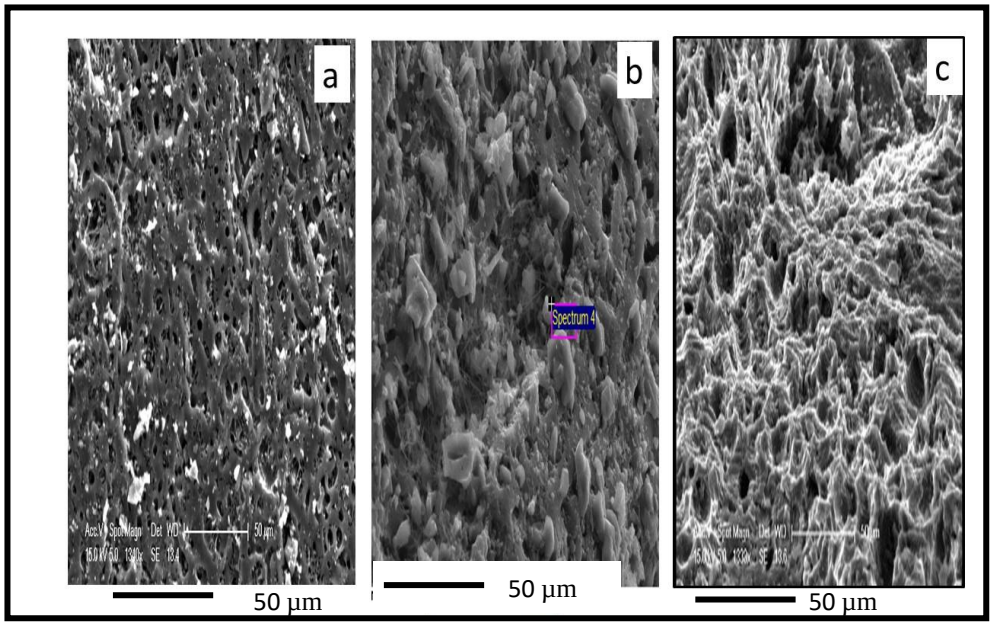


Figure 4. 16 : SEM images of carbon (a,) CSK, (b) CSKV (c) CSKV450.

EDX analysis was carried out with an SEM to investigate the atomic percentages of the principle elements on the surface of CSK, CSKV and CSKV450. The information obtained for all samples is listed in Table 4.11 and shown in Figure 4.17. SEM-EDX indicated a low content of potassium (1.2 wt%.) with an obvious peak of elemental K^+, indicating the successful intercalation of K^+ into activated carbon and a small amount of potassium found on the surface. The content of carbon and O_2 were 92.3 % and 6.5 %, respectively. After VTMOS coating, an increase in the percentage of atomic O_2 (13.4 %) was observed with an appearance of elemental silicon (0.8 %). It is noteworthy that the appearance of the elemental sodium was as

a result of the reduction process that was previously explained in Section 3.3.9. The temperature-induced changes in the surface chemistry of the coated sample were as a result of decomposing and volatilising a fraction of the grafted VTMOS. Therefore, the atomic ratio of Si doubled to 1.6 % and the O_2 content increased slightly to 16.1 %. In conclusion, although increasing temperature to 450 ^oC resulted in the enhancement of activated carbon porous structure development, no drastic change in the structure of the "coating" was observed. These results agree with those obtained by Cosnier et al. (2005).

Table 4. 11: EDX results of K and Si concentrations for CSKs.

	Atom. (at. %)				
Samples	**C**	**O**	**K**	**Si**	**Na**
CSK	92.3	6.5	1.2	-	-
CSKV	83.5	13.4	-	0.8	0.7
CSKV450	81.1	16.1	-	1.6	1.2

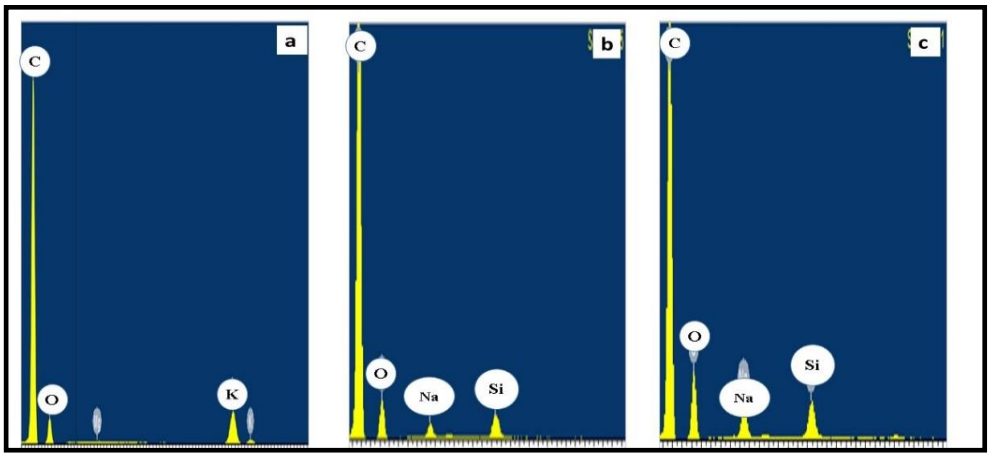


Figure 4. 17: SEM-EDX analysis of carbon (a,) CSK, (b) CSKV (c) CSKV450.

4.10 XPS

The chemical composition of the CSKV450 surface was investigated by XPS analysis which provides more quantitative composition results than that provided by SEM-EDX analysis. Coincidentally, the result obtained by XPS is almost similar to the result obtained by SEM-EDX, in which there is an obvious peak of elemental Si. The measurements of the CSKV450 surface were performed in the range of 0 to 1400 eV, as shown in Figure 4.18 (a). The peaks that centred on binding energy at ~285 eV, ~531 eV and ~100 eV were attributed directly to C1s, O1s and Si2p. The results clarify that CSKV450 surface is dominated by C and O, where the ratio of C to Si is 19.4, (Table 4.12).

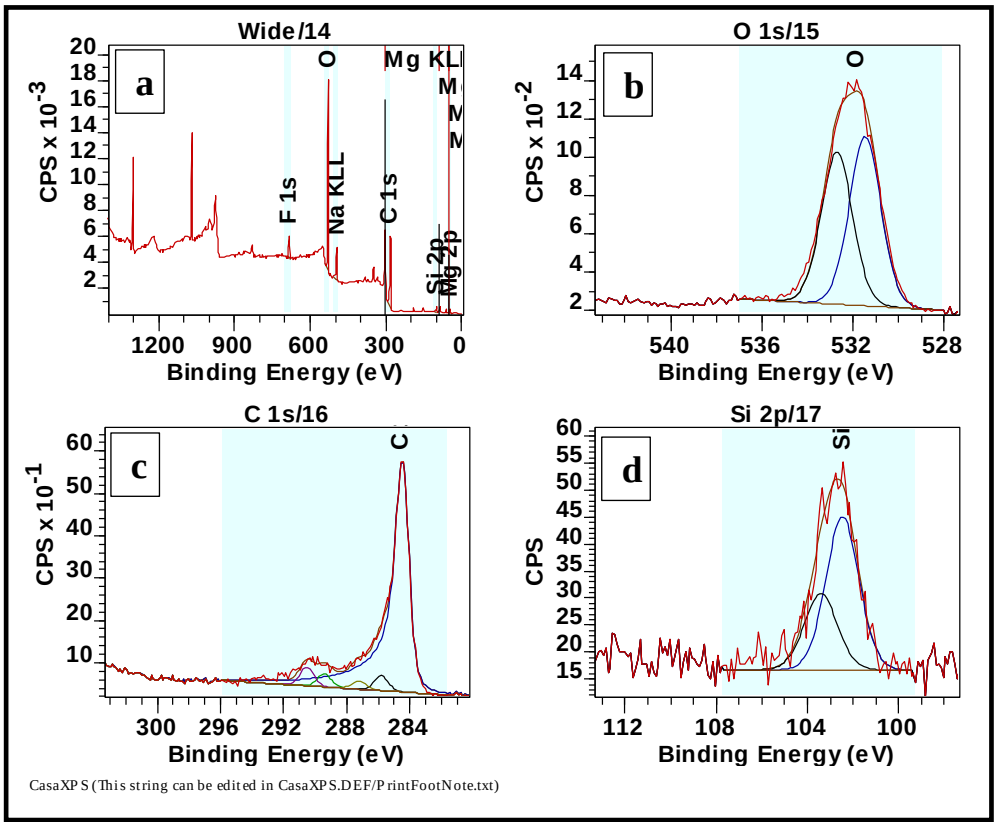


Figure 4. 18: XPS analysis of CSKV450 showing the high-resolution O, C and Si peaks.

Table 4. 12: Chemical composition of VTMOS coating film obtained by XPS measurement.

	Atom %						
Sample	**C**	**O**	**Si**	**Na**	**F**	**Mg**	**C:Si ratio**
CSKV450	49.8	34.6	2.6	5.9	3.9	3.2	19.2:1

According to the literature (Cosnier et al., 2005), a peak within the range 106-107 eV is due to the VTMOS while the peak centred on binding energy close to 102.5 eV is due to the presence of polysiloxane. Morevore, the XPS spectrum for the high-resolution C1s spectrum can provide more information about the concentration of Si in VTMOS. C1s region that measured within the range of 281.5 eV to 291.4 eV, is reported in Figure 4.13(c), affords three components. The first peak at 284.6 eV is due to C=C (sp2), a small shoulder caused by sp3 C-C bonding at 285.5 eV, the spectrum at 287.2 eV seems to be due to C=O configuration. The changes in the measured C1s core level spectra toward lower binding energy with a full width at half maximum of 1.5 eV reveal that the VTMOS contained a relatively high concentration of Si atoms. Further evidence of this was that the intensity of O 1s that peaked at 532.2 eV, as shown in Figure 4.18(b).

The Si2p spectrum was measured within the range 101.8 eV to 104.8 eV, as shown in Figure 4.13(d). Only one peak appeared at 102.0 eV. This reveals that the presence of Si existed in the VTMOS framework and also that the Si had not fully oxidized to silicon dioxide (SiO_2). This is because SiO_2 should show a pronounced Si2p state at 103.3 eV (Liu et al., 2016).

4.11 Effect of Humidity on Physical Characterisations of Activated Carbon

The structural characteristics of humid samples were analysed using a full N_2 isotherm at -196 ^oC (Figure 4.19) and compared with the dry samples. The calculated BET specific surface areas and pore volumes are reported in Table 4.13. N_2 adsorption isotherms for dry CS sample display a type I(a) isotherm with a high amount of N_2 adsorption at a low relative pressure (<0.01). This gives a good indication that the N_2 molecules have filled a large number of narrow micropores, and that the structure of the sample consists mainly of wide micropores and narrow mesopores (< ~2.5 nm) (Thommes et al., 2015). After increasing relative humidity to 10 %, N_2 adsorption reduced drastically to 30 % compared to that of vacuum dried samples, indicating that a large number of micropores have been occupied by water molecules. With increasing relative humidity to 50 %, the equilibrium isotherm sample was shifted toward a lower value (41 cm^3/g), reflecting that more micropores were filled in with water molecules. Finally, at 95 %RH, the micropores were totally blocked; the N_2 isotherm of the tested sample was essentially zero, which agrees with the typical shape of type III (IUPAC classification). This provides strong evidence that the texture properties of the CS sample depend on the equilibrium relative humidity.

As can be seen from Table 4.13, the textural properties of this sample showed better values than those at higher relative humidity. For instance, the CS sample displays surface area and micropores volume of 912 m^2/g and 0.33 cm^3/g under vacuum dried, and 235 m^2/g and 0.08 cm^3/g at 10 %RH. The latter values were reduced by

half at 50 %RH. At 95 %RH the micropore volume of the CS sample was close to zero and the surface area was only 1.03 m^2/g. Therefore, at 10%RH, the water molecules occupied about 70% of the volume of dry sample (0.34 cm^3/g), and the percent increased up to 99% with increasing relative humidity up to 95 %.Veneman et al. (2015) reported that at this high level of saturation, water vapour condenses inside the pores of the sorbent material and the condensed water grows and completely fills micro, then meso and macropore space.

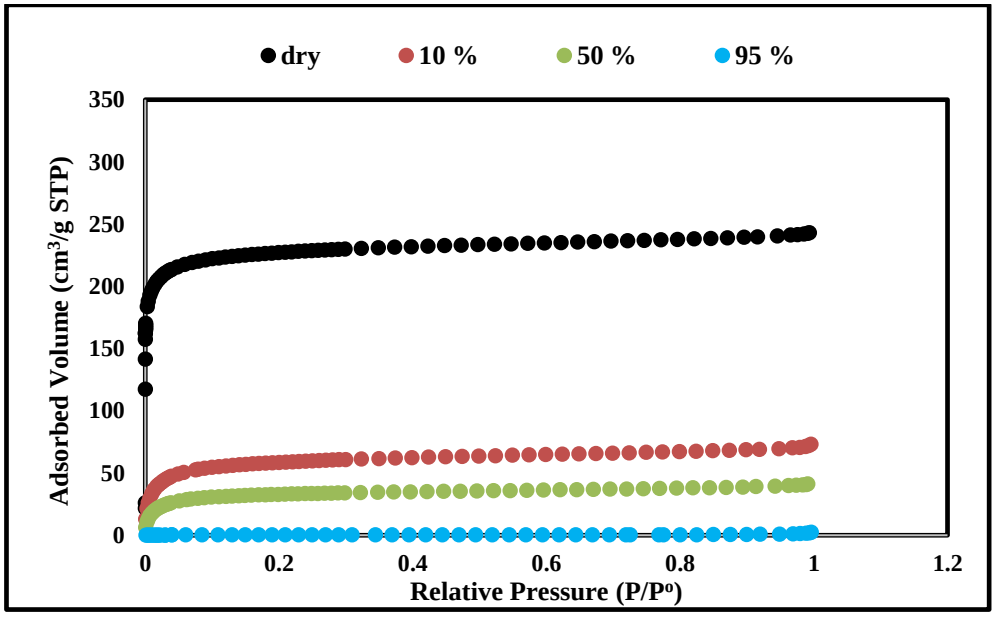


Figure 4. 19: N_2 isotherms of CS at the vacuum dried and 10 %, 50 %, 95 %RH.

Table 4. 13: Pore texture parameters for CS sample at the vacuum dried and 10 %, 50 %, 95 %RH.

Samples	S_{BET} (m^2/g)	V_{Micro} (cm^3/g)	V_{Meso} (cm^3/g)	V_{Total} (cm^3/g)	V_W^* (cm^3/g)
CS	912	0.3300	0.0100	0.3400	-
CS 10 %RH	235	0.0800	0.0200	0.1000	0.2400
CS 50 %RH	133	0.0400	0.0200	0.0600	0.2800
CS 95 %RH	1.03	0.0002	0.0028	0.0030	0.3370

V_W^*: Volume of pre-adsorbed water with the loss of externally-accessible volume to N_2 ($V_W = V_{Total\ (dry)} - V_{Total\ (\%RH)}$)

On the other hand, as shown in Figure 4.20, the N_2 adsorption isotherm pattern of the dry CSK shows a similar trend than that for CS with a significant amount of N_2 adsorption at a low relative pressure (<0.01), indicating the development of microporosity after intercalation of KOH. However, with increasing relative humidity to 10 %, CSK exhibited a greater reduction of equilibrium adsorption uptake than CS to reach 97 cm^3/g. At 50 % and 95 %RH, the N_2 isotherms of CSK samples were close to zero, which agrees with the typical shape of a type III. At equilibrium, the results showed that the CSK surface has become more hydrophilic due to the intercalation of alkali metal ions (K^+) and formation of hydrogen bonds. The surface chemistry of activated carbon may alter through increase in hydroxyl-rich polar groups, which offer strong interactions with H_2O molecules. The isotherms of samples are replotted on logarithmic P/P^0 scale (Figure 4.21). The dry sample showed a significant uptake of nitrogen in the relative pressure of 10^{-5}. Low uptake of nitrogen was observed in the relative pressure of 10^{-3} for the humid sample (10 %RH), indicating most ultra micropores were filled by the water molecules,

while most large pores were filled by water molecules for the other humid samples. Like unmodified activated carbon, dry CSK sample showed better texture properties than those at higher relative humidity. The dry sample displays a surface area and micropore volume of 1275 m^2/g and 0.46 cm^3/g, respectively (Table 4.14). The highest reduction in BET surface area and micropore volume occurred after increasing the relative humidity to 10 %, where the values decreased to 322 m^2/g and 0.1 cm^3/g respectively. Surface area and microporosity were continuously reduced for humid samples of CSK, reaching 22 m^2/g and 0.01 cm^3/g at 50 %RH, while increasing relative humidity to 95 % led to a decrease of the surface area to 0.43 m^2/g and a micropore volume of close to zero, indicating that most of the micropores were filled by water molecules. Investigation the humid sample (10 %RH) refers to water molecules occupied about 70 % of the volume of this sample (the volume of dry sample is 0.35 cm^3/g). At 50 %RH, the loss of externally-accessible volume to nitrogen increased to 96 % as water molecules occupied most pores. All pores filled with water molecules at 95%RH.

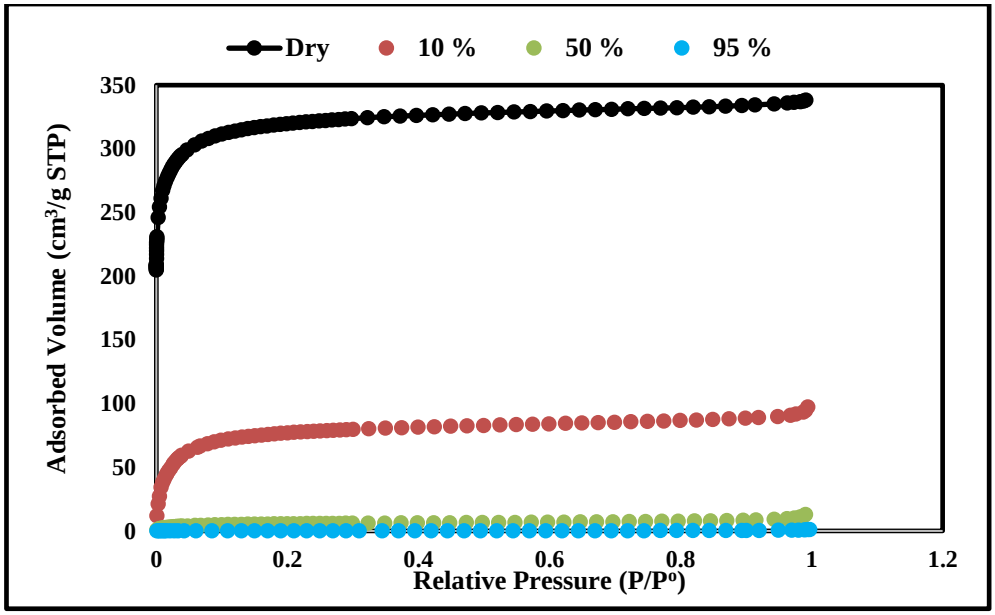


Figure 4. 20: N_2 isotherms of CSK at the vacuum dried and 10 %, 50 %, 95 %RH.

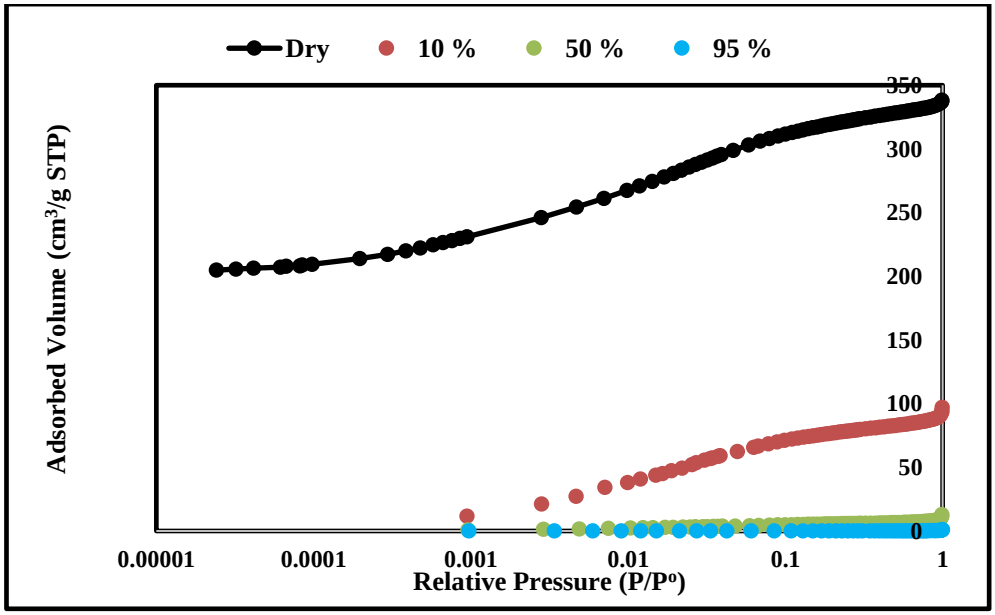


Figure 4. 21: Logarithmic N_2 isotherms of CSK at the vacuum dried and 10 %, 50 %, 95 %RH.

Table 4. 14: Pore texture parameters for coated CSK samples at the vacuum dried and 10 %, 50 %, 95 %RH.

Samples	S_{BET} (m^2/g)	V_{Micro} (cm^3/g)	V_{Meso} (cm^3/g)	V_{total} (cm^3/g)	V_W^* (cm^3/g)
CSK	1275	0.46000	0.03000	0.48000	-
CSK 10 %RH	322	0.10000	0.03000	0.13300	0.3500
CSK 50 %RH	22	0.01000	0.00800	0.01800	0.4600
CSK 95 %RH	0.43	0.00009	0.00091	0.00100	0.4800

N_2 isotherms were plotted for dry and wet CSKV samples to study the effect of VTMOS on the adsorption of N_2 at different conditions (Figure 4.22). Like other samples studied before, the dry CSKV showed a Type I(a) isotherm (the equilibrium N_2 uptake is 292.9 cm^3/g) and type I(b) was observed for CSKV at 10 % and 50 %RH (the equilibrium N_2 uptakes are 101.91 cm^3/g and 27.17 cm^3/g, respectively). At 95 %RH, the N_2 isotherm was essentially zero. The difference between the adsorption isotherms of CSK and CSKV indicates the effect of organosiloxane compounds on the porosity of activated carbon surface.

Based on the above, the texture properties of CSKV have been significantly changed (Table 4.15). For instance, the dry sample displays surface area and micropore volume of 1077 m^2/g and 0.39 cm^3/g, respectively. These values decreased to 420 m^2/g and 0.11 cm^3/g at 10 %RH, and to 72 m^2/g and 0.04 cm^3/g at 50 %RH. With increasing relative humidity to 95 %, the micropores may be completely blocked, and thus the surface area was only 1.49 m^2/g and micropore volume of 0.0003 m^3/g.

In general, the texture properties obtained from CSKV at different relative humidities were slightly better than those obtained by CSK due to the hydrophobic

surface of the coated sample, which provided more pore space to adsorb N_2. The loss of externally-accessible volume to nitrogen was in between 66% (at 10%RH) and 98% (at 95%RH) as the water molecules occupied 0.27 and 0.4 cm^3/g, respectively.

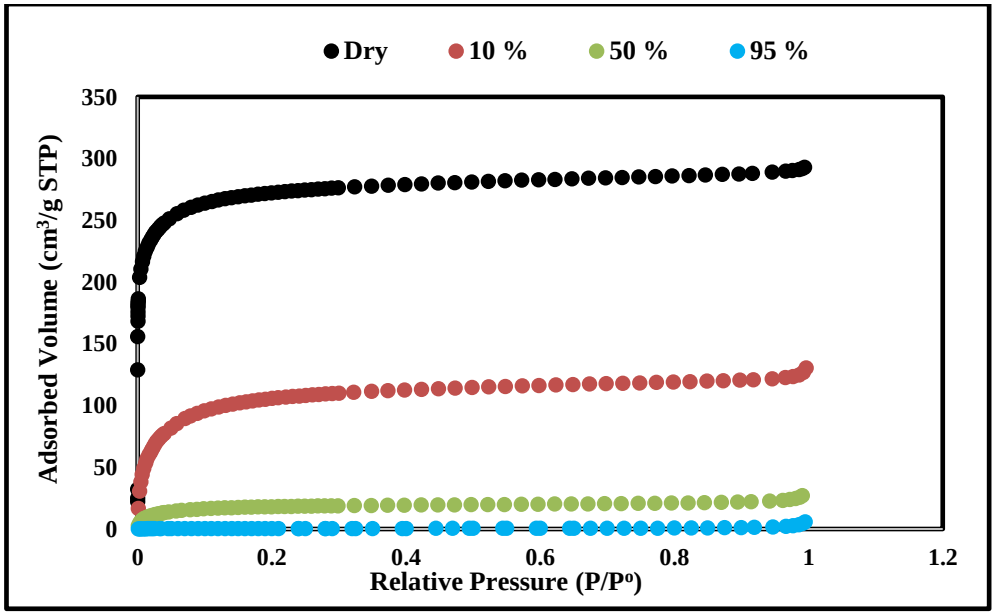


Figure 4. 22: N_2 isotherms of CSKV at the vacuum dried and 10 %, 50 %, 95 %RH.

Table 4. 15: Pore texture parameters for CSKV samples at the vacuum dried and 10 %, 50 %, 95 %RH.

Samples	S_{BET} (cm^2/g)	V_{Micro} (cm^3/g)	V_{Meso} (cm^3/g)	V_{Total} (cm^3/g)	V_W^* (cm^3/g)
CSKV	1077	0.3900	0.0100	0.4100	-
CSKV 10 %RH	420.0	0.1100	0.0300	0.1400	0.2700
CSKV 50 %RH	72.00	0.0200	0.0200	0.0400	0.3700
CSKV 95 %RH	1.490	0.0003	0.0061	0.0064	0.4000

Finally, as shown in Figures 4.23 and Table 4.16, no large differences were observed between the adsorption isotherms of CSKV450 and CSK in dry and wet conditions especially at 10 % and 50 %RH, and in addition the texture properties of the two samples were very close together. This provides evidence that most of the VTMOS layer was removed from the activated carbon surface after the heat treatment. The semi-logarithmic plots for the dry and humid CSKV450 sample showed similar results for CSK in the same conditions see Figure 4.24. Compared with the dry sample, and as a result of reopened some pores after increasing temperature, the water molecules occupied 64% of the pores of heat treated samples at 10 %RH, and occpied most the pores (91 %) at 50 %RH, and all pores at 100 %RH.

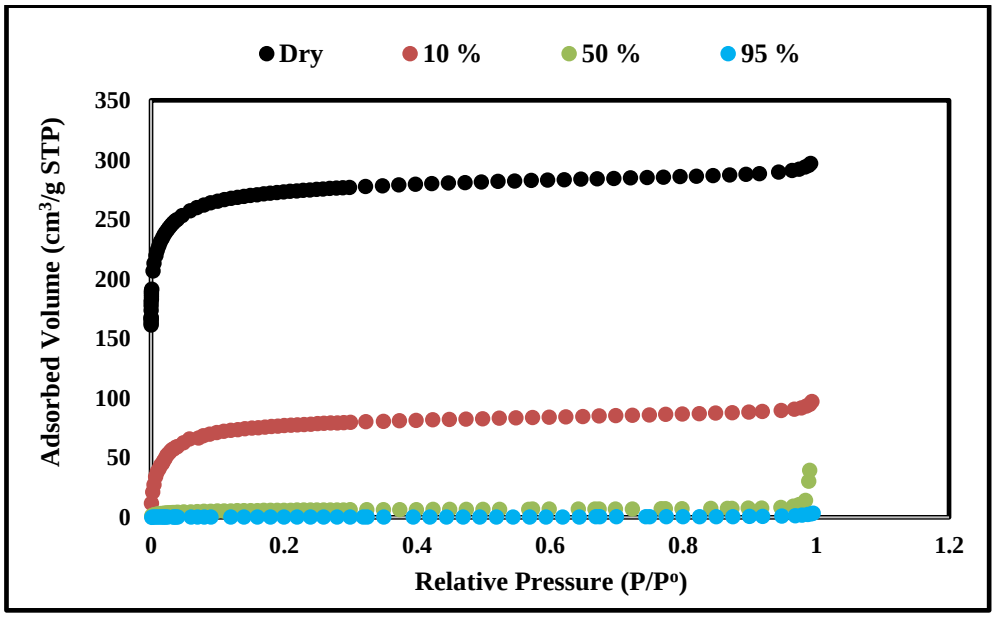


Figure 4. 23: N_2 isotherms of CSKV450 at the vacuum dried and 10 %, 50 %, 95 %RH.

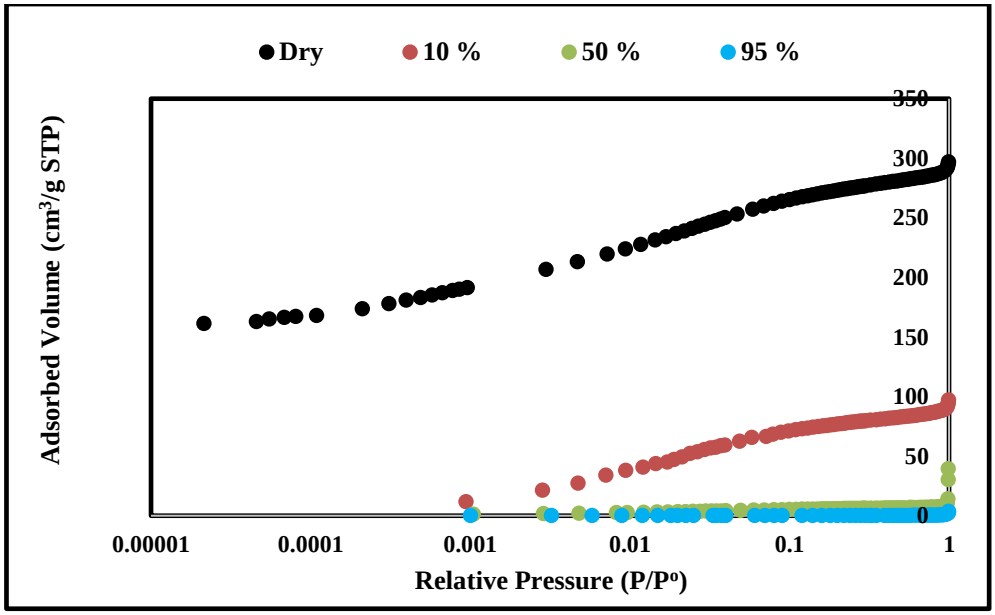


Figure 4. 24: Logarithmic N_2 isotherms of CSKV450 at the vacuum dried and 10 %, 50 %, 95 %RH.

Table 4. 16: Pore texture parameters for CSKV450 samples at the vacuum dried and 10 %, 50 %, 95 %RH.

Samples	S_{BET} (m^2/g)	V_{Micro} (m^3/g)	V_{Meso} (m^3/g)	V_{total} (m^3/g)	V_W^* (cm^3/g)
CSKV450	1249.00	0.4400	0.0300	0.4700	-
CSKV450 10 %RH	323.00	0.1400	0.0300	0.1700	0.3000
CSKV450 50 %RH	23.00	0.0100	0.0300	0.0400	0.4300
CSKV450 95 %RH	0.97	0.0002	0.0035	0.0037	0.4700

4.12 Conclusions

The surface area and pore volume of the CS and PR were increased by intercalation of KOH. However, decreasing of porosity has been noted after coating CSK and PRK with organosiloxane compounds. Heat treatment helped to restore most of the initial porosity although the pore structure of calcined activated carbons was negatively affected by heating in N_2 at temperatures ≥ 550 °C when the walls of pores began to collapse. N_2 sorption isotherms of the unmodified and modified activated carbons at 10 %, 50 % and 95 % equilibrium RH were compared with samples that were vacuumed dried to understand the effect of wet conditions on the porosity of activated carbon. The adsorption capacity of N_2 was reduced gradually with the increase of H_2O loading on activated carbon where humid conditions were extremely effective in blocking off narrow micropores. No significant differences were observed between the N_2 adsorption isotherms of CSK and CSKV450 in humid conditions. Therefore, the texture properties of the two samples showed similar results.

CHAPTER 5: Impact of KOH Treatment on Water Vapour Co-Adsorption for CO_2 Capture of Activated Carbons

5.1 Introduction

For CO_2 capture, the rate of adsorption is a very important parameter for the design and operation of adsorbers. In general, the adsorbent materials that show fast kinetic reactions with CO_2 and slow reaction with H_2O are most favourable. In this chapter, the adsorption kinetics of both CO_2 and H_2O on activated carbons derived separately from coconut shell and phenolic resin are evaluated both before and after modification with KOH. The bench-scale adsorption experiments were conducted in a TGA and a DVS as described in Sections 3.3.1.1 and 3.3.3.

5.2 Effect of Activation Temperature on CO_2 Adsorption

The performance of the three coconut shell-derived samples - CSK650, CSK700 and CSK750 for CO_2 adsorption were evaluated using TGA. The activation procedure was described in Section 3.2. It was expected that intercalation of potassium ions (K^+) may alter the surface chemistry of activated carbon leading to an increase in hydroxyl-rich polar groups on the CSK surface, offering strong dipole-quadrupole moment interactions with CO_2 molecules (Liu, 2017). Figure 5.1 shows that samples heated at 650 ^oC and 700 ^oC have almost identical CO_2 adsorption. Interestingly, although CSK750 has the largest porosity (see Section

4.2), it has the lowest CO_2 adsorption capacity as a result of a reduction in the surface polarity of KOH-activated carbons owing to the removal of some OH groups at this temperature (Huh, 2011, Lendzion-Bieluń et al., 2018). As the errors in Figure 5.1 are small (<0.02 mmol/g) compared with the differences in CO_2 adsorption between samples (0.5 mmol/g), this indicates a high level of confidence in the performance of the samples. The same activation procedure that was mentioned above was used for the PR sample at 700 ºC (the physical properties of the PR sample presented in Appendix C). Compared to unmodified sample, CO_2 adsorption capacity of PRK700 was increased from 0.8 to 1.7 mmol/g. Due to the high CO_2 adsorption capacity and porosity of the CSK700 and PRK700 samples, they will be used for further investigations in this study. The raw data for kinetics of adsorption experiments and demonstrate steps in data analysis process are shown in Appendix D.

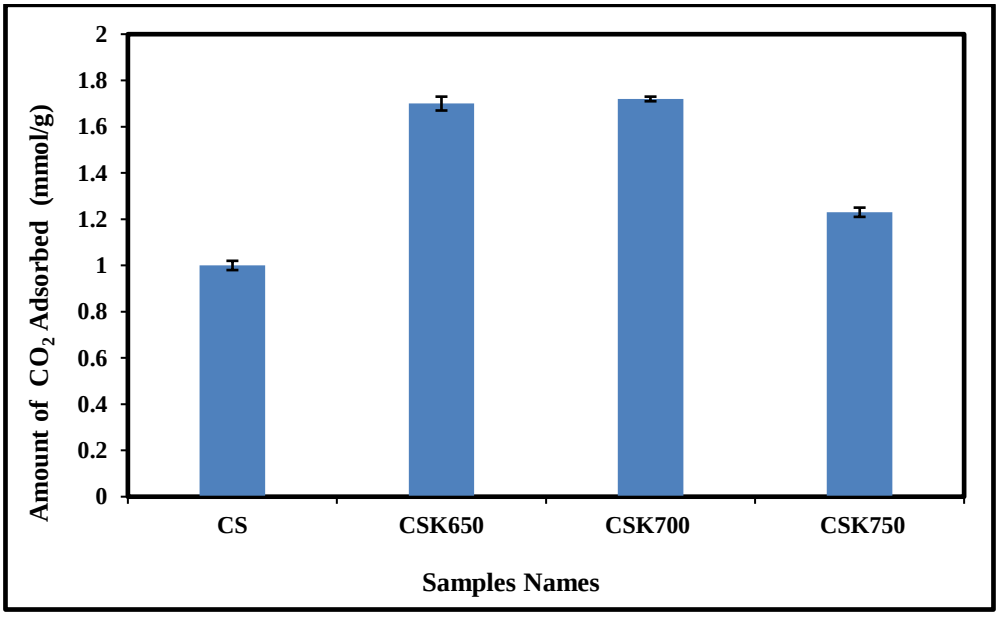


Figure 5. 1: CO_2 adsorption of CS, CSK650, CSK700, and CSK750 at 25 ºC using TGA in 15 % CO_2 and 85 % N_2 at 25 ºC. The mean of triplicate measurements are plotted and the error bars are the difference between the maximum and minimum values.

5.3 Measurement of the Kinetic Adsorption of CO_2

Dry flue gas was used to evaluate the kinetics of CO_2 adsorption on parent and modified ACs (CS, CSK, PR and PRK) in the TGA. The few parameters are defined are defined below:

x %: *The proportion of the CO_2 adsorption capacity to the equilibrium capacity*.

t_x: *Time needed to achieve this proportion where* **x** = 60, 80, 90 %.

The kinetics are relatively fast for all samples (Figure 5.2). The reason behind this could be a high diffusion coefficient of CO_2 in micropores, this having increased after modification (Zárate et al., 2016).

The detailed adsorption kinetics at t_{60}, t_{80} and t_{90} are further reported in Table 5.1. For the CS sample, approximately 1.4 and 2.2 minutes was enough to attain 80 % and 90 % of the CO_2 equilibrium loading capacity (0.80 and 2.23 mmol/g, respectively) while shorter times, 1.2 and 1.7 minutes, were enough to achieve this on the PR sample (0.59 and 0.65 mmol/g, respectively). This outcome confirms the results obtained by Rashidi et al. (2013) who showed that just short contact times are needed to achieve high values of x %.

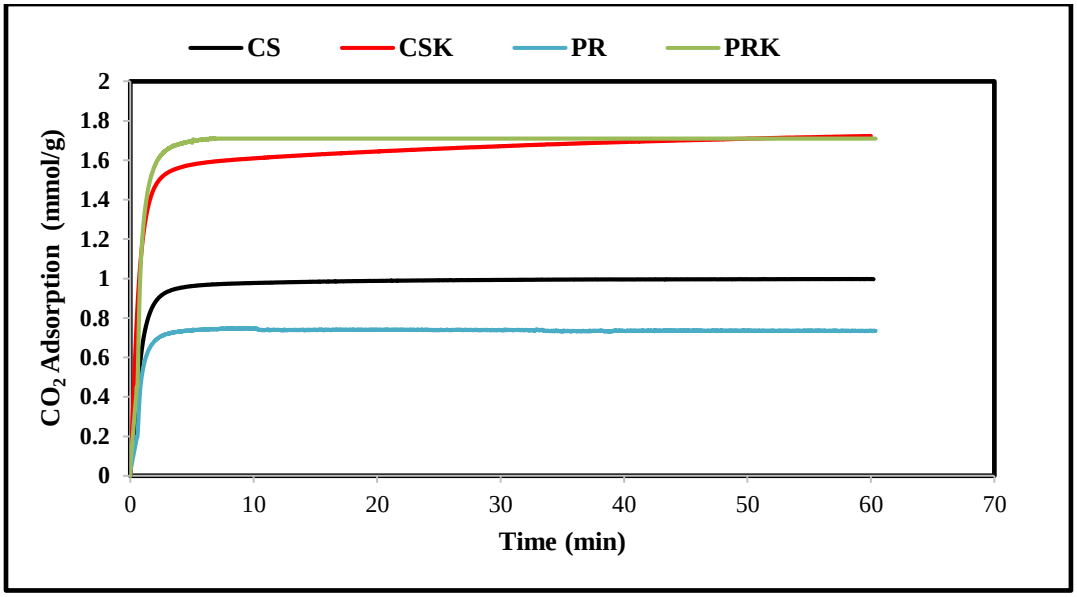


Figure 5. 2: CO_2 adsorption for the ACs using TGA in 15 % CO_2 and 85 % N_2 at 25 ºC.

Table 5. 1: Comparison of adsorption time of CO_2 for ACs using TGA in 15 % CO_2 and 85 % N_2 at 25 ºC.

Sample	Adsorption time of CO_2 (minutes)		
	t_{60}	t_{80}	t_{90}
CS	0.86	1.48	2.23
CSK	0.76	1.52	3.72
PR	0.82	1.20	1.66
PRK	0.81	1.22	1.80

After KOH treatment, the CO_2 adsorption of KOH-activated carbons was markedly enhanced and the kinetics was slightly slower, i.e. CSK and PRK achieved 80 % of equilibrium at 1.52 and 1.22 minutes respectively, and 90 % of equilibrium at 3.72 and 1.80 minutes. These results provide strong evidence for the role of K^+ ions in changing the surface chemistry of activated carbon. Although the introduction of OK-surface groups leads to the increase in levels of fine porosity, it also promotes the formation of O_2 functionalities on the AC surface by forming semi-chemical bonds, giving rise to highly polarised carbon surfaces (Liu, 2017).

5.4 Measurement of the Static & Dynamic Adsorption of H_2O

The adsorption isotherm data for H_2O on the same samples were tested by DVS. As shown in Figure 5.3, CS, CSK, PR and PRK samples exhibited a type IV isotherm according to the Brunauer classification (desorption data omitted for clarity).

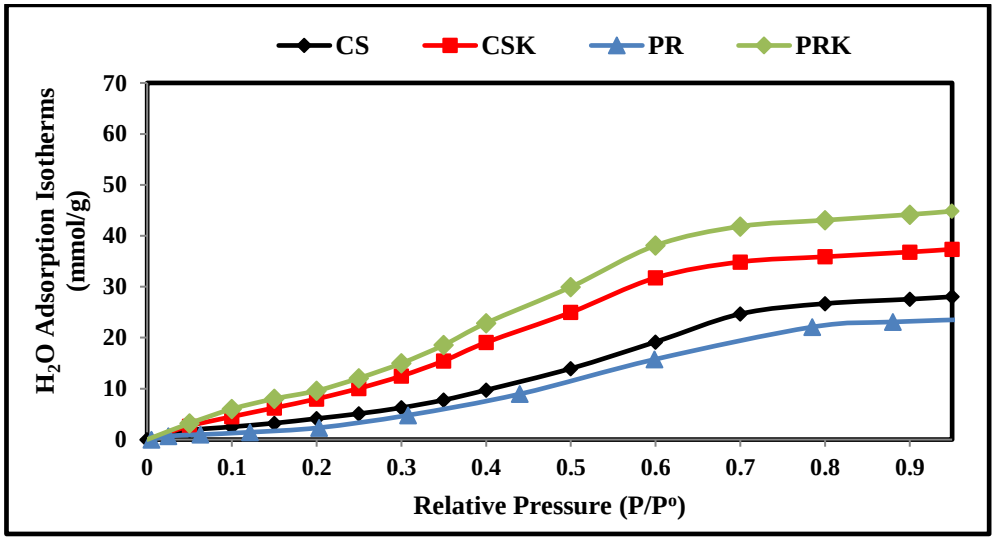


Figure 5. 3: H_2O adsorption isotherms of the ACs using DVS in 100 % N_2 at 25 ^oC.

As part of the adsorption mechanism of water onto active carbons, the hydrogen bonds between water vapour and surface functional groups (primary active sites) can create a film of water on the activated carbon surface at low relative pressure, as well as entering the pores with increasing pressure (Budarin et al., 2000, Mowla et al., 2003, Cosnier et al., 2005). Indeed, water molecules showed preferential adsorption on the CSK and PRK at low partial pressure ($P/P^o \leq 0.2$). The high adsorption of H_2O on the KOH-activated carbons can be attributed to the high density of hydroxyl groups (hydrophilic surface functions) on their surfaces which has increased as a result of the transformation of OK into OH groups during the washing process (Wang and Kaskel, 2012, G Plaza et al., 2015). Through increasing

relative pressure up to 0.7, the resulting attached molecules serve as secondary adsorptive sites for formation of clusters. The critical size of these clusters enables them to have sufficient dispersive energy to fill the carbon pores (Gregg and Sing, 1982, Budarin et al., 2000, Do and Do, 2000).

At high relative pressure ($P/P^o > 0.7$), there was not much difference in the trends of isotherms between the parent and modified activated carbons, and the modified samples maintained high adsorption uptakes. This suggests that extremely high level of micropores comprise the major proportion of the surface area for all samples, and the CSK and PRK samples have higher BET surface area (see Table 4.3).

At high relative pressures ($P/P^o = 0.95$), CS gave H_2O uptake of 28 mmol/g and CSK an uptake of 37 mmol/g. A large difference was observed between PR and PRK samples where H_2O uptake increased from 23.7 to 44.8 mmol/g respectively, indicating that the PR sample was more affected by intercalation of potassium than the CS sample. The comparative analysis of the H_2O isotherms and the textural characteristics of the samples has already shown that the H_2O uptake process depends on the surface chemistry of activated carbon rather than porosity. These results are consistent with those previously reported by Alcañiz-Monge et al. (2002) where the surface chemistry of some activated carbons was the significant factor in the H_2O uptake on these samples.

The kinetic H_2O sorption profiles of these samples at 10 %, 50 % and 95 %RH were obtained using DVS. As can be seen from the kinetic adsorption profiles in Figure 5.4 at 10 %RH, Figure 5.5 at 50 %RH and Figure 5.6 at 95 %RH, intercalation of

K^+ led to increasing H_2O loading for CSK and PRK, In general, under different relative humidities, the H_2O uptake reached equilibrium on PRK in less than 30 minutes while CSK required 220 minutes to get to the same point, and the amount of H_2O adsorbed was increased by increasing relative humidity for all samples.

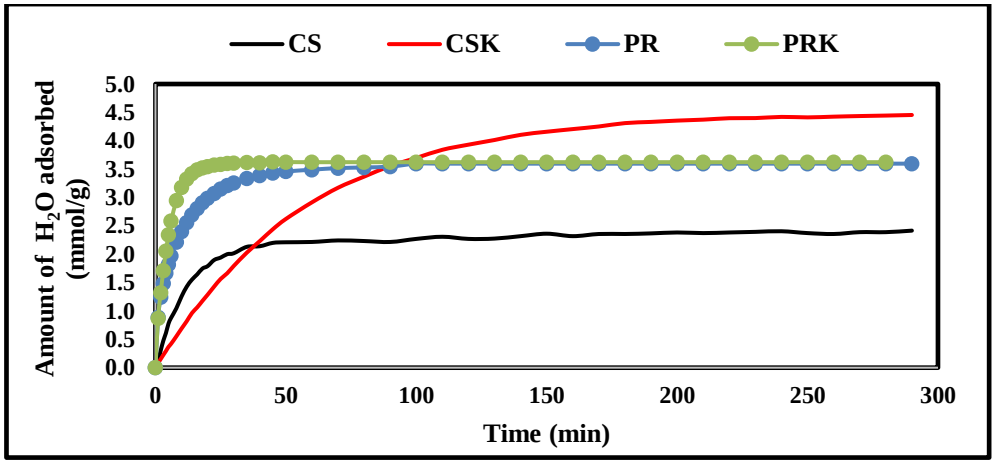


Figure 5. 4: H_2O uptake of the CS, CSK, PR, and PRK 10 %RH using a DVS in 100 % N_2 at 25 ^oC.

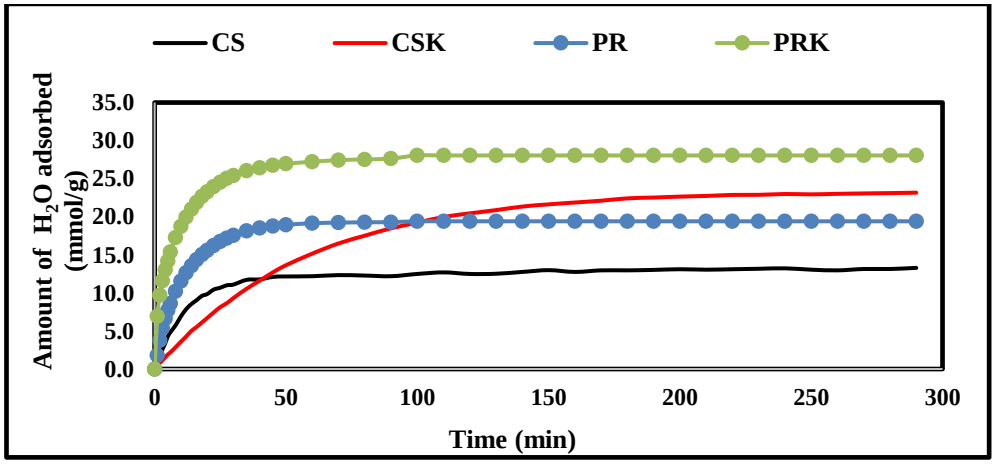


Figure 5. 5: H_2O uptake of the CS, CSK, PR, and PRK 50 %RH using a DVS in 100 % N_2 at 25 ^oC.

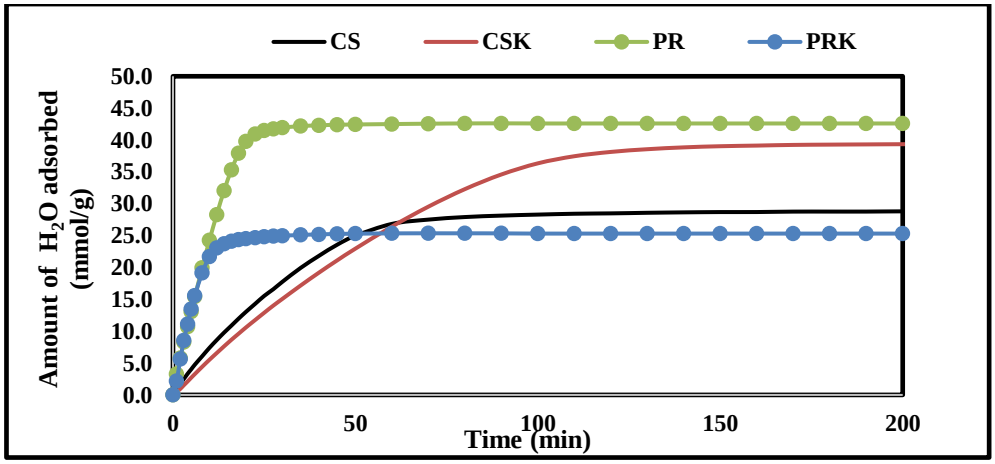


Figure 5. 6: H_2O uptake of the CS, CSK, PR, and PRK 95 %RH using a DVS in 100 % N_2 at 25 ^oC.

As indicated in Table 5.2, at 10 %RH and after10 minutes (typical residence time in fluidised and moving bed absorbers), the amount of H_2O adsorbed for CS was 1.25 mmol/g, and about half of this amount (0.69 mmol /g) had been adsorbed by CSK. In addition, the same percentage decrease was observed at 50 %RH. At 95 %RH, the adsorbed H_2O for CS and CSK was 7.40 and 5.52 mmol /g, respectively.

In contrast, PRK samples exhibited higher H_2O uptake than the initial activated sample at all relative humidities. Liu (2017) attributed increasing the adsorption kinetics of PRK to the increasing of -OK groups, which provide more surface adsorption sites for the oxygen-hydrogen interaction. However, the adsorption of H_2O on the CSK displays different and abnormal behaviour to the CS under all relative humidities, as the hydrophilicity of CSK requires a longer time to be more effective. In addition to the surface chemistry, some factors such as bridging among water molecules, the movements of water molecules deep into the adsorbents and the adsorbent structure may have an effect on the rate of the adsorption process of water (Rodriguez-Reinoso et al., 1992).

Table 5. 2: H_2O adsorption of the samples at different RH (10 %, 50 % and 95 %) after 10 minutes using DVS in 100 % N_2 at 25 ^oC.

	H_2O adsorption (mmol/g)		
Sample	**RH%**		
	10 %	**50 %**	**95 %**
CS	1.25	6.91	7.40
CSK	0.69	3.42	5.52
PR	2.40	11.50	14.57
PRK	3.17	18.70	24.28

5.5 Selectivity for CO_2

The selectivity ratio of the CO_2 capacity to H_2O is calculated as follows:

$$S_{(CO2/H2O)} = Adsorption\ CO_2\ (mmol/g) / Adsorption\ H_2O\ (mmol/g)$$

In this work, the selectivity ratio for the samples was evaluated after a period of 10 minutes. As shown in Figure 5.2 and Figure 5.4, the adsorbents became nearly saturated after 3 minutes with CO_2 while H_2O uptake was still in the early stages. These outcomes agree with the results obtained by Plaza et al. (2014). The increases in concentration of OH groups and in the polarity of the activated carbon surface as a result of intercalation of K^+ significantly increased the adsorption of CO_2. Thus, CSK and PRK exhibited higher CO_2 / H_2O selectivity than CS and PR. For example, at 10 %RH, the $S_{CO2/H2O}$ of CSK increased by about three times as much as CS to reach 2.37 while that of PRK increased from 0.31 to 0.54, as shown in Table 5.3. This indicates that the performance of KOH-activated carbons was better than that of parent-activated carbons under simulated post-combustion conditions.

Although the same trend was observed at a medium relative humidity (50 %RH), the selectivity values have decreased significantly for all samples, as shown in Table 5.4 due to increases in the adsorption of H_2O. No significant differences in selectivity were observed after testing the samples at 95 %RH (Table 5.5). This indicates that the effect of relative humidity on the adsorption kinetics of H_2O declines after 50 %RH.

Table 5. 3 :CO_2 and H_2O adsorption (10 %RH) capacities and the selectivity ratio of the CS, CSK, PR and PRK after 10 minutes.

Samples	CO_2 adsorption (mmol/g)	H_2O uptake (mmol/g)	$S_{CO2/H2O}$
CS	0.97	1.25	0.77
CSK	1.64	0.69	2.37
PR	0.74	2.40	0.31
PRK	1.70	3.17	0.54

Table 5. 4: CO_2 and H_2O adsorption (50 %RH) capacities and the selectivity ratio of the CS, CSK, PR and PRK after 10 minutes.

Samples	CO_2 adsorption (mmol/g)	H_2O uptake (mmol/g)	$S_{CO2/H2O}$
CS	0.97	6.91	0.14
CSK	1.64	3.42	0.48
PR	0.74	11.50	0.064
PRK	1.70	18.70	0.09

Table 5. 5: CO_2 and H_2O adsorption (95 %RH) capacities and the selectivity ratio of the CS, CSK, PR and PRK after 10 minutes.

Samples	CO_2 adsorption CO_2 (mmol/g)	H_2O uptake (mmol/g)	$S_{CO2/H2O}$
CS	0.97	7.40	0.13
CSK	1.64	5.52	0.29
PR	0.74	14.57	0.051
PRK	1.70	24.28	0.070

5.6 Conclusions

CSK and PRK samples that were activated at 700 ^{o}C exhabted the best preformance towred CO_2 adsaorption (around 1.7 mmol/g) and considered the best candidates for further invistigations. Testing the CO_2/H_2O selectivities of CS, CSK, PR and PRK samples after 10 minutes showed that all samples were negatively affected by increasing the relative humidity up to 95 %. The highest selectivity was obtained by CSK (2.37). While water molecules are firmly adsorbed by PR and PRK after 10 minutes, CSK has shown unique adsorption behaviour for H_2O over all relative humidities with lower amounts of H_2O were adsorbed by this sample. For instance, at 10 %RH, only 0.69 mmol/g of H_2O has been adsorbed on CSK, representing half the amount of H_2O adsorbed on the parent CS. The selectivity reduced after 50 %RH for all samples, but CSK still the best. Based on the above, CSK samples can be considered more suitable for use in post-combustion CO_2 capture.

Chapter 6: CO_2 & H_2O Adsorption Capacities of Physically and Organosiloxane Compounds-treated KOH-Activated Carbons

6.1 Introduction

The KOH-activated carbons (CSK and PRK) were modified both by physical treatment, by raising the temperature to 900 ^oC, and by organosiloxane compound treatment. This involved two steps: (1) grafting five different organosiloxane compounds to increase the surface hydrophobicity, and (2) thermal treatment of coated samples, at temperatures between 300 ^oC to 600 ^oC, to reduce their hydrophobic effects and maximise the amount of CO_2 adsorption. The procedure has been explained in Section 3.2.1. 2. The CO_2 and H_2O equilibrium capacities for the parent and modified samples, determined by TGA, are discussed in this chapter. Furthermore, CO_2 adsorption kinetics on the physically treated samples are addressed in this chapter while the Chapter 7 will present the CO_2 and H_2O adsorption kinetics in more detail on the chemically treatment samples having the highest CO_2 adsorption capacities.

6.2 Effect of Physical and Organosiloxane Compounds Treatment on CO_2 Adsorption Capacity of KOH-Activated Carbons

6.2.1 Coconut Shell-Activated Carbon

6.2.1.1 Physical Treatment

CO_2 adsorption was evaluated for the CSK, CSKN700 and CSKN900 samples using TGA (see Section 3.3.1.1). Compared to CSK, the results revealed that the reductions in the amount of adsorption CO_2 at 700 ^oC and 900 ^oC were 19 % and 37 % respectively, as shown in Figure 6.1. The decrease in porosity and the decomposition of surface hydroxyl groups (as mentioned in Section 4.3.1) may have contributed to the decrease in adsorption capacity of CO_2. The best result obtained was 1.4 mmol/g at 700 ^oC (CSKN700). As the errors in Figure 6.1 are small (<0.02 mmol/g) compared with the relative difference in CO_2 adsorption between samples (0.3 mmol/g), this indicates a good level of confidence in the performance of the samples. No more tests will be run on other samples, which are modified under the same conditions. The kinetics and adsorption of these samples are shown in Appendix C, no significant difference between the kinetics of these CSK samples were observed.

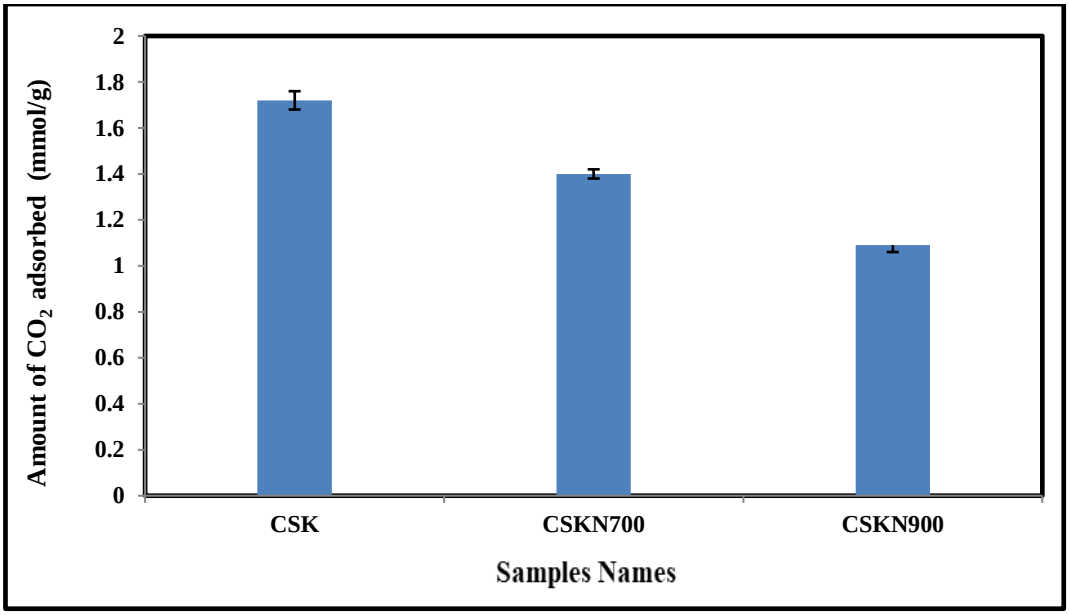


Figure 6. 1: CO_2 adsorption of CSK, CSKN700 and CSKN900 with error bars using TGA in 15 % CO_2 and 85 % N_2 at 25 ^oC. The mean of triplicate measurements are plotted and the error bars are the difference between the maximum and minimum values.

6.2.1.2 Organosiloxane Compound Treatment

The performances of five organosiloxane compounds (VTMOS, OTES, POTS, HDTMS and PTES) were evaluated according to their CO_2 adsorption on the CSK sample. The samples are designated CSKV, CSKO, CSKF, CSKH and CSKP using the first letter of the organosiloxane compounds. Firstly, in order to determine the best concentration of organosiloxane to use for coating, VTMOS and PTES were selected and mixed with different concentrations in toluene (1 %, 5 %, and 10 % v/v) following the procedure that was described in Section 3.2.1.2. CO_2 and H_2O uptakes were determined. As expected, the sample that was coated with low amount of VTMOS (1 %) showed the highest CO_2 adsorption at 0.70 mmol/g (Figure 6.2) and the highest H_2O uptake at 4.41 mmol/g (Figure 6.3), where the higher concentrations of VTMOS completely block the pores.

Increasing the concentration of VTMOS in toluene from 1 % to 5 % reduced CO_2 and H_2O adsorption capacities to 0.44 mmol/g and 3.94 mmol/g, resepctively. Increasing the VTMOS concentration further from 5 % to 10 %, reduced H_2O uptake further to 2.61 mmol/g. A very similar trends were obtained with PTES as shown in Figure 6.3. Taking into account the high cost of organosiloxane compounds (about £10 per 100 ml VTMOS and £70 per 50 g PTES from Sigma-Aldrich Company UK), a 1 % solution in toluene was selected for the comparative study.

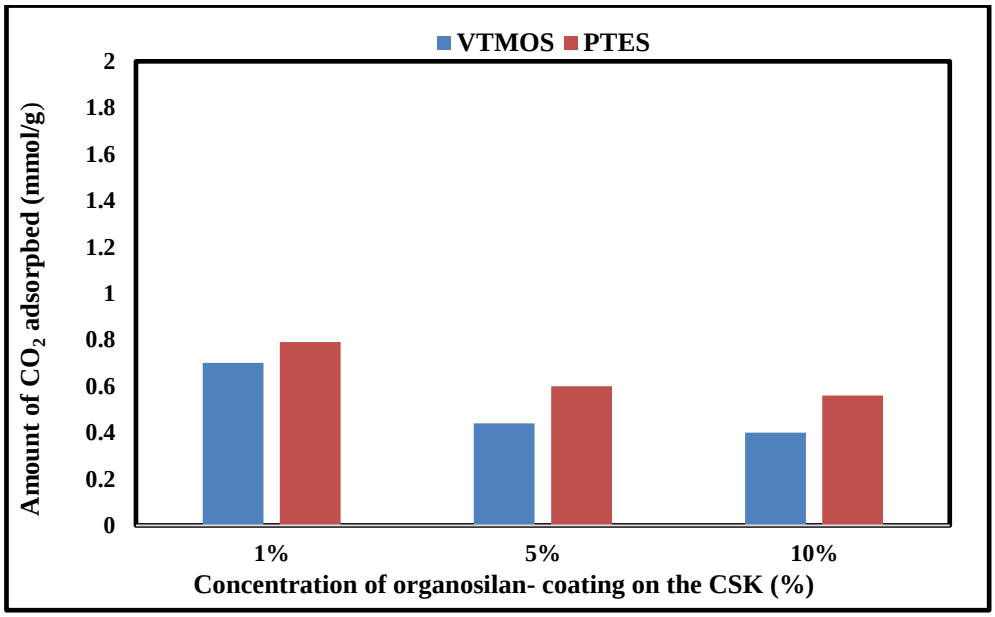


Figure 6. 2: CO_2 adsorption capacities of the CSK sample after coating with different concentration of VTMOS and PTES using TGA in 15 % CO_2 and 85 % N_2 at 25 ºC.

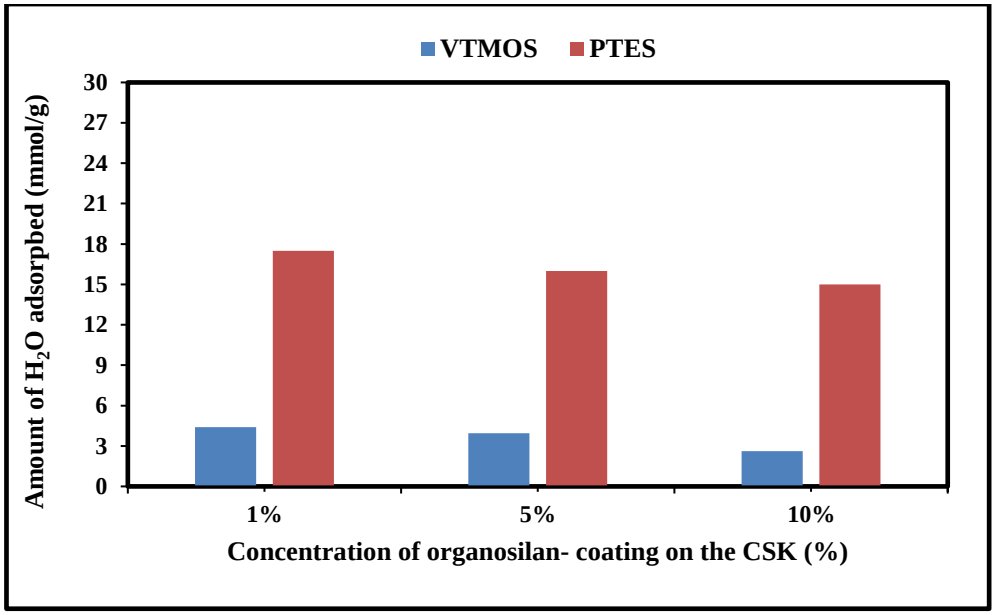


Figure 6. 3: H_2O uptake capacities of the CSK sample after coating with different concentration of VTMOS and PTES using TGA in 100 % N_2 at 25 ^oC and close to 100 %RH.

For coated CS with the different organosiloxane compounds, the resulting CO_2 adsorption capacities are given in Figure 6.4 and the samples follow the order: CSKP > CSKF > CSKV >CSKO > CSKH. It can be seen that the blocking the surface active sites with the coatings reduced the CO_2 adsorption by over 50 % in all cases. The aromatic ring in PTES had a little effect on the activated carbon surface due to presence the phenyl groups that provide additional sites for CO_2 adsorption. Thus, the interaction between the CSKP surface and CO_2 was more active compared to other coated samples, the CO_2 adsorption capacity was 0.79 mmol/g. Although the long non-polar chain in HDTMS could increase the resistance of CSKH to the diffusion of CO_2 molecules in the carbon pores .Therefore the lowest amount of CO_2 (0.6 mmol/g) was adsorbed on this sample. For the other organosiloxane compounds - OTES, VTMOS and POTS - the reduction in CO_2

adsorption capacity were broadly proportional of the size bulky groups (linear C=8, methylene and flurine group)

No obvious correlation was found between CO_2 adsorption capacity and the surface area or porosity of the coated adsorbents (Table 4.4). For example, the adsorption capacity of CSKO, which has a surface area of 1135 m^2/g, was found to be less than that of CSKP which has a lower surface area of 1005 m^2/g. Similarly, CSKH showed better performance than CSKV despite having a lower surface area. There is a high level of confidence in the performance of the samples, since the errors in Figure 6.4 are small (<0.03 mmol/g) compared with the relative difference in CO_2 adsorption between coated samples (0.1 mmol/g). The mean and error bars are calculated in the same manner as for Figure 6.1 above.

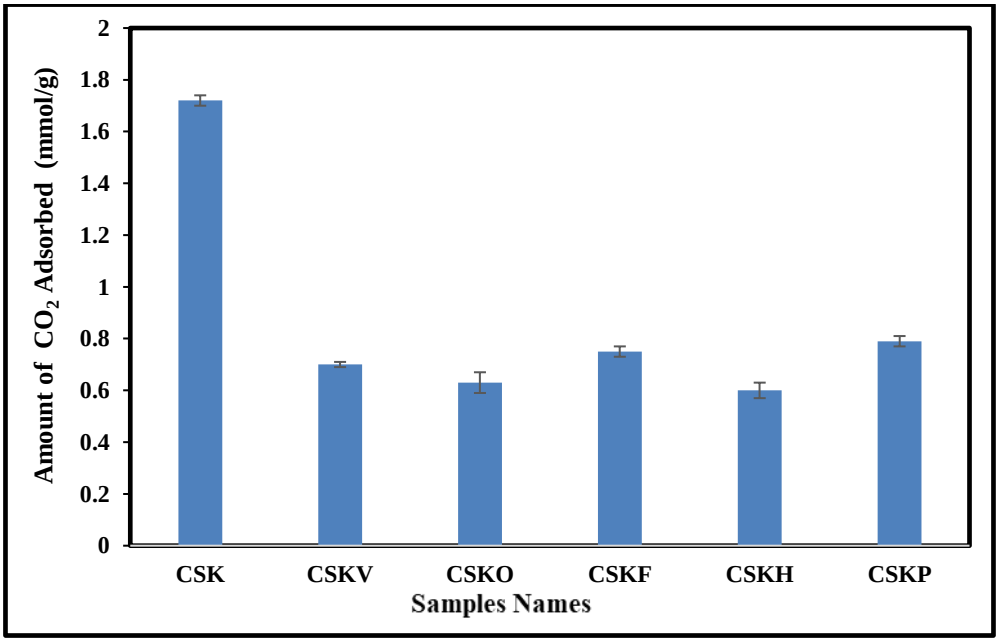


Figure 6. 4: CO_2 adsorption capacities of CSK and coated CSK samples using TGA in 15 % CO_2 and 85 % N_2 at 25 ºC. The mean of triplicate measurements are plotted and the error bars are the difference between the maximum and minimum values.

6.2.1.3 The Influence of Heat Treatment on the CO_2 Adsorption Capacities of the Organsiloxane-Coated Samples

The coated CSKV series treated at different temperatures (300-600 ^oC) was investigated to study the effect of heat treatment on CO_2 adsorption. By and large, the results presented in Figure 6.5 and Table 4.6 indicate increasing CO_2 adsorption capacities through development of surface area up to the optimum temperature of 500 ^oC, after which a slight decrease occurs (Figure 6.5). The mean and error bars in Figure 6.5 are calculated in the same manner as for Figure 6.1 above. The kinetics of adsorption of these samples are shown in Appendix C, no significant difference between the kinetics of these samples were seen for CSKs series of samples.

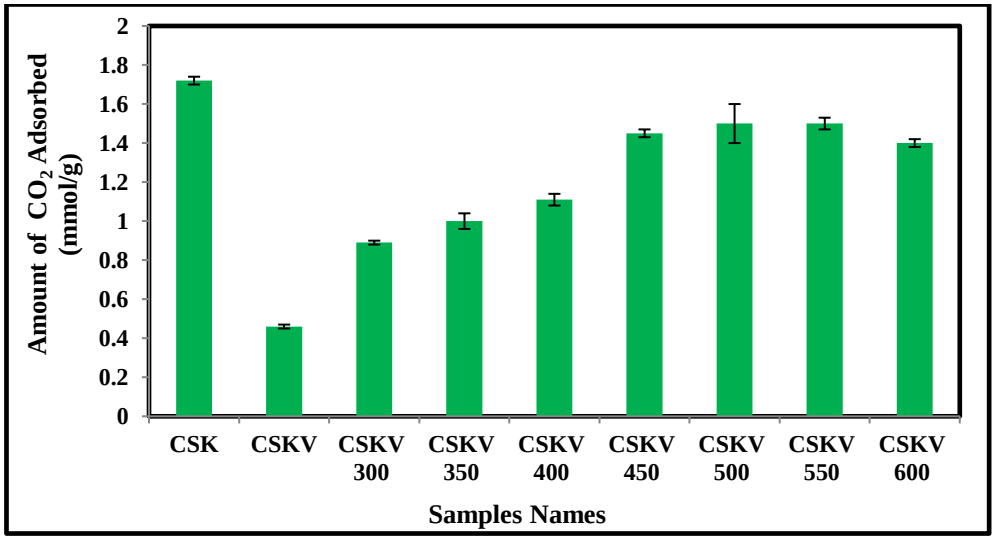


Figure 6. 5: CO_2 adsorption capacities of CSK before and after modification with VTMOS and different temperatures with error bars using TGA in 15 % CO_2 and 85 % N_2 at 25 ^oC. The mean of triplicate measurements are plotted and the error bars are the difference between the maximum and minimum values.

The other coated samples (SCKP, SCKF, SCKO and SCKH) give a very similar trend, as shown in Figures 6.6 to 6.9. Figure 6.10 shows that samples that were heated over the range 450 to 550 ^oC display the highest CO_2 adsorption capacities and approached that obtained for the KOH-activated carbon (CSK = 1.72 mmol/g).

More specifically, the maximum adsorption capacity of CO_2 was 1.66 mmol/g at 500 ^oC for CSKP while CSKV exhibited minimum adsorption capacity of 1.53 mmol/g at 450 ^oC. These results suggest that most of the functionalisation obtained after coating either vaporises or is destroyed at this range, and agree with the results obtained by Cosnier et al. (2005) that referred the thermal treatment of coated activated carbon up to 600 ^oC leads to the removed of most of VTMOS. However, a decrease in CO_2 adsorption was observed between 550 ^oC and 600 °C, providing evidence of a drop in the surface concentration of hydroxyl groups as a result of increasing temperature. The likely effect of increasing temperature in the removing surface hydroxyl groups was consistent with previous findings obtained by Zhuravlev (2000). In conclusion, the experimental results indicate that heat treatment can effectively enhance the CO_2 adsorption on the coated activated carbons and the behaviour of the organosiloxane compounds investigated is similar.

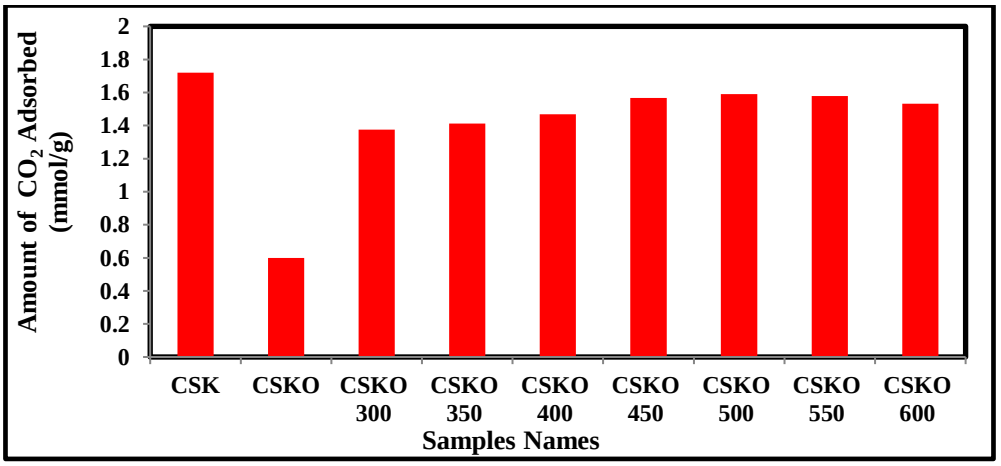


Figure 6. 6: CO_2 adsorption capacities of CSK before and after modification with OTES and different temperatures using TGA in 15 % CO_2 and 85 % N_2 at 25 ^oC.

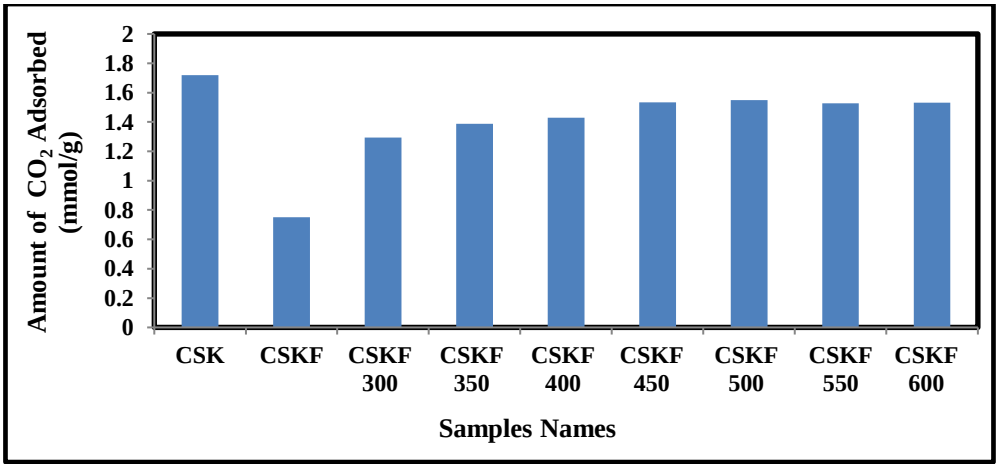


Figure 6. 7: CO_2 adsorption capacities of CSK before and after modification with POTS and different temperatures using TGA in 15 % CO_2 and 85 % N_2 at 25 ºC.

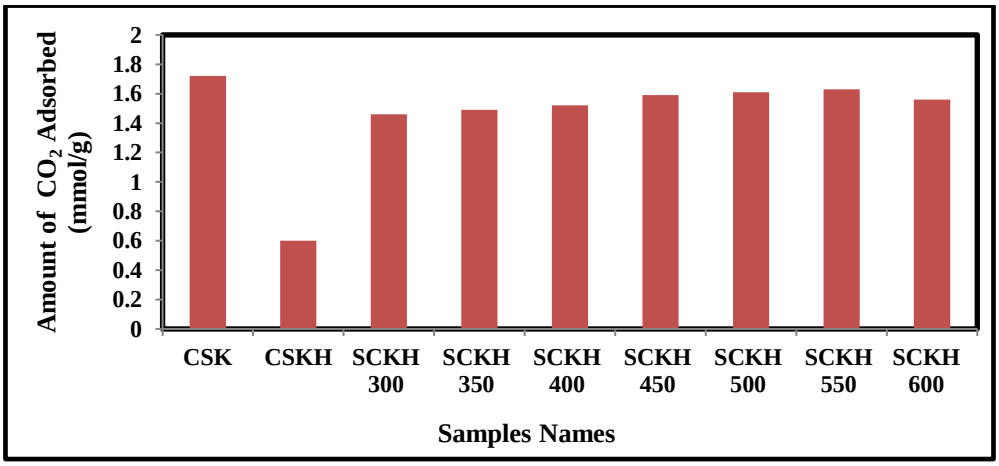


Figure 6. 8: CO_2 adsorption capacities of CSK before and after modification with HDTMS and different temperatures using TGA in 15 % CO_2 and 85 % N_2 at 25 ºC.

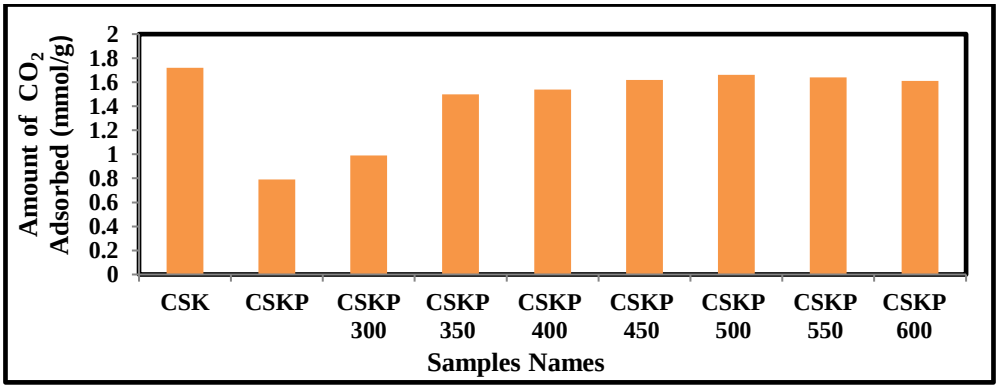


Figure 6. 9: CO_2 adsorption capacities of CSK before and after modification with PTES and different temperatures using TGA in 15 % CO_2 and 85 % N_2 at 25 ºC.

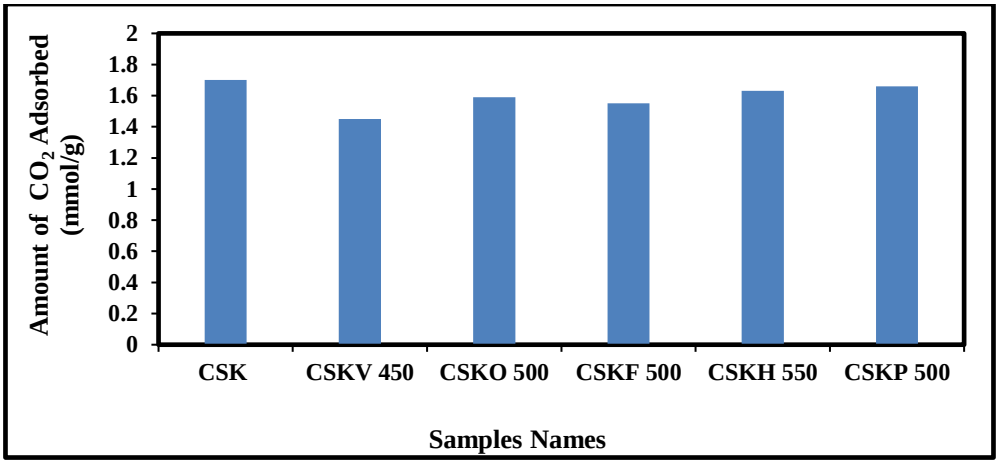


Figure 6. 10: CO_2 adsorption of the best performing coated-heated CSK samples using TGA in 15 % CO_2 and 85 % N_2 at 25 ^oC.

6.2.2 Phenolic Resin-Activated Carbon

The physical and organosiloxane compound treatments were carried out using the same procedures as coconut shell-activated carbon (Section 6.2.1).

6.2.2.1 Physical Treatment

In order to obtain a sample that has a high affinity and selectivity for CO_2, CO_2 adsorption was evaluated on PRK, PRKN700 and PRKN900 samples using a TGA. Compared to PRK, PRK700 and PRK900 have lower CO_2 adsorption capacities, specifically 1.26 mmol/g for PRK700 and 1.03 mmol/g for PRK900 (Figure 6.11) following the same trend as for the CS heat-treated samples. The relatively fast kinetics of CO_2 adsorption for these samples is shown in the TGA profiles presented in Appendix C.

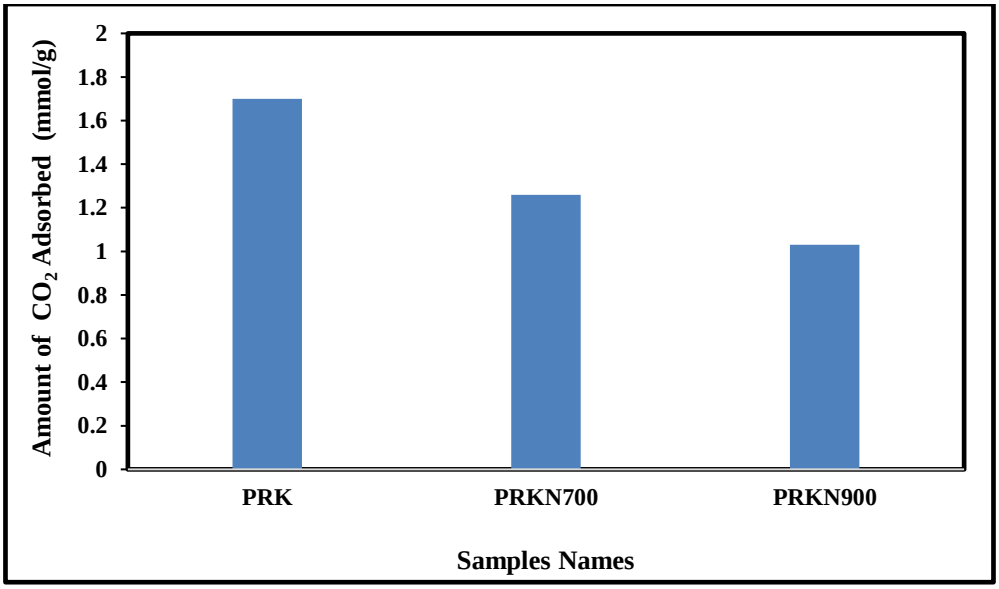


Figure 6. 11: CO_2 adsorption capacities of PRK, PRKN700 and PRKN900 using TGA in 15 % CO_2 and 85 % N_2 at 25 ^oC.

6.2.2.2 Organosiloxane Compounds Treatment

The performances of PRKV, PRKO, PRKF, PRKH and PRKP (that coated with 1% concentration of organosiloxane compounds) were evaluated according to their adsorption of CO_2. The adsorption profiles of the coated adsorbents are presented in Figure 6.12 and the samples followed the order: PRKH>PRKP >PRKF > PRKO > PRKV. For all the samples, the amount of CO_2 adsorbed was less than half the amount adsorbed by the PRK sample. With the exception of the PRKV that exhibited 0.68 mmol/g, the treated samples displayed comparable CO_2 adsorption (around 0.78 mmol/g). More importantly, the lack of correlation between CO_2 adsorption capacity and the surface area or the porosity of the coated adsorbents (Table 4.5) confirms the importance of the surface chemistry for CO_2 adsorption, with the role of organosiloxane-containing groups in reducing the effect of active

groups (-OH) on the activated carbon surface as mentioned previously in Section 6.2.1.2.

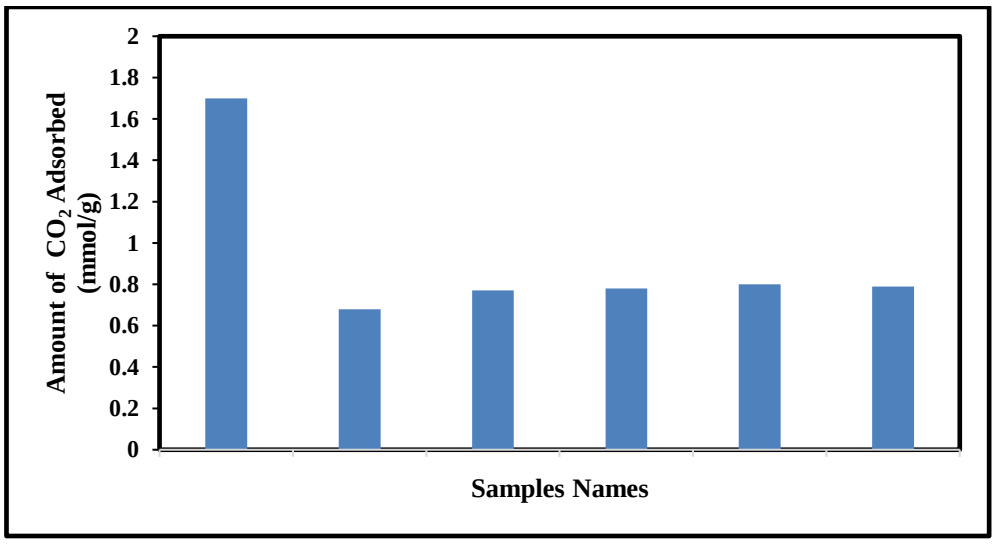


Figure 6. 12: CO_2 adsorption capacity of PRKs series using TGA in 15 % CO_2 and 85 % N_2 at 25 ^oC.

6.2.2.3 The Influence of Heat Treatment on CO_2 Adsorption Capacity

The resulting CO_2 adsorption capacities of all coated samples are shown in Figures 6.13- 6.17. As for the coconut shell samples, CO_2 adsorption capacity increased with increasing temperature. Samples that were heated over the range 450 to 550 ^oC have CO_2 adsorption capacities approaching that of the KOH-activated carbon (PRK=1.7 mmol/g). In general, the effect of heat treatment on the PRKV series was the same as for the CSKV series. In addition, the slight differences observed in the kinetics for these samples are presented in Appendix C.

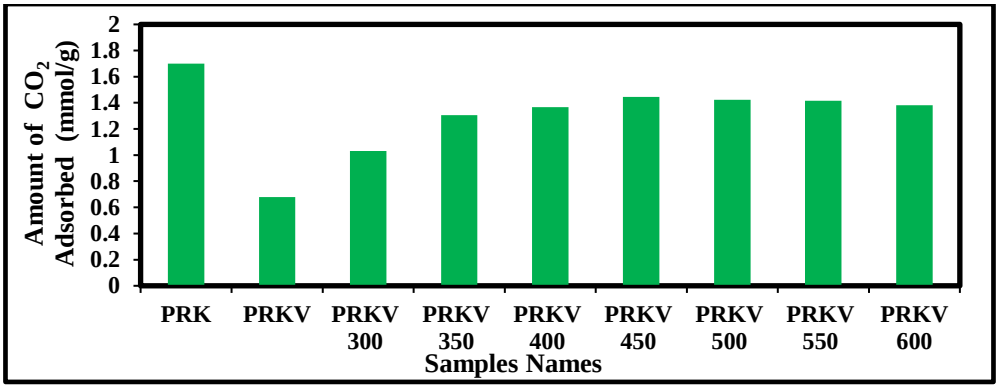


Figure 6. 13: CO_2 adsorption amounts of PRK before and after modification with VTMOS and different temperatures using TGA in 15 % CO_2 and 85 % N_2 at 25 ºC.

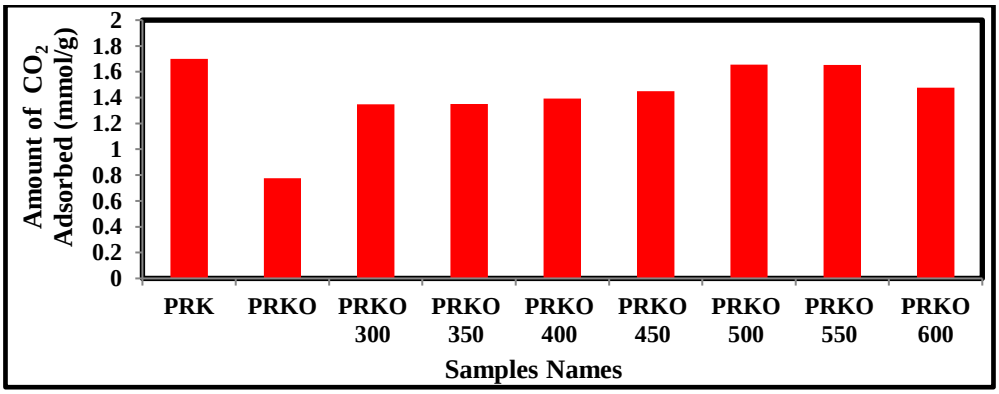


Figure 6. 14: CO_2 adsorption amounts of PRK before and after modification with OTES and different temperatures using TGA in 15 % CO_2 and 85 % N_2 at 25 ºC.

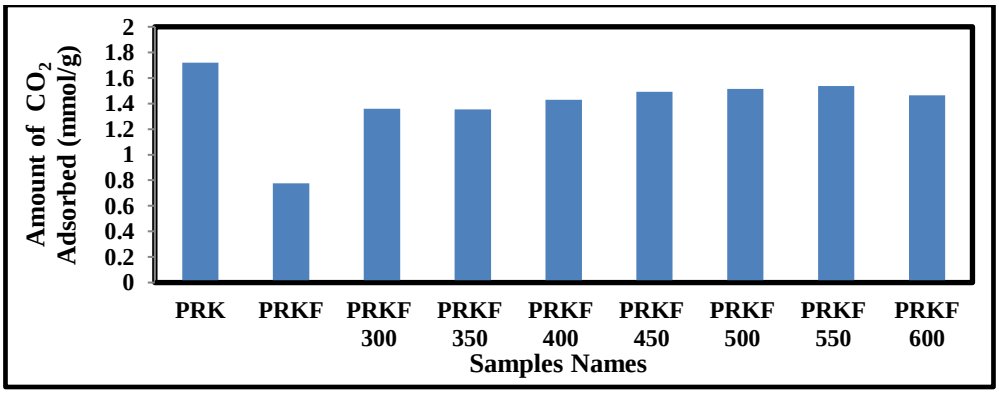


Figure 6. 15: CO_2 adsorption amounts of PRK before and after modification with POTS and different temperatures using TGA in 15 % CO_2 and 85 % N_2 at 25 ºC.

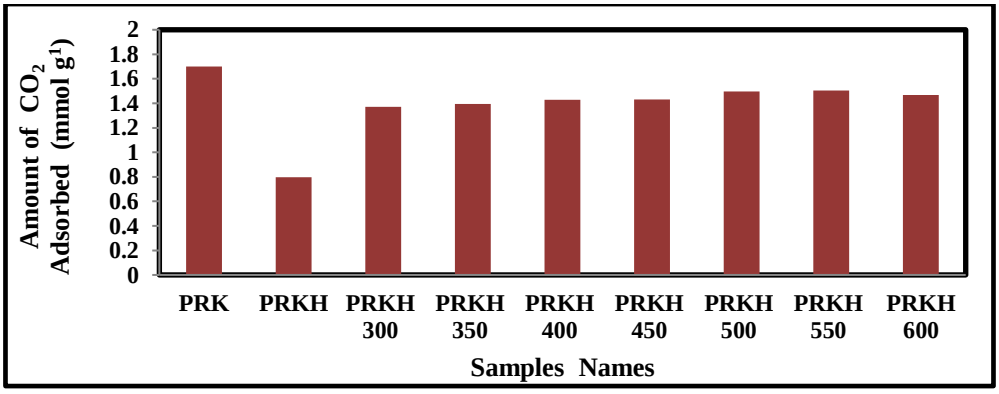


Figure 6. 16: CO_2 adsorption amounts of PRK before and after modification with HDTMS and different temperatures using TGA in 15 % CO_2 and 85 % N_2 at 25 ^oC.

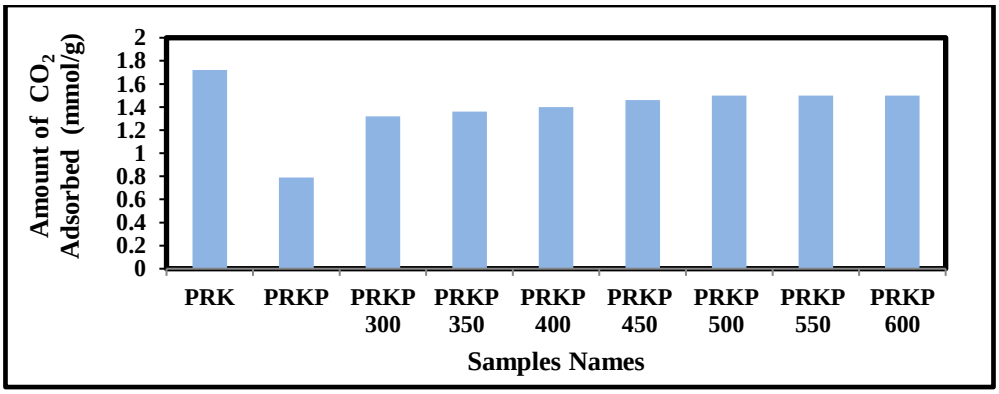


Figure 6. 17: CO_2 adsorption amounts of PRK before and after modification with PTES and different temperatures using TGA in 15 % CO_2 and 85 % N_2 at 25 ^oC.

For the calcined PRKO, PRKF, PRKH and PRKP series were investigated, the highest CO_2 adsorption capacity for each sample is shown in Figure 6.18. There were only small differences between the samples with specifically, the maximum adsorption capacity was 1.66 mmol/g at 500 ^oC for PRKO500 and 1.53 mmol/g at 450 ^oC for PRKV450. However, with increasing temperature, a reduction in CO_2 adsorption was observed at 600 °C as for the CSKV series.

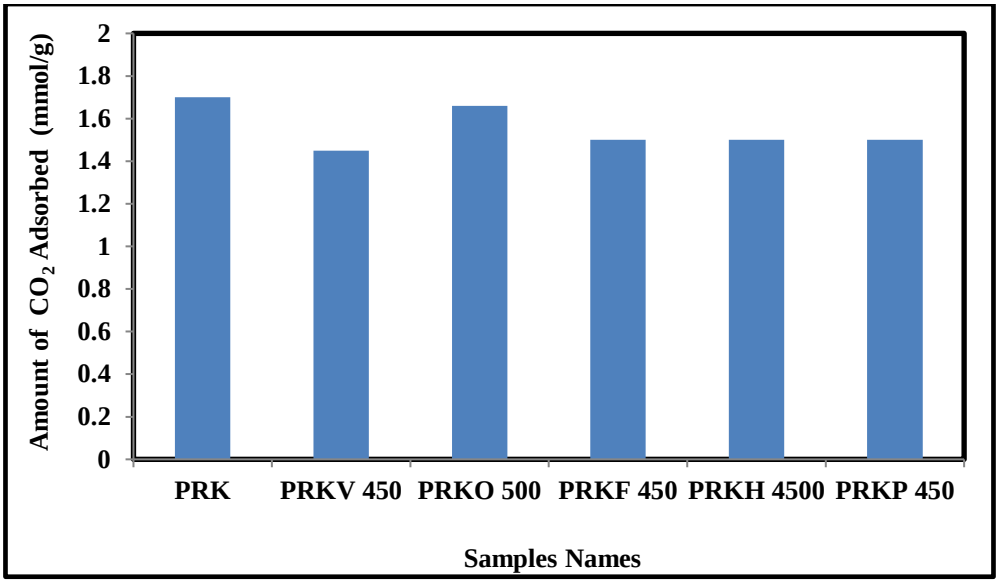


Figure 6. 18: CO_2 adsorption of the best performing coated-heated PRK samples using TGA in 15 % CO_2 and 85 % N_2 at 25 ^oC.

6.3 Effect of Physical and Organosiloxane Compounds Treatments on H_2O Equilibrium Capacities

6.3.1 Coconut Shell-Activated Carbon

6.3.1.1 Physical Treatment

H_2O equilibrium adsorption capacities with close to 100 %RH were evaluated for the CSK700 and CSK900 samples by passing wet N_2 (close to100 %RH) through the TGA (the procedure description in Section 3.3.1), and the results compared with those obtained for CSK. The H_2O equilibrium adsorption capacities for these samples are presented in Figure 6.19, where increasing heat treatment temperatures of up to 900 ^oC led to a decrease of 10 % in H_2O uptake and larger decreases in CO_2/H_2O selectivity. This decline can be attributed to some collapse of pore structure As described by Tazibet et al. (2013). The findings suggest that raising the temperature does not improve H_2O selectivity over activated carbon modified with potassium.

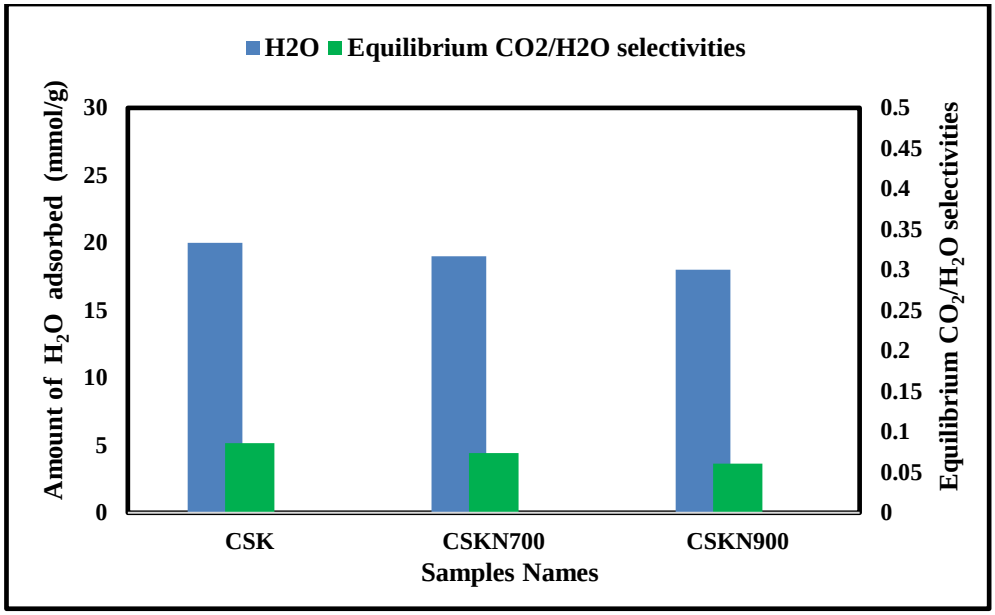


Figure 6. 19: H_2O adsorption capacities and equilibrium CO_2/H_2O selectivities of CSK, CSKN700 and CSKN900 using TGA in 100 % N_2 at 25 ^oC close to100 %RH.

6.3.1.2 Organosiloxane Compound Treatment

H_2O equilibrium capacities of the coated CSK samples (CSKV, CSKO, CSKF, CSKH and CSKP) were evaluated using TGA at close to 100 %RH and the results compared to that obtained for CSK. Coating CSK sample using the different organosiloxane led to decreasing in the amount of H_2O adsorbed on the coated samples as the following order CSKF< CSKP < CSKH < CSKO< CSKV. As shown in Figure 6.20, the amount of H_2O adsorbed by CSKV is approximately three times smaller than that of other samples. This strongly illustrates the effect of VTMOS on the surface polarity of CSs where polar functional groups (OH groups) are majorly affected by hydrophobisation. As a result, the CO_2/H_2O selectivity of CSKV has roughly doubled to 0.15 compared to the CSK sample. For other coated samples, the selectivity has decreased to approximately 0.05 as the adsorption of H_2O decreased to 17.3-15.6 mmol/g.

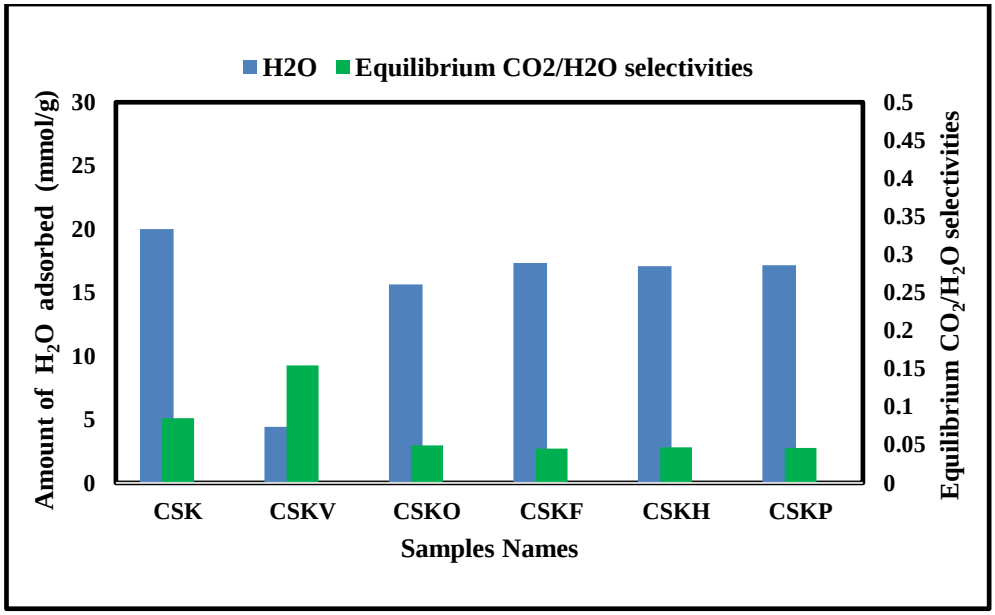


Figure 6. 20: H_2O uptakes and equilibrium CO_2/H_2O selectivities of coated CSKs using TGA in 100 % N_2 at 25 ºC close to 100 %RH.

6.3.1.3 The Influence of Heat Treatment on H_2O Uptakes

The samples that showed the best performance toward CO_2 adsorption (CSKV450, CSKO500, CSKF500, CSKH550, and CSKP500) were tested to evaluate their H_2O uptakes using TGA. The results are compared with the adsorption uptake for CSK in. Figure 6.21. H_2O uptakes of the heat-treated samples ranged from 17 to 19 mmol/g, and these results were close to the measured value for CSK (20.0 mmol/g). With the exception of CSKV450, all the treated samples gave similar H_2O uptakes and this suggested that they had approximately the same polarity and a similar number of active sites. Because of the roughly comparable performances of these samples towards the adsorption of CO_2, H_2O is the crucial factor in selecting the best candidate for practical applications. CSKV450 was considered the best of all tested samples**.** No large differences were observed for the CO_2/H_2O selectivity of the heat-treated samples that were in between 0.77 and 0.85, approaching the

selectivity of CSK. Thus, the modification processes (coating and heat treatment) did not affect drastically effect the CO_2/H_2O selectivity.

The relation between both the CO_2 and H_2O adsorption capacities with the textural properties of the coated CSK samples at ambient temperature and pressure can be found in Appendix E which shows no correlation exists.

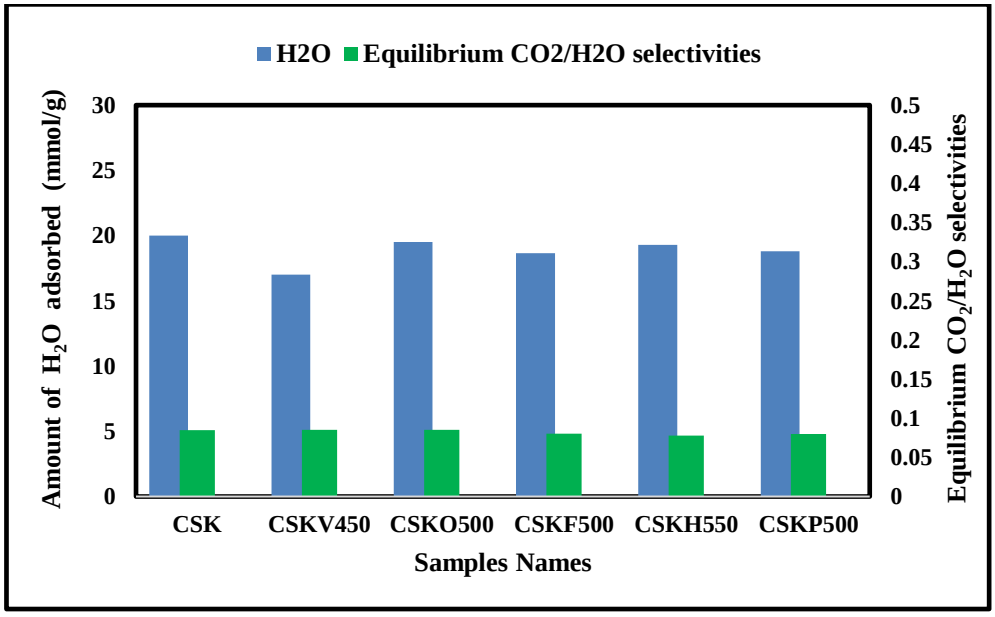


Figure 6. 21: H_2O uptakes and equilibrium CO_2/H_2O selectivities of the best performing coated–heated CSK samples at a different temperature using TGA in 100 % N_2 at 25 ^oC close to100 %RH.

6.3.2 Phenolic Resin-Activated Carbon

6.3.2.1 Physical Treatment

H_2O uptake were evaluated on the PRK, PRK700 and PRK900 samples using the TGA (Section 3.3.1). The H_2O equilibrium capacities for these samples can be seen in Figure 6.22, where increasing heat treatment temperatures up to 900 ^oC led to a decrease of 5 % in H_2O uptake with large decreases in CO_2/H_2O selectivity. The

findings indicate that raising the temperature led to the same trend with that observed using coconut shell-activated carbon.

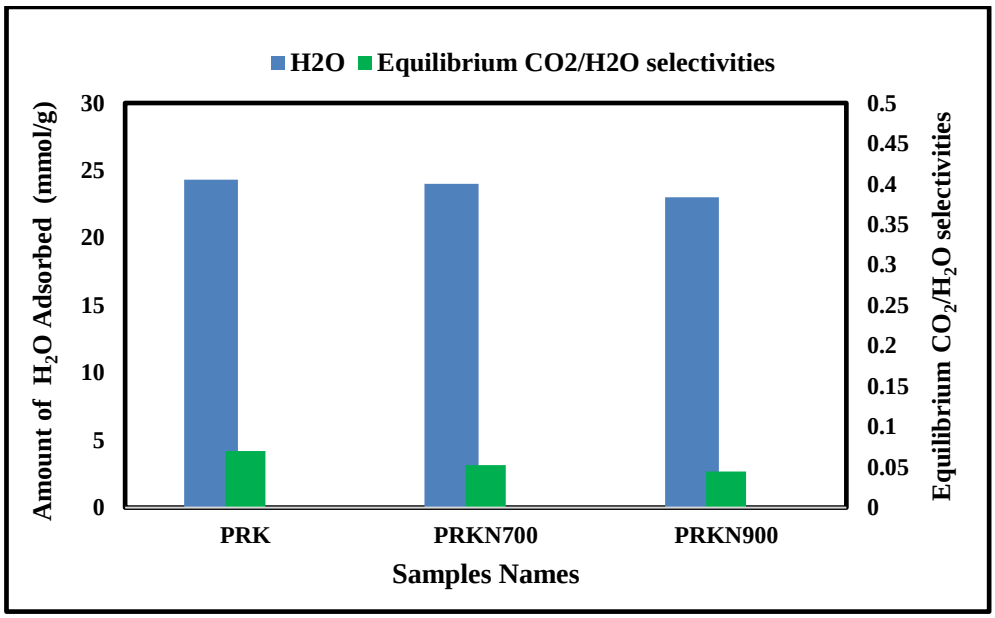


Figure 6. 22: H_2O uptake and equilibrium CO_2/H_2O selectivities of PRK, PRKN700 and PRKN900 using TGA in 100 % N_2 at 25 ^oC close to100 %RH.

6.3.2.2 Organosiloxane Compounds Treatment

H_2O uptake onto PRK and onto various coated phenolic samples (PRKV, PRKO, PRKF, PRKH and PRKP) were evaluated using TGA. As seen in Figure 6.23, the H_2O uptakes resulting for the samples show the order PRKF >PRKP >PRKH > PRKO >PRKV. PCKV gave minimum H_2O uptake of 13 mmol/g while other samples showed values between 18 to 19 mmol/g. This result illustrates similarities in the effects of OTES, POTS, HDTMS and PTES on the surface of the phenolic resin-derived activated carbon.

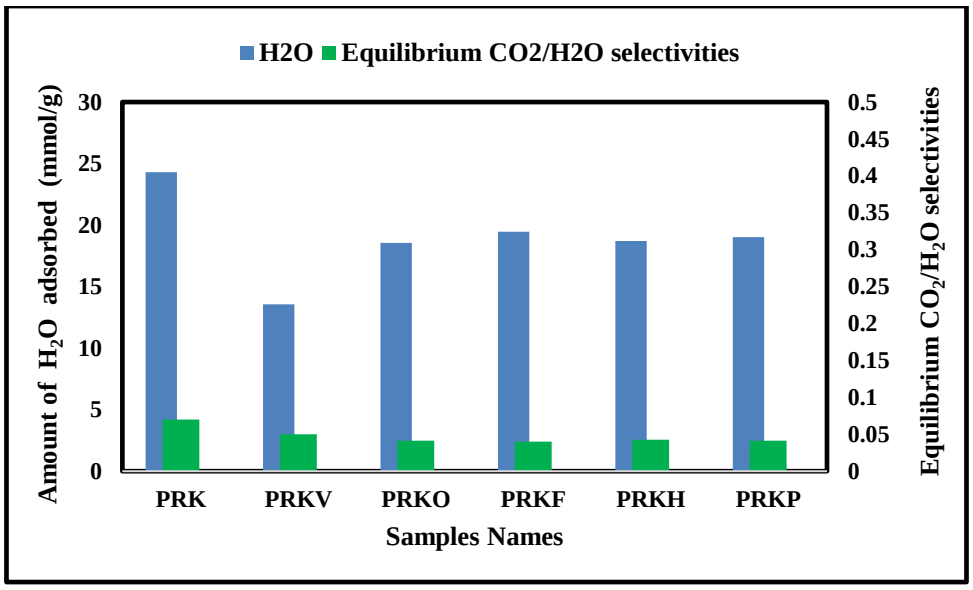


Figure 6. 23: H_2O uptake and equilibrium CO_2/H_2O selectivities of coated PRKs using TGA in 100 % N_2 at 25 ^oC close to100 %RH.

6.3.2.3 The Influence of Heat Treatment on H_2O Equilibrium Capacities

The heat-treated samples that gave the best performance toward CO_2 adsorption (PRKV450, PRKO500, PRKF450, PRKH500, and PRKP450) were then tested to evaluate the H_2O uptakes using TGA. The results were compared to that obtained by PRK. As shown in Figure 6.24, the H_2O adsorption capacities of the heat-treated samples ranged from 21 to 23 mmol/g and these values were close to the measured value for PRK (24 mmol/g). Except for PRKV450, the heat-treated samples showed similar H_2O uptakes (about 0.04 mmol/g).

Because of the roughly comparable performance of these samples toward adsorption of CO_2, H_2O uptake is seen to be the crucial factor in selecting the best candidate for practical applications. Thus, PRKV450 was considered as the best of all tested samples. Overall, the findings indicate that modification of phenolic resin-activated

carbon by coating with different types of organosiloxane compounds and heat treatment did not improve the selectivity of the modified samples.

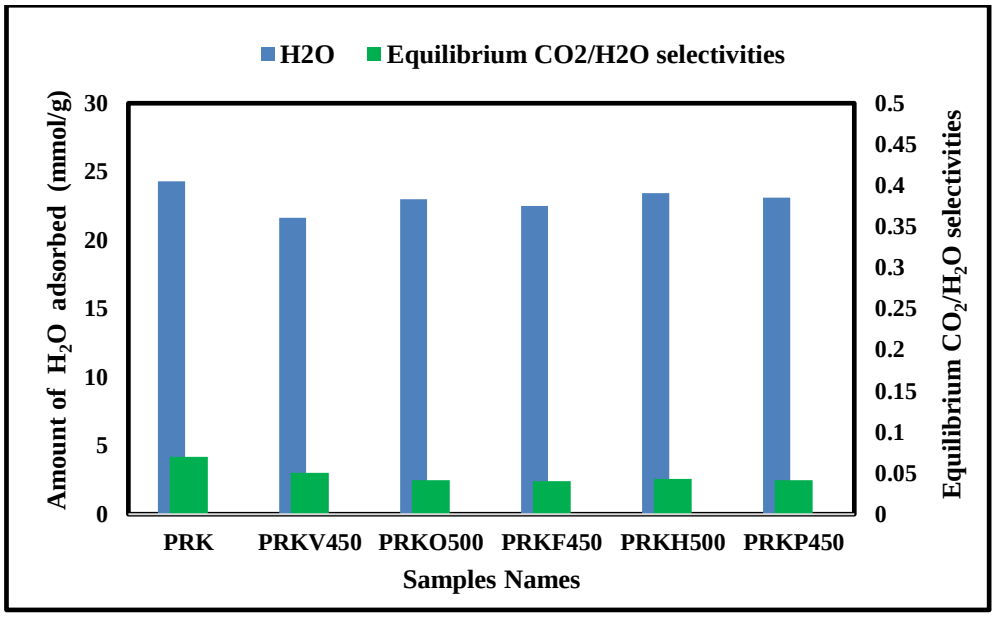


Figure 6. 24: H_2O uptake and equilibrium CO_2/H_2O selectivities of coated-heated PRK samples at a different temperature using TGA in 100 % N_2 at 25 ^oC close to 100 %RH.

6.4 Conclusions

For the two types of activated carbons investigated; CSK and PRK, grafting organosiloxanes on the activated carbon surfaces led to a decrease in the affinity for both CO_2 and H_2O. Therefore, heat treatment was carried out to enhance the CO_2 adsorption while minimising H_2O uptake. Although the CO_2/H_2O selectivities of the KOH-coconut shell-activated carbon and KOH-phenolic resin-activated carbon were roughly maintained after the heat treatment, the results obtained between 450 and 550 ^oC were the best. Compared to other calcined samples, the CO_2 adsorption capacities at 25 ^oC and 1 atm for CSKV450 and PRKV450 were 1.45 mmol/g, while H_2O uptakes of the two samples were in between 13.5 and 17 mmol/g.

CHAPTER 7: Impact of Organosiloxane Coatings on Water Vapour Co-Adsorption for CO_2 Capture on the KOH-Activated Carbons

7.1 Introduction

The general conclusion from the literature is that H_2O molecules strongly compete with CO_2 molecules for active sites located in the pores of sorbent materials (Xu et al., 2013, Canivet et al., 2014, G Plaza et al., 2015). The selectivity of CSKV450 sample that showed lowest H_2O uptake and acceptable CO_2 adsorption is investigated further in this chapter, and compared to other samples (CS, CSK, CSKV) to clarify the highest selectivites over H_2O before and after modification, both from an equilibrium and kinetic standpoint. Furthermore, the impact of preloading of water vapour on CO_2 adsorption has been investigated.

7.2 Measurement of the Dynamic Adsorption of CO_2

Plotting the variation of CO_2 adsorption as a function of time for samples CSKV and CSKV450 using TGA shows that most of the adsorption occurs after 3 minutes (Figure 7.1). The times to obtain 60 %, 80 % and 90 % of the equilibrium capacity, t_{60}, t_{80} and t_{90}, respectively, are reported in Table 7.1. Compared with the results obtained for CS and CSK (Section 5.2), CSKV has lower CO_2 adsorption than CSK due to reduction in the BET surface area of this sample as a result of blocking of

some pores (Section 4.3.2), but the adsorption kinetics of this sample were close to those for CS and CSK, with 80 % of the total CO_2 adsorption capacity within 80 seconds.

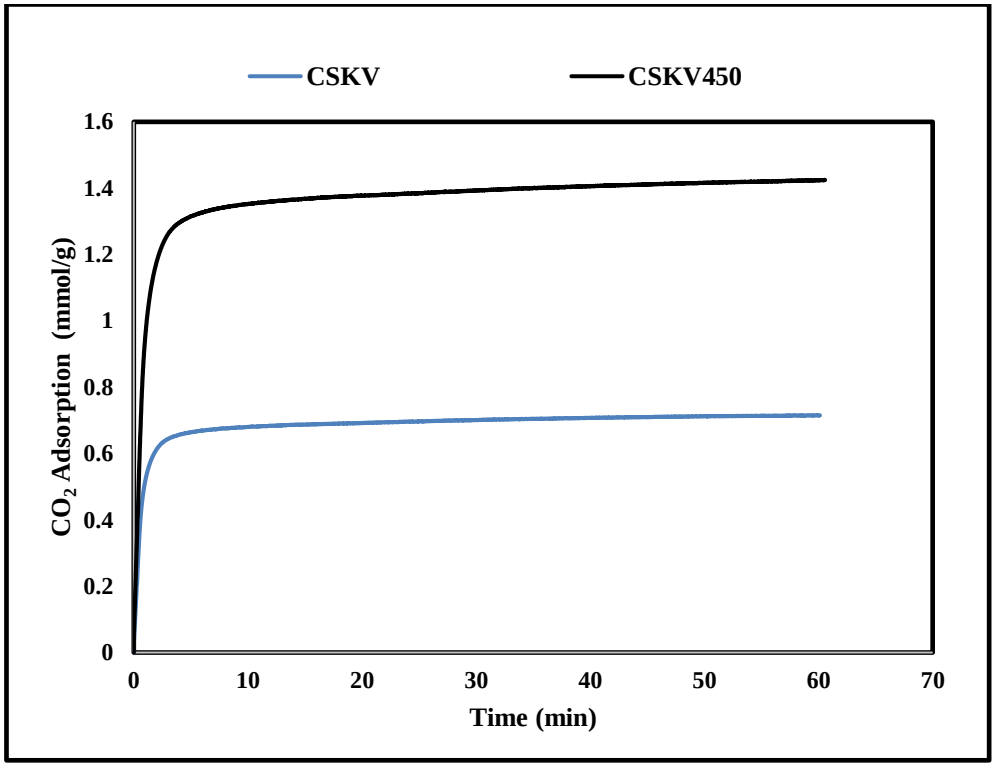


Figure 7. 1: CO_2 adsorption for the CSKV and CSKV450 using TGA in 15% CO_2 and 85 % N_2 at 25 ^oC.

Table 7. 1: Comparison of adsorption times of CO_2 under dry conditions for CSKV and CSKV450 using TGA in 15 % CO_2 and 85 % N_2 at 25 ^oC.

Sample	**Adsorption time (minutes)**		
	t_{60}	**t_{80}**	**t_{90}**
CS	0.86	1.48	2.23
CSK	0.76	1.52	3.72
CSKV	0.68	1.44	2.83
CSKV450	1.37	2.95	16.00

CSKV450 produced a very interesting result; the CO_2 adsorption was markedly increased, and the time needed to achieve this percentage doubled compared to CS, CSK and CSKV, it still did not exceed 3 minutes (Table 7.1). Short contact time is needed for practical applications. Therefore, three minutes can be considered acceptable to achieve 80 % of equilibrium CO_2 adsorption (1.14 mmol/g) compared to the amount of adsorption by CSK (0.80 mmol/g), where the difference was only 0.34 mmol/g. However, adsorption is slow for the final 10 %.

For CSKV450, and as listed in Table 7.2, there is clear difference between the CO_2 adsorption capacity determined by TGA and that tested by static volumetric method (Micrometrics ASAP 2420). With TGA, CO_2 partial pressure at 25 ^oC for 0.15 bar increased 75 % compared to that tested by Micrometrics ASAP 2420, while the percentage increase did not exceed 14 % for other samples at the same conditions. The higher results of CO_2 adsorption equilibrium in TGA may be attributed partly to N_2 co-adsorption.

Table 7. 2: CO_2 adsorption of the activated carbon samples, static vs Dynamic at 0 and 25 ^oC in 0.15 and 1.0 bar of CO_2 partial pressures using ASAP 2420 and TGA.

Samples	ASAP 2420 (Static)				TGA (Dynamic)
	CO_2 adsorption at 0 ^oC (mmol/g)		CO_2 adsorption at 25 ^oC (mmol/g)		CO_2 adsorption at 25 ^oC (mmol/g)
	0.15 bar	1.0 bar	0.15 bar	1.0 bar	0.15 bar
CS	1.63	4.12	1.00	2.70	1.00
CSK	2.45	5.81	1.48	3.81	1.72
CSKV	1.10	4.40	0.63	2.41	0.70
CSKV450	1.56	4.85	0.93	2.72	1.45

7.3 Measurement of the Static Adsorption of H_2O

Following the procedure that was described in Section 3.3.3, the static adsorption equilibrium isotherms for H_2O were measured for the CSKV and CSKV450 samples by DVS. As shown in Figure 7.2 (desorption data omitted for clarity), the CSKV and CSKV450 sample exhibited a type IV isotherm according to the IUPAC classification (Thommes et al., 2015). Although the two samples showed the same shape, there is a big difference in the H_2O uptake between them. For sample CSKV, it seems that the density of functional groups decreased after VTMOS coating. It can be expected the reaction between VTMOS molecules and hydroxyl groups would have a significant effect on the surface chemistry and thus, the CSKV sample would exhibit low uptake.

Compared to CSKV, water molecules showed significantly preferential adsorption on the CSKV450 at low partial pressures ($P/P^o \leq 0.4$). This may be due to removal of some coating layers that blocked a number of active sites (hydrophilic surface functions) on the surface of coated sample, resulting in the formation of a monolayer of water molecules on its surface as a result of the hydrogen bonds between the active sites and the water vapour.

The steep rise of the CSKV450 adsorption isotherm from 0.4 to 0.7 P/P^o indicates that the heat treatment of coated activated carbon tends to shift the H_2O isotherm to high uptake where the attached molecules serve as secondary adsorptive sites for formation of clusters. The critical size of these clusters enables them to have sufficient dispersive energy to fill the carbon pores. The slight rise of the CSKV

adsorption isotherm in this period may refer to a few number of active sites on the surface of coated sample.

At high relative pressures ($P/P^o > 0.7$), there is not much difference in the trends of isotherms. This suggests that extremely high level of micropores and mesopores comprise the major proportion of the surface area for the two samples, and the CSKV450 sample has higher BET surface area (see Table 4.6). At large relative pressures ($P/P^o = 0.95$), the CSKV and CSKV450 samples gave H_2O uptakes of 5.21 and 32.6 mmol/g, respectively.

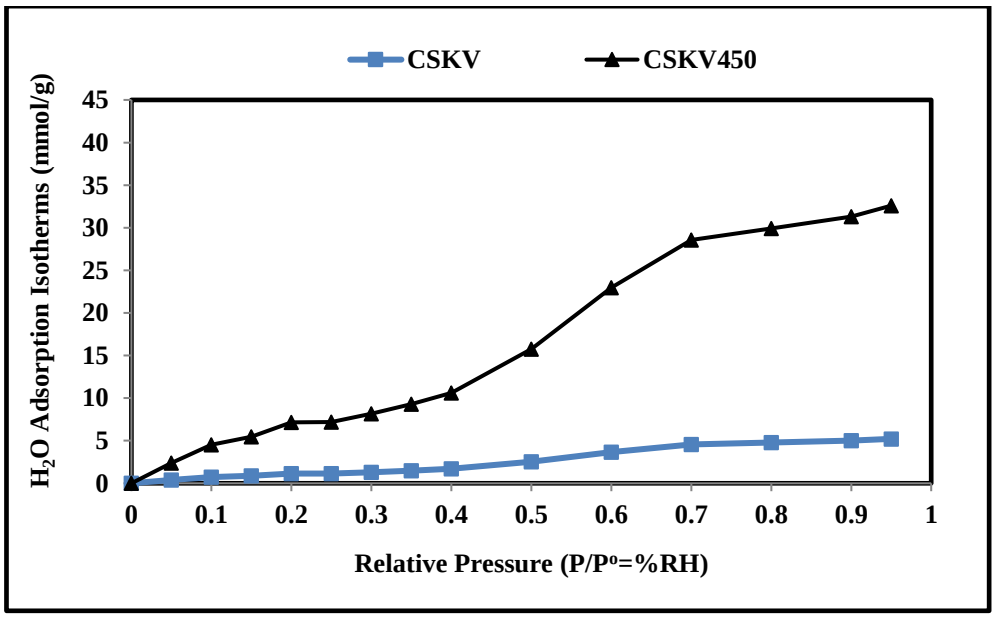


Figure 7. 2: Adsorption isotherms of H_2O for samples CSKV and CSKV450 using DVS in 100 % N_2 at 25 ^oC.

7.4 Measurement of the Dynamic Adsorption of H_2O

Using TGA, the sorption kinetics of H_2O (close to 100 %RH) were measured for CSKV and CSKV450 samples by plotting H_2O uptake as a function of time. After 40 minutes, CSKV sample reached equilibrium due to blocking a lot of pores, while a long time (more than 60 minutes) was needed to reach equilibrium on the CSKV450 as shown in Figure 7.3. According to these findings, it is very clear that the water vapour has a small diffusion coefficient in microporous materials compared to the diffusion coefficient of CO_2 in the same materials (see Figure 7.1). The binding of the VTMOS on the surface of CSK may be achieved through bridging hydroxyls (Cosnier et al., 2005). Therefore, it is expected that the amount of adsorbed H_2O reduces after hydrophobisation, while the heat treatment at 450 ^oC led to the decomposition and volatilisation of a fraction of the grafted VTMOS (see Section 4.4.1.2). This could explain why the adsorption of H_2O increase about 75 % on the CSKV450 after 60 minutes compared to CSKV sample.

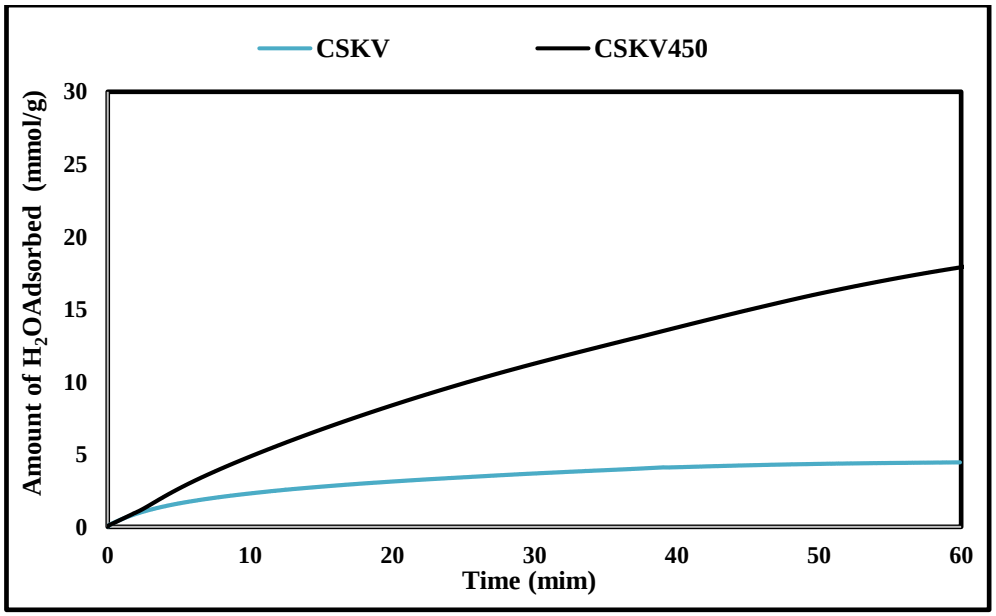


Figure 7. 3: H_2O uptake (close to 100 %RH) for samples CSKV, and CSKV450 at 25 ^oC using TGA in 100 % N_2.

The DVS instrument was also used to obtain the H_2O sorption profiles of the CSKV and CSKV450 at different RH (10 %, 50 % and 95 % respectively). Figures 7.4 to 7.6 illustrate that CSKV has low adsorption capacity and displayed slow adsorption kinetics over different relative humidities. The amounts of H_2O adsorbed were in between 1.5-5.6 mmol/g. After removing thermally some of the coating layer, the heat treatment made the carbon surfaces of CSKV450 more easily affected by relative humidity compared to CSKV. The amount of H_2O adsorbed on CSKV450 has doubled six times to reach 14.8 mmol/g after increasing relative humidity from 10 % to 50 %, and reached 32.1 mmol/g at 95 %RH. In general, under different relative humidities, the H_2O uptake reached equilibrium on CSKV450 in less than 200 minutes while CSKV required just 100 minutes to get to the same point at 10 %RH, and the time has increased with increasing relative humity up to 95 %.

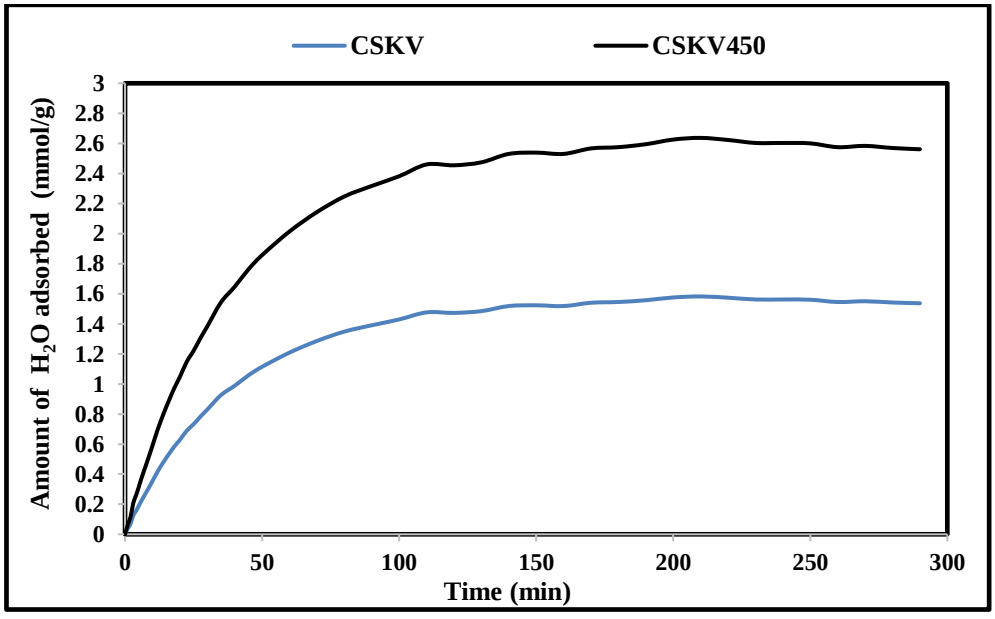


Figure 7. 4: H_2O uptake (10 %RH) for samples CSKV and CSKV450 using DVS in 100 % N_2 at 25 ^oC.

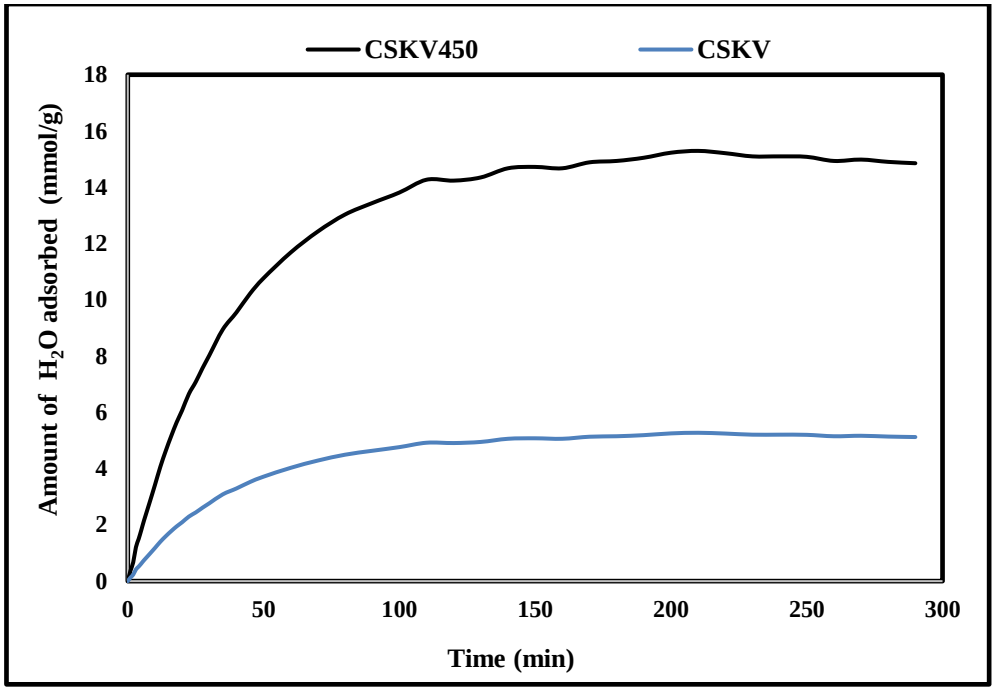


Figure 7. 5: H_2O uptake (50 %RH) for samples CSKV and CSKV450 using DVS in 100 % N_2 at 25 ^oC.

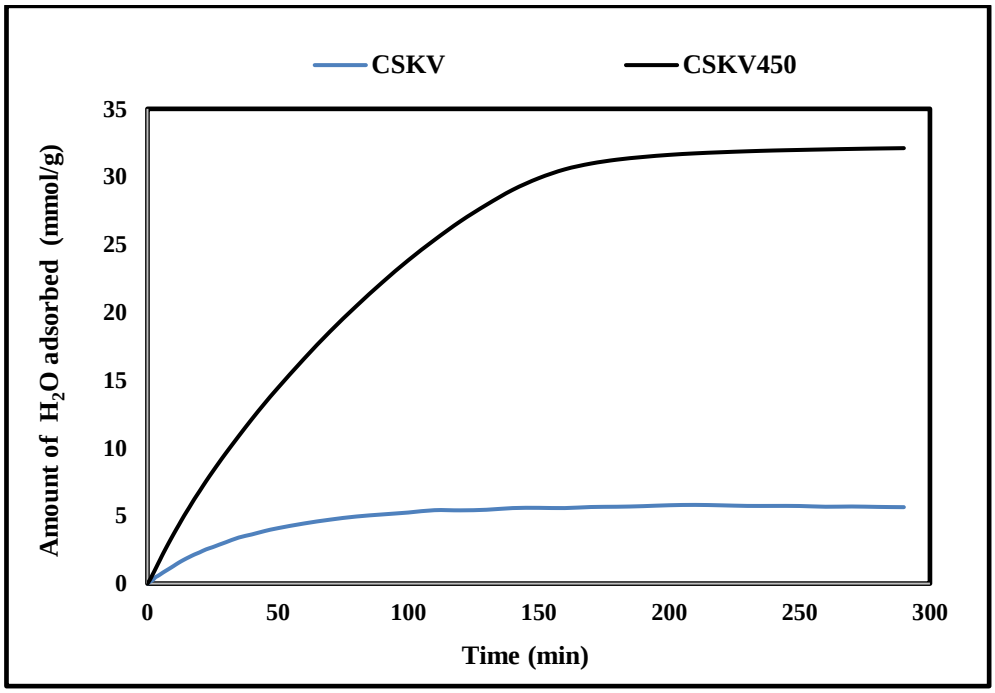


Figure 7. 6: H_2O uptake (95 %RH) for samples CSKV and CSKV450 using DVS in 100 % N_2 at 25 ^oC.

H_2O uptake rate for the tested samples under different relative humidities was investigated up to 10 minutes (as mintioned in Section 5.4). The results show that CSKV has adsorbed about 0.35 mmol/g and 1.18 mmol/g at 10 % and 50 %RH respectively, while no significant change in the amount of adsorption was observed with increased relative humidity of 95 %. Sample CSKV450 exhibited higher H_2O uptake than CSKV at all relative humidities (Table 7.3), indicating that the increase in hydrophilicity of CSKV450 enables more effective adsorption of water molecules after calcination due to removal of a portion of the VTMOS coating after heat treatment.

Table 7. 3: H_2O adsorption on samples CSKV and CSKV450 at different RH (10, 50 and 95 %) after 10 minutes using a DVS in 100 % N_2 at 25 ^oC.

	Uptake of H_2O (mmol/g)		
Sample	**RH%**		
	10 %	**50 %**	**95 %**
CSKV	0.35	1.18	1.29
CSKV450	0.59	3.42	3.64

7.5 Selectivity for CO_2

The selectivity ratios for samples CSKV and CSKV450 were evaluated after 10 minutes. As shown in Figures 7.1 and 7.4, the adsorbents became nearly saturated (80 % of equilibrium) after 3 minutes with CO_2 while H_2O was still in the early stages of adsorption. Decreasing the concentration of OH groups and the polarity of the hydrophilic surface significantly affected the adsorption selectivity after coating CSK with VTMOS. In accordance, the CSKV samples at 10 %RH exhibited lower selective ratio (1.94) than CSK. Finally, as expected, the calcination processes increased the selectivity ratio of CSKV450 to 2.12 as a result of doubling CO_2

adsorption and slightly increasing H_2O uptake to 0.59 mmol/g compared to CSKV (Table 7.4). This shows that the effect of heat treatment on the adsorption of CO_2 was higher than the effect on the adsorption of H_2O on the coated adsorbent.

Additionally, the selectivity of CSKV450 was lower than that of CSK. Although the same trend was observed at 50 and 95 %RH, as shown in Table 7.5 and Table 7.6, no significant differences were observed between the samples, and the selectivity remained at low values (not exceeding 0.6).

Table 7. 4: CO_2 and H_2O (10 %RH) adsorption capacities and the selectivity ratios for samples CSKV and CSKV450 after10 minutes.

Samples	**Adsorption of CO_2 (mmol/g)**	**Adsorption of H_2O (mmol/g)**	**$S_{CO2/H2O}$**
CSK	1.64	0.69	2.37
CSKV	0.68	0.35	1.94
CSKV450	1.25	0.59	2.12

Table 7. 5: CO_2 and H_2O (50 %RH) adsorption capacities and the selectivity ratios for samples CSKV and CSKV450 after 10 minutes.

Samples	**Adsorption of CO_2 (mmol/g)**	**Adsorption of H_2O (mmol/g)**	**$S_{CO2/H2O}$**
CSK	1.64	3.42	0.48
CSKV	0.68	1.18	0.58
CSKV450	1.25	3.42	0.36

Table 7. 6: CO_2 and H_2O (95 %RH) adsorption capacities and the selectivity ratios of the CSKV and CSKV450 after 10 minutes.

Samples	**Adsorption of CO_2 (mmol/g)**	**Adsorption of H_2O (mmol/g)**	**$S_{CO2/H2O}$**
CSK	1.64	5.52	0.29
CSKV	0.68	1.29	0.53
CSKV450	1.25	3.64	0.34

7.6 Humidity Control

7.6.1 Comparative Study between TGA and DVS on CS Sample

As shown in Figure 7.7, the TGA results for H_2O uptake were almost identical for at least 55 minutes to those obtained by DVS at 95 %RH and considerably higher than from the result obtained at 10 %RH confirming the relative humidity in the TGA is close to 100 %. At equilibrium, the amount of H_2O adsorbed by CS in TGA was 28.2 mmol/g, while 26.6 mmol/g was adsorbed in DVS. This can be explained by the water vapour condensation has been continued for a long time in TGA.

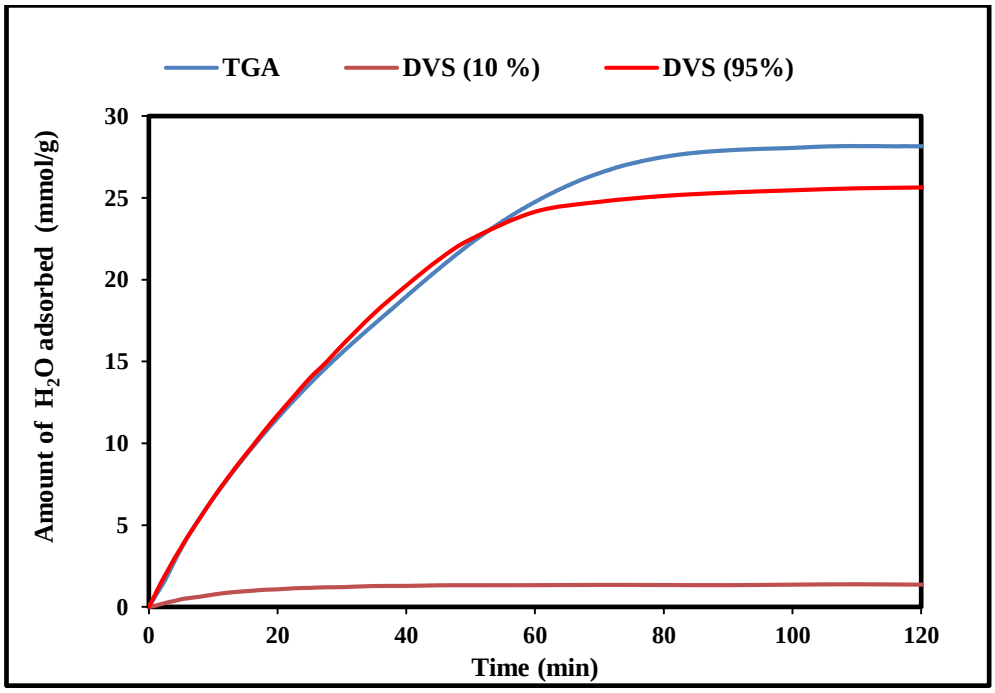


Figure 7. 7: H_2O uptake isotherms of the CS using DVS and TGA in 100 % N_2 at 25 ^oC.

7.6.2 CO_2 Adsorption Capacities on Water Vapour Equilibrated Samples

Table 7.7 explains how the H_2O uptake of the CS, CSK, CSKV and CSKV450 (that taken out of the desiccator and weighed as shown in Section 3.3.11) is a function of the relative humidity. At equilibrium, the samples follow the order: CSK > CSKV450 > CS > CSKV. It can be seen that CSK has the highest H_2O uptake due to increase hydrophilicity of the activated carbon by the intercalant K^+, and CSKV exhibited the lowest H_2O uptake due to blocking most of the surface active sites. The same trend was observed previously after testing the same samples in DVS (see Section 5.4 and 7.4).

Table 7. 7: H_2O equilibrium capacities of samples CS, CSK, CSKV and CSKV450 at 20 ^oC.

Samples	Mmol/g		
	10 %RH	**50 %RH**	**95 %RH**
CS	0.19	9.3	16.8
CSK	1.4	12.7	26.8
CSKV	0.1	5.6	14.3
CSKV450	1.2	12.3	22.8

The samples were then transferred to the TGA for CO_2 adsorption testing. Figures 7.8 to 7.11 show a comparison between the kinetics of CO_2 adsorption for the dry and humid (at 10 %, 50 % and 95 %RH) samples after 3 minutes. In general, all samples appear to have reached equilibrium. Compared to adsorption in dry conditions, the adsorption of CO_2 here was not significantly affected by increasing the relative humidity to 10 %, and just a slight decrease in the time required to reach equilibrium was observed as the sorbent loading increases. These results indicate

that the samples still retain a high number of active sites for CO_2 adsorption on their surface. Therefore, the adsorption of CO_2 at 10 %RH was almost identical to the amount of CO_2 adsorbed on the dry samples. Increasing humidity, led to a significant reduction in the amount of CO_2 adsorbed for all the samples tested. For example, when relative humidity increased to 50 %, the amount of CO_2 adsorbed on the CSKV450 decreased to 0.26 mmol/g. Moreover, increasing relative humidity up to 95 % led to decrease the amount of CO_2 adsorbed on the same sample to 0.11 mmol/g, which was 90 % lower than that adsorbed in dry conditions, suggesting that H_2O molecules have occupied the majority of activated carbon pores. This may be due to the exchange of H_2O between the atmosphere and pores. It is noteworthy that the equilibrium times have significantly decreased as relative humidity is increased to 50 % and 95 %.

In conclusion, filling the pores with the condensed water vapour largely depended upon two factors: ambient relative humidity and the pore structure of the adsorbent material. Whatever the equilibrium uptake of at 10 %RH, this is not having a major influence on CO_2 adsorption. In fact, low uptakes that observed after H_2O equilibration are not reflect the real situation where CO_2 and H_2O are effectively in competition. In contrast, the adsorption properties of the humid activated carbons at 50 % and 95 %RH became significantly different from that of the dry activated carbon. These results agree with those obtained by Cen et al. (2014) in that the adsorption of CO_2 onto wet carbons was generally reduced as the water vapour loading increases.

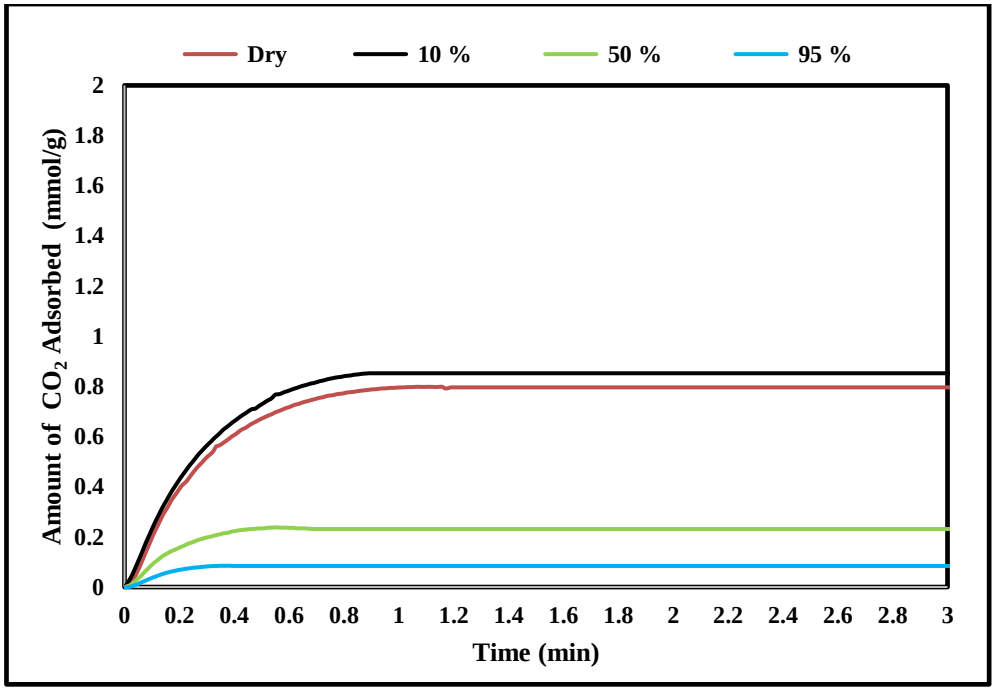


Figure 7. 8: CO_2 adsorption for sample CS at the dry conditions and 10 %, 50 %, 95 %RH using TGA in 15% CO_2 and 85% N_2 at 25 ^oC.

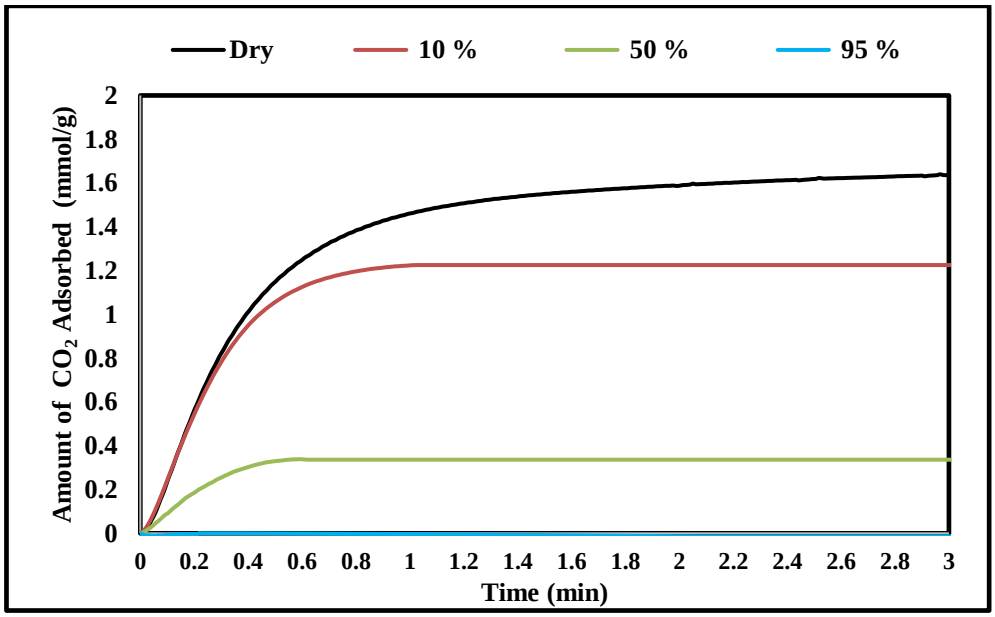


Figure 7. 9: CO_2 adsorption for sample CSK dry and at 10, 50, 95 %RH using TGA in 15 % CO_2 and 85 % N_2 at 25 ^oC.

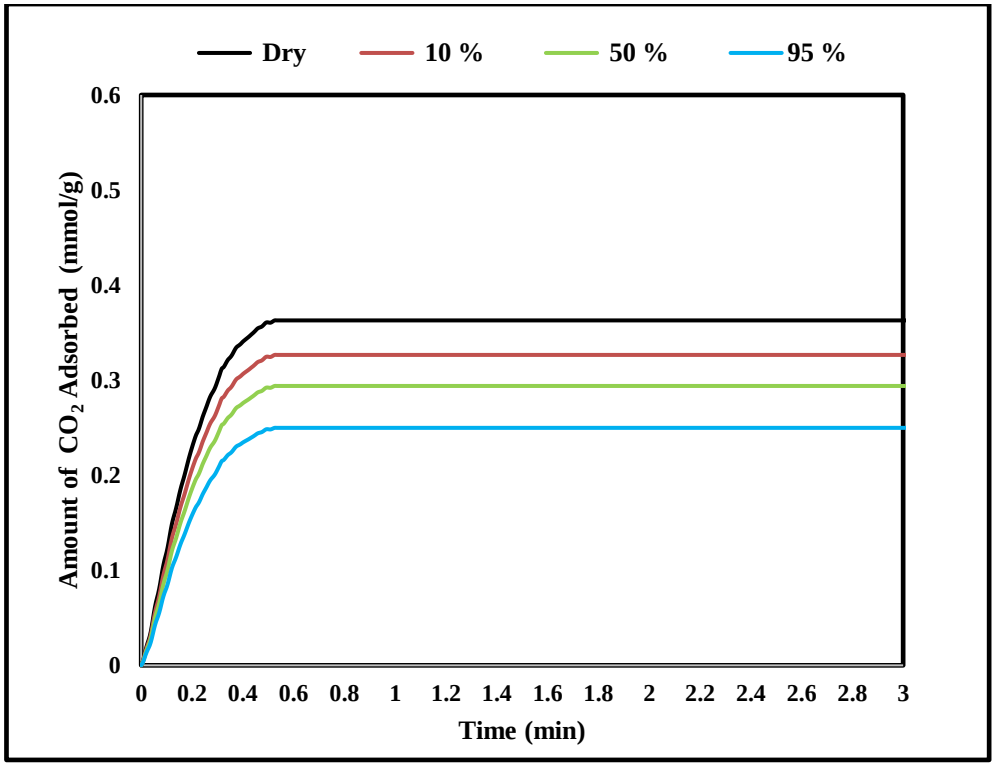


Figure 7. 10: CO_2 adsorption for sample CSKV dry and at 10 %, 50 %, 95 %RH using TGA in 15 % CO_2 and 85 % N_2 at 25 ^oC.

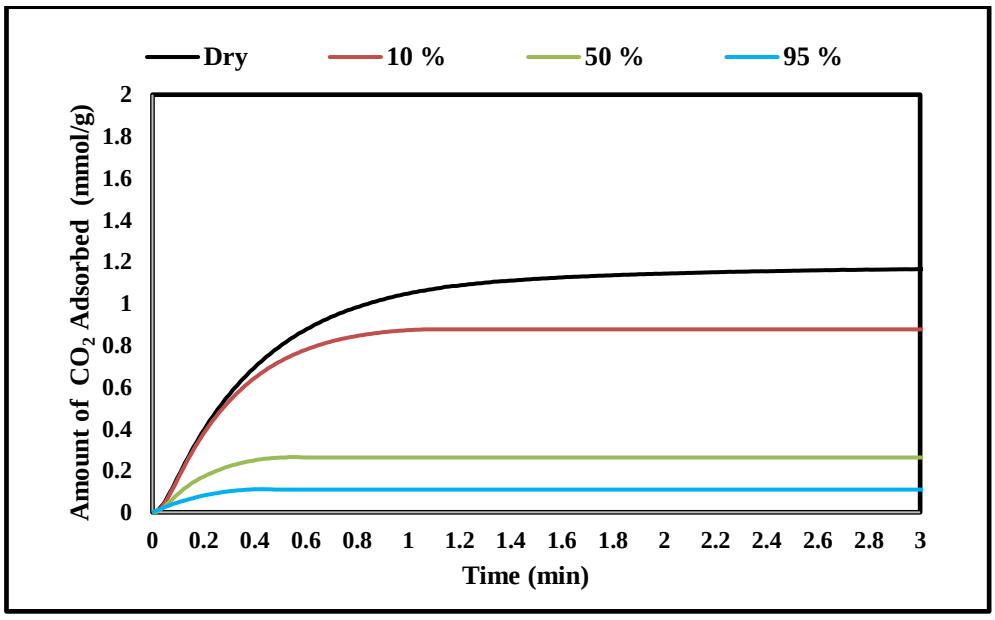


Figure 7. 11: CO_2 adsorption of CSKV450 dry and at 10 %, 50 %, 95 %RH using TGA in 15 % CO_2 and 85 % N_2 at 25 ^oC.

7.7 Conclusions

A clear reduction in CO_2 adsorption occurred on the four samples (CS, CSK, CSKV and CSKV450) as a result of the effect of pre-adsorption of H_2O, at 50 % and 95 %RH. However, at the lowest relative humidity (10 %RH) and for a relatively short period of time (10 minutes), the CO_2/H_2O selectivity of CSKV450 was 2.12 considerably higher than at 50 and 95 %RH. Interestingly, no significant difference was observed for the selectivity between CSK (2.37) and CSKV450. The same trend was observed at 50 % and 95 %RH. Although, heat treatment of the coated sample increased CO_2 and H_2O adsorption, there was no improvement in CO_2 adsorption capacity or CO_2 / H_2O selectivity after relatively short contact times.

CHAPTER 8: Investigation of Factors Affecting CO_2 Adsorption in Post Combustion Capture

8.1 Introduction

In the previous chapter, KOH-activated carbons derived from coconut shell, and their organsiloxane-coated and heat-treated counterparts showed high CO_2 adsorption capacity (1.64-1.25 mmol/g) and high CO_2/H_2O selectivity (2.12-2.37) at a relative humidity of 10 % after a period of 10 minutes. Heat treatment calcination of the coated activated carbons did not result in further improvements for the CO_2/H_2O selectivity after the KOH treatment.

In this chapter, factors other than adsorption capacity that play important roles in the performance of candidate adsorbents in practical applications of post-combustion CO_2 capture are described, where circulating fluidized beds or moving beds are applied of TSA processes (Wu et al., 2018). Volumetric adsorption capacities, mechanical strength and the heat of adsorption and regeneration heat of CSs are considered. In general, bulk density/volumetric capacity is most important for moving packed beds than for fluidised-beds where residence times controlled by minimum fluidising velocities (Kim et al., 2016). The results for CSK and CSKV450 are compared with the parent activated carbon (CS) and coated activated carbon (CSKV).

8.2 Volumetric Capacities of Selected Activated Carbons

The large quantities of continuous flue gas coming from power plants and from industrial processes dictates the need for large amounts of high-performance adsorbents. Granular activated carbon (GAC) has an advantage over the powder form of carbon in the adsorption of gases as it permits the passage of a gas through a packed bed of carbon without excessive restriction. Additionally, GAC can be easily regenerated (Strelko, 1999), and it is usually produced from commercial coconut shells. This type of activated carbon has extremely high surface area and a large pore volume which tends to capture a large amount of CO_2 but, like most other adsorbents, it generally has low density due to its high porosity and this would decrease the volumetric capacity (Wei et al., 2012). Smaller granules/particles are needed for fluidised beds; otherwise residence time is too short due to very high minimum fluidising velocities (Al-Hwayzee, 2016). Volumetric gas adsorption capacity and bulk density are important criteria in practical applications due to their role in determining the capture efficiency of a solid adsorbent based CCS system. Typically, the volumetric adsorption capacity is obtained by the multiplying gravimetric adsorption capacity with the bulk density of adsorbent.

In addition to the importance of the two factors above in maintaining the high CO_2 adsorption in adsorption beds , the mechanical strength of adsorbents is also of importance for their manufacturing and packaging, as well as during fluidisation, where this gives a good indication of the abrasion resistance of adsorbents during this process (Liu, 2017).

According to the literature (Vijayan et al., 2012, Prauchner and Rodriguez-Reinoso, 2008), the bulk density of coconut shell activated carbon is normally between 0.5 to 0.65 g/cm^3. Using natural coconut shell may achieve the desired and required balance between gravimetric and volumetric capacities for CO_2 capture. In this section, the volumetric CO_2 adsorption of coconut shell activated carbon samples and its relatives (CS, CSK, CSKV and CSKV450) were measured and compared as well as the bulk density, and mechanical strength values (the measuring methods were described in Chapter 3).

The parent activated carbon investigated was found to possess the highest value of bulk density (0.68 g/cm^3), highest mechanical strength (maximum load 15.6 N), and a volumetric CO_2 adsorption of 29.9 g/L. After intercalation of potassium ions, CSK offered the best option on both a gravimetric and volumetric basis (65.1 mg/g and 38.4 g/LTable 8.1). However, the uptake decreased by almost half after VTMOS coating. Heat treatment led to on increase in both gravimetric and volumetric CO_2 adsorption to 40.9 mg/g and 24.5 g/L. Bulk density and mechanical strength did not change drastically during the modifications.

Table 8. 1: Comparison of gravimetric and volumetric CO_2 adsorption at 25 ^oC and 0.15 bar for activated carbons .

Sample	Maximum load (N)	Bulk density (g/cm^3)	Gravimetric CO_2 uptake (mg/g)	Volumetric CO_2 uptake (g/L)
CS	15.6	0.68	44.0	29.9
CSK	10.8	0.59	65.1	38.4
CSKV	11.0	0.62	27.7	17.2
CSKV450	8.98	0.60	40.9	24.5

8.3 Heat of Adsorption and Specific Heat of CSs Series

Figure 8.1 shows the isosteric heats of adsorption for CSs at different CO_2 adsorption levels. Heat of adsorption (Q_{st}) has been calculated at 0 and 25 ^oC with Clausius–Clapeyron equation. Calculation of the CO_2 heat of adsorption involves the generation of an interpolated curve by spline fitting of data points using MicroActive software (version 3.0, Micromeritics Instrument Corporation) (see Section 3.3.5). Compared with CS, the Q_{st} of CSK is increased by about 22 % (to 42.8 kJ/mol) probably due to the increasing surface heterogeneity of the activated carbon after modification with KOH leading to more active adsorption sites on the carbon surface (Liu, 2017). VTMOS coating led to a decrease in the isosteric adsorption heat by half, as a result of the blocking of some pores on the CSKV surface, while the calcination process led to an increase in the Q_{st} to 25 kJ/mol as a result of reopening some of these pores.

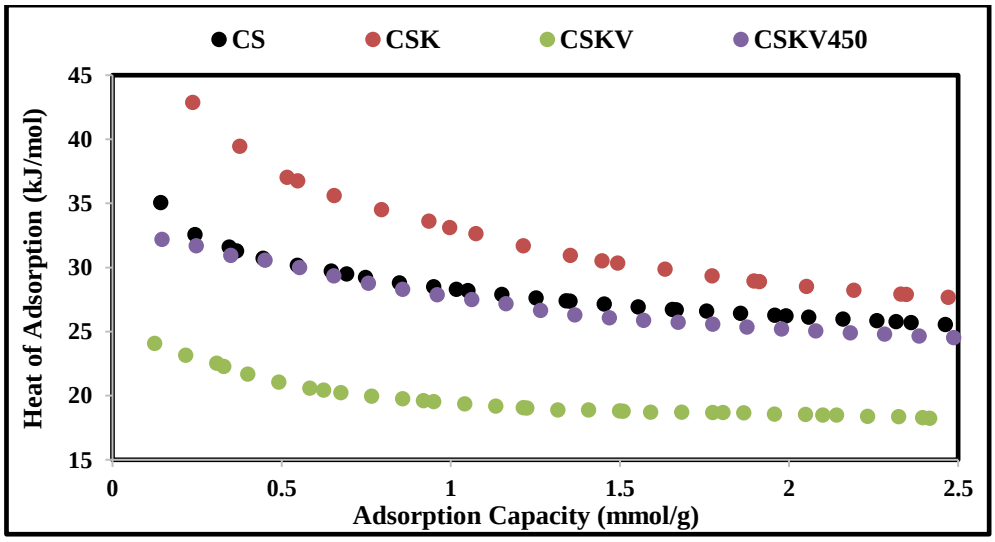


Figure 8. 1: Fitted isosteric adsorption heat of CSs series as a function of absolute CO_2 loading using MicroActive software.

The heat of adsorption for the CS, CSK, CSKV and CSKV450 measured directly via TGA-DSC were almost identical while the adsorption heat for CSKV was lower by ~ 6 kJ/mol CO_2 as shown in Table 8.2. The semi-congruence between the two adsorption heat assessment methods confirms the suitability of DSL modelling to calculate the adsorption heat for the surface modified activated carbons.

Table 8. 2: Comparison between analytical integral heat of adsorption by the DSL model and measured DSC heat of adsorption for CO_2.

Samples	Analytical integral heat of adsorption by DSL model (kJ/mole)	Experimental measurement heat of adsorption by TG-DSC (kJ/mole)
CS	27.7	24.0
CSK	29.9	29.6
CSKV	19.5	25.0
CSKV450	26.7	24.4

The specific heat capacity of adsorbents plays an important role in calculating: (1) the regeneration energy demand and (2) the heat flux required for recovering the sensible heat from the hot sorbent by a heat exchange process. Solid adsorbents have an advantage over aqueous amine solutions, such as MEA, because their specific heats are very close to that of water (Zhang et al., 2016). In contrast, activated carbons have low heat capacities even after being treated with KOH (less than or equal to 1 J/g·K), (Liu, 2017, Uddin et al., 2018).

In this work, VTMOS was coated on the CSK surface and calcined to investigate how these modifications would affect the heat capacity of the samples compared

with the raw and KOH-activated carbons. The results are shown in Figure 8.2 (measured via TGA-DSC). CS and CSK samples demonstrate an average heat capacities of 0.86 - 1.07 J/g·K, respectively, over a temperature range of 25 to 150 ^{o}C and this agrees with the values reported by Liu (2017). However, after coating and with greatly decreased CO_2 capacities, the heat capacities for CSKV samples decreased by 10 % compared to CSK, reaching 0.9 J/g·K. CSKV450 maintained this value after calcination.

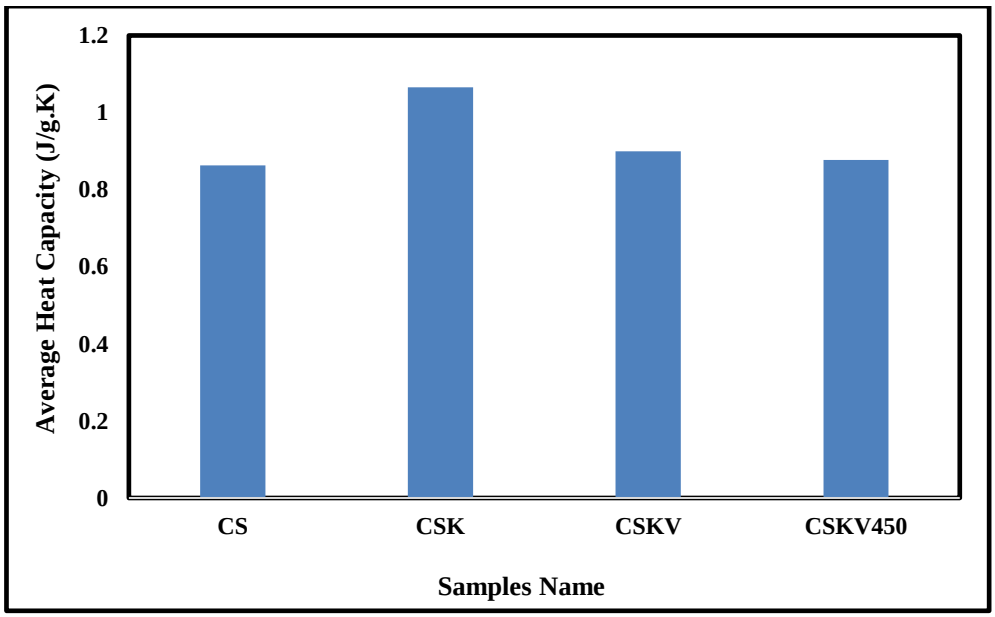


Figure 8. 2: Average heat capacities of CS samples over temperature range 25–150 ^{o}C.

8.4 Calculation of Regeneration Heat

Several researchers estimated the regeneration heats for different types of aqueous amine solutions between 3.3 – 4.2 GJ/tonne CO_2 depending on the type of amine used (such as MEA), the regeneration conditions (temperature, pressure and flow rate of purge gas) and working adsorption capacity (Chapel et al., 1999, Abu-Zahra et al., 2007). Using adsorbents instead of aqueous amines can potentially reduce the regeneration energy due to the much lower heat capacities, as well as avoiding the evaporation relatively large amounts of water vapour in the regeneration process (Zhang et al., 2016). In general, the total regeneration energy required for a solid adsorbent based system (Q_{reg}) can be determined by the summation of the three terms shown in equation (8.1).

$$Q_{reg} = Q_{sen} + Q_{des} + Q_v \qquad (8.1)$$

Where Q_{sen} is the sensible heat required to heat the adsorbent from the adsorption temperature to the regeneration temperature; Q_{des} is the CO_2 heat of desorption and Q_v is the latent heat of vaporisation of water (the amount of energy required to overcome the bonding energy between the adsorbed water molecules and the solvent or adsorbent).

The above equation can be written in more detail, including a number of variables (Zhang et al., 2016):

$$Q_{reg} = \frac{1-\alpha}{q_w} C_{p,s}(T_{de} - T_{ad}) + (1-\beta)\Delta H_a + (1-\gamma)\frac{Q_v f_{H_2O}}{q_w} \qquad (8.2)$$

Where q_w (mmol/g) is the working capacity of the adsorbent; α, β, γ are the recovered ratio of sensible heat, recovery ratio of heat of adsorption and recovery ratio of vaporisation heat, which were assumed as 0.75, 0 and 0.5, respectively for activated carbon (Liu, 2017); $C_{p,s}$ (kJ/kg .K) is the specific heat capacity of the adsorbent; T_{ad} and T_{de} (K) are the adsorption and desorption temperatures respectively; ΔH_a (kJ/kgCO_2) is the absolute value of the heat of adsorption; Q_v (J/kg) the specific latent heat of evaporation of water and f_{H2O} is the H_2O uptake in the adsorber, which was adsorbed simultaneously with CO_2 and has to be evaporated at desorption temperature.

The thermal energy required for the regeneration of adsorbents is related to the characteristic properties of these materials on the one hand and the process conditions on the other hand. For example, β values for MEA and carbons are different where the adsorption temperature is around 75 ^oC for MEA (β = 0.25) and 25 ^oC for carbons (β = 0) as the recovery ratio of adsorption for carbon materials is low grade. (Liu, 2017).

The estimated working capacity of the adsorbents is taken as 75 % of the equilibrium capacity obtained from TGA. For CSKV450, a q_w would be about 1.05 mmol/g as a contact time close to 2 minutes compared to the equilibrium capacity of 1.40 mmol/g. (Figure 7.1). The nominal values of all the parameters at dry conditions are listed in Table 8.3. After applying all parameters in equation 8.4, the regeneration heat and its individual components can be calculated. The low value of Q_{reg}, 1.1 GJ/tonne CO_2, can be attribute to the negligible of the vaprasation heat at $f_{H2O} = 0$.

Table 8. 3: Nominal parameters adopted for calculation regeneration heat for CSKV450.

Parameter	Value	Notes
ΔH_a(kJ/mol)	24.38	Measured by TG-DSC
$C_{p,s}$ (kJ/kg.K)	0.88	Measured by TG-DSC
ΔT (K)	125	T_{ad}=25 ^oC, T_{de}=150 ^oC
q_w (mmol/g)	1.05	Figure 7.1
α	0.75	Assumed
β	0	Assumed

8.4.1 Effect of Water Vapour on the Regeneration Heat

In general, increasing the adsorbed H_2O during the time leads to an increase in the regeneration heat required for the solid adsorbents. According to Figure 8.3, f_{H2O} would be 0.98 mmol/g (4.2 wt%) at the adsorption time close to 2 minutes. The nominal values of all the parameters are listed in Table 8.4. The Q_{reg} was calculated by applying all parameters in equation 8.1.The value of Q_{reg}, 2.26 GJ/tonne CO_2, is nearly double the regeneration heat in dry conditions due to a significant effect of the water on the regeneration heat.

Table 8. 4: Nominal parameters adopted for calculation Q_{Ve} for CSKV450.

Parameter	Value	Notes
Qv (kJ/kg)	2257.6	Reference
q_w (%)	0.045	Figure 7.1
f_{H2O} (%)	0.042	Figure 8.3
γ	0.5	Assumed

$$Q_{ve} = \left[(1 - 0.5) * 2257.6 * \frac{0.042}{0.045}\right] \frac{KJ}{Kg}$$

$$= 1053.54 \frac{KJ}{Kg}$$

Using equation 8.1 Q_{reg} ;

$$Q_{reg} = 654.76 \frac{KJ}{Kg} + 554.09 \frac{KJ}{Kg} + 1053.54 \frac{KJ}{Kg}$$

$$Q_{reg} = 2262.4 \frac{KJ}{Kg} = 2.26 \ \frac{GJ}{tonne\ CO2}$$

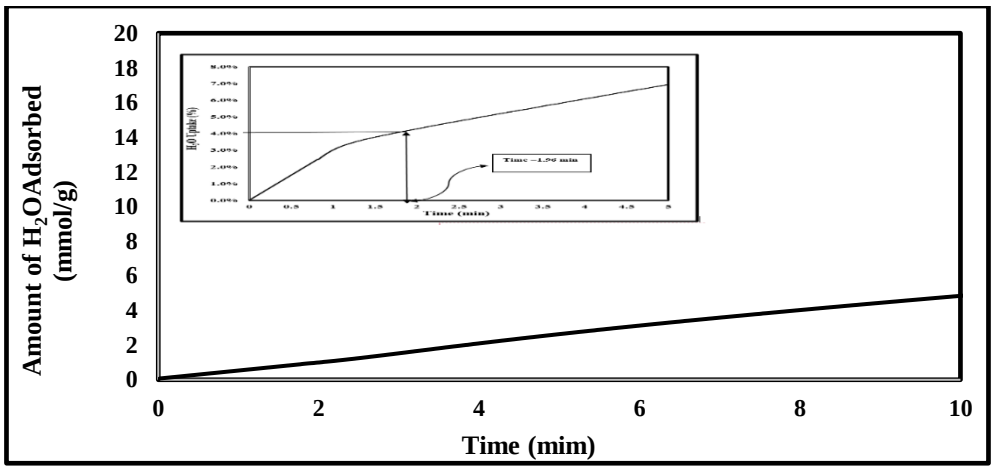


Figure 8. 3:H_2O adsorption of the CSKV450 using TGA in 100 % N_2 at 25 ^oC and 95 %RH.

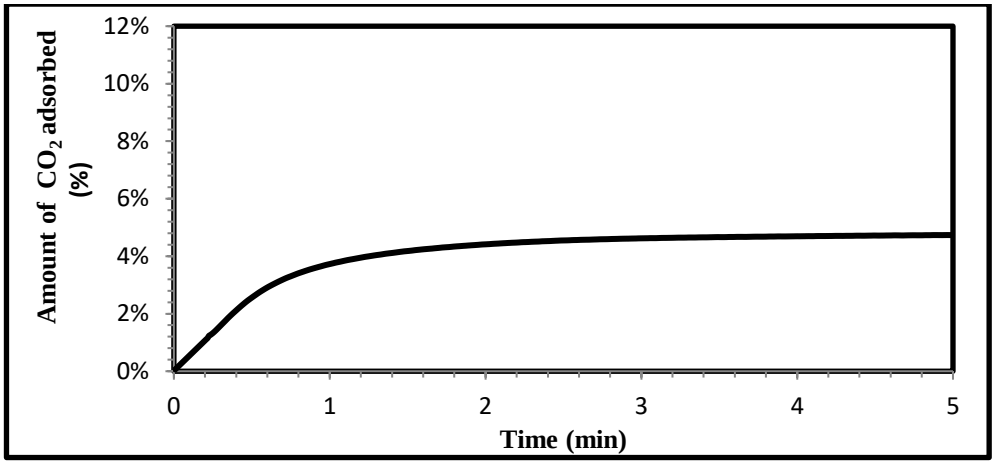


Figure 8.4: CO_2 adsorption of the CSKV450 using TGA in 15 % CO_2 and 85% N_2 at 25 ^oC.

8.5 Conclusions

The potential application for CSK and CSKV450 in CO_2 post combustion capture has been systematically investigated in this chapter. The results show that the best-performing sample, CSKV450, has a low heat of adsorption and low specific heat capacity (i.e. 24 kJ/mol and 0.8 J/kg.K, respectively) and this has a beneficial effect on the regeneration heat. Increasing the adsorbed H_2O during the time led to an increase in the regeneration heat required for the solid adsorbents, where a small amount of H_2O plays a significant role in increasing the Q_{reg} of the adsorbent.

Chapter 9: Conclusions and Future Work

9.1 Conclusions

Intercalation of potassium into the carbons derived from coconut shell (CS) and phenolic resin (PR) was investigated since it is established that this increases CO_2 adsorption capacities significantly. After10 minutes, CO_2 adsorption kinetics have increased to about 1.7 mmol/g for the two modified samples compared to less than 1 mmol/g for the parent sample. The CO_2/H_2O selectivity ratios for the four samples were evaluated after the same period. At 10 %RH, CSK had the highest selectivity at 2.37. The sample became nearly saturated with CO_2 after 3 minutes while H_2O adsorption was still in its initial stages. The selectivity of the other samples did not exceed 0.8 at different relative humidites (10 %, 50 % and 95 %RH). Based on the above, the CSK sample can be considered as the best suitable for use in post-combustion CO_2 capture under typical conditions

CSK and PRK samples were coated using a range of organosiloxane compounds and heat treatment of coated activated carbon at different temperatures was investigated to try to maximise CO_2/H_2O selectivity. CSK that coated with VTMOS and treated at 450 ^oC (CSKV450) exhibited highest selectivity value (2.12) at low relative humidity (10 %RH) compared with the other coated–heated samples. No significant differences were observed for the selectivity between CSK and CSKV450 at 10 %RH. This provides evidence that although heat treatment of the coated sample increased CO_2 and H_2O adsorption kinetics, it did not improve the

selectivity. At equilibrium, the CO_2/H_2O selectivity of CSK and PRK have roughly maintained on their values after modification processes.

The efficacy of water preloading on CO_2 adsorption behaviour was investigated also for CS, CSK, CSKV and CSKV450. A 10 %RH, this does not have a major influence on CO_2 adsorption. A clear reduction in CO_2 adsorption capacity observed on the four samples with increasing relative humidity to 50 % and 95 %.

At working capacity, the (Q_{reg}) for CSKV450 in wet condition is nearly double the regeneration heat in dry condition. Howevere, it is still lower than that in different types of aqueous amine solutions and PEI/silica in wet condition.

9.2 Recommendations for Further Research

Based on the course of this study and its findings, there are several areas that are worthy of additional research in this project. The following are recommended for future work:

1. The adsorption of CO_2 and H_2O have been considered to be independent of each other. Taking into account the competition between these components toward the adsorbent surface, the multi-component isotherm data can provide a clear image about the adsorption process.

2. Kinetic CO_2 adsorption tests for simulated flue gas were carried out a lab-scale. Similar tests are recommended for moving and fluidised bed reactors as well as testing CO_2 adsorption in the presence of H_2O at different operating conditions.

3. The results on KOH-activated carbons in this study were all carried out on a lab-scale. It is recommended to scale up the preparation of K^+ treatment of carbon adsorbents and testing it using circulating moving and fluidized bed.

4. The effect of 15vol% CO_2 in the feed with N_2 was studied to determine the adsorption capacity of KOH-activated carbon. It is recommended the investigations cover other industrial process streams, which are sources of CO_2 emissions such as cement production where the concentration of CO_2 is about 22 vol% in flue gas (Voldsund et al., 2019).

References

ABU-ZAHRA, M. R., SCHNEIDERS, L. H., NIEDERER, J. P., FERON, P. H. & VERSTEEG, G. F. 2007. CO_2 capture from power plants: Part I. A parametric study of the technical performance based on monoethanolamine. *International Journal of Greenhouse Gas Control,* 1**,** 37-46.

ADAMS, D. 2010. *Flue gas treatment for CO_2 capture*, IEA Clean Coal Centre London,UK, ISBN: 978-92-9029-489-4.

AHMADPOUR, A. & DO, D. 1996. The preparation of active carbons from coal by chemical and physical activation. *Carbon,* 34**,** 471-479.

AIRUSE 2016. The Control of Shipping Emissons.

http://airuse.eu/wp-content/uploads/2013/11/R21_AIRUSE-Control-of-shipping-emissons.pdf.[accessed 5th Aug 2017].

ALAYA, M., HOURIEH, M., YOUSSEF, A. & EL-SEJARIAH, F. 2000. Adsorption properties of activated carbons prepared from olive stones by chemical and physical activation. *Adsorption Science & Technology,* 18**,** 27-42.

ALCAÑIZ-MONGE, J., LINARES-SOLANO, A. & RAND, B. 2002. Mechanism of adsorption of water in carbon micropores as revealed by a study of activated carbon fibers. *The Journal of Physical Chemistry B,* 106**,** 3209-3216.

AL-HWAYZEE, M. 2016. Design and Development of Gasification Processes in Fluidised Bed Chemical Reactor Engineering, PhD thises, Cardiff University (UK).

ALLWAR, A. 2012. Characteristics of pore structures and surface chemistry of activated carbons by physisorption, ftir and boehm methods. *Journal of Applied Chemistry,* 2**,** 9-15.

ALMANZA-WORKMAN, A. M., RAGHAVAN, S., DEYMIER, P., MONK, D. J. & ROOP, R. 2004. Aqueous silane-surfactant co-dispersions for deposition of hydrophobic coatings onto pre-oxidized polysilicon. *Colloids and Surfaces A: Physicochemical and Engineering Aspects,* 232**,** 67-75.

ASENATH SMITH, E. & CHEN, W. 2008. How to prevent the loss of surface functionality derived from aminosilanes. *Langmuir,* 24**,** 12405-12409.

BANDOSZ, T. J. 2006. *Activated carbon surfaces in environmental remediation*, Elsevier, UK, ISBN: 978-0-12-370536-5.

BANSAL, R. C. & GOYAL, M. 2005. *Activated carbon adsorption*, CRC press ,TAYLOR & Francis Groups, New York, ISBN: 978-1-4200-2881-2.

BARBU, A.-D., GRIFFITHS, N. & MORTON, G. 2013. Achieving energy efficiency through behaviour change: what does it take? http://www.europa.eu. .[accessed 8th Aug 2018].

BARTON, S. S., EVANS, M. J. & MACDONALD, J. A. 1991. The adsorption of water vapor by porous carbon. *Carbon,* 29**,** 1099-1105.

BELMABKHOUT, Y., GUILLERM, V. & EDDAOUDI, M. 2016. Low concentration CO_2 capture using physical adsorbents: Are metal–organic frameworks becoming the new benchmark materials? *Chemical Engineering Journal,* 296**,** 386-397.

BEN, T., LI, Y., ZHU, L., ZHANG, D., CAO, D., XIANG, Z., YAO, X. & QIU, S. 2012. Selective adsorption of carbon dioxide by carbonized porous aromatic framework (PAF). *Energy & Environmental Science,* 5**,** 8370-8376.

BESWICK, A. J., GIBB, F. G. & TRAVIS, K. P. 2014. Deep borehole disposal of nuclear waste: engineering challenges. *Proceedings of the Institution of Civil Engineers-Energy,* 167**,** 47-66.

BOGLE, D. & FAIRWEATHER, M. 2012. *22nd European Symposium on Computer Aided Process Engineering*, Elsevier,ISBN: 978-0-444-59519-5.

BP 2018. BP statistical review of world energy. London, UK: BP. http://www.bp.com/statisticalreview. [accessed 8th Aug 2019]

BRENNAN, J. K., BANDOSZ, T. J., THOMSON, K. T. & GUBBINS, K. E. 2001. Water in porous carbons. *Colloids and surfaces A: Physicochemical and engineering aspects,* 187**,** 539-568.

BUCZEK, B. 2016. Preparation of active carbon by additional activation with potassium hydroxide and characterization of their properties. *Advances in Materials Science and Engineering,*. Volume 2016, Article ID 5819208, 4 pages.

BUDARIN, V., CLARK, J., MIKHALOVSKY, S., GORLOVA, A., BOLDYREVA, N. & K. YATSIMIRSKY, V. 2000. The hydrophobisation of activated carbon surfaces by organic functional groups. *Adsorption Science & Technology,* 18**,** 55-64.

BÜLOW, M., SHEN, D. & JALE, S. 2002. Measurement of sorption equilibria under isosteric conditions: The principles, advantages and limitations. *Applied Surface Science,* 196**,** 157-172.

CAZENAVE, A., PALANISAMY, H. & ABLAIN, M. 2018. Contemporary sea level changes from satellite altimetry: What have we learned? What are the new challenges? *Advances in Space Research,* 62**,** 1639-1653.

CCC 2018. Reducing UK emissions-2018 Progress Report to Parliament Committee on Climate Change. UK: CCC.

www.theccc.org.uk/publications. [accessed 5th Aug 2017].

CEN, Q., FANG, M., WANG, Z. & LUO, Z. Effect of water on CO_2 adsorption with activated carbon. 2013 International Conference on Materials for Renewable Energy and Environment, 2014. IEEE, 885-888.

CERETTA, F. 2013. Synthesis and Characterization of Fluorinated Compounds for Industrial Applications, PhD thesis, The University of Padova (Italy).

CHANG, J. Y., GODOVSKY, D., HAN, M., HASSAN, C., KIM, J., LEE, B., LEE, Y., PEPPAS, N., QUIRK, R. & YOO, T. 2000. *Biopolymers· PVA Hydrogels Anionic Polymerisation Nanocomposites,* Springer Science & Business Media, Berlin, ISBN: 3-540-354067313.

CHAPMAN, V. M. 1995. What we observe is not nature itself, but nature exposed to our mode of questioning--W. Heisenberg. *Japanese Journal of Cancer Research,* 12**,** 1240-1241.

Chapel D, Ernest J, Mariz C. Recovery of CO_2 from flue gases: commercial trends. Canadian Society of Chemical Engineers annual meeting, Canada; October 4–6, 1999.

CHEN, L.-C., PENG, P.-Y., LIN, L.-F., YANG, T. C. & HUANG, C.-M. 2014. Facile preparation of nitrogen-doped activated carbon for carbon dioxide adsorption. *Aerosol Air Qual. Res,* 14**,** 916-927.

CHEN, Z., DENG, S., WEI, H., WANG, B., HUANG, J. & YU, G. 2013. Activated carbons and amine-modified materials for carbon dioxide capture-a review. *Frontiers of Environmental Science & Engineering,* 7**,** 326-340.

CHOMIAK, K., GRYGLEWICZ, S., KIERZEK, K. & MACHNIKOWSKI, J. 2017. Optimizing the properties of granular walnut-shell based KOH activated carbons for carbon dioxide adsorption. *Journal of CO_2 Utilization,* 21**,** 436-443.

COSNIER, F., CELZARD, A., FURDIN, G., BEGIN, D., MARECHE, J. & BARRES, O. 2005. Hydrophobisation of active carbon surface and effect on the adsorption of water. *Carbon,* 43**,** 2554-2563.

DAVIS, S. J., CALDEIRA, K. & MATTHEWS, H. D. 2010. Future CO_2 emissions and climate change from existing energy infrastructure. *Science,* 329**,** 1330-1333.

DECC, C. 2012. Roadmap: Supporting deployment of carbon capture and storage. intheUK.*CCS.*

https://assets.publishing.service.gov.uk/government/uploads/system/uploads/attachment_data/file/48317/4899.pdf. [accessed 5th Aug 2017].

DEMIRBAS, A. 2007. Combustion of biomass. *Energy Sources, Part A: Recovery, Utilization, and Environmental Effects,* 29**,** 549-561.

DIRINGER, E. 2011. Climate policy: Letting go of Kyoto. *Nature,* 479**,** 291.

DO, D. & DO, H. 2000. A model for water adsorption in activated carbon. *Carbon,* 38**,** 767-773.

DONG, X., ZHANG, J., GANG, L., XIAO, P., WEBLEY, P. & ZHAI, Y.-C. 2011. Effect of water vapor from power station flue gas on CO_2 capture by vacuum swing adsorption with activated carbon. *Journal of Fuel Chemistry and Technology,* 39**,** 169-174.

DRAGE, T. C., SNAPE, C. E., STEVENS, L. A., WOOD, J., WANG, J., COOPER, A. I., DAWSON, R., GUO, X., SATTERLEY, C. & IRONS, R. 2012. Materials challenges for the development of solid sorbents for post-combustion carbon capture. *Journal of Materials Chemistry,* 22**,** 2815-2823.

DUBININ, M. 1980. Water vapor adsorption and the microporous structures of carbonaceous adsorbents. *Carbon,* 18**,** 355-364.

DUBININ, M. & SERPINSKY, V. 1981. Isotherm equation for water vapor adsorption by microporous carbonaceous adsorbents. *Carbon,* 19**,** 402-403.

ECONOMICS, E. E. A. V. 2018. Element-Energy-Vivid-Economics-Report-CCS-Market-Mechanisms.pdf. 26-28 Ely Place London EC1N 6TD . http://www.elementenergy.co.uk/wordpress/wpcontent/uploads/2018/05/Element-Energy-Vivid-Economics-Report-CCS-Market-Mechanisms.pdf. [accessed 20 May 2017].

FADLEY, C. & SHIRLEY, D. 1970. Electronic Densities of States from X-Ray Photoelectron Spectroscopy . *Journal of Research of the Natianal Bureau of Standards - A. Physics and Chemistry,* 74A, 543-558.

FANG, B. & BINDER, L. 2006. A novel carbon electrode material for highly improved EDLC performance. *The Journal of Physical Chemistry B,* 110**,** 7877-7882.

FARHA, O. K., YAZAYDıN, A. Ö., ERYAZICI, I., MALLIAKAS, C. D., HAUSER, B. G., KANATZIDIS, M. G., NGUYEN, S. T., SNURR, R. Q. & HUPP, J. T. 2010. De novo synthesis of a metal–organic framework material featuring ultrahigh surface area and gas storage capacities. *Nature chemistry,* 2**,** 944.

FIGUEIREDO, J., PEREIRA, M., FREITAS, M. & ORFAO, J. 1999. Modification of the surface chemistry of activated carbons. *Carbon,* 37**,** 1379-1389.

FIGUEIREDO, J. L. 2013. Functionalization of porous carbons for catalytic applications. *Journal of Materials Chemistry A,* 1**,** 9351-9364.

FREESE, S., NOZAIC, D., SMITH, R. & TROLLIP, D. 2000. Powdered activated carbon: can this be effectively assessed in the laboratory? WISA 2000 Conference, Sun City, South Africa, 29 May to 1 June.

FRYXELL, G. E. & CAO, G. 2012. *Environmental applications of nanomaterials: synthesis, sorbents and sensors*, World Scientific Publishing Co. Pte. Ltd. ,ISBN : 978-1-84816-803-9.

G PLAZA, M., GONZÁLEZ, A. S., RUBIERA, F. & PEVIDA, C. 2015. Water vapour adsorption by a coffee-based microporous carbon: effect on CO_2 capture. *Journal of Chemical Technology & Biotechnology,* 90**,** 1592-1600.

GHARAIE, M. 2013. Design and Optimization of Energy Systems with Effective Carbon Control, PhD thesis, The University of Manchester (UK).

GILLES, S. 2007. *Chemical modification of silicon surfaces for the application in soft lithography*, Forschungszentrum, Zentralbibliothek,IBSN: 0944-2952.

GLOBAL-ENERGY-PERSPECTIVE 2019.

https://minerals.usgs.gov/minerals/pubs/mcs/2019/mcs2019.pdf.[accessed 12th April 2019].

GLOBAL, B. & WORLDWIDE, B. 2011. BP Energy Outlook 2030. *London, UK.*

https://www.bp.com/content/dam/bp/businesssites/en/global/corporate/pdfs/energy-economics/energy-outlook/bp-energy-outlook-2011.pdf .[accessed 12th April 2019].

GLOBAL, B. P. 2017. BP statistical review of world energy June 2017. *Relatório. Disponívelem.*

https://www.bp.com/en/global/corporate/energyeconomics/statistical-review-of-world-energy. html. [accessed 20 May 2018].

GOLDSTEIN, J. I., NEWBURY, D. E., MICHAEL, J. R., RITCHIE, N. W., SCOTT, J. H. J. & JOY, D. C. 2017. *Scanning electron microscopy and X-ray microanalysis,* Springer, ISBN: 978-1-4939-6676-9

GONÇALVES, M., MOLINA-SABIO, M. & RODRIGUEZ-REINOSO, F. 2010. Modification of activated carbon hydrophobicity by pyrolysis of propene. *Journal of Analytical and Applied Pyrolysis,* 89**,** 17-21.

GOTTIPATI, R. 2012. Preparation and Characterization of Microporous Activated Carbon from Biomass and its Application in the Removal of Chromium (VI) from Aqueous Phase , PhD thesis, National Institute of Technology (India).

GOUGH, C., SHACKLEY, S., HOLLOWAY, S., BENTHAM, M., BULATOV, I., MCLACHLAN, C., KLEMES, J., PURDY, R. & COCKERILL, T. An integrated assessment of carbon dioxide capture and storage in the UK. In: 8th International Conference on greenhouse gas control technologies [proceedings]/edited by Greenhouse Gas Control Technologies. Trondheim, Norway: GHGT8, 2006.

GRANDE, C. A. 2012. Advances in pressure swing adsorption for gas separation. *ISRN Chemical Engineering,* 2012, *Article ID 982934,* 13 pages.

GRANT, T., GUINAN, A., SHIH, C. Y., LIN, S., VIKARA, D., MORGAN, D. & REMSON, D. 2018. Comparative analysis of transport and storage options from a CO_2 source perspective. *International Journal of Greenhouse Gas Control,* 72**,** 175-191.

GREENSPAN, L.1977. Humidity fixed points of binary saturated aqueous solutions. *Journal of Research of the National Bureau of Standards,* 81**,** 89-96.

GREGG, S. & SING, K. 1982. Adsorption, surface area and porosity, . *2nd Edn (Academic, New York, 1982).* 3. ISBN: 0123009561-9780123009562.

HARLICK, P. J. & SAYARI, A. 2007. Applications of pore-expanded mesoporous silica. 5. Triamine grafted material with exceptional CO_2 dynamic and equilibrium adsorption performance. *Industrial & Engineering Chemistry Research,* 46**,** 446-458.

HAUBRICH, D., MUSSER, J. & FRY, E. S. 2011. Instrumentation to measure the back scattering coefficient b b for arbitrary phase functions. *Applied Optics,* 50**,** 4134-4147.

HETEM, M. J. J. 1990. A Fundamental Study of Chemically Modified Silica Surfaces in Chromatography. PhD thesis, Technische University Eindhoven (South Netherlands).

HOLLANDER, J. M. & JOLLY, W. L. 1970. X-ray photoelectron spectroscopy. *Accounts of Chemical Research,* 3**,** 193-200.

HONGJUN, Y., SHUANSHI, F., XUEMEI, L., YANHONG, W. & JIANGHUA, N. 2011. Economic comparison of three gas separation technologies for CO_2 capture from power plant flue gas. *Chinese Journal of Chemical Engineering,* 19**,** 615-620.

HUANG, H. Y., YANG, R. T., CHINN, D. & MUNSON, C. L. 2003. Amine-grafted MCM-48 and silica xerogel as superior sorbents for acidic gas removal from natural gas. *Industrial & Engineering Chemistry Research,* 42**,** 2427-2433.

HUANG, X., GUO, J., LIU, Z. & ZHENG, C. 2018. *Opportunities and Challenges of Oxy-Fuel Combustion.* Elsevier,ISBN: 978-0-12-812145-0.

HUH, S. H. 2011. Thermal reduction of graphene oxide. *Physics and Applications of Graphene-Experiments, Intech,* ISBN: 978-953-307-217-3.

HUNG, J. J. 2012. The Production of Activated Carbon from Coconut Shells Using Pyrolysis and Fluidized Bed Reactors, BSc thesis, The university of Arizona (USA).

INAGAKI, M. 2000. *New carbons-control of structure and functions*, Elsevier, ISBN:0-08-0437133.

IPCC 2001. Climate change 2001: the scientific basis. Cambridge University Press Cambridge,UK.

https://pure.mpg.de/rest/items/item_995493/component/file_995492/content.[accessed 20 May 2018]

JAFARI, R. & FARZANEH, M. A simple method to create superhydrophobic aluminium surfaces. *Materials Science Forum,* 706-709,2874-2879.

JAGUARIBE, E. F., MEDEIROS, L. D. L., BARRETO, M. D. C. S. & ARAUJO, L. P. D. 2005. The performance of activated carbons from sugarcane bagasse, babassu, and coconut shells in removing residual chlorine. *Brazilian Journal of Chemical Engineering, 22, 41-47.*

KALCHAUER, W. & PACHALY, B. 2009. *Müller–Rochow Synthesis: The Direct Process to Methylchlorosilanes*. Handbook of Heterogeneous Catalysis. ISBN: 9783527620777.

KAREEM, F. A. A., SHARIFF, A., ULLAH, S., DREISBACH, F., KEONG, L., MELLON, N. & GARG, S. 2018. Experimental measurements and modeling of supercritical CO_2 adsorption on 13X and 5A zeolites. *Journal of Natural Gas Science and Engineering*, 50, 115-127.

KANNICHE, M., GROS-BONNIVARD, R., JAUD, P., VALLE-MARCOS, J., AMANN, J.-M. & BOUALLOU, C. 2010. Pre-combustion, post-combustion and oxy-combustion in thermal power plant for CO_2 capture. *Applied Thermal Engineering*, 30**,** 53-62.

KARIMI, M., HILLESTAD, M. & SVENDSEN, H. F. 2012. Natural gas combined cycle power plant integrated to capture plant. *Energy & Fuels*, 26**,** 1805-1813.

KELLER, J. U. & STAUDT, R. 2005. *Gas adsorption equilibria: experimental methods and adsorptive isotherms*, Springer Science & Business Media, ISBN: 0-387-23597-3.

KESKES, E., ADJIMAN, C. S. & GALINDO, A. 2006. 1 A physical absorption process for the capture of CO_2 from CO_2-rich natural gas streams,Chemical Engineering Department, Imperial College London,UK.*From https://www.geos.ed.ac.uk/ccs/Publications/Keskes.pdf [accessed 12th April 2019]*.

KHAN, A. Y. 2003. Titanium Dioxide Coated Activated Carbon: A Regenerative Technology for Water recovery, MSc thesis ,University of Florida (USA).

KHAN, J., IQBAL, N., ASGHAR, A. & NOOR, T. 2019. Novel amine functionalized metal organic framework synthesis for enhanced carbon dioxide capture. *Materials Research Express*, 6, 105539.

KHOSHANDAM, B., KUMAR, R. V. & ALLAHGHOLI, L. 2010. Mathematical modeling of CO_2 removal using carbonation with CaO: The grain model. *Korean Journal of Chemical Engineering,* 27**,** 766-776.

KLINGE JACOBSEN, H., HEVIA-KOCH, P. & WOLTER, C. 2019. Nearshore and offshore wind development: Costs and competitive advantage exemplified by nearshore wind in Denmark. *Energy for Sustainable Development,* 50**,** 91-100.

KIM, H., MILLER, D. C., MODEKURTI, S., OMELL, B., BHATTACHARYYA, D. & ZITNEY, S. E. 2016. Mathematical modeling of a moving bed reactor for post-combustion CO_2 capture. *AIChE Journal,* 62, 3899-3914.

KOTHANDARAMAN, A. 2010. Carbon Dioxide Capture by Chemical Absorption: a Solvent Comparison Study, PhD thesis, Massachusetts Institute of Technology (India).

KUTCHKO, B. G. & KIM, A. G. 2006. Fly ash characterization by SEM–EDS. *Fuel,* 85**,** 2537-2544.

KUTORGLO, E. M., HASSOUNA, F., BELTZUNG, A., KOPECKÝ, D., SEDLÁŘOVÁ, I. & ŠOÓŠ, M. 2019. Nitrogen-rich hierarchically porous polyaniline-based adsorbents for carbon dioxide (CO_2) capture. *Chemical Engineering Journal,* 360**,** 1199-1212.

LANDERS, J., GOR, G. Y. & NEIMARK, A. V. 2013. Density functional theory methods for characterization of porous materials. *Colloids and Surfaces A: Physicochemical and Engineering Aspects,* 437**,** 3-32.

LE QUÉRÉ, C., ANDRES, R. J., BODEN, T., CONWAY, T., HOUGHTON, R. A., HOUSE, J. I., MARLAND, G., PETERS, G. P., VAN DER WERF, G. & AHLSTRÖM, A. 2012. The global carbon budget 1959–2011. *Earth System Science Data Discussions,* 5**,** 1107-1157.

LEAL, O., BOLÍVAR, C., OVALLES, C., GARCÍA, J. J. & ESPIDEL, Y. 1995. Reversible adsorption of carbon dioxide on amine surface-bonded silica gel. *Inorganica Chimica Acta,* 240**,** 183-189.

LEE, G.-J. & PYUN, S.-I. 2007. *Modern aspects of electrochemistry,* Springer , ISBN :978-0-387-46107-6.

LEE, T., OOI, C.-H., OTHMAN, R. & YEOH, F.-Y. 2014. Activated carbon fiber-The hybrid of carbon fiber and activated carbon. *Rev. Adv. Mater. Sci,* 36**,** 118-136.

LEE, W. & REUCROFT, P. 1999. Vapor adsorption on coal-and wood-based chemically activated carbons:(I) surface oxidation states and adsorption of H_2O. *Carbon,* 37**,** 7-14.

LENDZION-BIELUŃ, Z., CZEKAJŁO, Ł., SIBERA, D., MOSZYŃSKI, D., SREŃSCEK-NAZZAL, J., MORAWSKI, A. W., WROBEL, R. J., MICHALKIEWICZ, B., ARABCZYK, W. & NARKIEWICZ, U. 2018. Surface characteristics of KOH-treated commercial carbons applied for CO_2 adsorption. *Adsorption Science & Technology,* 36**,** 478-492.

LI, G., SINGH, R., XIAO, P. & WEBLEY, P. Binary Adsorption Equilibrium of Carbon Dioxide and Water Vapor on Zeolite HY. 10th International Conference on Fundamentals of Adsoroption, May, Awaji, Hyogo, Japan, 2010.

LI, G., XIAO, P., WEBLEY, P. A., ZHANG, J. & SINGH, R. 2009. Competition of CO_2/H_2O in adsorption based CO_2 capture. *Energy Procedia,* 1**,** 1123-1130.

LI, J., WANG, X., ZHAO, G., CHEN, C., CHAI, Z., ALSAEDI, A., HAYAT, T. & WANG, X. 2018. Metal–organic framework-based materials: superior adsorbents for the capture of toxic and radioactive metal ions. *Chemical Society Reviews,* 47**,** 2322-2356.

LIM, T.-C. 2009. Alignment of buckingham parameters to generalized Lennard-Jones potential functions. *Zeitschrift für Naturforschung A,* 64**,** 200-204.

LING, J., NTIAMOAH, A., XIAO, P., XU, D., WEBLEY, P. & ZHAI, Y. 2014. Overview of CO_2 capture from flue gas streams by vacuum pressure swing adsorption technology. *Austin J. Chem. Eng,* 1**,** 1-7.

LIU, H.-B., YANG, B. & XUE, N.-D. 2016. Enhanced adsorption of benzene vapor on granular activated carbon under humid conditions due to shifts in hydrophobicity and total micropore volume. *Journal of Hazardous Materials,* 318**,** 425-432.

LIU, J. 2017. Effective Carbon Adsorbents of Solid Looping Technologies for Post Combustion Carbon Capture, PhD thesis, The University of Nottingham (UK).

LIU, J., LIU, X., SUN, Y., SUN, C., LIU, H., STEVENS, L. A., LI, K. & SNAPE, C. E. 2018 a. High density and super ultra-microporous-activated carbon macrospheres with High volumetric capacity for CO_2 capture. *Advanced Sustainable Systems,* 2**,** 1700115.

LIU, J., SUN, N., SUN, C., LIU, H., SNAPE, C., LI, K., WEI, W. & SUN, Y. 2015a. Spherical potassium intercalated activated carbon beads for pulverised fuel CO_2 post-combustion capture. *Carbon,* 94**,** 243-255.

LIU, J., SUN, N., SUN, C., LIU, H., SNAPE, C., LI, K., WEI, W. & SUN, Y. 2015b. Spherical potassium intercalated activated carbon beads for pulverised fuel CO_2 post-combustion capture. *Carbon,* 94**,** 243-255.

LIU, J., TIAN, J., THALLAPALLY, P. K. & MCGRAIL, B. P. 2012. Selective CO_2 capture from flue gas using metal–organic frameworks-a fixed bed study. *The Journal of Physical Chemistry C,* 116**,** 9575-9581.

LIU, L., JIN, S., PARK, Y., PARK, Y. C. & LEE, C.-H. 2018b. Sorption equilibria and kinetics of CO_2, N_2, and H_2O on KOH-treated activated carbon. *Industrial & Engineering Chemistry Research,* 57**,** 17218-17225.

LIU, X., SUN, Y., LIU, J., SUN, C., LIU, H., XUE, Q., SMITH, E. & SNAPE, C. 2017. Potassium and zeolitic structure modified ultra-microporous adsorbent materials from a renewable feedstock with favorable surface chemistry for CO_2 capture. *ACS Applied Materials & Interfaces,* 9**,** 26826-26839.

LIZZIO, A. A., JIANG, H. & RADOVIC, L. R. 1990. On the kinetics of carbon (char) gasification: reconciling models with experiments. *Carbon,* 28**,** 7-19.

LOZANO-CASTELLO, D., CALO, J., CAZORLA-AMOROS, D. & LINARES-SOLANO, A. 2007. Carbon activation with KOH as explored by temperature programmed techniques, and the effects of hydrogen. *Carbon,* 45**,** 2529-2536.

LU, W., SCULLEY, J. P., YUAN, D., KRISHNA, R. & ZHOU, H.-C. 2013. Carbon dioxide capture from air using amine-grafted porous polymer networks. *The Journal of Physical Chemistry C,* 117**,** 4057-4061.

MADHU, R., VEERAMANI, V. & CHEN, S.-M. 2014. Heteroatom-enriched and renewable banana-stem-derived porous carbon for the electrochemical determination of nitrite in various water samples. *Scientific Reports,* 4**,** 4679.

MARCUS, G. H. 2019. Nuclear power around the world. *Nature Reviews Physics https://www.nature.com/articles/s42254-019-0020-z.*

MAROTO-VALER, M. M., TANG, Z. & ZHANG, Y. 2005. CO_2 capture by activated and impregnated anthracites. *Fuel Processing Technology,* 86**,** 1487-1502.

MARSH, H. & REINOSO, F. R. 2006. *Activated carbon,* Elsevier, ISBN: 978008-0455969.

MARTÍN, C., GARCIA, S., PIS, J., RUBIERA, F. & PEVIDA, C. 2011. Doped phenol-formaldehyde resins as precursors for precombustion CO_2 capture adsorbents. *Energy Procedia,* 4**,** 1222-1227.

MARTÍN, C. F., PLAZA, M. G., PIS, J., RUBIERA, F., PEVIDA, C. & CENTENO, T. 2010. On the limits of CO_2 capture capacity of carbons. *Separation and Purification Technology,* 74**,** 225-229.

MATERNE, T., DE BUYL, F. & WITUCKI, G. L. 2012. Organosilane technology in coating applications: review and perspectives. *Dow Corning Corporation., AGP11933, Form No*.

MATTHEW SPENCER, W. A. T. & COATS, A. E. 2014. UK offshore wind in the 2020s.

https://www.greenalliance.org.uk/resources/UK%20 offshore [accessed 12th April 2019].

MCCALLUM, C., BANDOSZ, T., MCGROTHER, S., MÜLLER, E. & GUBBINS, K. 1999. A molecular model for adsorption of water on activated carbon: comparison of simulation and experiment. *Langmuir,* 15**,** 533-544.

MCDOUGALL, G. 1991. The physical nature and manufacture of activated carbon. *Journal of the Southern African Institute of Mining and Metallurgy,* 91**,** 109-120.

MCFARLAND, J. R. & HERZOG, H. J. 2006. Incorporating carbon capture and storage technologies in integrated assessment models. *Energy Economics,* 28**,** 632-652.

MEGHANI, B. 2015. Moving Bed Temperature Swing Adsorption Processes for Post-Combustion CO_2 Capture, PhD thesis,The University of Nottingham (UK).

MENENDEZ-DIAZ, J. & MARTIN-GULLON, I. 2006. *Activated Carbon Surfaces in Environmental Remediation (eds TJ Bandosz),* Elsevier**,,** ISBN: 0-12-370536-3

METZ, B., DAVIDSON, O., DE CONINCK, H., LOOS, M. & MEYER, L. 2005. IPCC special report on carbon dioxide capture and storage. *https://www.osti.gov/biblio/20740954.* Intergovernmental Panel on Climate Change, Geneva (Switzerland). [accessed 12th April 2019].

MILLER, B., SONG, C., SCARONI, A. & XU, X. 2005. Influence of moisture on CO_2 separation from gas mixture by a nanoporous adsorbent based on polyethylenimine-modified molecular sieve MCM-41. *Industrial & Engineering Chemistry Research**,*** 8113-8119.

MOWLA, D., DO, D. & KANEKO, K. 2003. Adsorption of water vapor on activated carbon: a brief overview. *Chemistry and Physics of Carbon,* 28**,** 229-229.

NAKANISHI, Y., HONJOH, T. & HONJO, K. 1998. Surface hydrophobic active carbon and method for production thereof. Google Patents. https://patents.google.com/patent/US5837644A/en. [accessed 12th April 2019].

NTIAMOAH, A., LING, J., XIAO, P., WEBLEY, P. A. & ZHAI, Y. 2016. CO_2 capture by temperature swing adsorption: use of hot CO_2-rich gas for regeneration. *Industrial & Engineering Chemistry Research,* 55**,** 703-713.

O'KOYE, I., BENHAM, M. & THOMAS, K. 1997. Adsorption of gases and vapors on carbon molecular sieves. *Langmuir,* 13**,** 4054-4059.

OECD, I. 2016. Energy and Air Pollution: World Energy Outlook Special Report 2016.

https:// www.worldenergyoutlook.org/airpollution. [accessed 12th April 2019].

OGBUKA, C. P. 2013. Development of Solid Adsorbent Materials for CO_2 Capture, PhD thesis, The University of Nottingham (UK) .

OKIEIMEN, C. & OGBEIDE, S. The dependence on temperature of carbonization and chemical activation on characteristics of granular activated carbon characteristics. *Advanced Materials Research*, 62-64: 398-403.

OLAJIRE, A. A. 2010. CO_2 capture and separation technologies for end-of-pipe applications–a review. *Energy,* 35**,** 2610-2628.

OTOWA, T., TANIBATA, R. & ITOH, M. 1993. Production and adsorption characteristics of MAXSORB: high-surface-area active carbon. *Gas Separation & Purification,* 7**,** 241-245.

PACHAURI, R. K. & MEYER, L. 2014. Climate change 2014 Synthesis Report-Summary for Policymakers.

https://www.ipcc.ch/site/assets/uploads/2018/02/AR5_SYR_FINAL_SPM.pdf. [accessed 12th April 2019].

PIRNGRUBER, G. D., CASSIANO-GASPAR, S., LOURET, S., CHAUMONNOT, A. & DELFORT, B. 2009. Amines immobilized on a solid support for postcombustion CO_2 capture–a preliminary analysis of the performance in a VSA or TSA process based on the adsorption isotherms and kinetic data. *Energy Procedia,* 1**,** 1335-1342.

PLAZA, M., PEVIDA, C., ARENILLAS, A., RUBIERA, F. & PIS, J. 2007. CO_2 capture by adsorption with nitrogen enriched carbons. *Fuel,* 86**,** 2204-2212.

PLAZA, M. G., GONZÁLEZ, A. S., PEVIDA, C. & RUBIERA, F. 2014. Influence of water vapor on CO_2 adsorption using a biomass-based carbon. *Industrial & Engineering Chemistry Research,* 53**,** 15488-15499.

PLAZA, M. G., PEVIDA, C., MARTÍN, C. F., FERMOSO, J., PIS, J. & RUBIERA, F. 2010. Developing almond shell-derived activated carbons as CO_2 adsorbents. *Separation and Purification Technology*, 71**,** 102-106.

PLANTIER, F. D. R., MARQUES FERNANDES, K., MALHEIRO, C., DELANGHE, B. & MIQUEU, C. 2015. Water vapor adsorption/desorption on two fully characterized commercial activated carbons. Journal of Chemical & Engineering Data, 61, 622-627.

POOLE, C. F. 2003. *The essence of chromatography*, Elsevier. ISBN: 9780080505879.

POUR, A. A., SHARIFNIA, S., NEISHABORISALEHI, R. & GHODRATI, M. 2015. Performance evaluation of clinoptilolite and 13X zeolites in CO_2 separation from CO_2/CH_4 mixture. *Journal of Natural Gas Science and Engineering,* 26**,** 1246-1253.

PRAUCHNER, M. J. & RODRIGUEZ-REINOSO, F. 2008. Preparation of granular activated carbons for adsorption of natural gas. *Microporous and Mesoporous Materials,* 109**,** 581-584.

PRZEPIÓRSKI, J., SKRODZEWICZ, M. & MORAWSKI, A. 2004. High temperature ammonia treatment of activated carbon for enhancement of CO_2 adsorption. *Applied Surface Science*, 225**,** 235-242.

PUTTA, K. R., SVENDSEN, H. F. & KNUUTILA, H. K. 2017. Kinetics of CO_2 absorption in to aqueous MEA solutions near equilibrium. *Energy Procedia,* 114**,** 1576-1583.

QUANG, D. V., HATTON, T. A. & ABU ZAHRA, M. R. 2016. Thermally stable amine-grafted adsorbent prepared by impregnating 3-aminopropyltriethoxysilane on mesoporous silica for CO_2 capture. Industrial & Engineering Chemistry Research, International Conference on Carbon Dioxide Utilization .

RASHIDI, N. A., YUSUP, S. & HAMEED, B. H. 2013. Kinetic studies on carbon dioxide capture using lignocellulosic based activated carbon. *Energy,* 61**,** 440-446.

REED, S. J. B. 2005. *Electron microprobe analysis and scanning electron microscopy in geology*, Cambridge University Press, ISBN : 0-511-12414-7.

RISING, A. 2018. world-nuclear-performance-report-2018.pdf. World Nuclear Association .

https://www.world-nuclear.org/getmedia/b392d1cd-f7d2-4d54-9355-9a65f71a3419/performance-report.pdf.aspx. [accessed 19th April 2019].

RODRIGUEZ-REINOSO, F. 1998. The role of carbon materials in heterogeneous catalysis. *Carbon,* 36**,** 159-175.

RODRIGUEZ-REINOSO, F., MOLINA-SABIO, M. & MUNECAS, M. 1992. Effect of microporosity and oxygen surface groups of activated carbon in the adsorption of molecules of different polarity. *The Journal of Physical Chemistry,* 96**,** 2707-2713.

RODRÍGUEZ-MIRASOL, J., BEDIA, J., CORDERO, T. & RODRÍGUEZ, J. J. 2005. Influence of water vapor on the adsorption of VOCs on Lignin-Based activated carbons. *Separation Science and Technology,* 40**,** 3113-3135.

ROGELJ, J., DEN ELZEN, M., HÖHNE, N., FRANSEN, T., FEKETE, H., WINKLER, H., SCHAEFFER, R., SHA, F., RIAHI, K. & MEINSHAUSEN, M. 2016. Paris Agreement climate proposals need a boost to keep warming well below 2 C. *Nature,* 534**,** 631.

RUBIN, E. & DE CONINCK, H. 2005. IPCC special report on carbon dioxide capture and storage. UK: Cambridge University Press. TNO (2004): Cost Curves for CO_2 Storage, Part.

https://www.osti.gov/biblio/20740954. [accessed 17thApril 2019].

RUDZIŃSKI, W. 2013. Editorial: Effects of surface heterogeneity in adsorption and catalysis on solids. *Adsorption,* 19**,** 209-210.

SAADI, R., SAADI, Z., FAZAELI, R. & FARD, N. E. 2015. Monolayer and multilayer adsorption isotherm models for sorption from aqueous media. *Korean Journal of Chemical Engineering,* 32, 787-799.

SALAME, I. I. & BANDOSZ, T. J. 1999. Experimental study of water adsorption on activated carbons. *Langmuir,* 15**,** 587-593.

SAMANTA, A., ZHAO, A., SHIMIZU, G. K., SARKAR, P. & GUPTA, R. 2011. Post-combustion CO_2 capture using solid sorbents: a review. *Industrial & Engineering Chemistry Research,* 51**,** 1438-1463.

SÁNCHEZ-SOTO, P. J., AVILÉS, M., DEL RıO, J., GINÉS, J., PASCUAL, J. & PÉREZ-RODRıGUEZ, J. 2001. Thermal study of the effect of several solvents on polymerization of acrylonitrile and their subsequent pyrolysis. *Journal of Analytical and Applied Pyrolysis,* 58**,** 155-172.

SCHWARZ, J. A. & CONTESCU, C. I. 1999. *Surfaces of nanoparticles and porous materials,* CRC press,ISBN : 9780367800567.

SEMBA, K. & MORITA, H. 2002. Chemical reactivity of vinyltrimethoxysilane in aerosol particle formation with acrolein under two-photon excitation. *Journal of Photochemistry and Photobiology A: Chemistry,* 146**,** 141-147.

ŞENTORUN-SHALABY, Ç. D., UÇAK-ASTARLıOGˇLU, M. G., ARTOK, L. & SARıCı, C. 2006. Preparation and characterization of activated carbons by one-step steam pyrolysis/activation from apricot stones. *Microporous and Mesoporous Materials,* 88**,** 126-134.

SEVILLA, M., VALLE-VIGÓN, P. & FUERTES, A. B. 2011. N-doped polypyrrole-based porous carbons for CO_2 capture. *Advanced Functional Materials,* 21**,** 2781-2787.

SHAFEEYAN, M. S., DAUD, W. M. A. W., HOUSHMAND, A. & SHAMIRI, A. 2010. A review on surface modification of activated carbon for carbon dioxide adsorption. *Journal of Analytical and Applied Pyrolysis,* 89**,** 143-151.

SHEN, W., HE, Y., ZHANG, S., LI, J. & FAN, W. 2012. Yeast-based microporous carbon materials for carbon dioxide capture. *ChemSusChem,* 5**,** 1274-1279.

SHER, F. 2017. Design and Operation of a 20 kWth Fluidised Bed Combustor for Biomass-Oxyfuel Combustion, PhD thesis,The University of Nottingham (UK).

SIM, K., LEE, N., KIM, J., CHO, E.-B., GUNATHILAKE, C. & JARONIEC, M. 2015. CO_2 adsorption on amine-functionalized periodic mesoporous benzenesilicas. *ACS Applied Materials & Interfaces,* 7, 6792-6802.

SINGH, G., KIM, I. Y., LAKHI, K. S., SRIVASTAVA, P., NAIDU, R. & VINU, A. 2017. Single step synthesis of activated bio-carbons with a high surface area and their excellent CO_2 adsorption capacity. *Carbon,* 116, 448-455.

SJOSTROM, S. & KRUTKA, H. 2010. Evaluation of solid sorbents as a retrofit technology for CO_2 capture. *Fuel,* 89, 1298-1306.

SMIT, B., REIMER, J. A., OLDENBURG, C. M. & BOURG, I. C. 2014. *Introduction to Carbon Capture and Sequestration, World Scientific,* ISBN: 978-1-78326-330-1.

SONGOLZADEH, M., SOLEIMANI, M., TAKHT RAVANCHI, M. & SONGOLZADEH, R. 2014. Carbon dioxide separation from flue gases: a technological review emphasizing reduction in greenhouse gas emissions. *The Scientific World Journal,* Volume 2014, Article ID 828131, 34 pages.

SORRELS, J. L., BAYNHAM, A., RANDALL, D. D. & SCHAFFNER, K. S. 2018. Carbon Adsorbers.

https://www.epa.gov/sites/production/files/201810/documents/final_carbonadsorberschapter_7thedition.pdf[accessed 17th May 2019].

STARKIE, C. 2016. The Design, Synthesis and Characterisation of Amine Functionalised Silica Adsorbents for Post Combustion Carbon Capture, PhD thesis,The University of Nottingham (UK).

STRELKO, V. 1999. Selective Removal of Heavy Metals Using Novel Active Carbons, PhD thesis, Loughborough University (UK).

SUN, K., LENG, C.-Y., JIANG, J.-C., BU, Q., LIN, G.-F., LU, X.-C. & ZHU, G.-Z. 2017. Microporous activated carbons from coconut shells produced by self-activation using the pyrolysis gases produced from them, that have an excellent electric double layer performance. *New Carbon Materials,* 32**,** 451-459.

SUN, N., TANG, Z., WEI, W., SNAPE, C. E. & SUN, Y. 2015. Solid adsorbents for low-temperature CO_2 capture with low-energy penalties leading to more effective integrated solutions for power generation and industrial processes. *Frontiers in Energy Research,* 3**,** 9.

SUN, Y. & ZHOU, H.-C. 2015. Recent progress in the synthesis of metal–organic frameworks. *Science and Technology of Advanced Materials,* 16**,** 054202.

SUPEKAR, S. D. & SKERLOS, S. J. 2015. Reassessing the efficiency penalty from carbon capture in coal-fired power plants. *Environmental Science & Technology,* 49**,** 12576-12584.

SWANN, G. E. & PATWARDHAN, S. 2011. Application of Fourier Transform Infrared Spectroscopy (FTIR) for assessing biogenic silica sample purity in geochemical analyses and palaeoenvironmental research. *Climate of the Past,* 7, 65-74.

TANDE, B., SEAMES, W. & BENSON, S. 2013. Efficient Regeneration of Physical and Chemical Solvents for CO_2 Capture. University. of North Dakota, Grand Forks, (USA),

https://www.osti.gov/biblio/1113825. [accessed 17th April 2019].

TAZIBET, S., BOUCHEFFA, Y. & LODEWYCKX, P. 2013. Heat treatment effect on the textural, hydrophobic and adsorptive properties of activated carbons obtained from olive waste. *Microporous and Mesoporous Materials,* 170, 293-298.

THOMMES, M., KANEKO, K., NEIMARK, A. V., OLIVIER, J. P., RODRIGUEZ-REINOSO, F., ROUQUEROL, J. & SING, K. S. 2015. Physisorption of gases, with special reference to the evaluation of surface area and pore size distribution (IUPAC Technical Report). *Pure and Applied Chemistry,* 87**,** 1051-1069.

TRAVIS, W. 2015. Porous Carbon Based Solid Adsorbents for Carbon Dioxide Capture, PhD thesis, University College London (UK).

UDDIN, K., ISLAM, M. A., MITRA, S., LEE, J.-B., THU, K., SAHA, B. B. & KOYAMA, S. 2018. Specific heat capacities of carbon-based adsorbents for adsorption heat pump application. *Applied Thermal Engineering,* 129**,** 117-126.

UN 2018. Compilation and synthesis of third biennial reports of Parties included in Annex I to the Convention .https://unfccc.int/sites/default/files/resource/SBI2018_inf8a1.pdf [accessed 17th May 2019].

UN 2019. World Economic Situation and Prospects. United Nations, Economic Analysis and Policy Division, Department of Economic and Social Affairs. https://www.un.org/development/desa/publications/publication/world-economic-situation-and-prospects-2019 [accessed 17th April 2019].

VAN DER HEIDE, P. 2014. *Secondary ion mass spectrometry: an introduction to principles and practices*, John Wiley & Sons , ISBN : 978-1-118-48048-9.

VENEMAN, R., FRIGKA, N., ZHAO, W., LI, Z., KERSTEN, S. & BRILMAN, W. 2015. Adsorption of H_2O and CO_2 on supported amine sorbents. *International Journal of Greenhouse Gas Control,* 41**,** 268-275.

VIJAYAN, S., MAKESHKUMAR, M. & SRIDHAR, K. 2012. Physical and chemical analysis of activated carbon preparation from coconut shell charcoal and usage-a case study. *International Journal of Advanced Scientific Research and Technology* 3**,** 168-175.

VISION, W. 2015. A new era for wind power in the United States. *US Department of Energy.*

https://www.energy.gov/sites/prod/files/WindVision_Report_final.pdf. [accessed 17th April 2019].

VISWANATHAN, B., NEEL, P. I. & VARADARAJAN, T. 2009. Methods of activation and specific applications of carbon materials. National Centre for Catalysis Research -IIT Madras, India, Chennai.

VOLDSUND, M., GARDARSDOTTIR, S. O., DE LENA, E., PÉREZ-CALVO, J.-F., JAMALI, A., BERSTAD, D., FU, C., ROMANO, M., ROUSSANALY, S. & ANANTHARAMAN, R. 2019. Comparison of technologies for CO_2 capture from cement production—Part 1: *Technical Evaluation. Energies*, 12, 559.

VU, D.-L., SEO, J.-S., LEE, H.-Y. & LEE, J.-W. 2017. Activated carbon with hierarchical micro–mesoporous structure obtained from rice husk and its application for lithium–sulfur batteries. *RSC Advances,* 7**,** 4144-4151.

WANG, J., HUANG, L., YANG, R., ZHANG, Z., WU, J., GAO, Y., WANG, Q., O'HARE, D. & ZHONG, Z. 2014. Recent advances in solid sorbents for CO_2 capture and new development trends. *Energy & Environmental Science,* 7**,** 3478-3518.

WANG, J. & KASKEL, S. 2012. KOH activation of carbon-based materials for energy storage. *Journal of Materials Chemistry,* 22**,** 23710-23725.

WEBB, P. & ORR, C. 1997. Surface area and pore structure by gas adsorption. *Analytical Methods in Fine Particle Technology***,** 53-153.

WEBB, P. A. & ORR, C. 2008. Modern methods of particle characterization. *Chapter,* 1**,** 1-17.1998.

WEI, L., GAO, Z., JING, Y. & WANG, Y. 2013. Adsorption of CO_2 from simulated flue gas on pentaethylenehexamine-loaded mesoporous silica support adsorbent. *Industrial & Engineering Chemistry Research,* 52**,** 14965-14974.

WEI, H., DENG, S., HU, B., CHEN, Z., WANG, B., HUANG, J. & YU, G. 2012. Granular bamboo-derived activated carbon for high CO_2 adsorption: the dominant role of narrow micropores. *ChemSusChem*, 5, 2354-2360.

WERTHEIMER, M., KLEMBERG-SAPIEHA, J., CERNY, J. & LIANG, S. 1998. Modification of active carbon by hydrophobic plasma polymers: II fabric substrates. *Plasmas and Polymers,* 3**,** 151-163.

WHO 2018. Global status report on road safety 2018. https://apps.who.int/iris/bitstream/handle/10665/277370/WHO-NMH-NVI-18.20-eng.pdf. World Health Organization. [accessed 5th April 2019].

WICKRAMARATNE, N. P. & JARONIEC, M. 2013. Activated carbon spheres for CO_2 adsorption. *ACS Applied Materials & Interfaces,* 5**,** 1849-1855.

WU, F., ARGYLE, M. D., DELLENBACK, P. A. & FAN, M. 2018. Progress in O_2 separation for oxy-fuel combustion–a promising way for cost-effective CO_2 capture: A review. *Progress in Energy and Combustion Science,* 67**,** 188-205.

XIAO, P., WILSON, S., XIAO, G., SINGH, R. & WEBLEY, P. 2009. Novel adsorption processes for carbon dioxide capture within a IGCC process. *Energy Procedia,* 1**,** 631-638.

XIE, Z., WANG, F., ZHAO, N., WEI, W. & SUN, Y. 2011. Hydrophobisation of activated carbon fiber and the influence on the adsorption selectivity towards carbon disulfide. *Applied Surface Science,* 257**,** 3596-3602.

XING, W., LIU, C., ZHOU, Z., ZHOU, J., WANG, G., ZHUO, S., XUE, Q., SONG, L. & YAN, Z. 2014. Oxygen-containing functional group-facilitated CO_2 capture by carbide-derived carbons. *Nanoscale Research Letters,* 9**,** 189.

XU, W. 2018. Literature Survey and the Conceptual Design of an Unmanned Arctic Ocean Scientific Vessel, MSc thesis, Florida Atlantic University (USA).

XU, X., SONG, C., MILLER, B. G. & SCARONI, A. W. 2005. Influence of moisture on CO_2 separation from gas mixture by a nanoporous adsorbent based on polyethylenimine-modified molecular sieve MCM-41. *Industrial & Engineering Chemistry Research,* 44**,** 8113-8119.

YANG, H., XU, Z., FAN, M., GUPTA, R., SLIMANE, R. B., BLAND, A. E. & WRIGHT, I. 2008. Progress in carbon dioxide separation and capture: A review. *Journal of Environmental Sciences,* 20**,** 14-27.

YANG, R. T. 2013. *Gas separation by adsorption processes,* Butterworth-Heinemann, ISBN;0-409-90004-4.

YEHASKEL, A. 1978. *Activated carbon: Manufacture and regeneration,* Noyes Data Corporation Park Ridge, New Jersey, USA, SBN-13: 978-0815507253.

YIN, C. & YAN, J. 2016. Oxy-fuel combustion of pulverized fuels: Combustion fundamentals and modeling. *Applied Energy,* 162**,** 742-762.

YIN, J., OVERPECK, J., PEYSER, C. & STOUFFER, R. 2018. Big Jump of Record Warm Global Mean Surface Temperature in 2014-2016 Related to Unusually Large Oceanic Heat Releases. *Geophysical Research Letters,* 45**,** 1069-1078.

YOSHIDA, W., CASTRO, R. P., JOU, J.-D. & COHEN, Y. 2001. Multilayer alkoxysilane silylation of oxide surfaces. *Langmuir,* 17**,** 5882-5888.

ZÁRATE, A., PERALTA, R. A., BAYLISS, P. A., HOWIE, R., SÁNCHEZ-SERRATOS, M., CARMONA-MONROY, P., SOLIS-IBARRA, D., GONZÁLEZ-ZAMORA, E. & IBARRA, I. A. 2016. CO_2 capture under humid conditions in NH 2-MIL-53 (Al): the influence of the amine functional group. *RSC Advances,* 6**,** 9978-9983.

ZARUBIN, D. 1999. Infrared spectra of hydrogen bonded hydroxyl groups in silicate glasses. A re-interpretation. *Physics and Chemistry of Glasses,* 40**,** 184-192.

ZHANG, W., LIU, H., SUN, C., DRAGE, T. C. & SNAPE, C. E. 2014. Capturing CO_2 from ambient air using a polyethyleneimine–silica adsorbent in fluidized beds. *Chemical Engineering Science,* 116**,** 306-316.

ZHAI, H. & RUBIN, E. S. 2018. Systems analysis of physical absorption of CO_2 in ionic liquids for pre-combustion carbon capture. *Environmental science & technology*, 52, 4996-5004.

ZHANG, W., LIU, H., SUN, Y., CAKSTINS, J., SUN, C. & SNAPE, C. E. 2016. Parametric study on the regeneration heat requirement of an amine-based solid adsorbent process for post-combustion carbon capture. *Applied Energy,* 168**,** 394-405.

ZHOU, Y. 2015. *Eco-and renewable energy materials*, Springer , ISBN : 978-7-03-035260-6.

ZHURAVLEV, L. 2000. The surface chemistry of amorphous silica. Zhuravlev model. *Colloids and Surfaces A: Physicochemical and Engineering Aspects,* 173**,** 1-38.

ZHURAVLEV, L. & POTAPOV, V. 2006. Density of silanol groups on the surface of silica precipitated from a hydrothermal solution. *Russian Journal of Physical Chemistry,* 80**,** 1119-1128.

Appendix A

BET Isotherm Analysis

The plot for the linearised version of the BET equation is given in Figure A.1 for CS sample with a trend line included. The slope of the trend line is 0.004768 ± 0.000001 g cm^{-3} STP and the y-intercept is 0.000004 ± 0.000000 g cm^{3} STP.

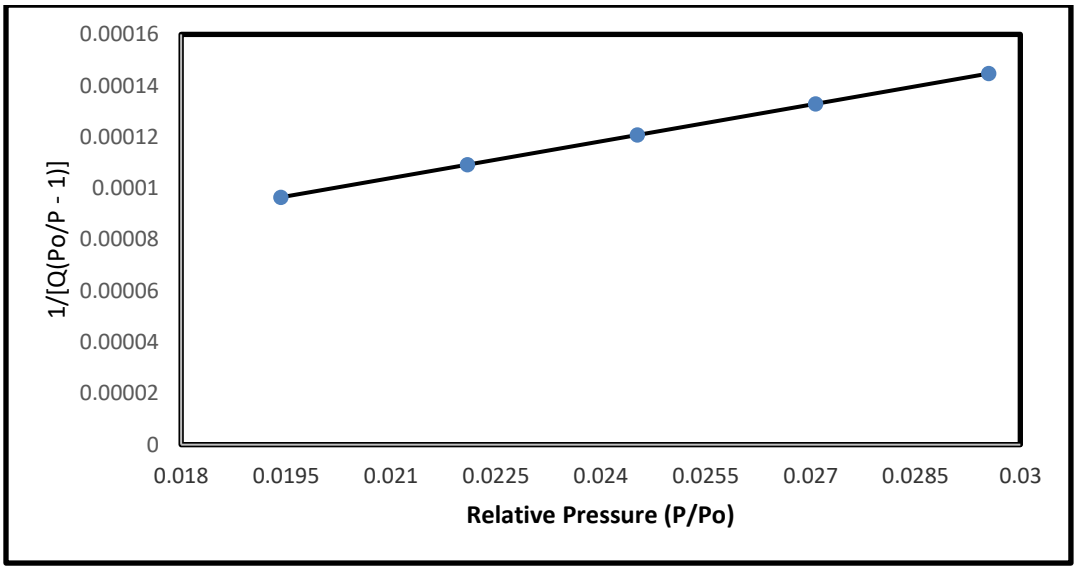


Figure A.1 linearised version of the BET equation

The plot for the linearised version of the BET equation is given in Figure A.2 for CSK sample with a trend line included. The slope of the trend line is 0.003410 ± 0.000000 g/cm³ STP g cm^{-3} STP and the y-intercept is 0.000004 ± 0.000000 g cm^{3} STP.

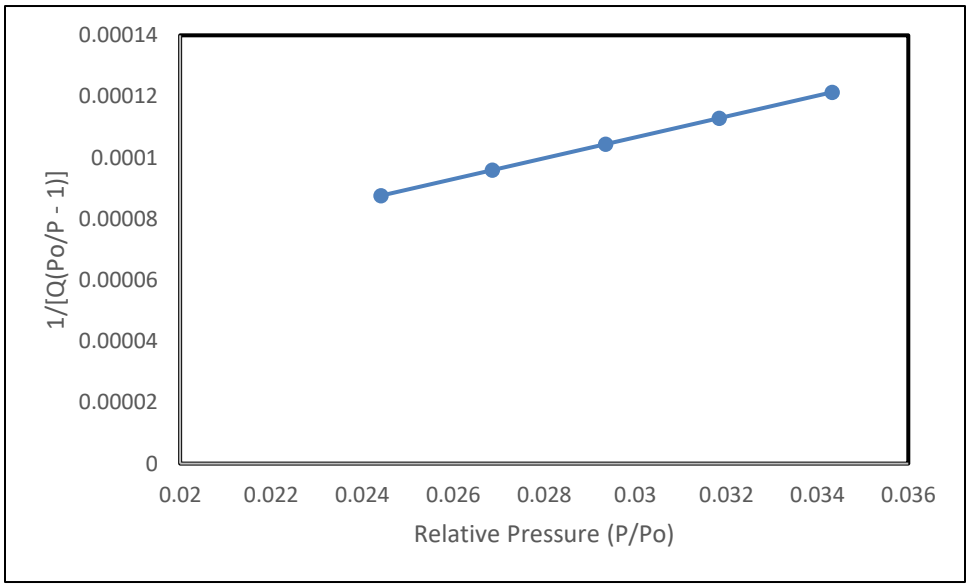


Figure A.2 linearised version of the BET equation

Appendix B

Table A.1: Parameters for dual site Langmuir model at 0 ^{o}C (Figure 4.7).

Samples	qS,A	qS,B	bA	bB
CS	0.451748814	5.352034469	0.029521451	0.000717462
CSK	0.634549554	6.403056024	0.102161951	0.000959709
CSKV	0.230870459	6.22659096	0.057180811	0.000525546
CSKV450	0.346530556	5.752588053	0.049001569	0.000688224

Table A.2: Parameters for dual site Langmuir model at 25 ^{o}C (Figure 4.8).

Samples	qS,A	qS,B	bA	bB
CS	0.792499653	6.026337727	0.046910917	0.001186681
CSK	1.099128389	8.052804588	0.135526279	0.001323291
CSKV	0.370749871	0.06368832	7.166744829	0.000769568
CSKV450	0.734315508	0.051197023	7.228419827	0.000928633

Appendix C

Table A. 1: Pore texture parameters for PR.

Samples	S_{BET} (cm^2/g)	V_{Micro} (cm^3/g)	V_{Meso} (cm^3/g)	V_{Total} (cm^3/g)
PR	1204	0.43	0.03	0.46

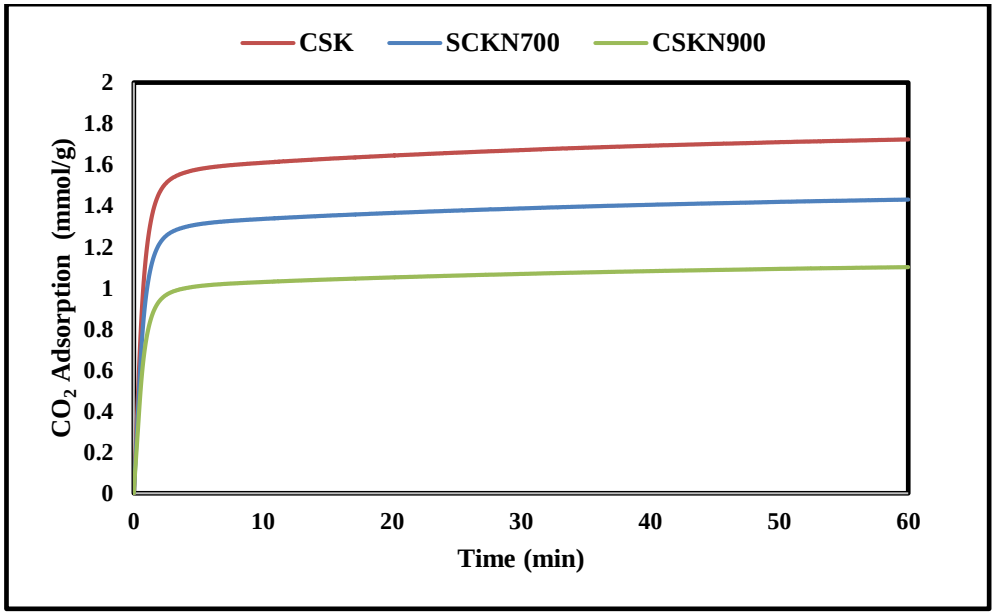


Figure C.1: CO_2 adsorption of the ACs using TGA in 15% CO_2 and 85% N_2 at 25 ºC.

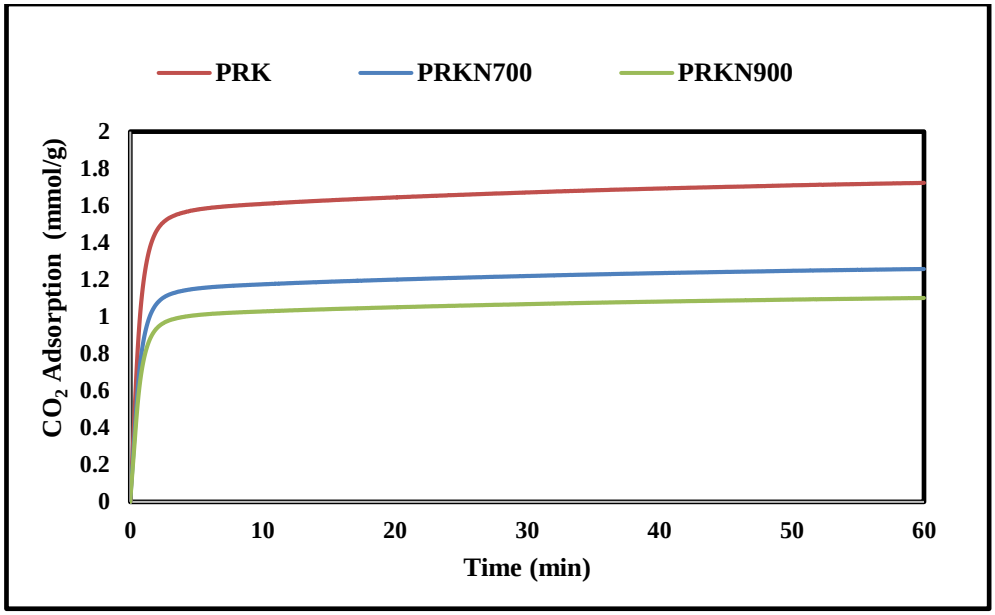


Figure C.2: CO_2 adsorption of the PRs using TGA in 15 % CO_2 and 85 % N_2 at 25 ^oC.

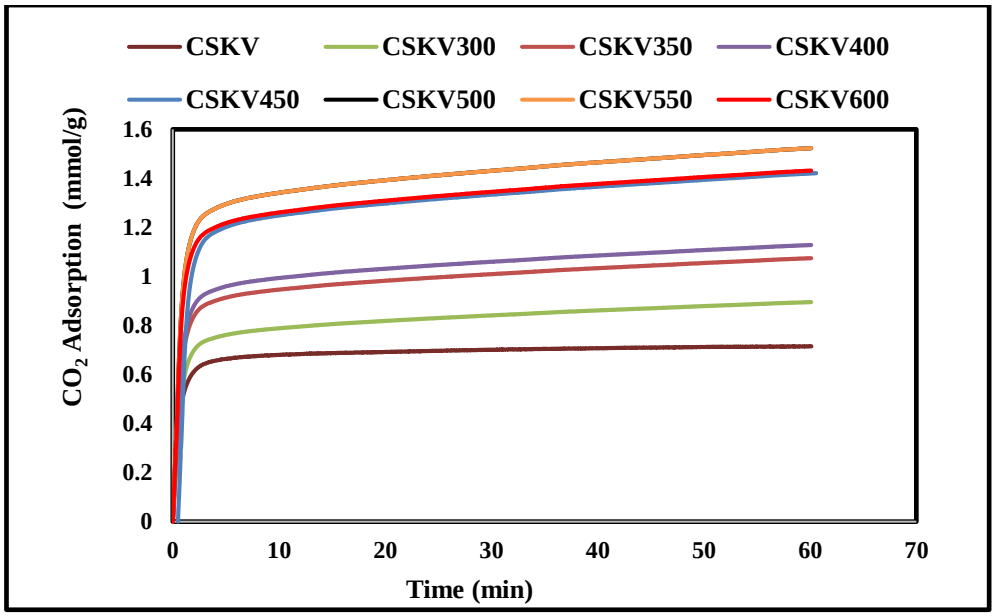


Figure C.3: CO_2 adsorption of the ACs using TGA in 15 % CO_2 and 85 % N_2 at 25 ^oC.

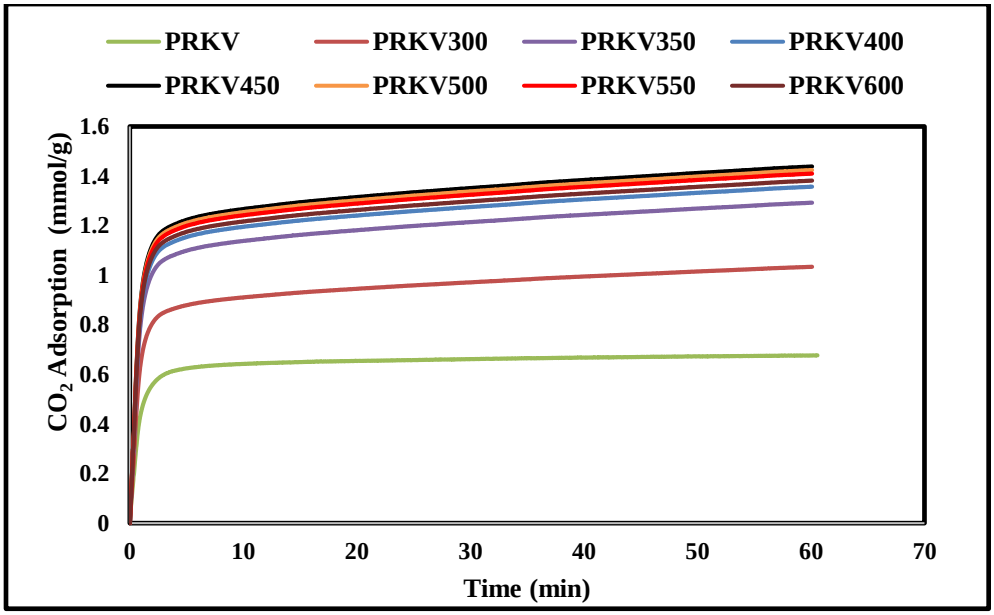


Figure C.4: CO_2 adsorption of the PRs using TGA in 15 % CO_2 and 85 % N_2 at 25 ^oC.

Appendix D

1: Select gas 1
2: Mass flow 100.00 mL/min
3: Ramp 30.00 °C/min to 450.00 °C
4: Isothermal for 60.00 min
5: Ramp 30.00 °C/min to 150.00 °C
6: Isothermal for 10.00 min
7: Ramp 20.00 °C/min to 25.00 °C
8: Equilibrate at 25.00 °C
9: Select gas 2
10: Mass flow 100.00 mL/min
11: Isothermal for 60.00 min

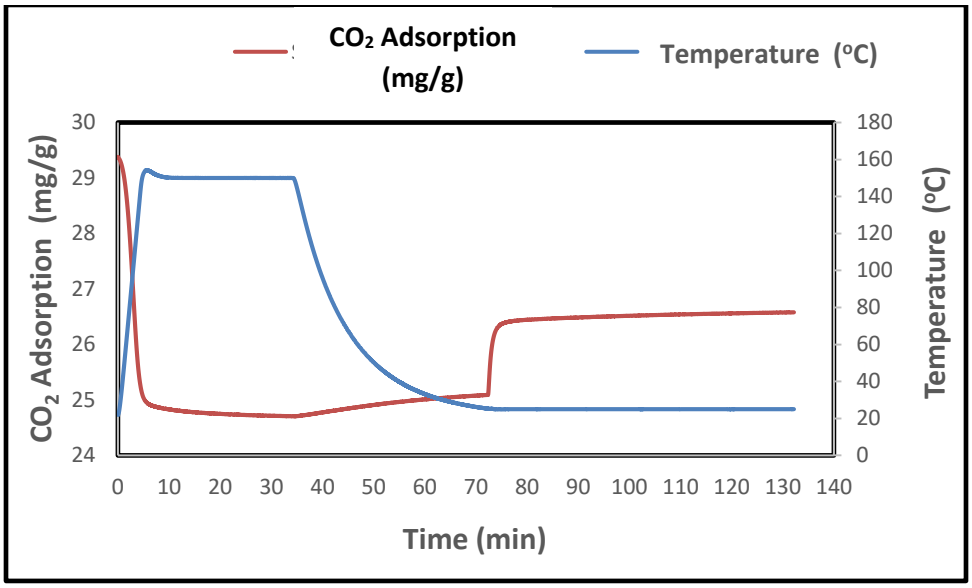


Figure D.1: CO_2 adsorption of the ACs using TGA in 15 % CO_2 and 85 % N_2 at 25 °C.

Appendix E

No statistically significant correlation was found between the CO_2 adsorption capacity of coated CSK and surface area, micropore volume or total pore volume where the correlation coefficients (R^2) were 0.1045, 0.042 and 0.0062, respectively to each variable (Figures 6.25-6.27). Similarly, H_2O uptake did not show a clear relations with the surface area, micropore volume and total pore volume and the correlation coefficients being 0.1388, 0.0148 and 0.0182 respectively (Figures 6.28 and 6.30). These results indicate that the adsorption of carbon dioxide and water vapour on the coated activated carbon surface depends on the surface chemistry rather than the porosity of these materials.

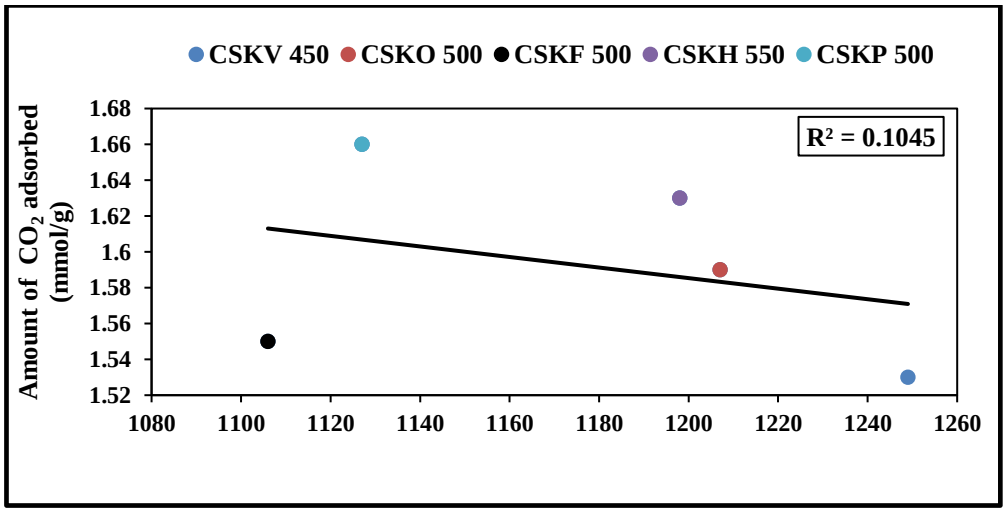


Figure E.1: CO_2 adsorption capacity in relation to the BET surface area at ambient temperature and pressure.

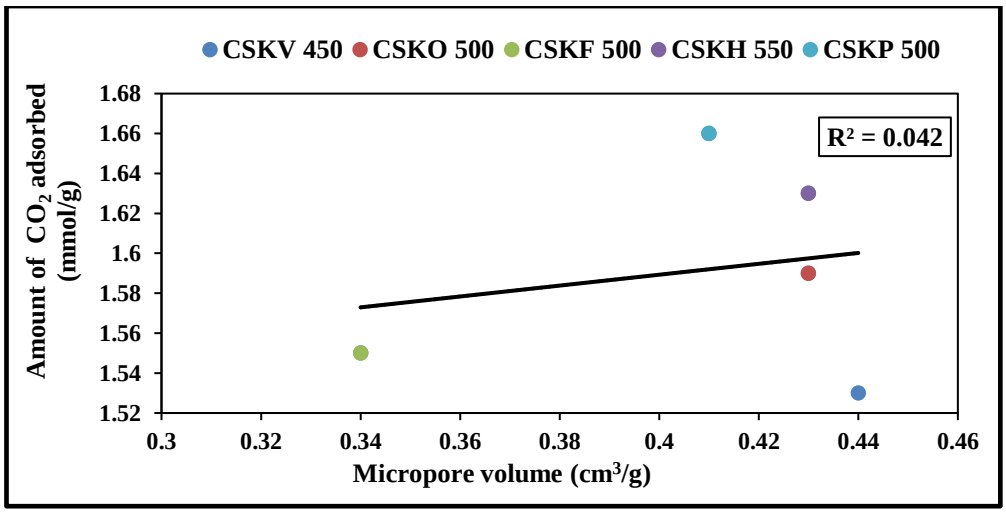


Figure E.2: CO_2 adsorption capacity in relation to micropore volume at ambient temperature and pressure.

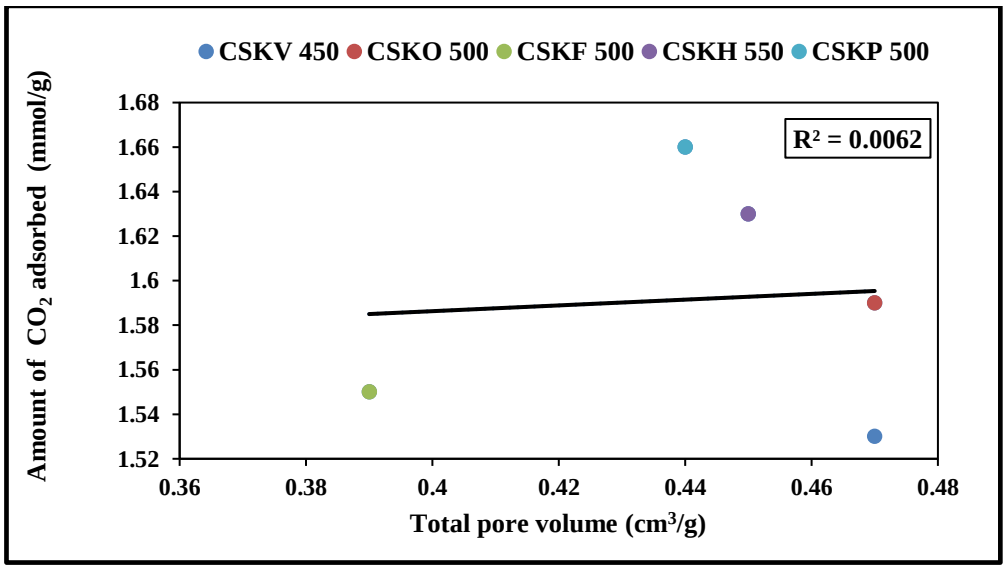


Figure E.3: CO_2 adsorption capacity in relation to total pore volume at ambient temperature and pressure.

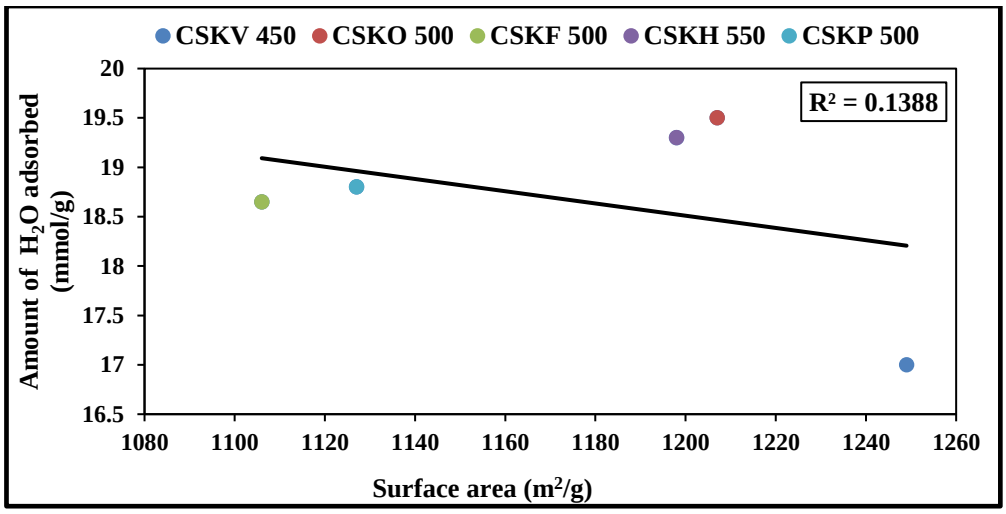


Figure E.4: H_2O uptake capacity in relation to the BET surface area at ambient temperature and pressure.

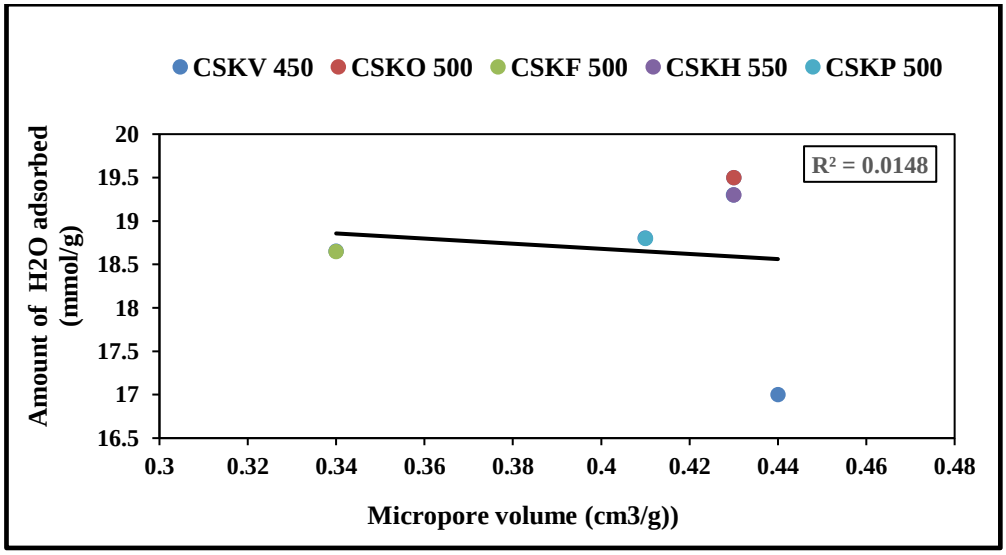


Figure E.5: H_2O uptake capacity in relation to micropore volume at ambient temperature and pressure.

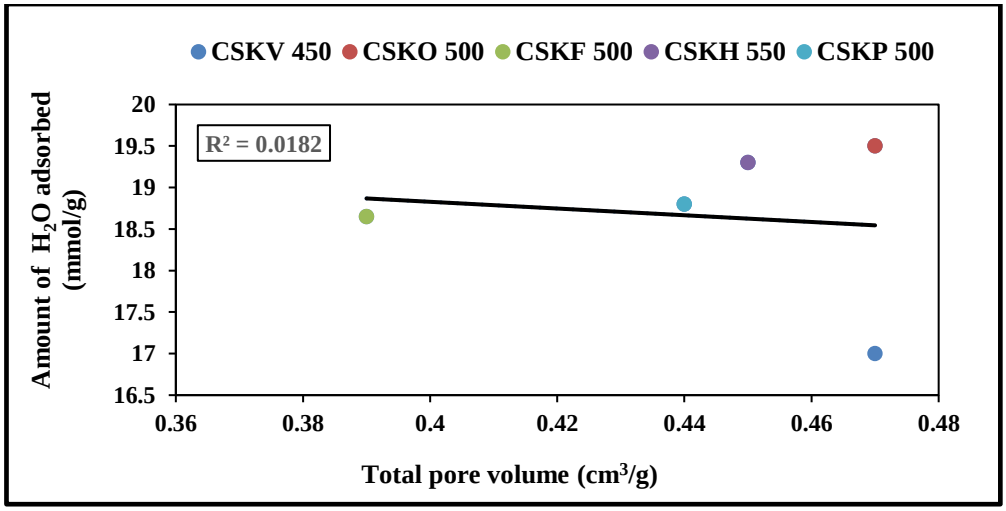


Figure E.6: H_2O uptake capacity in relation to total pore volume at ambient temperature and pressure